DYNAMIC WAKE DISTORTION MODEL FOR HELICOPTER MANEUVERING FLIGHT

A Thesis
Presented to
The Academic Faculty

by

Jinggen Zhao

In Partial Fulfillment
of the Requirements for the Degree
Doctor of Philosophy

School of Aerospace Engineering
Georgia Institute of Technology
March 2005

DYNAMIC WAKE DISTORTION MODEL FOR HELICOPTER MANEUVERING FLIGHT

Approved by:

Dr. J.V.R. Prasad, Chair
School of Aerospace Engineering
Georgia Institute of Technology

Dr. Daniel P Schrage
School of Aerospace Engineering
Georgia Institute of Technology

Dr. Lakshmi N Sankar
School of Aerospace Engineering
Georgia Institute of Technology

Dr. Chengjian He
Advanced Rotorcraft Technology, Inc.

Dr. David A. Peters
Washington University

Date Approved: March 25, 2005

ACKNOWLEDGEMENTS

I would first like to express my deepest appreciation to Professor J.V.R Prasad who has been my advisor on this research, for his wisdom, patience and generosity, which have been uniquely instrumental in the successful completion of this thesis.

I would also like to thank Professor David A. Peters from Washington University for his special contributions of knowledge and advisement on this research. His expertise in this field is unequaled, and his enthusiasm and patience to help enrich and enlighten others is boundless.

I would also like to express my sincere gratitude to my thesis committee members: Professor Daniel P. Schrage, Professor Lakshmi N. Sankar and Dr. Chengjian He of ART (Advance Rotorcraft Technology, Inc.) for taking their time to read and evaluate my thesis. I have gained much from their valuable suggestions.

Also, I would like to extend my appreciation to Professor Guohua Xu of NUAA (Nanjing University of Aeronautics and Astronuatics, China) and Dr. Jeffrey D. Keller for their valuable discussions and suggestions, to Dr. Mark B. Tischler of the Aeroflightdynamics Directorate at the NASA Ames Research Center for his help with the UH-60 Black Hawk helicopter flight test data.

To the students and scholars in Georgia Institute of Technology that have been my friends, I thank you all dearly for your support and help. These people include, but are not limited to: Jidong Kang, Chen Zhang, Hong Xin, Chenghuai Lu, Yi He, Yongjun Huang, Zeping Wu, Peng Zhang, Xianghui Huang, Yang Lu, Chang Chen, Matt Johnson, Geoffrey Jeram, Surresh Kannan, Suraj Unnikrishnan, Ilkay Yavrucuk and Manuj Dhingra.

Finally but most importantly, I would like to thank my wife and parents in China for their love, support and encouragement. Without them, I could not have succeeded in completing this thesis.

This research was conducted under the US Army/NASA sponsored NRTC Center of

TABLE OF CONTENTS

LIST OF TABLES

LIST OF FIGURES

LIST OF SYMBOLS AND ABBREVIATIONS

$[A_F]$ influence coefficient matrix for fuselage interference velocity due to fuselage pressure

a_{sound} sound velocity

$[A_{UA}]$ coefficient matrix in the state-space airfoil unsteady aerodynamics model

$\bar{\Gamma}$ rotor bound circulation, nondimensional

$\bar{\gamma}$ nondimensional vorticity density around vortex tube

$\bar{\gamma}_0$ nondimensional mean vorticity density around vortex tube

$\bar{\Gamma}_0$ mean rotor bound circulation, nondimensional

$\bar{\gamma}_{1c}$ longitudinal cyclic variation of vorticity density around vortex tube, nondimensional

$\bar{\Gamma}_{1c}$ longitudinal cyclic variaton of rotor bound circulation, nondimensional

$\bar{\gamma}_{1s}$ lateral cyclic variation of vorticity density around vortex tube, nondimensional

$\bar{\Gamma}_{1s}$ lateral cyclic variaton of rotor bound circulation, nondimensional

$\bar{b}$ normalized half-width of the fuselage panel, dimensionless on rotor radius R

$\bar{e}$ flap hinge offset, dimensionless on Rotor radius R

$\bar{h}$ normalized height of the rotor center above the fuselage panel, dimensionless on rotor radius R

$\bar{l}^{HT/TR}$ longitudinal distance between tail rotor center and the aerodynamic center of horizontal tail, in the tail rotor coordinate system

$\bar{l}^{VT/MR}$ longitudinal distance between main rotor center and the aerodynamic centers of vertical tail/tail rotor, in the main rotor coordinate system

$\bar{p}$ nondmiensional roll rate, $\frac{p}{\Omega}$

$\bar{P}$ normalized associated Legendre function of the first kind

$\bar{q}$ nondmiensional pitch rate, $\frac{q}{\Omega}$

$\bar{Q}$ normalized associated Legendre function of the second kind

$\bar{r}$ radial position on rotor disk, dimensionless on rotor radius R

$\bar{r}_0$ vortex tube radius, normalized by rotor radius R

$\bar{V}$ mass flow parameter associated with the first and higher harmonics of inflow

β_{1c}	longitudinal tip-path-plane tilt angle, positive foward
β_{1s}	lateral tip-path-plane tilt angle, positive towards retreating side
β_{pg}	Prandtl-Glauert compressibility factor, $\sqrt{1 - M_{mach}^2}$
$[B_F]$	influence coefficient matrix for fuselage pressure due to rotor pressure
$[B_{UA}]$	coefficient matrix in the state-space airfoil unsteady aerodynamics model
c	airfoil chord length
$[C]_{c1}$	matrix of coupling effect between rotor inflow and longitudinal wake curvature
$[C]_{cX}$	matrix of coupling effect between rotor inflow, longitudinal wake curvature and linear wake skew
$[C]_{cX^2}$	matrix of coupling effect between rotor inflow, longitudinal wake curvature and quadratic wake skew
χ	steady wake skew angle
C_L	rotor roll moment coefficient
C_M	rotor pitch moment coefficient
C_n	airfoil section normal force coefficient
$[C]_{s1}$	matrix of coupling effect between rotor inflow and lateral wake curvature
$[C]_{sX}$	matrix of coupling effect between rotor inflow, lateral wake curvature and linear wake skew
$[C]_{sX^2}$	matrix of coupling effect between rotor inflow, lateral wake curvature and quadratic wake skew
C_T	rotor thrust coefficient
$[C_{UA}]$	coefficient matrix in the state-space airfoil unsteady aerodynamics model
$\Delta\alpha_j^r, \Delta\beta_j^r$	perturbation of induced inflow coefficients due to rotor wake distortion effect
$[\Delta L]$	perturbation of the inflow gain matrix during maneuvering flight
$[\Delta L_1]$	coupling between wake curvatures and rotor mean loading
$[\Delta L_2]$	coupling between wake curvature-wake skew and rotor mean loading
$[\Delta L_3]$	coupling between wake curvature-wake skew and rotor cyclic loading
$\Delta\lambda_0$	rotor mean inflow perturbation during maneuvering flight
$\Delta\lambda_{1c}$	rotor longitudinal inflow gradient perturbation during maneuvering flight

$\Delta\lambda_{1s}$	rotor lateral inflow gradient perturbation during maneuvering flight
$\Delta\nu_{y_{MR}}^{VT}$	side wash indued at the aerodynamic center of vertical tail and/or tail rotor due to main rotor wake curvature effect, expressed along the main rotor $y-$ axis
$\Delta\nu_{y_{TR}}^{HT}$	up/down wash indued at the aerodynamic center of horizontal tail due to tail rotor wake curvature effect, expressed along the tail rotor $y-$ axis
$\Delta\theta$	blade elastic twist about feathering hinge due to the gyroscopic feathering moment, $\Delta\theta = \Delta\theta_{1c}cos\psi + \Delta_{1s}sin\psi$
Δv_z	inflow perturbations due to wake distortions
$[D_{UA}]$	coefficient matrix in the state-space airfoil unsteady aerodynamics model
$[F]$	influence coefficient matrix for fuselage interference velocity due to rotor pressure
f_j^{rc}, f_j^{rs}	fuselage interference velocity coefficients
γ_{lock}	blade Lock number
$(\hat{\nu}, \hat{\eta}, \hat{\psi})$	fuselage panel ellipsoidal coordinates, nondimensional
$i_0^{MR}, i_1^{MR}, i_2^{MR}$	interference coefficients in the sidewash expression induced at vertical tail and/or tail rotor due to main rotor wake curvature effect
$i_0^{TR}, i_1^{TR}, i_2^{TR}$	interference coefficients in the up/down wash expression induced at horizontal tail due to tail rotor wake curvature effect
$[K]$	apparent mass matrix in the finite state inflow model
κ_c, κ_s	longitudinal and lateral wake curvatures
K_F	fuselage blockage effect factor (ratio of the mean induced veloicty with fuselage blockage effect to that without fuselage blockage effect)
$[L]$	inflow gain matrix in the augmented Pitt-Peters dynamic inflow model and the augmented finite state inflow model
λ_β	blade flapping frequency
λ_θ	blade nondimensional natural feathering frequency in the rotating frame
λ	total mean inflow across the rotor disk plane
λ_0	mean induced inflow across the rotor disk plane
λ_{1c}	longitudinal inflow gradient across the rotor disk plane
λ_{1s}	lateral inflow gradient across the rotor disk plane
$[M]$	apparent mass matrix
$\overset{*}{\beta}_{1c}, \overset{*}{\beta}_{1s}$	nondimensional longitudinal and lateral flapping rates

$M_{F_{1c}}$	longitudinal aerodynamic flap moment coefficient
$M_{F_{1s}}$	lateral aerodynamic flap moment coefficient
M_{mach}	Mach number
μ	advance ratio
(ν, η, ψ)	rotor ellipsoidal coordinates, nondimensional
Φ_F	pressure perturbation due to fuselage panel, dimensionless on $\rho\Omega^2 R^2$
ϕ_j^r	radial expansion function used in the induced inflow expansion
Φ_R	pressure perturbation due to rotor, dimensionless on $\rho\Omega^2 R^2$
ψ	azimuth angle on the rotor disk plane
ψ_0	azimuth angle on the circular cross section of vortex tube
$\psi^{HT/TR}$	azimuth angle of the aerodynamic center of horizontal tail in the tail rotor disk plane
$\psi^{VT/MR}$	azimuth angle of the aerodynamic center of vertical tail/tail rotor in the main rotor disk plane
q	pitch rate, rad/sec
S	wake spacing
$\sigma_k^{lc}, \sigma_k^{ls}$	fuselage pressure coefficients
$[\tau_D]$	nondimensional time constant matrix associated with dynamic wake distortions
τ_i	time constant in the Pitt-Peters dynamic inflow model in hover, $\tau_i = \dfrac{16}{45\pi\lambda_0}$
τ_n^{mc}, τ_n^{ms}	rotor forcing functions, also called rotor pressure coefficients
τ_R	nondimensional time constant associated with dynamic wake bending
τ_S	nondimensional time constant associated with dynamic wake spacing
τ_X	nondimensional time constant associated with dynamic wake skew
T_I	non-circulatory time constant, used in the state-space airfoil unsteady aerodynamics model
$[\tilde{L}]$	inflow gain matrix for steady flight in the Pitt-Peters dynamic inflow model and the Peters-He finite state inflow model
$[V]$	mass flow parameter matrix
$(\vec{i}, \vec{j}, \vec{k})$	unit vectors along rotor disk coordinate system
v_h	mean induced velocity in hover, $\sqrt{\dfrac{C_T}{2}}$

V_m mass flow parameter associated with mean inflow

V_{sec} resultant velocity at airfoil section

w_F normal component of fuselage interference velocity at rotor disk, positive upward, dimensionless on ΩR

X wake skew

SUMMARY

The prediction of vehicle dynamic response is an essential aspect of helicopter flight mechanics, having relevance to flight simulation, handling quality assessment, aeroelasticity analysis and control law development. Many current helicopter simulation models suffer from an off-axis response correlation discrepancy problem, where the predicted initial off-axis response to cyclic control stick input is opposite in variation trend to that of the corresponding flight test data. This off-axis response correlation discrepancy problem is believed to be caused by inaccurate representation of inflow across the rotor disk during a pitch or roll maneuver.

In this dissertation, a new rotor dynamic wake distortion model, which can be used to account for the rotor transient wake distortion effect on inflow across the rotor disk during helicopter maneuvering and transitional flight in both hover and forward flight conditions, is developed. The dynamic growths of the induced inflow perturbation across the rotor disk during different transient maneuvers, such as a step pitch or roll rate, a step climb rate and a step change in advance ratio are investigated by using a dynamic vortex tube analysis. The dynamic vortex tube analysis results indicate that the dynamic growths of rotor inflow perturbations during different transient maneuvers exhibit a first order behavior with time. Therefore, a rotor dynamic wake distortion model, which is expressed in terms of a set of ordinary differential equations, with rotor longitudinal and lateral wake curvatures, wake skew and wake spacing as states, is developed. Also, both the Pitt-Peters dynamic inflow model and the Peters-He finite state inflow model for axial and forward flight are augmented to account for rotor dynamic wake distortion effect during helicopter maneuvering flight. To model the aerodynamic interaction among main rotor, tail rotor and empennage during helicopter maneuvering flight, a reduced order model based on a vortex tube analysis is developed to account for the effect of main rotor wake curvature on main rotor downwash at tail rotor and empennage, for the side wash induced at the aerodynamic centers of vertical

tail and tail rotor by the main rotor wake curvature and for the up/down wash induced at the aerodynamic center of horizontal tail by the tail rotor wake curvature effect. To account for the fuselage blockage effect on the main rotor mean induced inflow, a reduced order model is developed by treating the fuselage as an equivalent flat plate panel.

Both the augmented Pitt-Peters dynamic inflow model and the augmented Peters-He finite state inflow model, combined with the developed dynamic wake distortion model, together with the main rotor/tail rotor/empennage interaction model are implemented in a generic helicopter simulation program of UH-60 Black Hawk helicopter and the simulated vehicle control responses in both time domain and frequency domain are compared with flight test data of a UH-60 Black Hawk helicopter in both hover and low speed forward flight conditions. Effect of model refinements in hover on the correct off-axis response predictions is also addressed.

CHAPTER I

INTRODUCTION

Rotorcraft are versatile flying vehicles characterized by their rotating rotors. Unlike their contemporary fixed wing aircraft, rotorcraft do not depend on forward motion to produce lift. Due to their unique design, rotorcraft rotors are used to produce lift, control forces and moments as well as propulsive forces while for fixed-wing aircraft, these forces and moments are usually generated through different mechanisms. Actually, due to the novel design of rotating rotors, rotorcraft are versatile flying vehicles that possess the abilities to take-off and land vertically, hover motionless in air and even fly backward.

However, the appealing agility and maneuverability of rotorcraft come at a price. They tend to be much more noisy, suffering from high level of vibrations and various types of aeroelastic instabilities. Compared with fixed-wing aircraft, rotorcraft rotors are composed of large aspect ratio flexible blades. By virtue of rotation of blades, the airflow through the rotor disk is very slow. Hence, unlike fixed-wing aircraft where the trailed wake behind wings convects far downstream very quickly, the trailed wake behinds rotors remains in close proximity to the rotor disk for a significant long time. These trailed and shed vortices will induce strong nonlinear inflow over rotor blades, hence resulting in complex three dimensional airloads on rotor blades. In turn, flapping response of rotor blades due to these airloads will also alter the structure of the rotor wake. Hence, the whole problem is a highly nonlinear coupled problem between rotor inflow, rotor wake and blade dynamics even during steady motion. With the advancement in aerodynamics, materials, flight mechanics and control system design methods, modern helicopters can carry out some highly challenging maneuvers, similar to their contemporary fixed-wing aircraft. One example is shown in Figure 1.1, where the Lynx helicopter is carrying out an agile pitch maneuver [1]. It is perceivable that the rotor wake structure and the inflow field around the helicopter during the maneuver are extremely complex. Due to the maneuver, the rotor wake geometry will

Figure 1.1: The Empire Test Pilot School's Lynx in an agile pitch maneuver

be different from that during steady flight. Since the rotor wake is in close proximity to the rotor disk plane for a significant long time, changes in rotor wake geometry will also result in significant changes in the induced inflow over the rotor disk, and hence, the incurred blade flapping and vehicle responses will also change. In turn, the vehicle response change will also be fed back to the whole system and will influence the rotor wake structure. Therefore, the coupling between the rotor wake, inflow and dynamic response is severe during maneuvering flight.

Due to the unique and dominant role of rotors in rotorcraft, a proper understanding and the ability to accurately predict rotor wake effect on the whole coupled rotor wake, inflow and dynamic response problem, especially when the helicopter is carrying out maneuvers or changing flight phases, is important in the development process, such as aeroelasticity analysis, handling quality assessment and flight control law development for modern helicopters. Also, many flight operational procedures require extensive flight testing for pilot training and for certifications. Due to the prohibitive expense and difficulty involved with obtaining the required experimental database, it is highly desirable to accurately model important flight dynamics aspects through mathematical models. While it may be beyond dispute that well developed theories are vital to correctly predict the behavior of rotorcraft before the first flight, however, rotorcraft experience to date is still not so good. For example, In the AHS Nikolsky Lecture (1989) [2], Crawford promotes a "back to basics" approach to improve rotorcraft modeling in order to avoid major redesign effort resulting from poor understanding and predictive capability.

Since rotorcraft rotors are used to produce lift, propulsive forces, control forces and moments, rotorcraft are characterized by severe cross-couplings in practically every axis-pairing. The prediction of helicopter control response is complicated by the fact that the main rotor introduces additional degrees of freedom associated with each blade as well as those associated with the rotor wake. It is perceivable that the cross couplings will have significant influence on the whole helicopter's characteristics. Padfield [1] pointed out that satisfying the direct, or "on-axis", response characteristics, is necessary but not sufficient to guarantee good flying qualities. The off-axis, i.e., cross-coupled response, is also essential

in order to obtain good flying and handling qualities. In fact, FAA Level D rotorcraft flight simulator certification requires that the simulated off-axis response be similar to that of the real rotorcraft [3]. The development of flight dynamic models for helicopters has matured to the point where the prediction of the primary response of single rotor helicopters to small control inputs, or the on-axis response, is fairly well estabilished. However, accurate prediction of the off-axis response is still problematic. For many years, helicopter flight simulation models have predicted the off-axis response in hover and low speed forward flight to be opposite in sign to the corresponding flight test data [4, 5, 6, 7, 8, 9], a mystery [10] that has perplexed researchers for many years. As an example, Figure 1.2, taken from Takahashi [4], shows the predicted control response of a UH-60 Black Hawk helicopter to a lateral cyclic control stick doublet input in hover condition. As can clearly be seen from Figure 1.2, the initial on-axis roll rate response is predicted fairly well in simulation, at least in the initial seconds, both quantitatively and qualitatively. However, this is not the case for the off-axis pitch rate response to the same lateral cyclic control stick doublet input. The predicted result for the initial pitch rate response is in sign reversal when compared with the actual flight test data.

1.1 Literature Review

Since the similar off-axis response correlation discrepancy problem, i.e., the simulated helicopter off-axis response to cyclic control stick input is reversed in sign when compared with the corresponding flight test data, has been observed and documented for different helicopters [4, 5, 6, 7, 8, 9], there must have been some fundamental phenomena missing or not treated correctly in all the previous flight simulation models. To understand this perplexing off-axis phenomena, there have been many attempts in the literature to explain the primary source of this problem. Most of the theories and methods to explain this off-axis coupling response correlation discrepancy problem can be classified as

1. gyroscopic forces due to the angular momentum of the rotor wake [11]

2. aerodynamic interaction between helicopter rotor and body [12]
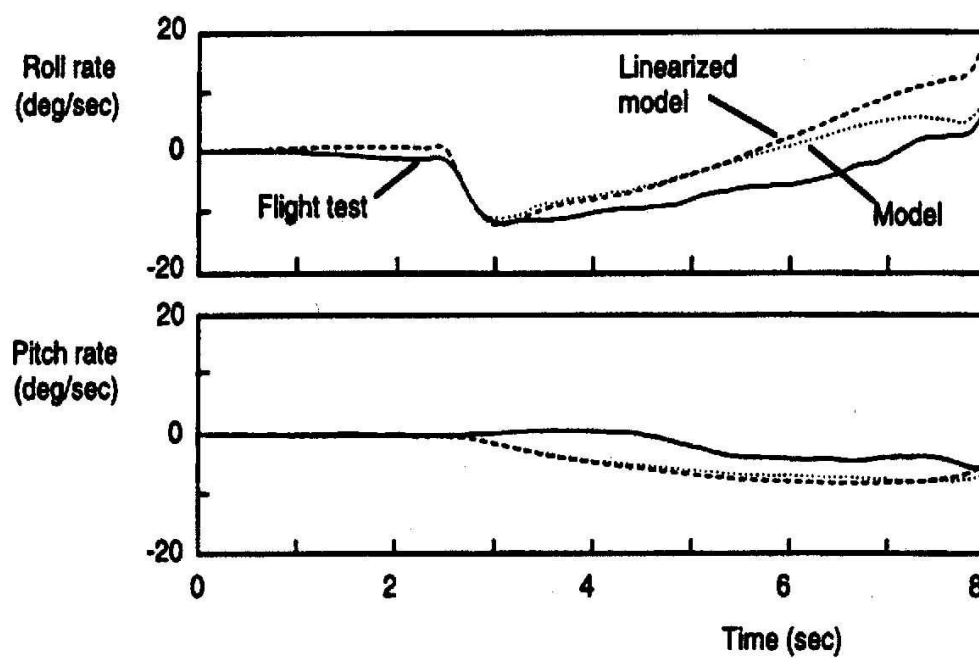
Figure 1.2: Comparison of simulation models (linearized and full nonlinear) with flight test data responses of a hovering UH-60 Black Hawk helicopter to a lateral cyclic control stick doublet input

3. filtering of the airfoil lift and drag coefficients and the aerodynamic phase lag method [13, 14, 15, 16, 17]

4. dynamic twisting due to the gyroscopic feathering moment effect [18]

5. wake distortion/curvature effect

   - Free wake approach [19, 20, 21, 22, 23, 24, 25]

   - dynamic vortex ring model [26, 27, 28]

   - extended momentum model [29, 30, 31, 32, 33, 34, 35, 36]

   - Augmented Pitt-Peters dynamic inflow model and augmented Peters-He finite state inflow model [37, 38, 39, 40, 41, 42, 43]

One of the explanations for the off-axis response correlation discrepancy problem was offered by von Grünhagen [11]. It was claimed that the inplane rotational component of the induced velocity by rotor wake would induce an equivalent angular momentum, which leads to a virtual magnification of the moment of inertia of the helicopter rotor, and was termed "virtual inertia effect". The global effect of this "virtual inertia effect", treated similar to the effect of a spinning rotor, can be coupled into the body and the inflow differential equations, which results in simple correction terms that can be added to a dynamic inflow theory. By including this "virtual inertia effect" associated with the swirl in the rotor wake, the agreement of the predicted off-axis response of a BO-105 helicopter to cyclic control stick input with flight test data can be improved.

Ballin, et al, [12] argued that the off-axis response correlation discrepancy problem was due to the effect of interactions between helicopter rotor and fuselage. Although including the aerodynamic interactions between the main rotor wake and the fuselage may improve the agreement of the off-axis response prediction with test data, it should be noticed that an isolated rotor can still suffer to the same off-axis response phenomena [7, 16].

A different approach was proposed by Mansur and Tischler, et al, [13, 14, 15, 16, 17]. They emphasized the potential role of commpressibility effect in the airfoil unsteady aerodynamics. They propose that this effect can be modeled as an increased aerodynamic phase

lag for the lift and drag coefficients of blade airfoils. The value of this equivalent phase lag was then determined from flight test data using system identification techniques. Their results indicate that the total aerodynamic phase lag contributes to improve the prediction of the off-axis flapping response to cyclic control stick input when compared with the SBMR (Sikorsky Bearingless Main Rotor) wind tunnel data.

Simons, et al, [18] argued that the feathering moments caused by the gyroscopic forces acting on rotor blades during a pitch and/or roll maneuver would have influence on the off-axis response coupling problem. The consequent blade elastic feathering motion incurred by the gyroscopic moment was shown to give rise to reduced cross-coupling in blade flapping motion. Especially, for blades of low feathering stiffness, inclusion of the gyroscopic feathering moment effect would account for some part of the off-axis flapping response.

It is fairly certain that the main source of the above mentioned off-axis coupling problem is aerodynamic in nature and therefore, the coupling effect can be captured by aerodynamic principles. Since rotorcraft are characterized by the uniquely designed rotating rotors, proper modeling of the rotor wake effect during different flight conditions can be generalized to all rotor systems, rather than using an ad hoc method which can only produce solutions to a specific helicopter configuration. A flight simulation model that can be applicable to arbitrary vehicle configuration and can accurately predict the vehicle dynamic response to control stick input during all flight regimes would be of great benefit in the design and development phases of rotorcraft.

Some researchers pointed out that a key source of the off-axis dynamic response correlation discrepancy arises from the interaction of rotor flapping dynamics and rotor inflow environment during maneuvering flight. It is proposed that the effect on rotor inflow resulting from rotor wake distortion during maneuvering flight is one of the main contributing factors of the off-axis response correlation discrepancy problem, which manifests as a pitch response resulting from a lateral cyclic control stick input, and/or a roll response resulting from a longitudinal cyclic control stick input. It is perceivable that a maneuver, whether it is a pitch maneuver or a roll maneuver or a combination of both, will cause additional

distortion to the rotor wake geometry, which will be significantly different from that obtained under steady flight conditions. In turn, the distorted wake geometry will change the induced inflow across the rotor disk, and hence, will affect the blade loads, rotor blade dynamic flapping response and finally the vehicle response characteristics. Therefore, the required control stick for the maneuver will also be different from that required for steady flight.

The first major contribution to the understanding of the off-axis response correlation discrepancy problem came from Rosen and Isser [19, 20]. Rosen and his colleagues use a complex dynamic model of the rotor wake to show that a geometric distortion of the rotor wake structure occurs under a steady rotor shaft pitch and/or roll motion. This distorted rotor wake geometry induces a lateral inflow gradient perturbation across the rotor disk for a roll motion and a longitudinal inflow gradient perturbation for a pitch motion, which is counter to the kinematic inflow perturbation due to the shaft pitch and/or roll rate. Therefore, they proposed that this inflow change due to the wake geometric distortion effect could yield a sign reversal in the off-axis flapping response in hover condition. Through including the wake geometric distortion effect during a pitch and/or roll maneuver in their unsteady aerodynamic model (TEMURA), a significant improvement in the off-axis response correlation with a UH-60 Black Hawk helicopter flight test identification results was achieved.

Bagai, Leishman and Bhagwat, et al, [21, 22, 23, 24] used a free vortex method for the rotor wake to study the aerodynamics of a helicopter undergoing a steady pitch and/or roll maneuver. Through solving the rotor wake geometry under a prescribed pitch and/or roll rate using either a five-point central difference algorithm [44, 45] or a time accurate free vortex algorithm [23, 24], it is shown that the rotor pitch and/or roll maneuver is an additional source of distortion to the rotor wake geometry in both hover and forward flight. However, the wake distortion effect strongly depends on flight condition. In hover and low speed forward flight, the distorted rotor wake geometry due to the pitch and/or roll maneuver induces an inflow gradient across the rotor disk, which is proportional to the rotor pitch and/or roll rate and manifests as a counter effect to the kinematic inflow across

the rotor disk. At higher advance ratios, the effect of maneuver induced wake distortion is still present, but is reduced by about half relative to that in hover condition.

In [25], Theodore and Celi investigated the effect of rotor wake modeling on the prediction of the off-axis response to pilot cyclic control stick input by incorporating a free wake model [21, 22, 23] for helicopters with both a hingeless and an articulated rotor configuration and compared the simulation results with available flight test data. Although some improvements on the initial off-axis response prediction are achieved, their results suggest that deficiencies are still present in the wake model, and that other aerodynamic mechanisms associated with the rotor wake dynamics may play a roll in affecting the off-axis dynamic response correlation. They suggested that these mechanisms potentially might include the effect of unsteady aerodynamics and the transient effect associated with the development of the wake itself.

At the same time, Park and Leishman [22] studied the unsteady aerodynamics effect on the rotor wake distortion for a helicopter undergoing a prescribed pitch and/or roll rate. A conventional blade element unsteady aerodynamics model based on the indicial function [46] was incorporated to partly represent the unsteady effect associated with the shed wake downstream of the blade. However, their results show that the effect of unsteady aerodynamics on the prediction of the rotor wake geometry and inflow during a steady maneuver is relatively small.

Although the free wake method for rotor wake has the advantage of directly computing the wake geometry distortion effect without imposing any pre-assumed aerodynamic inflow on the rotor and wake geometry, it is computationally expensive and therefore, not suitable for applications, such as flight simulation, where a stringent computational efficiency is required. Also, the state of the art of the free wake method is still suffering from potential instabilities, especially near hover condition. Since fast calculations of the rotor wake induced inflow and rotor aerodynamic loads are necessary for flight dynamics applications such as real-time and pilot-in-the-loop simulation, it would be much more beneficial to approximate the rotor wake effect by using a reduced order model. In the point of view of investigating the off-axis response correlation discrepancy problem, there have been some

other simpler but computationally more efficient methods, which are appealing for flight simulation, in the literature to study the rotor wake distortion effect on inflow across rotor disk during a steady maneuvering flight.

In [26, 27, 28], Basset modeled the wake distortion effect during a steady pitch and/or roll maneuver by using a dynamic vortex wake model. In his model the main rotor wake is represented by a series of vortex rings distributed along the wake to model the trailing vortices together with radial vortex segments to account for the effect of shed vortices. The attitude and vorticity of each vortex ring evolve dynamically as a function of rotor airloads and motion. The induced velocity at an arbitrary point in the flow field due to a vortex ring can be obtained in a closed form, which uses the first and the second elliptic integrals. Through computing the inflow perturbations across the rotor disk for a prescribed rotor pitch and/or roll rate, the variations of the rotor wake distortion effect are studied to investigate the influence of different configuration and operation parameters such as airspeed, center of rotation, climb rate and rotor thrust. By including the rotor wake geometric distortion effect, improvements in the prediction of the off-axis response of a BO-105 helicopter to cyclic control stick input near hover were shown.

In recent years, the Pitt-Peters dynamic inflow model [47] and the Peters-He finite state inflow model [48], which are now routinely used in rotorcraft industry, have emerged as a robust and efficient tool for helicopter flight simulation, handling quality evaluation and vibration analysis. In these models, a finite number of inflow states are used to represent the global rotor wake effect. One unique advantage of these models is that they are expressed in state space. Recently, some researchers have also investigated the rotor wake distortion effect on the off-axis response correlation discrepancy problem by extending the Peters-He finite state inflow model and the Pitt-Peters dynamic inflow model to account for the rotor wake curvature effect during a steady helicopter maneuvering flight.

Keller [29, 30, 31] investigated the off-axis dynamic response correlation discrepancy problem by using a combination of a vortex ring representation for the rotor wake and an extended momentum model. In his work, the rotor wake geometry during a steady pitch and/or roll rate was prescribed and the inflow gradient across the rotor disk due to the

10

maneuver was calculated by using a vortex ring representation for the rotor wake. His results show that the inflow gradient due to maneuver is approximately proportional to the pitch and/or roll rate for a hovering rotor. Therefore, it is proposed that the wake geometric distortion effect on the inflow perturbation across the rotor disk can be captured by using an empirical wake distortion parameter called K_R. Subsequently, he extended the induced inflow model based on momentum theory to include rotor wake distortion effect. His results demonstrate that inclusion of the rotor wake distortion effect results in a significant change in the rotor blade off-axis flapping response to a steady rotor pitch and/or roll rate. Then the extended inflow model was coupled with a linearized rotor/body dynamics model, and comparisons were made between the simulated results and flight test data for a UH-60 Black Hawk in hover [29, 30, 31, 32]. The Results show that inclusion of the rotor wake distortion effect improves correlation between the off-axis response to cyclic control stick input and the flight test data.

Rosen [35, 36] derived an approximate actuator disk model for a rotor in hover and axial flight based on both a vortex modeling for the rotor wake and an approximate solution of the equations for an imcompressible/inviscid potential flow through the rotor disk. The wake distortion effect during a pitch and/or roll maneuver was included in his model and the longitudinal and lateral inflow gradient perturbations due to the wake distortion effect during maneuvering were represented by using two first order ordinary differential equations. A comparison of his simulation results using the actuator disk model with flight test data of a UH-60 Black Hawk helicopter and an AH-64 helicopter in hover showed improvements in the off-axis response correlation.

He [43] adopted a full span prescribed vortex wake model consisting of discrete trailing and shed vortex elements to model the rotor wake geometric distortion effect during a pitch and/or roll rate. The vortex wake is modeled with respect to the physical blade tips and blade lifting segments to account for the effects from both the hub linear translation and angular rotation. At each time step, the first trailed vortex element is attached to the physical blade bound vortex while all the other vortex elements follow the summation of the current freestream velocity and the mean induced downwash. Then the rotor wake geometric

distortion effect was extracted as perturbational induced velocities, which were added to the Peters-He finite state inflow model [48] to model the rotor wake geometric wake distortion effect. This rotor geometric wake distortion effect was implemented in a comprehensive rotorcraft simulation program, FLIGHTLAB, and simulated control response of a UH-60 Black Hawk helicopter to a lateral cyclic control stick doublet input in hover was compared with the corresponding flight test data. The comparison showed that the correlation of the off-axis pitch rate response prediction to a lateral cyclic control stick doublet input with flight test data was improved, although the magnitude was under predicted.

Considerable work was done at the FlightSim Lab at the Georgia Institute of Technology to improve the fidelity of rotorcraft simulations by including more complex models of helicopter dynamics. Lewis [49] and later Sturisky [50] examined the off-axis response prediction of an AH-64 helicopter with a FLIGHTLAB simulation model by including both an elastic blade bending model and an inflow model that incorporated up to the 2nd harmonics for rotor inflow. It was theorized that the higher harmonic inflow coupled the rotor and body dynamics and that properly modeling these effects could improve the off-axis response prediction. In the frequency domain, improvements were shown for the off-axis response prediction when the simulation results that includes an elastic blade model with the 2nd harmonic inflow were compared with those using only a simple rigid blade model with uniform inflow.

Most recently, Krothapalli, et al, [37, 38, 39, 40, 41, 42] studied the rotor wake distortion effect during helicopter maneuvering flight by using various analytical tools, and finally obtained a generalized dynamic wake model with quasi-steady wake curvature augmentation in hover. The effect of the prescribed rotor angular rate on the inflow gradient across the rotor disk plane was captured by using an empirical parameter called K_{Re}, which is equivalent to the wake distortion parameter K_R proposed by Keller (as will be shown in Section 3.8). Their newly developed wake model, when coupled with a rigid blade flapping dynamics model, showed that the reversal in sign of the off-axis flapping response to a cyclic control stick input in hover condition was captured when the quasi-steady wake curvature terms were included. Using the extended generalized wake model coupled with a rigid blade

flapping model, the simulated off-axis flapping response to both longitudinal and lateral cyclic control stick inputs have shown fairly well qualitative results, when compared with the SBMR (Sikorsky Bearingless Main Rotor) wind tunnel test data [7], for all but a few notable exceptions in the range of frequencies below the first lag mode. In addition, including the wake curvature terms has nearly no effect on the on-axis response predictions. Also, a nonlinear coupling term between steady wake skew and wake curvatures was identified from the SBMR wind tunnel test data. When this nonlinear coupling term was considered, the correlation of the simulated off-axis response with the SBMR wind tunnel test data was improved.

In the previous studies, an empirical wake distortion/curvature parameter is used to capture the effect of the prescribed rotor angular rate on inflow across the rotor disk during maneuvering flight. However, there is a rather large discrepancy between the values of the wake curvature parameter obtained by different researchers. For example, Table 1 summarizes the results in hover given by different researchers. The identified aerodynamic phase lag angle by Schulein, et al, [34, 51] for the UH-60A Black Hawk helicopter in hover is 42.6^o, which is converted to an equivalent wake curvature parameter using the formula in Refs. [34] and [51] and the value is shown in Table 1. The discrepancies between the results are due to the nature of various vortex wake models used where different numerical assumptions have been made among the researches. Also, as pointed out by Barocela and Peters, et al, [38] the theoretical maximum value for the wake distortion/curvature parameter is 2.0, and for realistic rotor circulation distribution, this value should fall between 1.0 and 2.0.

1.2   Present Work

The rotor wake/inflow/body dynamics is highly coupled. When a helicopter transitions through different flight phases, such as carrying out a pitch and/or roll maneuver, the rotor wake geometry will also change from one steady shape to another steady shape. It is perceivable that the transient effects between these steady phases will have important influences on the response and controllability of the helicopter. It would be highly desirable

13

Table 1: Comparison of values for the wake distoriton/curvature parameter in hover

Reference	Model	K_R (K_{Re})
Rosen [19]	Prescribed wake	0.75
Keller, et al [29]	Spiral vortex tube	1.5
Basset [26]	Spiral vortex ring	1.5
Bagai, et al [21]	Free wake	1.75
He [52]	Prescribed full span wake	1.2
Peters, et al [38]	Momentum, prescribed wake	1.0
Krothapalli [41]	vortex lattice	1.33
Tischler, et al [7, 51]	Aerodynamic phase lag	1.89

to accurately model these transient effects of the rotor wake in the analyses, especially for real-time simulation and control law design development. Most of the previous investigations on the off-axis dynamic response correlation discrepancy problem as reviewed in the previous section assume a quasi-steady wake geometry model, which implies that the rotor wake distortion is developed simultaneously at each time instant, and therefore,does not account for the transient wake distortion effect whenever there is a change in flight conditions. The quasi-steady assumption gives rise to erroneous response predictions during helicopter maneuvering flight phases where the rotor wake transitions through different shapes. Also, most of the previous investigations only look at specific flight condition, therefore, their methods (models) do not rigorously apply to the whole flight regimes.

The objective of this research is to investigate the dynamic wake distortion effect during helicopter maneuvering and transitional flight, and develop a generalized dynamic wake distortion model, which can be applied to most of the helicopter flight regimes and when combined with an appropriate flight dynamics model, can be easily used in a simulation application to account for the transient rotor wake distortion effect for high fidelity simulations and analyses.

This thesis describes the details of the development of a rotor dynamic wake distortion model in both hover and forward flight conditions to account for the transient wake distortion effect by using a dynamic vortex tube analysis including comparisons with results from a free wake method. The dynamic vortex tube analysis is used to systematically develop the

generalized dynamic wake distortion model, which can be expressed as a compact set of ordinary differential equations with four states for the wake skew, wake spacing, longitudinal and lateral wake curvatures. Also, the inflow perturbations across the rotor disk plane for arbitrary rotor loading distribution in both hover and forward flight are obtained and are used to augment the Pitt-Peters dynamic inflow model [47] and the Peters-He finite state inflow model [48]. A reduced order model is developed to account for the main rotor/tail rotor/empennage interaction during maneuvering flight. The augmented Pitt-Peters dynamic inflow model and the augmented Peters-He finite state inflow model, combined with the developed dynamic wake distortion model, together with the interaction model among main rotor, tail rotor and empennage, are implemented into a generic helicopter flight simulation program [53]. The developed model is validated through comparing simulation results, especially the off-axis response predictions of a UH-60 Black Hawk helicopter to cyclic control stick inputs from both hover and forward flight conditions, with the available flight test data [54]. Also, the effect of wake distortion parameters on the off-axis response predictions is investigated.

1.3   *Organization of Dissertation*

The fundamental problem of the off-axis dynamic response correlation discrepancy and the current state-of-the-art method on this topic are introduced through a literature review given in Chapter I. The focus of the current work stems from the need to properly and systematically model the transient wake distortion effect on the inflow across the rotor disk and on the vehicle dynamic response, and to account for the dynamic wake distortion effects in all helicopter flight regimes.

In Chapter II, variations of inflow across the rotor disk during helicopter maneuvering and transitional flight phases, such as undergoing a step pitch and/or roll rate, a step change in advance ratio and a step change in climb rate are investigated by using a dynamic vortex tube analysis. Based on the numerical results from the dynamic vortex tube analysis, time constants associated with rotor wake distortion dynamics are extracted and a rotor dynamic wake distortion model, which uses four additional states, that is, longitudinal and lateral

wake curvatures, wake skew and wake spacing, is developed.

In Chapter III, both the Pitt-Peters dynamic inflow model and the Peters-He finite state inflow model for axial and steady forward flight are augmented to account for the rotor wake distortion effect. The augmented dynamic inflow model and the augmented Peters-He finite state inflow model, combined with the rotor dynamic wake distortion model, are implemented in a generic helicopter simulation program to investigate the influence of coupling effect between rotor inflow and rotor mean/cyclic loading due to rotor wake distortion during maneuvering flight. The effect of rotor dynamic wake distortion on the stability of flapping dynamics is also investigated.

In Chapter IV, a reduced order model is developed to account for the aerodynamic interaction among main rotor, tail rotor and empennage during helicopter maneuvering flight, which includes an equivalent wake skew due to main rotor wake curvature effect, an additional side wash induced at the aerodynamic center of vertical tail and/or tail rotor due to main rotor wake curvature and an additional up/down wash induced at the aerodynamic center of horizontal tail due to tail rotor wake curvature.

In Chapter V, model refinements in hover condition, which include a state-space representation of airfoil unsteady aerodynamics, a reduced order model to account for fuselage blockage effect on mean induced inflow across the rotor disk and representation of gyroscopic feathering moment effect during helicopter maneuvering flight are described.

In Chapter VI, both the augmented Pitt-Peters dynamic inflow model and the augmented Peters-He finite state inflow model (developed in Chapter III), together with the main rotor/tail rotor/empennage interaction model (Chapter IV) and model refinements in hover condition (Chapter V), combined with the rotor dynamic wake distortion model (Chapter II), are implemented in a generic helicopter simulation program and the developed model is validated through comparing simulated response predictions, especially the off-axis response predictions, with flight test data of a UH-60 Black Hawk helicopter in both hover and forward flight conditions. Also, the effect of model refinements in hover condition is investigated.

An overview of the conclusions and accomplishments in this research is given in Chapter

VII. Also, recommendations for future work are given.

Appendix A gives the detailed derivation of a dynamic vortex tube model, which describes the dynamic variations of inflow across the rotor disk for a rotor undergoing a step pitch and/or roll rate, a step change in advance ratio and a step change in climb rate.

Appendix B gives the detailed derivation of the quasi-steady inflow perturbations across the rotor disk due to rotor mean and cyclic loading effect during a steady pitch and/or roll motion.

Appendix C gives the detailed derivation of a reduced order model to account for the aerodynamic interaction among main rotor, tail rotor and empennage during helicopter maneuvering flight.

Appendix D is a summary of the developed rotor dynamic wake distortion model and the augmented inflow models for helicopter maneuvering flight.

CHAPTER II

DYNAMIC WAKE DISTORTION MODEL

In this chapter, a model is established to account for rotor dynamic wake distortion effect during helicopter maneuvering flight, such as undergoing a step pitch and/or roll rate, a step change in advance ratio and a step climb rate, by using a dynamic vortex tube analysis (Appendix A). In the vortex tube method, the vortices generated around rotor blades are assumed to be wrapped around a tube of continuous vorticity, representing the outer surface of the rotor wake. The induced inflow across the rotor disk due to the wake tube can be obtained by using the Biot-Savart law. This method can be easily extended to the case of a rotor undergoing transient maneuvers, by prescribing the distorted rotor wake geometry at each time instant, corresponding to a dynamic vortex tube, whose shape continuously changes with time.

2.1 *Dynamic Wake Distortions In Hover*

2.1.1 Dynamic Wake Bending Effect In Hover

Figure 2.1 schematically shows the dynamic vortex tube geometry for a helicopter rotor undergoing a step pitch rate q from hover (side view, in the rotor disk coordinate system). The dynamic vortex tube, as shown in Figure 2.1, is comprised of two parts, a curved part and a noncurved part. The curved part has an equivalent radius of curvature $d_0 = \lambda/\bar{q}$, which is measured from the center of wake curvature to the center axis of the wake tube. The noncurved part is smoothly connected to the curved part and extends downstream to infinity. A circular cross section of the wake displaced downstream along the rotor wake axis by a distance η and subtending an angle α to the rotor disk plane is shown in Figure 2.1. The position of a point on this circular section can be specified in terms of the vortex tube radius $\bar{r}_0$ and azimuth angle ψ_0. The general case of the induced inflow (positive along negative z-axis) across the rotor disk due to a dynamic vortex tube of a pitching rotor in forward
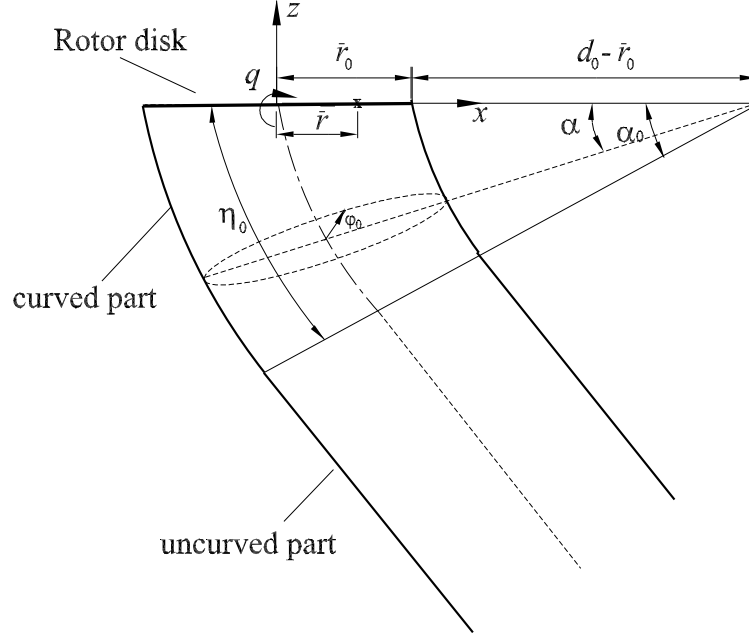
Figure 2.1: Dynamic vortex tube geometry of a rotor undergoing a step change in pitch-up velocity from hover(port side)

flight is given in Appendix A (Equations A.12.e and A.12.f). With the assumption that the equivalent radius of wake curvature $d_0 = \lambda/\bar{q}$ is large, i.e., the curvature $1/d_0 = \bar{q}/\lambda$ is small, the mean induce inflow and longitudinal inflow gradient ($\psi = 0$ in Equations A.12.e and A.12.f) across the rotor disk can be extracted from Equations A.12.e and A.12.f by substituting $\mu = 0$ and carrying out Taylor series expansion about $\bar{q}/\lambda$ up to the first order as follows (which is valid up to the first order of pitch rate)

$$v_0^{(I)} = \frac{\bar{\gamma}}{4\pi} \int_0^1 \int_0^{2\pi} \frac{(1 - \hat{r}cos\psi_0)}{1 + \hat{r}^2 - 2\hat{r}cos\psi_0} \left[\frac{\bar{\eta}_0}{\sqrt{1 + \hat{r}^2 + \bar{\eta}_0^2 - 2\hat{r}cos\psi_0}} \right] d\psi_0 d\hat{r} \tag{2.1.a}$$

$$v_c^{(I)} = \frac{3\bar{\gamma}\bar{r}_0}{8\pi d_0} \int_0^1 \int_0^{2\pi} \frac{(1 - \hat{r}cos\psi_0)(\hat{r} + cos\psi_0)}{\hat{r}(1 + \hat{r}^2 - 2\hat{r}cos\psi_0)} \left[\frac{1}{4}sin\theta_0 - \frac{1}{12}sin3\theta_0 \right] d\psi_0 d\hat{r}$$

$$+ \frac{\bar{\gamma}\bar{r}_0}{8\pi d_0} \int_0^1 \int_0^{2\pi} \frac{cos\psi_0}{\hat{r}} \left[tan\left(\frac{\pi}{4} + \frac{\theta_0}{2} \right) - sin\theta_0 \right] d\psi_0 d\hat{r} \tag{2.1.b}$$

$$v_0^{(II)} = \frac{\bar{\gamma}}{4\pi} \int_0^1 \int_0^{2\pi} \frac{(1 - \hat{r}cos\psi_0)}{1 + \hat{r}^2 - 2\hat{r}cos\psi_0} \left[1 - \frac{\bar{\eta}_0}{\sqrt{1 + \hat{r}^2 + \bar{\eta}_0^2 - 2\hat{r}cos\psi_0}} \right] d\psi_0 d\hat{r} \tag{2.1.c}$$

$$v_c^{(II)} = \frac{3\bar{\gamma}\bar{r}_0}{8\pi d_0} \int_0^1 \int_0^{2\pi} \frac{(1 - \hat{r}cos\psi_0)(\hat{r} + \hat{r}_0cos\psi_0)}{\hat{r}(1 + \hat{r}^2 - 2\hat{r}cos\psi_0)} tan^2\theta_0 \left[\frac{2}{3} - \frac{3}{4}sin\theta_0 - \frac{1}{12}sin3\theta_0 \right] d\psi_0 d\hat{r}$$

$$+ \frac{\bar{\gamma}\bar{r}_0}{8\pi d_0} \int_0^1 \int_0^{2\pi} \frac{cos\psi_0}{\hat{r}} tan^2\theta_0 (1 - sin\theta_0) \, d\psi_0 d\hat{r} \tag{2.1.d}$$

where superscripts (I) and (II), respectively, denote contributions from the curved part and the noncurved part of the dynamic vortex tube, $\bar{\gamma}$ is vorticity density around the vortex tube. In Equations 2.1.a to 2.1.d,

$$tan\theta_0 = \frac{\bar{\eta}_0}{\sqrt{1 + \hat{r}^2 - 2\hat{r}cos\psi_0}} \tag{2.2}$$

where $\bar{\eta}_0 = \eta_0/\bar{r}_0$ and η_0 is the length of the curved tube part along the tube axis.

The total mean induced inflow across the rotor disk is

$$\lambda_0 = v_0^{(I)} + v_0^{(II)} = \frac{\bar{\gamma}}{2} \tag{2.3}$$

which is independent of the rotor pitch rate. Similarly, the total longitudinal inflow gradient across the rotor disk induced by the whole dynamic vortex tube can be written as

$$\Delta\lambda_{1c} = v_c^{(I)} + v_c^{(II)} \tag{2.4}$$

For the case where the curvature of the dynamic vortex tube is fully developed, an analytical solution to the integrals in equation 2.4 can be obtained as

$$(\Delta\lambda_{1c})_{ss} = \frac{\bar{\gamma}}{2d_0} \tag{2.5}$$

which is consistent with the results given by Barocela [38]. For the general case of the dynamic vortex tube with both curved and noncurved parts, the integrals in equation 2.4 are evaluated numerically.

A typical variation with time of the longitudinal inflow gradient across the rotor disk is shown in Figure 2.2 for a nondimensional pitch rate of $\bar{q} = 0.005$ and thrust coefficient of $C_T = 0.0065$. It can be seen that the inflow gradient exhibits a first order behavior with time. Figure 2.2 shows a first order approximation with a nondimensional time constant of 6.1 superimposed in the plot. Also shown in the plot are the results from a free wake analysis [55, 56]. From a comparison of the vortex tube and free wake analysis results, it is clear that the global effect due to dynamic wake bending on the variation of the inflow gradient with time is captured by the current dynamic vortex tube model.

The free wake analysis results by Zhao, et al [55, 56], show that the nondimensional time constant associated with dynamic wake bending effect in hover is roughly constant for
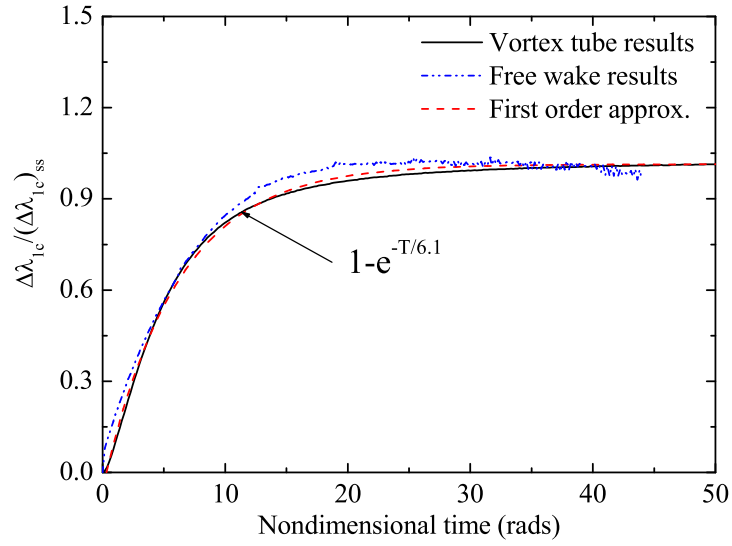
Figure 2.2: Inflow gradient growth with time due to wake curvature effect for a four-bladed isolated rotor in hover, $\bar{q} = 0.005, C_T = 0.0065$

Figure 2.3: Variation of the nondimensional time constant associated with wake curvature effect versus rotor thrust coefficient near hover

a nondimensional pitch rate up to $q/\Omega \leq 0.015$. Therefore, for each specific rotor thrust coefficient, one nondimensional time constant can be used to represent the rotor dynamic wake bending effect for small pitch and roll rates.

Figure 2.3 shows the values of the nondimensional time constant associated with the wake bending dynamics for different values of thrust coefficient (C_T) as extracted from the dynamic vortex tube analysis results. In Figure 2.3, the symbols are those predicted by the dynamic vortex tube analysis and the solid line is an empirical approximation obtained as

$$\tau_R = \frac{16}{15\pi v_h} \tag{2.6}$$

where v_h denotes the mean induced velocity in hover. It can be seen that the above empirical formula (Equation 2.6) agrees well with the results predicted by the dynamic vortex tube model. On the other hand, equation 2.5 shows that the steady inflow gradient across the rotor disk is proportional to the steady wake curvature $(1/d_0)$ of the vortex tube. Therefore, it can also be assumed that the transient wake curvature follows the same variation as the inflow gradient. Since the wake bending dynamics is characterized by the wake curvature, the formula in Equation 2.6 can also be used to represent the time constant associated with the wake bending dynamics near hover.

2.1.2 Dynamic Wake Skew Effect In Hover

Figure 2.4 schematically shows the dynamic vortex tube geometry (side view, in the rotor disk coordinate system) for a helicopter rotor undergoing a step change in advance ratio from hover, i.e., transition from hover to low speed forward flight. The dynamic vortex tube is composed of two parts, a skewed part and a vertically straight part as shown in Figure 2.4. The skewed part will gradually convect far downstream and finally dominate the inflow across the rotor disk, whereas the influence of the vertically straight down part will gradually diminish. When the transient effect diminishes, the steady skewed wake shape corresponding to the specific value of the advance ratio will be achieved. The general case of the induced inflow across the rotor disk for a rotor undergoing a step change in advance ratio in forward flight is given in Appendix A (Equations A.34.a and A.34.b). Under the assumption that the change in advance ratio $(\Delta \mu)$ is small, i.e., the wake skew angle

22
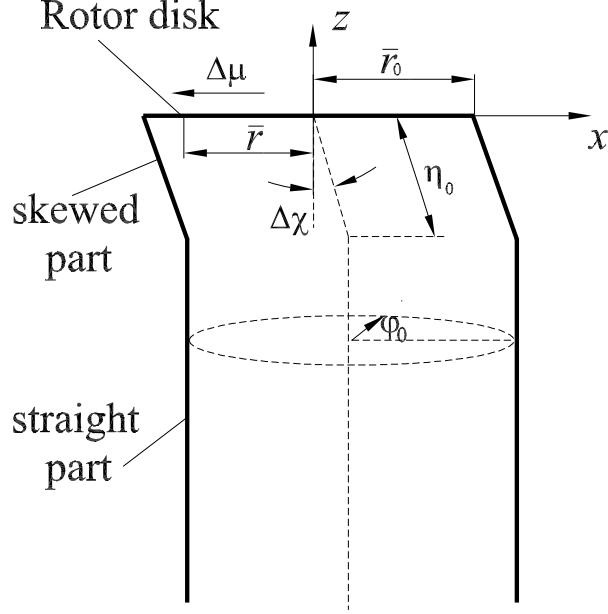
Figure 2.4: Dynamic vortex tube geometry of a rotor undergoing a step change in advance ratio from hover (side view)

perturbation $\Delta\chi$ is small, the mean induced inflow and longitudinal inflow gradient ($\psi = 0$) across the rotor disk can be extracted from Equations A.34.a and A.34.b by substituting $\mu = 0$ ($\chi = 0$) and carrying out Taylor series expansion for $\Delta\chi$ up to the first order as follows

$$
v_0^{(I)} = \frac{\bar{\gamma}}{4\pi} \int_0^1 \int_0^{2\pi} \frac{(1 - \hat{r}cos\psi_0)}{1 + \hat{r}^2 - 2\hat{r}cos\psi_0} \left[\frac{\bar{\eta}_0}{\sqrt{1 + \hat{r}^2 + \bar{\eta}_0^2 - 2\hat{r}cos\psi_0}} \right] d\psi_0 d\hat{r} \tag{2.7.a}
$$

$$
v_c^{(I)} = \frac{\bar{\gamma}\Delta\chi}{4\pi} \int_0^1 \int_0^{2\pi} \frac{cos\psi}{\hat{r}\sqrt{1 + \hat{r}^2 - 2\hat{r}cos\psi}}(1 - cos\theta_0) \, d\psi_0 d\hat{r}
$$

$$
+ \frac{3\bar{\gamma}\Delta\chi}{4\pi} \int_0^1 \int_0^{2\pi} \frac{(1 - \hat{r}cos\psi_0)(\hat{r} + cos\psi_0)}{\hat{r}(1 + \hat{r}^2 - 2\hat{r}cos\psi_0)^{3/2}} \left[\frac{1}{3} - \frac{cos\theta_0}{4} - \frac{cos3\theta_0}{12} \right] d\psi_0 d\hat{r} \tag{2.7.b}
$$

$$
v_0^{(II)} = \frac{\bar{\gamma}}{4\pi} \int_0^1 \int_0^{2\pi} \frac{(1 - \hat{r}cos\psi_0)}{1 + \hat{r}^2 - 2\hat{r}cos\psi_0} \left[1 - \frac{\bar{\eta}_0}{\sqrt{1 + \hat{r}^2 + \bar{\eta}_0^2 - 2\hat{r}cos\psi_0}} \right] d\psi_0 d\hat{r} \tag{2.7.c}
$$

$$
v_c^{(II)} = \frac{\bar{\gamma}\Delta\chi}{4\pi} \int_0^1 \int_0^{2\pi} \frac{cos\psi}{\hat{r}\sqrt{1 + \hat{r}^2 - 2\hat{r}cos\psi}}tan\theta_0(1 - sin\theta_0) \, d\psi_0 d\hat{r}
$$

$$
+ \frac{3\bar{\gamma}\Delta\chi}{4\pi} \int_0^1 \int_0^{2\pi} \frac{(1 - \hat{r}cos\psi_0)(\hat{r} + cos\psi_0)}{\hat{r}(1 + \hat{r}^2 - 2\hat{r}cos\psi_0)^{3/2}}tan\theta_0 \left[\frac{2}{3} - \frac{3sin\theta_0}{4} - \frac{sin3\theta_0}{12} \right] d\psi_0 d\hat{r}
$$

$$
\tag{2.7.d}
$$

where $\Delta\chi$ is the steady wake skew angle corresponding to the advance ratio change $\Delta\mu$, superscripts (I) and (II) denote contributions from the skewed tube part and the vertically straight part, respectively. $\bar{\gamma}$ is the vorticity density around the vortex tube and

$$tan\theta_0 = \frac{\bar{\eta}_0}{\sqrt{1 + \hat{r}^2 - 2\hat{r}cos\psi_0}} \tag{2.8}$$

where $\bar{\eta}_0 = \eta_0/\bar{r}_0$ and η_0 is the length of the skewed tube part along the vortex tube axis as shown in Figure 2.4.

The total inflow gradient perturbation induced by the whole dynamic vortex tube across the rotor disk can be written as

$$\Delta\lambda_{1c} = v_c^{(I)} + v_c^{(II)} \tag{2.9}$$

The integrals in Equation 2.9 are evaluated numerically.

Figure 2.5 shows a typical variation of the inflow gradient across the rotor disk with time to a step change in advance ratio of $\Delta\mu = 0.01$ from hover for a thrust coefficient of $C_T = 0.0065$. It can be seen that the inflow gradient variation exhibits a first order behavior with time, and therefore, a first order approximation is superimposed on the plot. Also shown in the plot are the results predicted by a free wake method [55, 56]. From a comparison between the vortex tube and free wake analysis results, it is seen that the global effect due to dynamic wake skew on the inflow gradient variation with time is captured by the dynamic vortex tube model used here.

Figure 2.6 shows the values of the nondimensional time constant associated with the dynamic wake skew effect for different values of thrust coefficient as extracted from the vortex tube analysis results. In the figure, the symbols are the results predicted by the dynamic vortex tube analysis used here and the solid line is an empirical approximation obtained as

$$\tau_X = \frac{16}{15\pi v_h} \tag{2.10}$$

where v_h denotes the mean induced velocity in hover. It can be seen that the above formula agrees well with the results predicted by the dynamic vortex tube analysis. Therefore, it can be used to represent the time constant associated with the wake skew dynamics near hover.

24
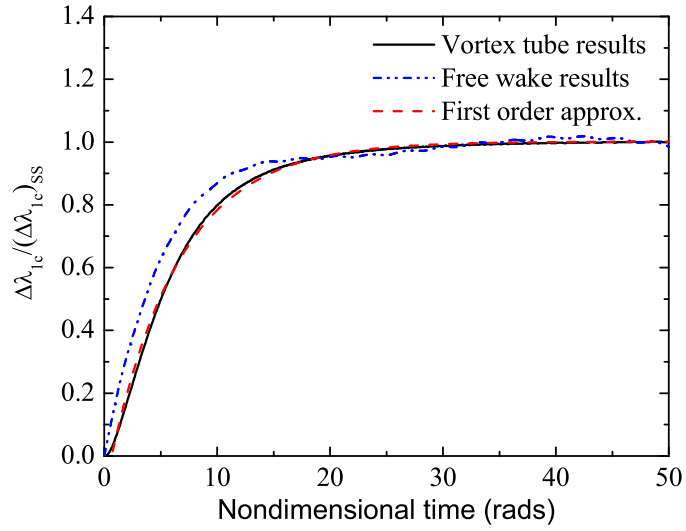
Figure 2.5: Inflow gradient across the rotor disk due to a step change in advance ratio from hover, $\Delta\mu = 0.01, C_T = 0.0065$
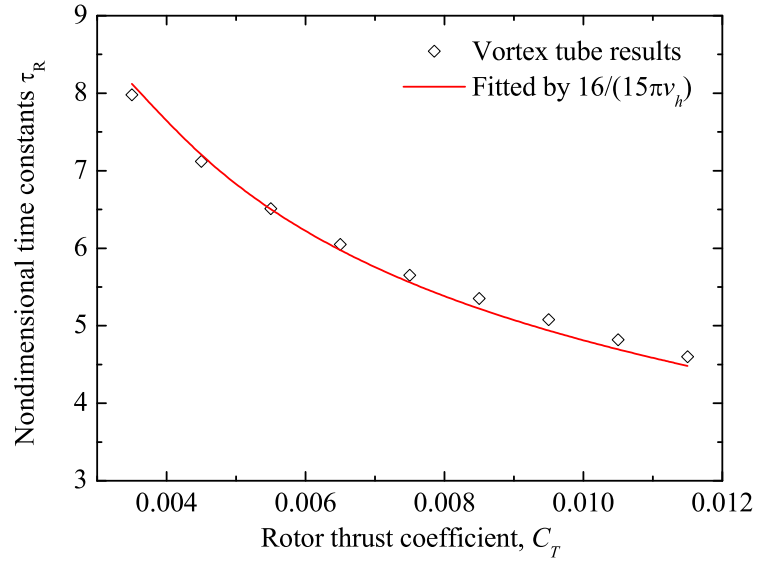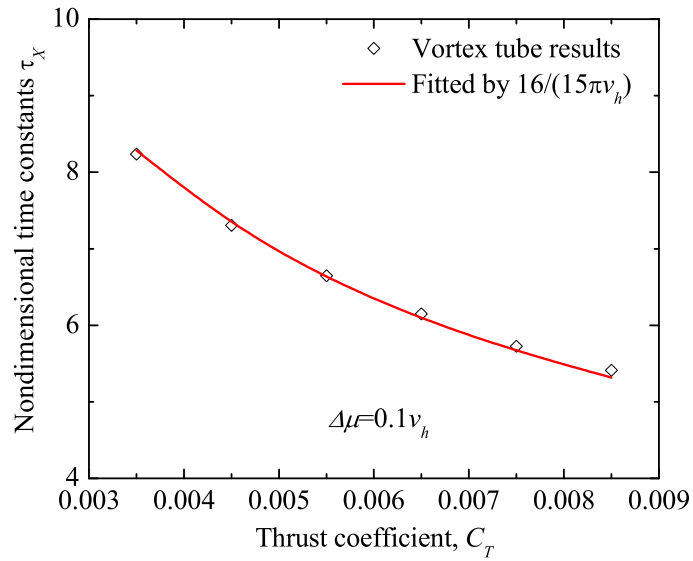

Figure 2.6: Variation of the nondimensional time constant associated with wake skew effect versus rotor thrust coefficient near hover

2.1.3 Dynamic Wake Spacing Effect In Hover

Figure 2.7 schematically shows the dynamic vortex tube geometry (side view, in the rotor disk plane coordinate system) for a helicopter rotor undergoing a step change in climb rate V_c from hover. During the transient, the net mean inflow across the rotor disk will gradually increase to a higher value due to the climb velocity. Hence, the wake spacing will also gradually increase to a higher value. The dynamic vortex tube shown in Figure 2.7 is comprised of two parts, one with a higher wake spacing corresponding to the steady climb state and the other with a lower wake spacing corresponding to the steady hover condition. The tube part with higher wake spacing will gradually convect far downstream and finally dominate the wake effect on inflow across the rotor disk. The general case of the mean induced inflow across the rotor disk by the dynamic vortex tube of a rotor undergoing a step change in climb rate in forward flight is given in Appendix A (Equations A.44.a and A.44.b). After substituting $\mu = 0$, i.e., $\chi = 0$, Equations A.44.a and A.44.b can be rewritten as follows

$$v_0^{(I)} = \frac{\bar{\gamma}_1}{4\pi} \int_0^1 \int_0^{2\pi} \frac{(1 - \hat{r}cos\psi_0)}{1 + \hat{r}^2 - 2\hat{r}cos\psi_0} sin\theta_0 \, d\psi_0 d\hat{r} \tag{2.11.a}$$

$$v_0^{(II)} = \frac{\bar{\gamma}_2}{4\pi} \int_0^1 \int_0^{2\pi} \frac{(1 - \hat{r}cos\psi_0)}{1 + \hat{r}^2 - 2\hat{r}cos\psi_0} (1 - sin\theta_0) \, d\psi_0 d\hat{r} \tag{2.11.b}$$

where $\bar{\gamma}_1$ and $\bar{\gamma}_2$, are the vorticity densities around the two parts of the dynamic vortex tube in Figure 2.7 with higher and lower wake spacings, respectively. In equations 2.11.a and 2.11.b,

$$tan\theta_0 = \frac{\bar{\eta}_0}{\sqrt{1 + \hat{r}^2 - 2\hat{r}cos\psi_0}} \tag{2.12}$$

where $\bar{\eta}_0 = \eta_0/\bar{r}_0$ and η_0 is the length of the part with a higher wake spacing along the vortex tube axis. The mean induced inflow across the rotor disk induced by the whole dynamic vortex tube shown in Figure 2.7 can be written as

$$\lambda_0 = v_0^{(I)} + v_0^{(II)} \tag{2.13}$$

There are two limiting cases corresponding to the initial and the steady state of the maneuver. At the initiation of the maneuver, equation 2.13 reduces to

$$\lambda_0 = \frac{\bar{\gamma}_2}{4\pi} \int_0^1 \int_0^{2\pi} \frac{(1 - \hat{r}cos\psi_0)}{1 + \hat{r}^2 - 2\hat{r}cos\psi_0} \, d\psi_0 d\hat{r} = \frac{\bar{\gamma}_2}{2} \tag{2.14}$$

26
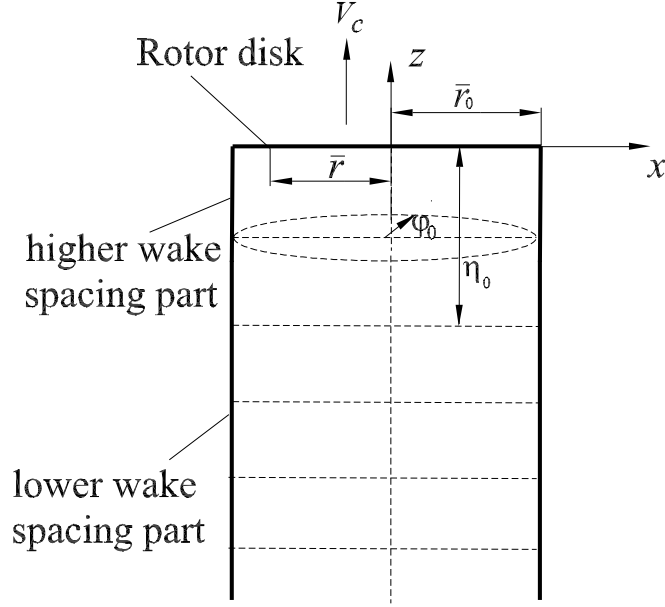
Figure 2.7: Dynamic vortex tube geometry of a rotor undergoing a step change in climb rate (side view)

when the wake reaches its steady shape corresponding to the steady climb rate, Equation 2.13 becomes

$$\lambda_0 = \frac{\bar{\gamma}_1}{4\pi} \int_0^1 \int_0^{2\pi} \frac{(1 - \hat{r}cos\psi_0)}{1 + r^2 - 2\hat{r}cos\psi_0} d\psi_0 d\hat{r} = \frac{\bar{\gamma}_1}{2} \tag{2.15}$$

Further more, under the assumption of small climb rate V_c and uniform circulation distribution, we have

$$\lambda_0 = \frac{\bar{\gamma}_2}{2} = \sqrt{\frac{C_T}{2}} = v_h \tag{2.16}$$

at the initiation of the maneuver and

$$\lambda_0 = \frac{\bar{\gamma}_1}{2} = \frac{C_T}{V_c + 2v_h} \tag{2.17}$$

when the wake reaches its steady shape at the end of the maneuver. Equations 2.16 and 2.17 are consistent with the results from momentum theory [57]. During the transient phase of the maneuver, the integrals in equation 2.13 are evaluated numerically.

Figure 2.8 shows a typical variation with time of the mean induced inflow normalized by the inflow at hover for a step climb rate of $V_c = 0.1v_h$. Each curve in the plot corresponds
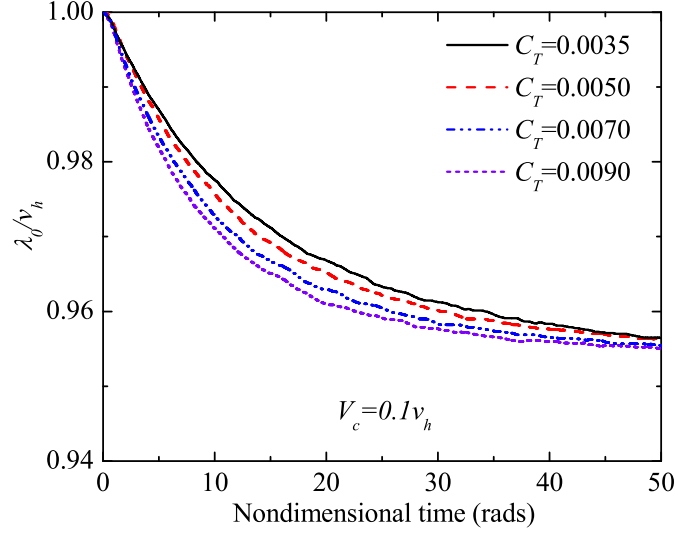
Figure 2.8: Mean induced inflow variation with time for different values of C_T following a step change in climb rate, $\Delta V_c = 0.1 v_h$

to a different value of thrust coefficient. It can be seen that all the inflow variations exhibit a first order behavior with time. The normalized steady inflow (normalized by the value of inflow at hover) for different values of thrust coefficient is the same, which is consistent with momentum theory. Also, for higher values of thrust coefficient, the mean induced inflow reaches its steady state faster.

In Figure 2.9, the thrust coefficient is fixed to a value of $C_T = 0.0065$ while the climb rate is varied. Each curve in the plot corresponds to a different climb rate. It can be seen again that all the inflow variations exhibit a first order behavior with time. With an increase in climb rate, the steady value of the induced mean inflow is reduced because of the wake vorticity will convect far downstream faster, which is consistent with momentum theory.

Figure 2.10 shows values of the nondimensional time constant associated with wake spacing dynamics for different values of thrust coefficient as extracted from the vortex tube analysis results. The solid line in the figure is an empirical approximation obtained as

$$\tau_S = \frac{32}{15\pi v_h} \qquad (2.18)$$

Where v_h is the mean induced velocity in hover.

28
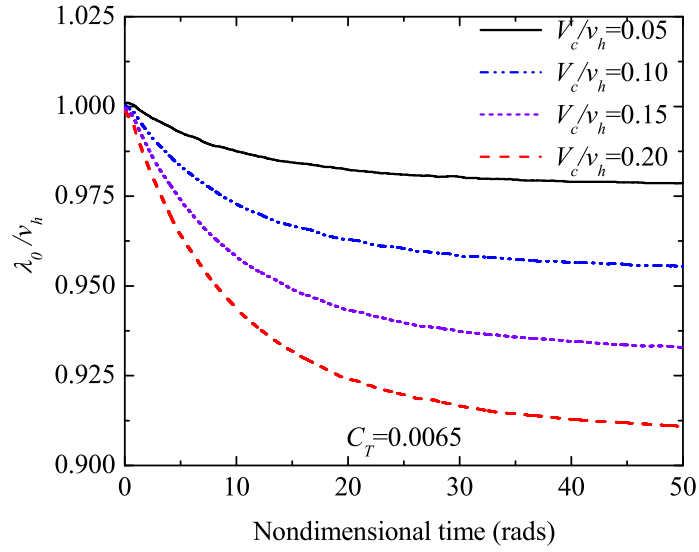
Figure 2.9: Mean induced inflow variation with time across the rotor disk for different values of climb rate, $C_T = 0.0065$
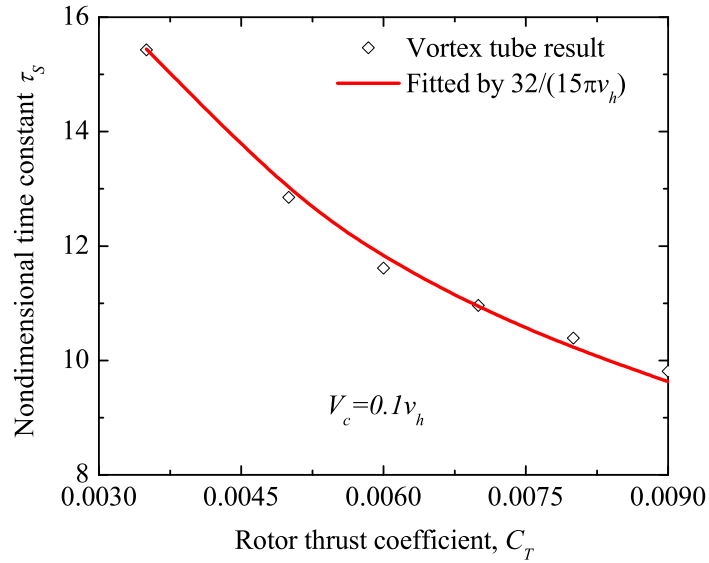
Figure 2.10: Variation of the nondimensional time constant associated with wake spacing effect versus rotor thrust coefficient near hover

2.2 Dynamic Wake Distortions In Forward Flight

2.2.1 Dynamic Wake Bending Effect in Forward Flight

A typical variation of the longitudinal inflow gradient across the rotor disk with time, predicted by the dynamic vortex tube analysis developed in Appendix A, is shown in Figure 2.11, for a nondimensional pitch rate of $\bar{q} = 0.005$ and thrust coefficient of $C_T = 0.0065$ at a forward flight advance ratio of $\mu = 0.05$. It can be clearly seen that the inflow gradient variation exhibits a first order behavior with time. Therefore, a first order approximation is also superimposed on the plot.

Figure 2.12 shows the values of the nondimensional time constant associated with wake bending dynamics in forward flight with an advance ratio of $\mu = 0.05$ versus thrust coefficient as extracted from the dynamic vortex tube analysis results. In Figure 2.12, the symbols are those predicted by the dynamic vortex tube analysis and the solid line is an empirical approximation obtained as

$$\tau_R = \frac{32}{15\pi\bar{V}} \tag{2.19}$$

where $\bar{V}$ is the mass flow parameter associated with the first and higher harmonics of inflow and is given by

$$\bar{V} = \frac{\mu^2 + (\lambda_0 + V_c)(2\lambda_0 + V_c)}{V_m} \tag{2.20}$$

where V_m is the mass flow parameter associated with the mean inflow, which is given by

$$V_m = \sqrt{\mu^2 + (\lambda_0 + V_c)^2} \tag{2.21}$$

From Figure 2.12, it can be seen that the extracted empirical formula (Equation 2.19) agrees well with the results predicted by the dynamic vortex tube model. For hover case, $\mu = 0$ and equation 2.19 reduces to

$$\tau_R = \frac{16}{15\pi v_h} \tag{2.22}$$

where v_h denotes the nondimensional mean induced velocity in hover. It can be seen that in hover case the time constant associated with wake curvature effect reduces to exactly the same form as that given by Equation 2.6.
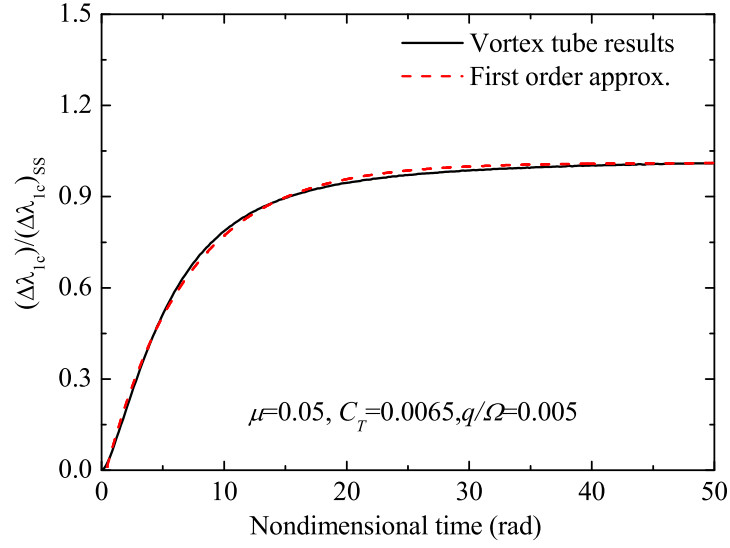
Figure 2.11: Inflow gradient variation with time due to wake curvature effect for a four-bladed rotor in forward flight, $\mu = 0.05, C_T = 0.0065, \bar{q} = 0.005$.
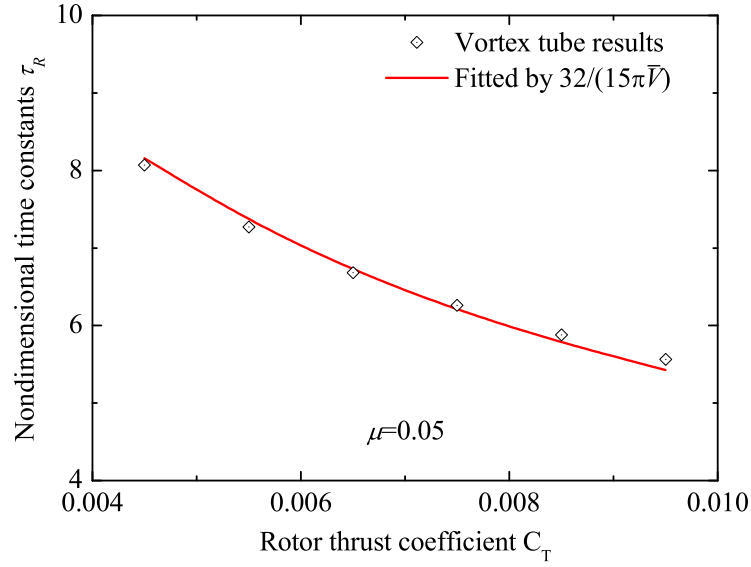
Figure 2.12: Variation of nondimensional time constant associated with wake curvature effect versus rotor thrust coefficient in forward flight, $\mu = 0.05$.

2.2.2 Dynamic Wake Skew Effect In Forward Flight

Figure 2.13 shows a typical variation of the longitudinal inflow gradient with time to a step advance ratio of $\Delta\mu = 0.01$ from forward flight ($\mu = 0.05$) at a thrust coefficient of $C_T = 0.0065$, predicted using the dynamic vortex tube analysis developed in Appendix A. It can be seen from Figure 2.13 that the inflow gradient once again exhibits a first order variation with time. Figure 2.14 shows the values of the nondimensional time constant associated with the dynamic wake skew effect in forward flight for different values of thrust coefficient as extracted from the dynamic vortex tube analysis results. In Figure 2.14, the symbols are the results predicted by the dynamic vortex tube analysis and the solid line is an empirical approximation obtained as

$$\tau_X = \frac{32}{15\pi\bar{V}} \tag{2.23}$$

where $\bar{V}$ is the mass flow parameter associated with the first and higher harmonics of inflow and is given by Equation 2.20.

It can be seen from Figure 2.14 that the formula given in Equation 2.23 agrees well with the results predicted by the dynamic vortex tube analysis. Therefore, it can be used to represent the time constant associated with the wake skew dynamics in low speed forward flight. For hover case, $\mu = 0$, Equation 2.23 reduces to

$$\tau_X = \frac{16}{15\pi v_h} \tag{2.24}$$

which is exactly the same expression for the time constant associated with dynamic wake skew effect in hover as that given by Equation 2.10.

2.2.3 Dynamic Wake Spacing Effect in Forward Flight

Figure 2.15 shows a typical variation with time of the mean induced inflow normalized by the mean induced inflow in hover for a step change in climb rate of $V_c = 0.1v_h$ at forward flight with an advance ratio of $\mu = 0.05$, as predicted from the dynamic vortex tube analysis developed in Appendix A. It can be seen that the inflow variation exhibits a first order behavior with time. Figure 2.16 shows values of the nondimensional time constant
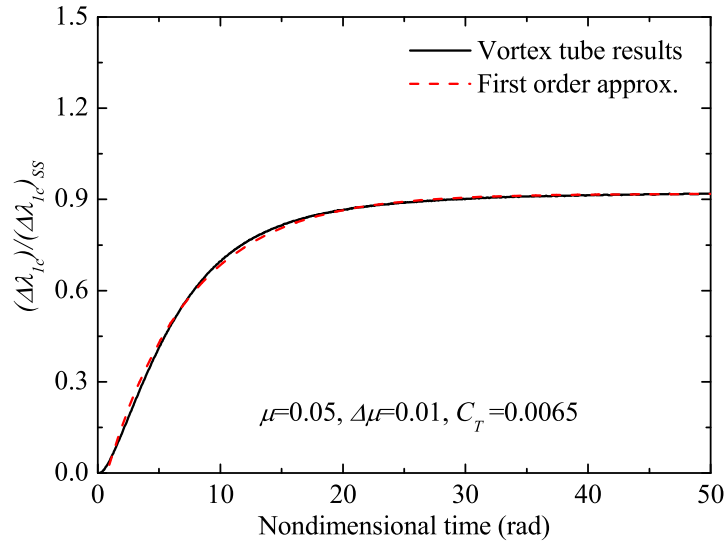
Figure 2.13: Inflow gradient across the rotor disk due to a step advance ratio from forward flight, $\mu = 0.05, C_T = 0.0065, \Delta\mu = 0.01$.
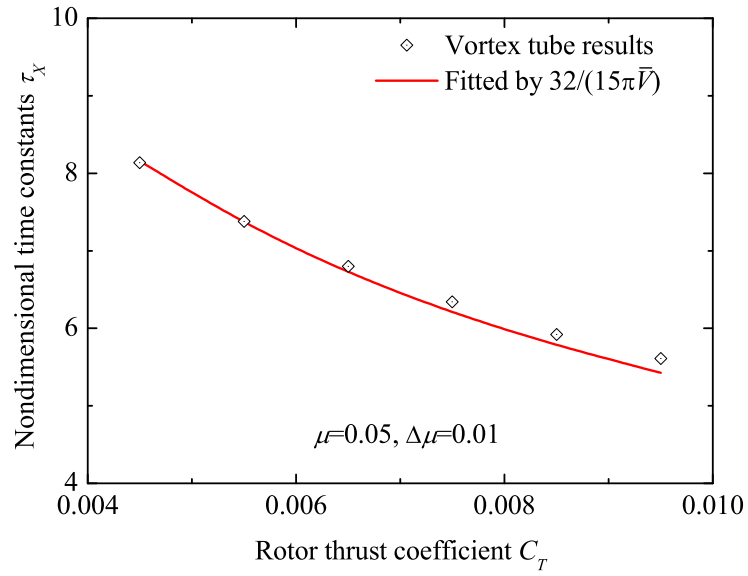
Figure 2.14: Variation of nondimensional time constant associated with dynamic wake skew effect with rotor thrust coefficient in forward flight, $\mu = 0.05$

associated with wake spacing dynamics in forward flight for different values of rotor thrust coefficient as extracted from the vortex tube analysis results. The solid line in Figure 2.16 is an empirical approximation obtained as

$$\tau_S = \frac{32}{15\pi V_m} \tag{2.25}$$

where V_m is the mass flow parameter associated with the mean inflow and is given by Equation 2.21.

For hover case, $\mu = 0$, equation 2.25 reduces to

$$\tau_S = \frac{32}{15\pi v_h} \tag{2.26}$$

and is exactly the same form as the time constant for dynamic wake spacing effect in hover given by Equation 2.18.

2.3   *Dynamic Wake Distortion Model*

It is clear from the dynamic vortex tube analysis in the previous sections that dynamic wake distortion effects, i.e., dynamic wake bending, wake skew and wake spacing have significant influence on the rotor inflow during maneuvering and transitional flight phases where the rotor wake transitions through different shapes. The results given by the dynamic vortex tube model in the previous section show that the variations of inflow across the rotor disk due to dynamic wake bending, wake skew and wake spacing essentially exhibit a first order behavior with time. Therefore, the effect of dynamic wake distortions on the inflow across the rotor disk can be represented by a set of first order differential equations as

$$[\tau_D] \begin{Bmatrix} \overset{\star}{X} \\ S \\ \kappa_c \\ \kappa_s \end{Bmatrix} + \begin{Bmatrix} X \\ S \\ \kappa_c \\ \kappa_s \end{Bmatrix} = \begin{Bmatrix} X \\ S \\ \kappa_c \\ \kappa_s \end{Bmatrix}_{qs} \tag{2.27}$$

where X, S, κ_c, κ_s, are wake skew, wake spacing, longitudinal and lateral wake curvatures, respectively, $\overset{\star}{()}$ denotes differentiation with respect to nondimensional time, subscript qs
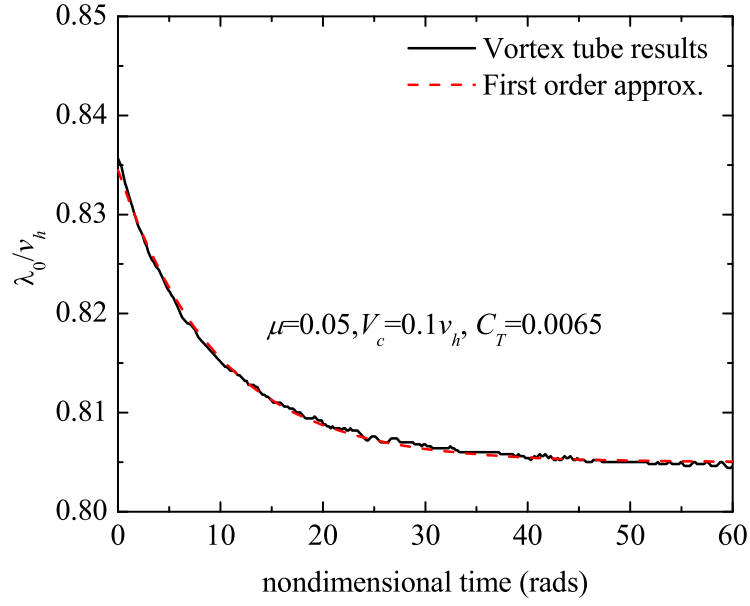
Figure 2.15: Mean induced inflow variation with time following a step climb rate in forward flight, $\mu = 0.05, V_c = 0.1v_h$.
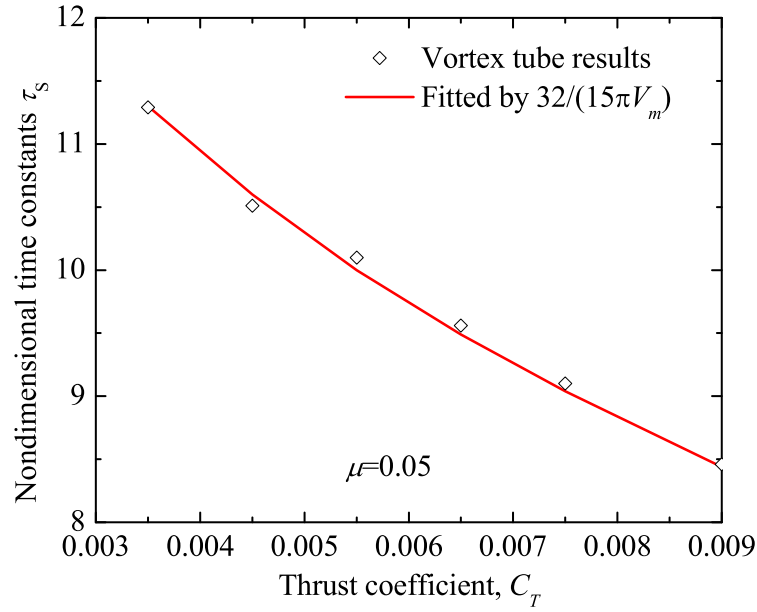
Figure 2.16: Variation of nondimensional time constant associated with dynamic wake spacing effect versus rotor thrust coefficient in forward flight, $\mu = 0.05$.

denotes quasi-steady values. Matrix $[\tau_D]$ contains the nondimensional time constants associated with dynamic wake distortion effects, i.e., dynamic wake bending, wake skew and wake curvature effect. In general, the wake skew, wake spacing and wake curvatures are fully coupled. However, the coupling effects among these states are neglected in the present study and the time constant matrix $[\tau_D]$ is assumed to take a diagonal form as

$$[\tau_D] = \begin{bmatrix} \tau_X & & & O \\ & \tau_S & & \\ & & \tau_R & \\ O & & & \tau_R \end{bmatrix} \tag{2.28}$$

Where τ_X, τ_S, τ_R are given by the empirical formulae (Equations 2.23, 2.25, and 2.19, respectively) developed in the previous section using a dynamic vortex tube analysis. The right hand side of Equation 2.27 corresponds to the quasi-steady wake skew, wake spacing, longitudinal and lateral curvatures, which are given by

$$(X)_{qs} = \tan\left(\frac{\chi}{2}\right) \tag{2.29.a}$$

$$(S)_{qs} = 2\pi V_m \tag{2.29.b}$$

$$(\kappa_c)_{qs} = \frac{\bar{q} - \overset{\star}{\beta}_{1c}}{\lambda_0 + V_c} \tag{2.29.c}$$

$$(\kappa_s)_{qs} = \frac{\bar{p} - \overset{\star}{\beta}_{1s}}{\lambda_0 + V_c} \tag{2.29.d}$$

In the above equations, $\bar{q}$ and $\bar{p}$, respectively, denote the nondimensional pitch and roll rates. $\overset{*}{\beta}_{1c}, \overset{*}{\beta}_{1s}$ are the rotor disk longitudinal and lateral flapping rates. χ is the steady wake skew angle, which can be calculated from the momentum theory [57] as

$$\chi = \tan^{-1}\left(\frac{\mu}{\lambda_0 + V_c}\right) \tag{2.30}$$

V_m is the mass parameter associated with rotor mean inflow and is given by Equation 2.21. The wake spacing parameter S defined by Equation 2.29.b physically represents the distance that the rotor wake travels at a velocity of V_m during one rotor revolution.

CHAPTER III

ROTOR INFLOW MODEL FOR MANEUVERING FLIGHT

For helicopters in maneuvering and transitional flight, the rotor wake trailed behind rotor blades will be distorted and will be significantly different from that in steady flight. Since the rotor wake remains in close proximity to the rotor disk, it is perceivable that the distorted rotor wake will induce strong variations in rotor inflow and therefore alter the blade dynamic response and vehicle response. Alternatively, the blade and vehicle dynamic responses will influence the rotor wake distortion. To account for the rotor wake distortion effect for flight simulation and control law development, it would be highly desirable to represent the wake distortion effect in closed form solutions. In this chapter, a reduced order model using a vortex tube analysis is developed to model the couplings between inflow perturbations across the rotor disk and rotor mean and cyclic loadings during helicopter maneuvering flight. Then, both the Pitt-Peters dynamic inflow model [47] and the Peters-He finite state inflow model [48], which are routinely used in rotorcraft industry, are augmented to account for rotor wake distortion effect during maneuvering flight.

3.1   Inflow Perturbations Due To Rotor Wake Distortions

In this section, a reduced order model is developed to account for the couplings between rotor inflow perturbations and rotor mean and cyclic loadings due to rotor wake distortions during maneuvering flight.

3.1.1   Inflow Perturbations Due to Mean Loading

The coupling between inflow perturbations and rotor mean loading due to rotor wake distortion effect during helicopter maneuvering flight is obtained by using a vortex tube analysis as developed in Appendix B. In the present vortex tube analysis, the vortices generated at

the rotor blades are assumed to be wrapped around a tube of continuous vorticity, representing the outer surface of the rotor wake. The induced inflow across the rotor disk due to the vortex tube can be calculated using the Biot-Savart Law. For the representation of rotor mean loading effect, it is assumed that the vorticity strength around the vortex tube is circumferentially uniform.

Using the vortex tube analysis [58, 59, 60], the inflow perturbations across the rotor disk (Δv_z) induced by a single distorted rotor wake tube with a radius of $\bar{r}_0$ and a uniform strength of $\bar{\gamma}_0$ during a steady rotor pitch and/or roll motion is developed in Appendix B (Equation B.20) and can be written as

$$\Delta v_z^{(mean)}(\bar{r}, \psi) = \begin{cases} \dfrac{\bar{\gamma}_0}{2}\kappa_c X\bar{r}_0 e_1(\hat{r}) + \dfrac{\bar{\gamma}_0}{2}\bar{r}_0 X e_2(\hat{r})(\kappa_c cos2\psi + \kappa_s sin2\psi) \\ +\dfrac{\bar{\gamma}_0}{2}\kappa_c\bar{r}\left(1 - \dfrac{3}{2}X^2\right)cos\psi + \dfrac{\bar{\gamma}_0}{2}\kappa_s\bar{r}\left(1 + \dfrac{3}{2}X^2\right)sin\psi \qquad (\hat{r} < 1) \\[2ex] \dfrac{\gamma_0}{2}\kappa_c X\bar{r}_0 e_3(\hat{r}) + \dfrac{\bar{\gamma}_0}{2}\bar{r}_0 X e_4(\hat{r})(\kappa_c cos2\psi + \kappa_s sin2\psi) \\ +\dfrac{3\bar{\gamma}_0}{4}\bar{r}_0 X^2 e_5(\hat{r})(\kappa_c cos\psi + \kappa_s sin\psi) \qquad (\hat{r} > 1) \\ +\dfrac{3\bar{\gamma}_0}{4}\bar{r}_0 X^2 e_6(\hat{r})(\kappa_c cos3\psi + \kappa_s sin3\psi) \end{cases}$$

$$(3.1)$$

where superscript $(mean)$ denotes the rotor mean loading effect, $\hat{r} = \bar{r}/\bar{r}_0$, $\bar{r}$ and ψ, respectively, are the radial position and azimuth angle on the rotor disk, κ_c, κ_s are the longitudinal and lateral wake curvatures, X is wake skew, $e_i(\hat{r}), i = 1, 2, \ldots, 6$ are defined in Appendix B (Equations B.11.a, B.11.b, B.11.c, B.11.d, B.11.e, B.11.f).

3.1.2 Inflow Perturbations Due to Cyclic Loading

For helicopters in maneuvering flight, rotor bound circulation also changes circumferentially, and therefore, the inflow perturbations due to the circumferential variation of rotor bound circulation during helicopter maneuvering flight need to be investigated and its effect on response prediction need to be assessed. In the current study, only the first harmonic cyclic variation of rotor bound circulation is considered, that is, the longitudinal variation of bound circulation $(\bar{\Gamma}_{1c})$ and the lateral variation of bound circulation $(\bar{\Gamma}_{1s})$.

When rotor bound circulation $(\bar{\Gamma})$ changes around the azimuth by a $d\bar{\Gamma}$, a free radial

vortex of strength $-d\bar{\Gamma}$ is released at the same time and the free tip vortex strength is increased by $d\bar{\Gamma}$. The calculation of the induced inflow due to rotor cyclic loading distribution is very complicated. Dress [61] proposed a simplified approach to calculate the induced inflow across the rotor disk due to a cyclic variation of rotor bound circulation for a rotor in steady forward flight. A similar approach is followed in the present study to approximate the inflow perturbations due to rotor cyclic loading effect during maneuvering flight. As illustrated in Figures B.1 and B.2, the shed radial and tip vortices due to the cosine and sine parts of the cyclic variation of rotor bound circulation are taken together and it is assumed that they form two tube cylinders with uniform vortex strength on both sides of the y-axis (x-axis), i.e., two hypothetical rotor wake tubes, each with a radius of $\bar{r}_0/2$, one with a vortex strength of $\bar{\gamma}_{1c}$ ($\bar{\gamma}_{1s}$) and the other with a vortex strength of $-\bar{\gamma}_{1c}$ ($-\bar{\gamma}_{1s}$) to account for the effect of $\bar{\Gamma}_{1c}$ ($\bar{\Gamma}_{1s}$). Therefore, the problem is reduced to a simpler one similar to the mean loading case and Equation 3.1 can be used to calculate the inflow perturbations due to the cyclic loading effect for helicopters in maneuvering flight.

To account for the effect of longitudinal variation (*cosine* part) of rotor bound circulation, as shown in Figures B.1, the shed radial and tip vortices due to the cosine part of the circumferential variation of rotor bound circulation is approximated by two hypothetical vortex tubes placed on both sides of the y-axis, each of them with a radius of $\bar{r}_0/2$, one tube with a vortex strength of $\bar{\gamma}_{1c}$ at $\psi = 0^0$ and the other with a vortex strength of $-\bar{\gamma}_{1c}$ at $\psi = 180^0$. For the effect of lateral variation (*sine* part) of rotor bound circulation, as shown in Figures B.2, the shed radial and tip vortices due to the sine part of the circumferential variation of rotor blade bound circulation is approximated by two hypothetical vortex tubes placed on both sides of the x-axis, each of them with a radius of $\bar{r}_0/2$, one tube with a vortex strength of $\bar{\gamma}_{1s}$ at $\psi = 90^0$ and the other with a vortex strength of $-\bar{\gamma}_{1s}$ at $\psi = 270^0$. Since the two hypothetical vortex tubes have uniform vorticity density ($\bar{\gamma}_{1c}$ or $\bar{\gamma}_{1s}$) around the tubes, the problem is reduced to a simpler one similar to the mean loading case. The details of derivation are given in Appendix B. From Appendix B, the contributions to the mean and first harmonic variations of inflow perturbations across the rotor disk due to rotor

cyclic loading effect during maneuvering flight can be written as

$$\Delta v_z^{(cyc)}(\bar{r}, \psi) = \begin{cases} \dfrac{\bar{\gamma}_{1c}}{2}\left\{\kappa_c X \bar{r}_0 d_1(\hat{r})cos\psi + \kappa_s X \bar{r}_0 d_2(\hat{r})sin\psi\right\} \\[2mm] +\dfrac{\bar{\gamma}_{1s}}{2}\left\{\kappa_c X \bar{r}_0 d_4(\hat{r})sin\psi\right\} \\[2mm] +\dfrac{\bar{\gamma}_{1s}}{2}\left\{\kappa_s X \bar{r}_0 d_2(\hat{r})cos\psi\right\} & (\hat{r} < 1) \\[4mm] \dfrac{\bar{\gamma}_{1c}}{2}\left\{\kappa_c X \bar{r}_0 d_3(\hat{r})cos\psi + \kappa_s X \bar{r}_0 d_2(\hat{r})sin\psi\right\} \\[2mm] +\dfrac{\bar{\gamma}_{1s}}{2}\left\{\kappa_c X \bar{r}_0 d_5(\hat{r})sin\psi\right\} \\[2mm] +\dfrac{\bar{\gamma}_{1s}}{2}\left\{\kappa_s X \bar{r}_0 d_2(\hat{r})cos\psi\right\} & (\hat{r} > 1) \end{cases} \tag{3.2}$$

where superscript (cyc) denotes contribution from rotor cyclic loading effect, $d_i(\hat{r}), i = 1, 2, \ldots, 5$ are defined in the Appendix B (Equations B.27, B.28, B.34, B.41 and B.47). Therefore, the total inflow perturbations across the rotor disk due to rotor mean and cyclic loadings during maneuvering flight can be written as the sum of those due to the mean loading effect and those due to the cyclic loading effect, respectively, i.e.,

$$\Delta v_z(\bar{r}, \psi) = \Delta v_z^{(mean)}(\bar{r}, \psi) + \Delta v_z^{(cyc)}(\bar{r}, \psi) \tag{3.3}$$

3.2 Augmentation of the Pitt-Peters Dynamic Inflow Model

In the Pitt-Peters dynamic inflow model [47], the rotor wake is represented by a straight wake, which does not account for the rotor wake distortion effect during helicopter maneuvering flight. In this section, the Pitt-Peters dynamic inflow model is augmented to account for rotor wake distortion effect during helicopter maneuvering flight conditions.

In the current study, the rotor wake is represented by a single vortex tube with a tube radius of $\bar{r}_0 = 1$ and the rotor bound circulation can be written as

$$\bar{\Gamma}(\psi) = \bar{\Gamma}_0 + \bar{\Gamma}_{1c}cos\psi + \bar{\Gamma}_{1s}sin\psi \tag{3.4}$$

where $\bar{\Gamma}_0$ is the mean rotor bound circulation, $\bar{\Gamma}_{1c}$ and $\bar{\Gamma}_{1s}$, respectively, are the longitudinal and lateral variations of rotor bound circulation. Therefore, the mean and cyclic vorticity strengths around the vortex tube in Equations 3.1 and 3.2 can be related to the mean and

cyclic variations of rotor bound circulation as follows

$$\bar{\gamma}_0 = \frac{\bar{\Gamma}_0}{V_m} \tag{3.5.a}$$

$$\bar{\gamma}_{1c} = \frac{\bar{\Gamma}_{1c}}{V_m} \tag{3.5.b}$$

$$\bar{\gamma}_{1s} = \frac{\bar{\Gamma}_{1s}}{V_m} \tag{3.5.c}$$

where V_m is the mass flow parameter associated with the rotor mean inflow, which is given by Equation 2.21.

Similarly, the inflow perturbations across the rotor disk due to the rotor mean and cyclic loadings during helicopter maneuvering flight can be expanded up to the mean and first harmonic terms as

$$\Delta v_z(\bar{r}, \psi) = \Delta \lambda_0 + \Delta \lambda_{1c} \bar{r} cos\psi + \Delta \lambda_{1s} \bar{r} sin\psi \tag{3.6}$$

where $\Delta \lambda_0$ is the mean inflow perturbation, $\Delta \lambda_{1c}$ and $\Delta \lambda_{1s}$ are the longitudinal and lateral inflow gradient perturbations, respectively. Using the orthogonal property of trigonometric functions, these inflow perturbation coefficients can be extracted from Eqnuations 3.1, 3.2 and 3.3 as

$$\Delta \lambda_0 = \frac{1}{\pi} \int_0^{2\pi} \int_0^1 \Delta v_z(\bar{r}, \psi) \bar{r} \, d\bar{r} d\psi \tag{3.7.a}$$

$$\Delta \lambda_{1c} = \frac{4}{\pi} \int_0^{2\pi} \int_0^1 \Delta v_z(\bar{r}, \psi) \bar{r}^2 cos\psi \, d\bar{r} d\psi \tag{3.7.b}$$

$$\Delta \lambda_{1s} = \frac{4}{\pi} \int_0^{2\pi} \int_0^1 \Delta v_z(\bar{r}, \psi) \bar{r}^2 sin\psi \, d\bar{r} d\psi \tag{3.7.c}$$

where $\Delta v_z(\bar{r}, \psi)$ is given by Equation 3.3. Also, the rotor thrust, pitch and roll moment coefficients, i.e., C_T, C_M and C_L, can be calculated from momentum theory [57] as

$$C_T = \frac{1}{2\pi} \int_0^{2\pi} \int_0^1 (\bar{r} + \mu sin\psi) \bar{\Gamma} \, d\bar{r} d\psi \tag{3.8.a}$$

$$C_L = -\frac{1}{2\pi} \int_0^{2\pi} \int_0^1 (\bar{r} + \mu sin\psi) \bar{\Gamma} \bar{r} sin\psi \, d\bar{r} d\psi \tag{3.8.b}$$

$$C_M = -\frac{1}{2\pi} \int_0^{2\pi} \int_0^1 (\bar{r} + \mu sin\psi) \bar{\Gamma} \bar{r} cos\psi \, d\bar{r} d\psi \tag{3.8.c}$$

Substituting the expression for rotor bound circulation in Equation 3.4 into Equations 3.8.a, 3.8.b, 3.8.c and solving for the rotor bound circulation in terms of rotor thrust,

pitch and roll moment coefficients gives rise to

$$\bar{\Gamma}_0 = \frac{C_T}{1 - \frac{3}{2}\mu^2} + \frac{3\mu C_L}{1 - \frac{3}{2}\mu^2} \tag{3.9.a}$$

$$\bar{\Gamma}_{1c} = -3C_M \tag{3.9.b}$$

$$\bar{\Gamma}_{1s} = -3C_L - \frac{3}{2}\mu C_T \tag{3.9.c}$$

In Equation 3.9.a, the factor $(1 - 3\mu^2/2)$ is taken to be 1.0 since μ^2 is much smaller compared with 1.0 for low speed forward flight. Substituting Equations 3.1, 3.2, 3.3, 3.9.a, 3.9.b and 3.9.c into Equations 3.7.a, 3.7.b and 3.7.c and rearranging the result in matrix form gives rise to

$$\begin{Bmatrix} \Delta\lambda_0 \\ \Delta\lambda_{1c} \\ \Delta\lambda 1s \end{Bmatrix} = \frac{1}{V_m}[\Delta L] \begin{Bmatrix} C_T \\ -C_L \\ -C_M \end{Bmatrix} \tag{3.10}$$

where matrix $[\Delta L]$ represent perturbation to the inflow gain matrix due to the mean and cyclic loading effects during helicopter maneuvering flight. To clearly illustrate the contributions to this matrix due to different sources, $[\Delta L]$ can be further decomposed to the sum of three sub matrices as

$$[\Delta L] = [\Delta L_1] + [\Delta L_2] + [\Delta L_3] \tag{3.11}$$

where $[\Delta L_1]$ denotes coupling between wake curvature and rotor mean loading. $[\Delta L_2]$ accounts for the coupling effect between wake curvature/wake skew and rotor mean loading, and matrix $[\Delta L_3]$ represents the coupling effect between wake curvature/wake skew and rotor cyclic loading. They can be expressed as

$$[\Delta L_1] = K_{Re} \begin{bmatrix} 0 & 0 & 0 \\ \frac{\kappa_s}{2} & 0 & 0 \\ \frac{\kappa_c}{2} & 0 & 0 \end{bmatrix} \tag{3.12}$$

$$[\Delta L_2] = K_{Re} \begin{bmatrix} 0 & 0 & 0 \\ \frac{3}{4}\kappa_s X^2 & 0 & 0 \\ -\frac{3}{4}\kappa_c X^2 & 0 & 0 \end{bmatrix} \tag{3.13}$$

42

$$[\Delta L_3] = K_{Re} \begin{bmatrix} 0 & 0 & 0 \\ \dfrac{5}{4}\mu\kappa_c X & l_{22} & -\dfrac{5}{2}\kappa_s X \\ \dfrac{5}{4}\mu\kappa_s X & l_{32} & -\dfrac{3}{10}\kappa_c X \end{bmatrix} \qquad (3.14)$$

where

$$l_{22} = -\frac{5}{2}\kappa_c X - \frac{3\mu}{2}\kappa_s(1 + \frac{3}{2}X^2)$$

$$l_{32} = -\frac{5}{2}\kappa_s X - \frac{3\mu}{2}\kappa_c(1 - \frac{3}{2}X^2)$$

Replacing the mass flow parameter V_m in Equation 3.10 by the mass flow parameter matrix $[V]$ gives rise to

$$\left\{ \begin{array}{c} \Delta\lambda_0 \\ \Delta\lambda_{1c} \\ \Delta\lambda1s \end{array} \right\} = [V]^{-1}[\Delta L] \left\{ \begin{array}{c} C_T \\ -C_L \\ -C_M \end{array} \right\} \qquad (3.15)$$

The Pitt-Peters dynamic inflow model [47] for helicopter axial and steady forward flight can be formulated as

$$[M] \left\{ \begin{array}{c} \overset{\star}{\lambda_0} \\ \lambda_{1s} \\ \lambda_{1c} \end{array} \right\} + [V][\tilde{L}]^{-1} \left\{ \begin{array}{c} \lambda_0 \\ \lambda_{1s} \\ \lambda_{1c} \end{array} \right\} = \left\{ \begin{array}{c} C_T \\ -C_L \\ -C_M \end{array} \right\} \qquad (3.16)$$

where λ_0, λ_{1c} and λ_{1s} are the mean induced inflow, longitudinal and lateral inflow gradients across the rotor disk, respectively. The apparent mass matrix $[M]$, mass flow parameter matrix $[V]$ and inflow gain matrix $[\tilde{L}]$, respectively, can be written as

$$[M] = \begin{bmatrix} \dfrac{128}{75\pi} & & O \\ & \dfrac{16}{45\pi} & \\ O & & \dfrac{16}{45\pi} \end{bmatrix} \qquad (3.17)$$

$$[V] = \begin{bmatrix} V_m & & O \\ & \bar{V} & \\ O & & \bar{V} \end{bmatrix} \qquad (3.18)$$

43

$$[\tilde{L}] = \begin{bmatrix} \dfrac{1}{2} & 0 & -\dfrac{15\pi}{64}X \\ 0 & 2(1+X^2) & 0 \\ \dfrac{15\pi}{64}X & 0 & 2(1-X^2) \end{bmatrix} \tag{3.19}$$

where X is wake skew, the mass flow parameters V_m and $\bar{V}$ associated with mean and higher harmonics of inflow are given by Equations 2.21 and 2.20, respectively.

Assuming that the unsteady part of rotor pressure perturbations due to wake distortion effect is negligible, the Pitt-Peters dynamic inflow model (Equation 3.16) can be augmented with Equation 3.15 to account for the wake distortion effect during helicopter maneuvering flight as follows

$$[M] \begin{Bmatrix} \overset{\star}{\lambda_0} \\ \lambda_{1s} \\ \lambda_{1c} \end{Bmatrix} + [V][L]^{-1} \begin{Bmatrix} \lambda_0 \\ \lambda_{1s} \\ \lambda_{1c} \end{Bmatrix} = \begin{Bmatrix} C_T \\ -C_L \\ -C_M \end{Bmatrix} \tag{3.20}$$

where the augmented inflow gain matrix $[L]$ can be written as

$$[L] = [\tilde{L} + \Delta L] = [\tilde{L} + \Delta L_1 + \Delta L_2 + \Delta L_3] \tag{3.21}$$

The inflow gain matrix perturbation $[\Delta L]$ is obtained based on the vortex tube results, which uses Taylor expansion up to the first order of pitch and/or roll rate and up to the second order of wake skew, therefore, matrices $[\Delta L_1]$, $[\Delta L_2]$ and $[\Delta L_3]$ are valid up to the first order of wake curvatures (κ_c, κ_s), and the second order of wake skew X.

3.3 Augmentation of the Finite State Inflow Model

Similarly, the Peters-He finite state inflow model [48] for axial and steady forward flight can be augmented to include rotor wake distortion effect during helicopter maneuvering flight as described in the following.

The relationship between inflow perturbation distribution across the rotor disk and rotor mean/cyclic loadings induced by a single distorted vortex tube is given by Equation 3.3. With superposition of concentric vortex tubes, the inflow perturbation distribution across the rotor disk plane for a maneuvering rotor with radially non-uniform loading distribution

can be obtained as

$$\Delta\lambda(\bar{r},\psi) = \int_0^1 \Delta v_z(\bar{r},\psi)\, d\bar{r}_0 \tag{3.22}$$

where Δv_z denotes the inflow perturbation induced by a single vortex tube, which is given by Equation 3.3. The inflow perturbations induced by the whole distorted rotor wake (Equation 3.22), which includes a series of concentric distorted vortex tubes, can be expanded in terms of the normalized associated Legendre functions and trigonometric functions as

$$\Delta\lambda(\bar{r},\psi) = \sum_{r=0}^{\infty} \sum_{j=r+1,r+3,\ldots}^{\infty} \phi_j^r \left[\Delta\alpha_j^r cosr\psi + \Delta\beta_j^r sinr\psi \right] \tag{3.23}$$

where ϕ_j^r is the radial expansion function used in the induced inflow expansion as given by He [48]. The perturbations of the inflow coefficients, i.e., $\Delta\alpha_j^r, \Delta\beta_j^r$, can be extracted from Equation 3.23 by using the orthogonality property of the trigonometric functions and the associated Legendre functions as

$$\Delta\alpha_j^0 = -\frac{1}{2\pi} \int_0^1 \int_0^{2\pi} \bar{r}\Delta\lambda(\bar{r},\psi)\bar{P}_j^0(\bar{\nu})\, d\bar{r} \tag{3.24.a}$$

$$\Delta\alpha_j^r = -\frac{1}{\pi} \int_0^1 \int_0^{2\pi} \bar{r}\Delta\lambda(\bar{r},\psi)\bar{P}_j^r(\bar{\nu})cosr\psi\, d\bar{r} \tag{3.24.b}$$

$$\Delta\beta_j^r = -\frac{1}{\pi} \int_0^1 \int_0^{2\pi} \bar{r}\Delta\lambda(\bar{r},\psi)\bar{P}_j^r(\bar{\nu})sinr\psi\, d\bar{r} \tag{3.24.c}$$

where $\bar{P}$ is the normalized associated Legendre function of the first kind. Similarly, rotor mean and cyclic loadings can be expanded as linear combinations of the normalized associated Legendre function of the first kind as

$$\bar{\Gamma}_0 = \sum_n \tau_n^0 \bar{P}_n^0 \tag{3.25.a}$$

$$\bar{\Gamma}_{1c} = \sum_n \tau_n^{1c} \bar{P}_n^1 \tag{3.25.b}$$

$$\bar{\Gamma}_{1s} = \sum_n \tau_n^{1s} \bar{P}_n^1 \tag{3.25.c}$$

where τ_n^{mc}, τ_n^{ms} ($m = 0, 1$ here) are the rotor forcing functions. Substituting Equations 3.3, 3.23, 3.25.a, 3.25.b and 3.25.c into Equations 3.24.a, 3.24.b and 3.24.c, the perturbations of inflow coefficients induced by the concentric distorted rotor wake tubes can be obtained in matrix form as follows

$$\left\{ \begin{array}{c} \Delta\alpha_j^r \\ \Delta\beta_j^r \end{array} \right\} = \frac{K_{Re}}{2V_m} \left[[D]_0 + [D]_1 X + [D]_2 X^2 \right] \left\{ \begin{array}{c} \tau_n^{mc} \\ \tau_n^{ms} \end{array} \right\} \tag{3.26}$$

where

$$[D]_0 = \kappa_c[C]_{c1} + \kappa_s[C]_{s1} \tag{3.27.a}$$

$$[D]_1 = \kappa_c[C]_{cX} + \kappa_s[C]_{sX} \tag{3.27.b}$$

$$[D]_2 = \kappa_c[C]_{cX^2} + \kappa_s[C]_{sX^2} \tag{3.27.c}$$

where the $[C]$'s matrices denote coupling effects among rotor inflow, wake curvatures and wake skew. For example, $[C]_{c1}$ and $[C]_{s1}$ denote coupling effect between rotor inflow, longitudinal and lateral wake curvatures, respectively. $[C]_{cX}$ and $[C]_{sX}$, respectively, denote the inflow-wake curvatures-linear wake skew coupling effect. Similarly, $[C]_{cX^2}$ and $[C]_{sX^2}$, respectively, represent the inflow-wake curvatures-quadratic wake skew coupling effect.

Assuming that the unsteady part of rotor pressure perturbations due to wake distortion effect is negligible, the inflow gain matrix $[L]$ of the Peters-He finite state inflow model can be augmented to include rotor wake distortion effect during helicopter maneuvering flight as follows

$$[L] = \left[[\tilde{L}] + [\Delta L] \right] \tag{3.28}$$

In Equation 3.28, $[\tilde{L}]$ retains its original form from the Peters-He finite state inflow model and $[\Delta L]$ accounts for the inflow perturbations induced by the concentric distorted wake tubes during helicopter maneuvering flight, which can be written as

$$[\Delta L] = K_{Re} \left([D]_0 + [D]_1 X + [D]_2 X^2 \right) \tag{3.29}$$

Hence, the augmented Peters-He finite state inflow model can be written as

$$[K] \left\{ \begin{matrix} \overset{\star}{\alpha_j^r} \\ \beta_j^r \end{matrix} \right\} + [V] [L]^{-1} \left\{ \begin{matrix} \alpha_j^r \\ \beta_j^r \end{matrix} \right\} = \frac{1}{2} \left\{ \begin{matrix} \tau_n^{mc} \\ \tau_n^{ms} \end{matrix} \right\} \tag{3.30}$$

where $[K]$ is the apparent mass matrix given by He [48].

Both the augmented Pitt-Peters dynamic inflow model (Equation 3.20) and the augmented Peters-He finite state inflow model (Equation 3.30) depend on the wake skew X, longitudinal and lateral wake curvatures, i.e., κ_c, κ_s, respectively. The mass flow parameter matrix $[V]$ depends on the wake spacing S. Therefore, the augmented inflow models

(Equations 3.20 and 3.30) and the rotor dynamic wake distortion model (Equation 2.27) developed in Chapter II can be solved simultaneously to account for rotor dynamic wake distortion effect during helicopter maneuvering and transitional flight.

In the following sections of this chapter, the dynamic wake distortion model (Equation 2.27), combined with the Augmented Pitt-Peters dynamic inflow model (Equation 3.20) is implemented in a generic helicopter simulation program [53] to study the coupling effect between rotor inflow and rotor mean/cyclic loading due to rotor wake distortions during helicopter maneuvering flight.

3.4 Effect of Wake Distortion Dynamics on the Stability of Flapping Dynamics

Initially, simulation runs are carried out to investigate the adequacy of the quasi-steady wake distortion model (using only Equations 3.20 or 3.30 without Equation 2.27). Figure 3.1 presents the off-axis pitch rate response of a UH-60 Black Hawk helicopter to a lateral cyclic control stick doublet input from hover for four different values of wake curvature parameter K_{Re}, predicted with the quasi-steady wake distortion model. For comparison purposes, the corresponding flight test data are also superimposed on the plot. From Figure 3.1, it can be clearly seen that the off-axis pitch rate response prediction without any wake curvature effect, i.e., the wake curvature parameter K_{Re} is zero, goes opposite to the corresponding flight test data. Also, it can be observed that the off-axis pitch rate response prediction is improved with a higher value of K_{Re}. However, a simulation divergence problem is observed when the value of wake curvature parameter (K_{Re}) is increased to 1.8 and beyond. This is in agreement with a similar finding in the literature [34]. It is felt that this may be due to the fact that, with a quasi-steady wake distortion model, the wake curvature effect is brought in too quickly. However, the simulation divergence problem is alleviated with the use of the developed dynamic wake distortion model as shown in the later results in this study. To gain further insight into this phenomena, the effect of wake distortion dynamics on the stability of rotor flapping dynamics is investigated in this section.

For small flapping angles, the coupled cyclic mode equations of flapping dynamics for
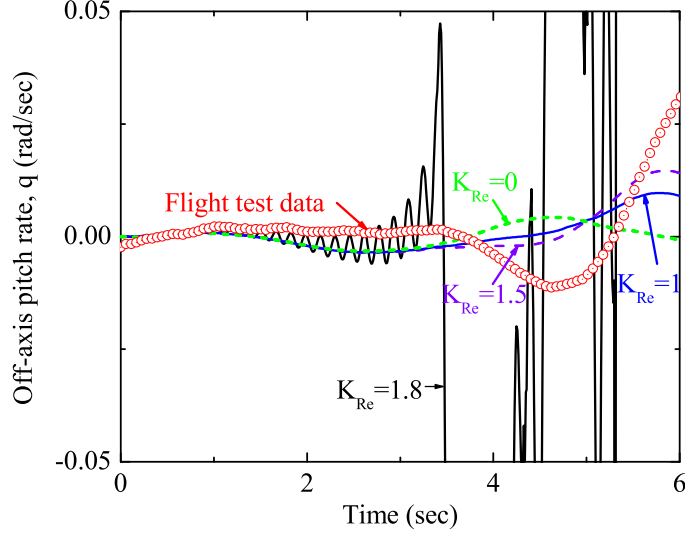
Figure 3.1: Simulation divergence observed with a quasi-steady wake distortion model in hover

an articulated rotor in hover can be written in the multi-blade coordinate system as [1, 57]

$$
\left\{
\begin{array}{c}
\overset{\star\star}{\beta}_{1c} + 2\overset{\star}{\beta}_{1s} + e_\beta \beta_{1c} \\
\overset{\star\star}{\beta}_{1s} - 2\overset{\star}{\beta}_{1c} + e_\beta \beta_{1s}
\end{array}
\right\}
= \gamma_{lock}
\left\{
\begin{array}{c}
M_{F_{1c}} \\
M_{F_{1s}}
\end{array}
\right\}
\tag{3.31}
$$

where β_{1c} and β_{1s}, respectively, are the longitudinal and lateral tip path plane tilt angles, $\overset{\star}{()}$ denotes differentiation with respect to nondimensional time. $e_\beta = \lambda_\beta^2 - 1$, λ_β is the blade flapping frequency, $M_{F_{1c}}$ and $M_{F_{1s}}$, respectively, are the longitudinal and lateral aerodynamic flapping moment coefficients, which can be formulated as

$$
\left\{
\begin{array}{c}
M_{F_{1c}} \\
M_{F_{1s}}
\end{array}
\right\}
= M_\theta
\left\{
\begin{array}{c}
\theta_{1c} \\
\theta_{1s}
\end{array}
\right\}
+ M_{\dot{\beta}}
\left\{
\begin{array}{c}
\overset{\star}{\beta}_{1c} + \beta_{1s} \\
\overset{\star}{\beta}_{1s} - \beta_{1c}
\end{array}
\right\}
+ M_{\lambda_c}
\left\{
\begin{array}{c}
\lambda_{1c} \\
\lambda_{1s}
\end{array}
\right\}
\tag{3.32}
$$

where

$$
M_\theta = \frac{1}{8} c_2 \qquad M_{\dot{\beta}} = -\frac{1}{8} d_1 \qquad M_{\lambda_c} = -\frac{1}{8} c_2
$$

and

$$
c_2 = 1 - \frac{\bar{e} + \bar{e}^2 + \bar{e}^3}{3} \qquad\qquad d_1 = 1 - \frac{2\bar{e} + \bar{e}^2}{3}
$$

where $\bar{e}$ is the equivalent flapping hinge offset.

48

The augmented Pitt-Peters dynamic inflow model (Equation 3.20) for helicopter maneuvering flight, involving only the cyclic inflow modes, can be written in hover as

$$
\tau_i \left\{ \begin{array}{c} \overset{\star}{\lambda_{1c}} \\ \lambda_{1s} \end{array} \right\} + \left\{ \begin{array}{c} \lambda_{1c} \\ \lambda_{1s} \end{array} \right\} = \left\{ \begin{array}{c} \dfrac{C_M}{\lambda_0} + K_{Re}\lambda_0 \kappa_c \\ \dfrac{C_L}{\lambda_0} + K_{Re}\lambda_0 \kappa_s \end{array} \right\} \tag{3.33}
$$

where τ_i is the time constant in the Pitt-Peters dynamic inflow model in hover and can be formulated as

$$
\tau_i = \frac{16}{45\pi\lambda_0}
$$

The dynamic wake distortion model, involving only the wake curvature dynamics in hover, can be written as

$$
\tau_R \left\{ \begin{array}{c} \overset{\star}{\kappa_c} \\ \kappa_s \end{array} \right\} + \left\{ \begin{array}{c} \kappa_c \\ \kappa_s \end{array} \right\} = \left\{ \begin{array}{c} \kappa_c \\ \kappa_s \end{array} \right\}_{qs} \tag{3.34}
$$

where the time constant for the wake curvature dynamics in hover is given by Equation 2.6, the quasi-steady longitudinal and lateral wake curvatures, i.e., κ_c and κ_s, in the right hand side of Equation 3.34 are given by Equations 2.29.c and 2.29.d.

To couple the inflow dynamics with rotor flapping dynamics, expressions for the aerodynamic pitch and roll moment coefficients, i.e., C_M and C_L, can be related to the flapping moment coefficients ($M_{F_{1c}}$ and $M_{F_{1s}}$) as follows [62]

$$
\left\{ \begin{array}{c} C_M \\ C_L \end{array} \right\} = -\frac{a\sigma}{2} \left\{ \begin{array}{c} M_{F_{1c}} \\ M_{F_{1s}} \end{array} \right\} \tag{3.35}
$$

Carrying out the Laplace transform for the flapping equation (Eqnuation 3.31), the flapping moment equation (Eqnuation 3.32), the dynamic wake distortion equation (Equation 3.34) and the inflow dynamics equation (Equation 3.33) gives rise to the characteristics polynomial of the coupled flapping-inflow-wake distortion dynamics as

$$
\begin{aligned}
\Delta(s) &= \left[(\tau_i s + 1 + K_L)(\tau_R s + 1)(s^2 + e_\beta) - \gamma M_{\dot{\beta}}(\tau_i s + 1)(\tau_R s + 1)s + \gamma K_{Re} M_{\lambda_c} s \right]^2 \\
&+ \left[2s(\tau_i s + 1 + K_L)(\tau_R s + 1) - \gamma M_{\dot{\beta}}(\tau_i s + 1)(\tau_R s + 1) \right]^2
\end{aligned} \tag{3.36}
$$
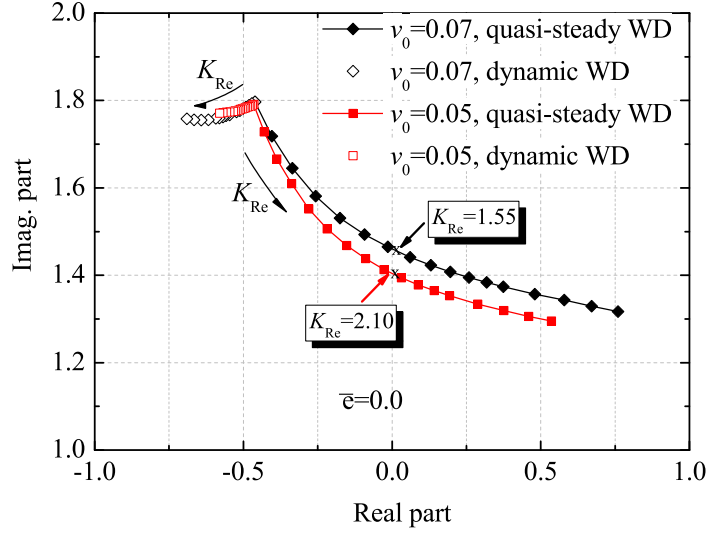
Figure 3.2: Variation of the root for the progressive flapping mode with the wake curvature parameter K_{Re}, $\bar{e} = 0.0$

The eigenvalues of the characteristics polynomial (Equation 3.36) of the coupled flapping-inflow-wake distortion dynamics are solved numerically for different values of the wake curvature parameter K_{Re} and the equivalent hinge offset $\bar{e}$. It is assumed that the flapping frequency (λ_β) can be written as

$$\lambda_\beta^2 = 1 + \frac{3\bar{e}}{1 - \bar{e}}$$

Figures 3.2, 3.3 and 3.4 show the "K_{Re}" root locus for the progressive flapping mode at different values of hinge offset $\bar{e}$, with K_{Re} ranging from 0.0 to 5.0 in incremental step of 0.25. It can be clearly seen from these figures that with a quasi-steady wake distortion model, the progressive flapping mode becomes unstable as K_{Re} is increased beyond a certain value. However, with the dynamic wake distortion model, the progressive flapping mode is still stable for all the values of K_{Re} considered in this study. Also, from Figures 3.2 through 3.4, it is seen that higher values of hinge offset somewhat reduce the instability problem with a quasi-steady wake distortion model.
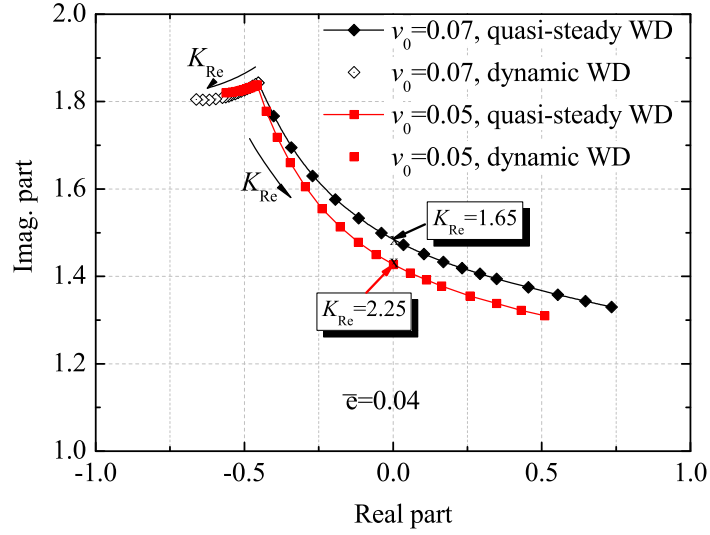
Figure 3.3: Variation of the root for the progressive flapping mode with the wake curvature parameter K_{Re}, $\bar{e} = 0.04$
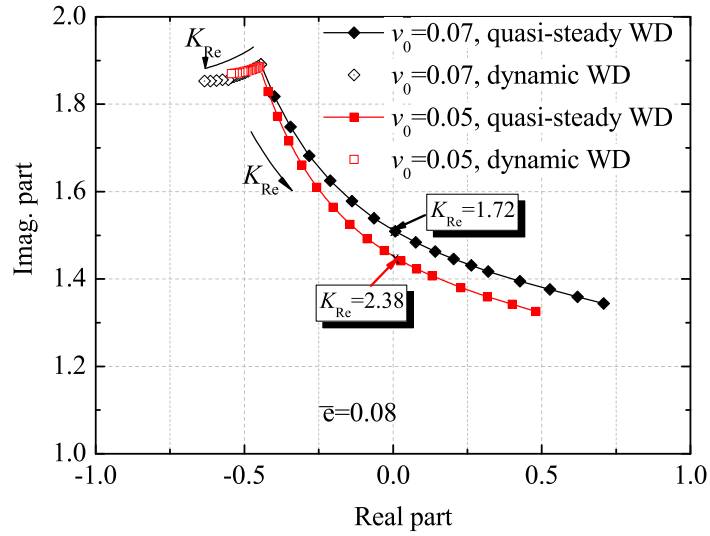
Figure 3.4: Variation of the root for the progressive flapping mode with the wake curvature parameter K_{Re}, $\bar{e} = 0.08$

3.5 Rotor Mean Loading Effect

From the augmented Pitt-Peters dynamic inflow model (Equation 3.20), it can be seen that the cyclic loading effect ($[\Delta L_3]$) manifests as product of wake curvatures and wake skew ($\kappa_c X, \kappa_s X$). Similarly, the coupling effect between wake curvatures and wake skew ($[\Delta L_2]$) manifests as product of wake curvatures and quadratic wake skew ($\kappa_c X^2, \kappa_s X^2$). Therefore, the cyclic loading effect and the coupling effect between quadratic wake skew and wake curvautres are small for maneuvering flight near hover condition since wake skew X is close to zero. However, the mean loading effect ($[\Delta L_1]$) will be the most significant effect.

Figures 3.6 and 3.7, respectively, show the on-axis roll rate and off-axis pitch rate response predictions of a UH-60 Black Hawk helicopter to a lateral cyclic control stick doublet input as shown in Figure 3.5. Also, for comparison purposes, the flight test data [54] are also superimposed on Figures 3.6 and 3.7. From Figure 3.6, which is the on-axis roll rate response to the lateral cyclic control stick doublet input of Figure 3.5, it can be seen that dynamic wake distortion has very little effect on the on-axis response prediction, which is consistent with previous findings in the literature [41, 42]. From Figure 3.7, which is the off-axis pitch rate response to the lateral cyclic control stick doublet input as shown in Figure 3.5, it can be clearly seen that the prediction without any wake distortion effect, i.e., $K_{Re} = 0.0$, goes opposite to the flight test data. However, the developed dynamic wake distortion model with a value of 3.8 for the wake curvature parameter K_{Re} gives good correlation of off-axis response with flight test data.

Similarly, Figures 3.9 and 3.10, respectively, are the vehicle on-axis pitch rate and off-axis roll rate responses to a longitudinal cyclic control stick doublet input with a profile shown in Figure 3.8. For comparison purposes, the results from the corresponding flight test data are also shown in Figures 3.9 and 3.10. Once again, it is seen from Figure 3.9, which is the on-axis pitch rate response to the longitudinal cyclic control stick doublet input of Figure 3.8, that dynamic wake distortion has very little effect on the on-axis response prediction. However, the off-axis roll rate response prediction (Figure 3.10) to the same longitudinal cyclic control stick doublet input of Figure 3.8 is significantly improved with

Figure 3.5: Profile of the lateral cyclic control stick doublet input used in the UH-60 Black Hawk helicopter flight test program in hover

Figure 3.6: UH-60 Black Hawk helicopter on-axis roll rate response from hover to the lateral cyclic control stick doublet input of Figure 3.5
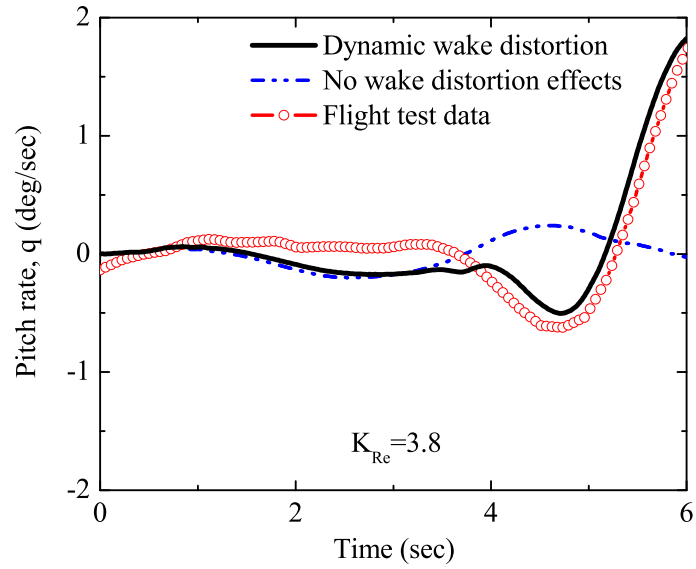
Figure 3.7: UH-60 Black Hawk helicopter off-axis pitch rate response from hover to the lateral cyclic control stick doublet input of Figure 3.5
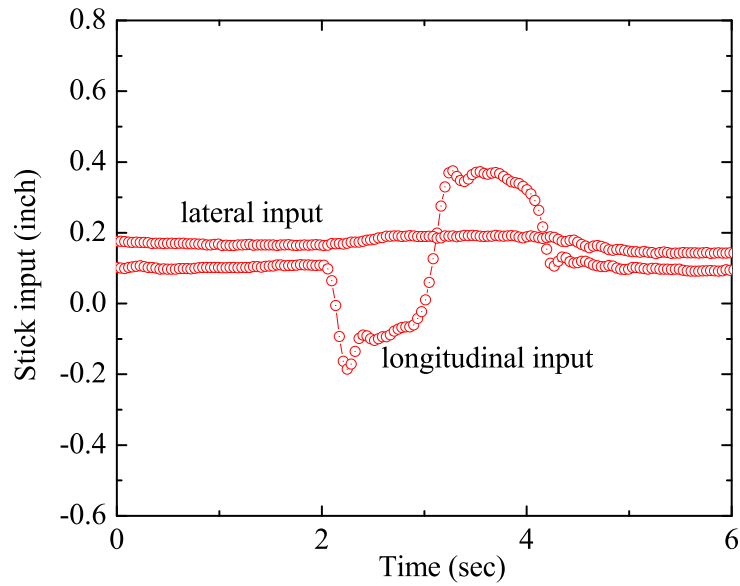
Figure 3.8: Profile of the longitudinal cyclic control stick doublet input used in the UH-60 Black Hawk helicopter flight test program in hover
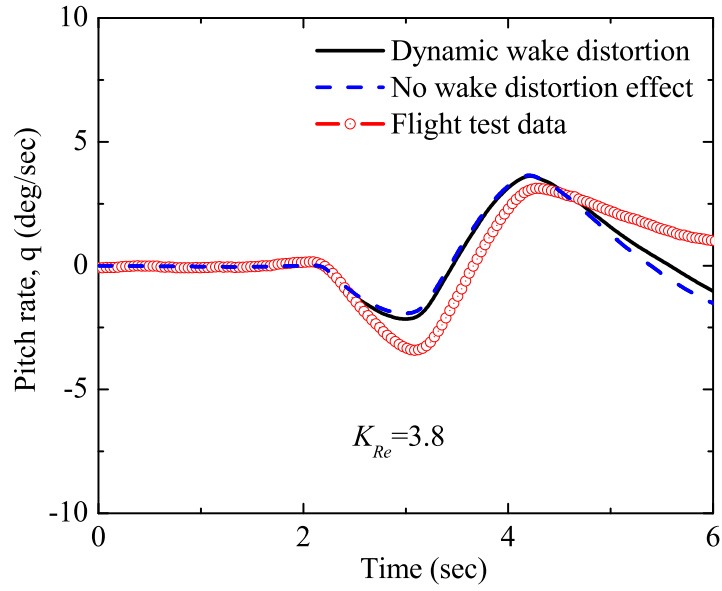
Figure 3.9: UH-60 Black Hawk helicopter on-axis pitch rate response from hover to the longitudinal cyclic control stick doublet input of Figure 3.8
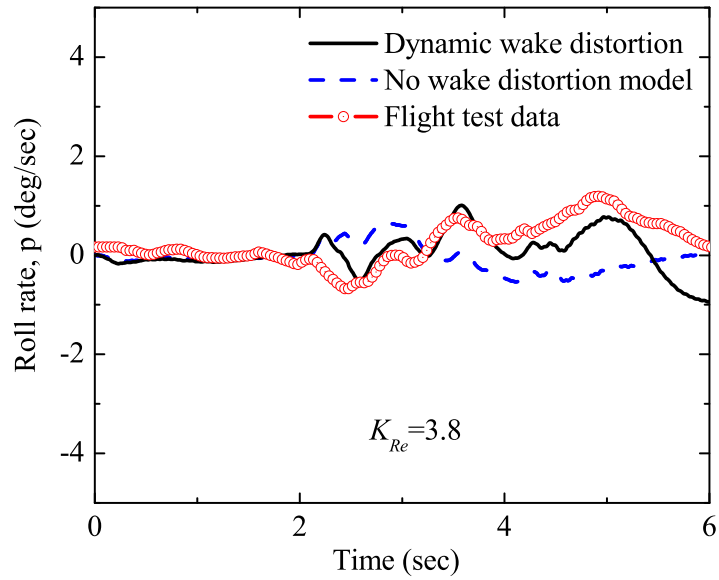
Figure 3.10: UH-60 Black Hawk helicopter off-axis roll rate response from hover to the longitudinal cyclic control stick doublet input of Figure 3.8

the dynamic wake distortion model with a value of 3.8 for the wake curvature parameter K_{Re}.

3.6 Rotor Cyclic Loading Effect

In the augmented Pitt-Peters dynamic inflow model (Equation 3.20), the $[\Delta L_3]$ matrix accounts for the coupling effect between wake curvatures/wake skew and rotor cyclic loading during helicopter maneuvering flight. An inspection of the $[\Delta L_3]$ matrix reveals that the coupling manifests in the form of product of wake curvatures and wake skew $(\kappa_c X, \kappa_s X)$. Therefore, the cyclic loading effect will exist mainly in maneuvering at forward flight conditions. Figures 3.12 and 3.13, respectively, show the on-axis roll rate and off-axis pitch rate response predictions of a UH-60 Black Hawk helicopter to a lateral cyclic control stick doublet input starting from 40 knots with a profile shown in Figure 3.11. On the plots, the results predicted with only the mean loading effect ($[\Delta L_1]$) are also shown. The value of 3.8 for the wake curvature parameter K_{Re} is taken from the hover value. From Figure 3.12, which is the on-axis roll rate response to the lateral cyclic control stick doublet input of Figure 3.11, it can be seen that the initial on-axis response prediction is slightly improved with including the cyclic loading effect ($[\Delta L_3]$). Also, it can be see from Figure 3.13 that the off-axis pitch rate response to the same lateral cyclic control stick doublet input is slightly improved with including the cyclic loading effect.

3.7 Wake Curvature/Skew Coupling Effect

In the augmented Pitt-Peters dynamic inflow model (Equation 3.20), the $[\Delta L_2]$ matrix accounts for the coupling effect between wake curvature/wake skew and rotor mean loading during maneuvering flight. An inspection of the $[\Delta L_2]$ matrix reveals that the coupling manifests in the form of product of wake curvatures and quadratic wake skew $(\kappa_c X^2, \kappa_s X^2)$. Therefore, the wake curvature/skew coupling effect will also exist mainly in maneuvering at forward flight conditions. Figures 3.14 and 3.15, respectively, show the on-axis roll rate and off-axis pitch rate response predictions of a UH-60 Black Hawk helicopter to the lateral cyclic control stick doublet input starting from 40 knots as shown in Figure 3.11. From
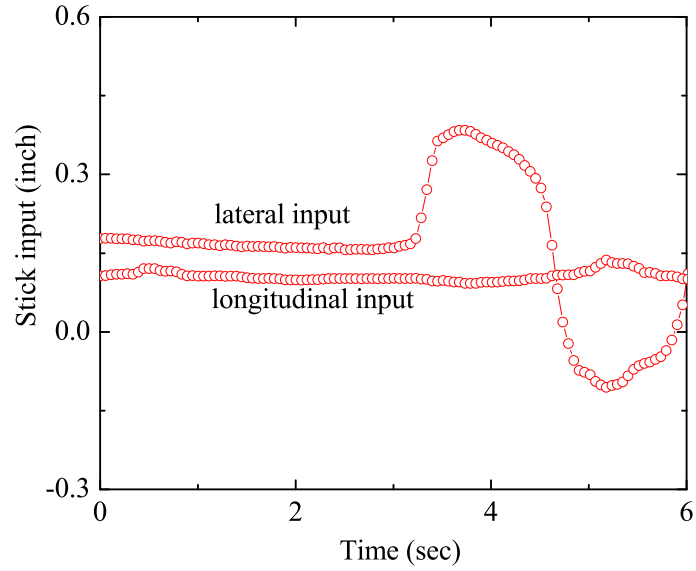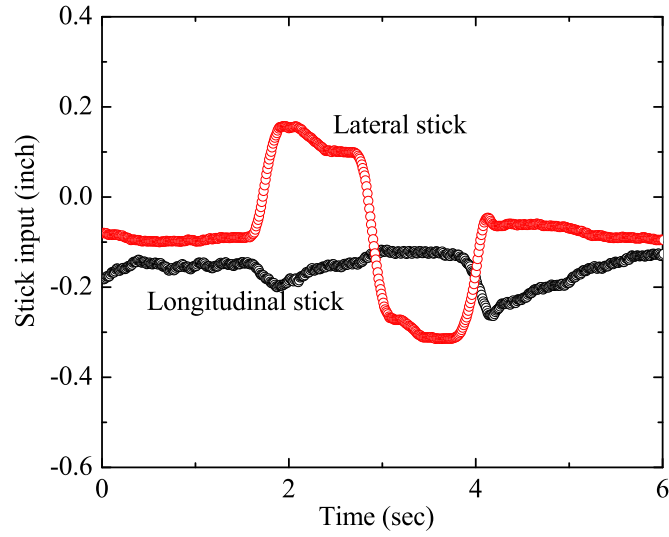
Figure 3.11: Profile of the lateral cyclic control stick doublet input used in the UH-60 Black Hawk helicopter flight test program at 40 knots
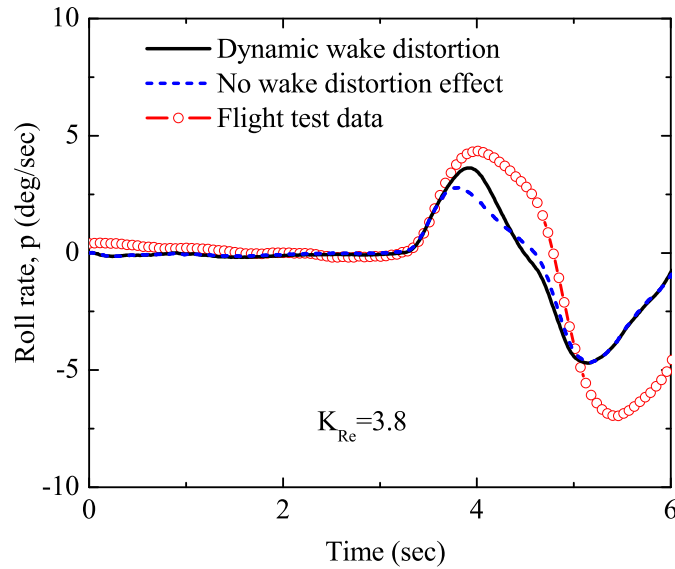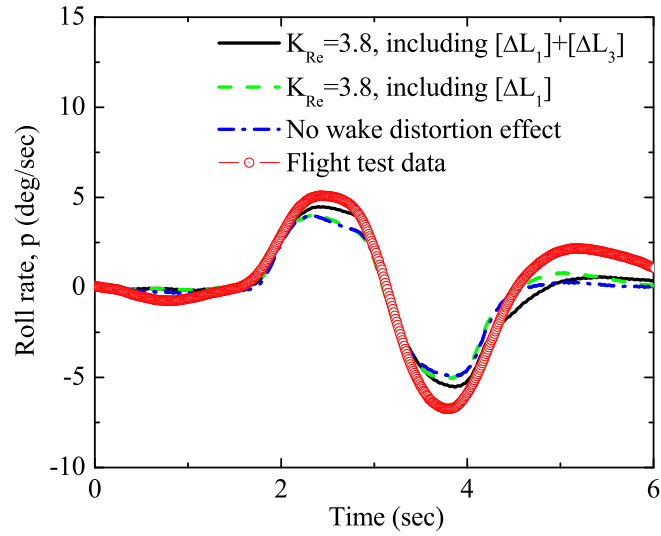

Figure 3.12: Effect of cyclic loading on on-axis roll rate response of a UH-60 Black Hawk helicopter at 40 knots flight speed to the lateral cyclic control stick doublet input of Figure 3.11
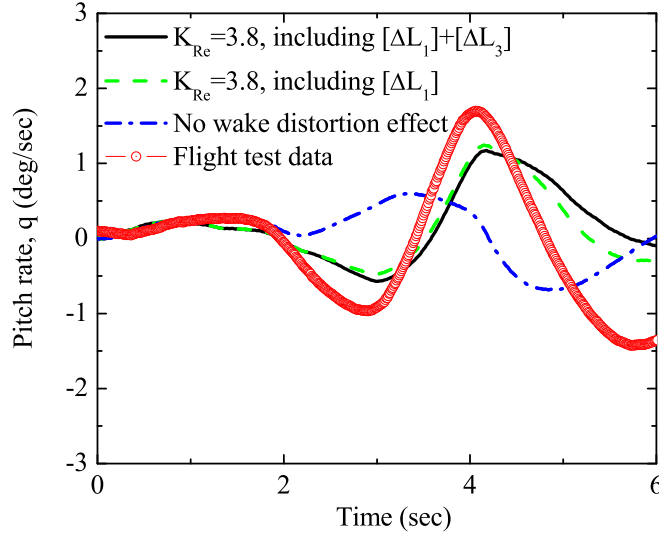
Figure 3.13: Effect of cyclic loading on off-axis pitch rate response of a UH-60 Black Hawk helicopter at 40 knots flight speed to the lateral cyclic control stick doublet input of Figure 3.11

Figure 3.14, which is the on-axis roll rate response to the lateral cyclic control stick doublet input of Figure 3.11, it can be seen that the initial on-axis response prediction is also improved by including the $[\Delta L_2]$ matrix. Also, The results in Figure 3.13 show that, when the coupling effect between wake curvature/skew and mean loading ($[\Delta L_2]$) is accounted for, a lower value of 2.5 for the wake curvature parameter K_{Re} gives comparable off-axis pitch rate response predictions to those obtained using a value of 3.8 for K_{Re} with only the mean loading effect.

3.8 Comparison of Wake Distortion Models

In this section, the augmented Pitt-Peters dynamic inflow model (Equation 3.20) developed in this study will be compared with the inflow model proposed by Keller in order to clarify any difference between them.

Keller [29] proposed a method to represent the quasi-steady wake distortion effect during helicopter maneuvering flight. The corresponding augmented inflow model can be written as (only the longitudinal case is considered here, the same analysis can be applied to the
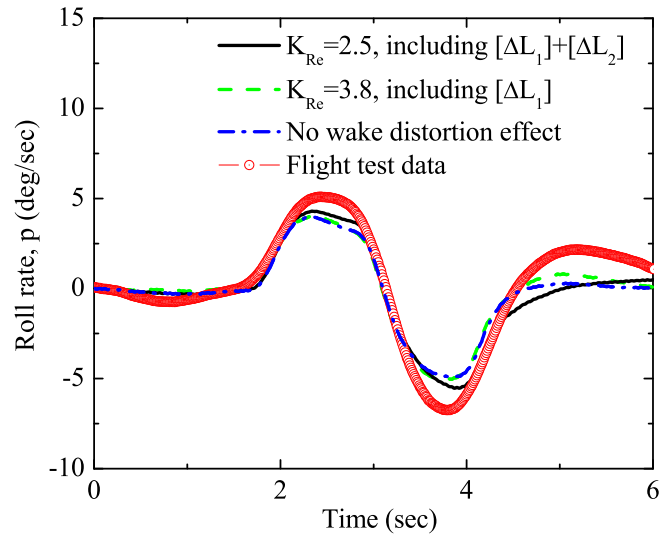
Figure 3.14: Effect of wake curvature/skew coupling on on-axis roll rate response of a UH-60 Black Hawk helicopter at 40 knots flight speed to the lateral cyclic control stick doublet input of Figure 3.11
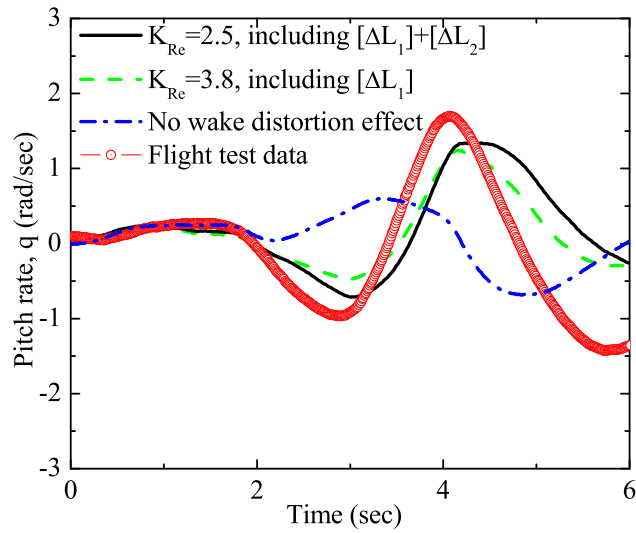
Figure 3.15: Effect of wake curvature/skew coupling on off-axis pitch rate response of a UH-60 Black Hawk helicopter at 40 knots flight speed to the lateral cyclic control stick doublet input of Figure 3.11

lateral case)

$$[M]\begin{Bmatrix} \overset{\star}{\lambda_0} \\ \lambda_{1c} \end{Bmatrix} + [V]\begin{bmatrix} \dfrac{1}{2} & -\dfrac{15\pi X}{64} \\ \dfrac{15\pi X}{64} & 2(1-X^2) \end{bmatrix}^{-1}\begin{Bmatrix} \lambda_0 \\ \lambda_{1c} - K_R(\bar{q} - \overset{\star}{\beta}_{1c}) \end{Bmatrix} = \begin{Bmatrix} C_T \\ -C_M \end{Bmatrix}$$
(3.37)

where K_R is the wake distortion parameter. In Equation 3.37, Keller models the wake curvature effect as additional forcing terms in the inflow model. Carrying out the matrix inversion in Equation 3.37 and simplifying the resulting equation gives rise to

$$[M]\begin{Bmatrix} \overset{\star}{\lambda_0} \\ \lambda_{1c} \end{Bmatrix} + \begin{bmatrix} 2V_m\lambda_0 + \dfrac{15\pi X}{64(1-X^2)}V_m\left[\lambda_{1c} - K_R(\bar{q} - \overset{\star}{\beta}_{1c})\right] \\ -\dfrac{15\pi X}{64(1-X^2)}\bar{V}\lambda_{1c} + \dfrac{1}{2(1-X^2)}\bar{V}\left[\lambda_{1c} - K_R(\bar{q} - \overset{\star}{\beta}_{1c})\right] \end{bmatrix} = \begin{Bmatrix} C_T \\ -C_M \end{Bmatrix}$$
(3.38)

where V_m and $\bar{V}$, respectively, are the mass flow parameters associated with the mean inflow and higher harmonics of inflow.

On the other hand, the augmented Pitt-Peters dynamic inflow model with quasi-steady wake curvature effect in the present study is given by Equation 3.20, which includes rotor mean/cyclic loading effect and wake curvature/skew coupling effect. Since the model proposed by Keller only considers the mean loading effect, only the mean loading effect in the augmented Pitt-Peters dynamic inflow model (Equation 3.20) will be compared with Keller's model. The augmented Pitt-Peters dynamic inflow model (Equation 3.20), only including the rotor mean loading effect can be written as (only the longitudinal case is considered here, the same application can be carried out for the lateral case)

$$[M]\begin{Bmatrix} \overset{\star}{\lambda_0} \\ \lambda_{1c} \end{Bmatrix} + [V]\begin{bmatrix} \dfrac{1}{2} & -\dfrac{15\pi X}{64} \\ \dfrac{K_{Re}\kappa_c}{2} + \dfrac{15\pi X}{64} & 2(1-X^2) \end{bmatrix}^{-1}\begin{Bmatrix} \lambda_0 \\ \lambda_{1c} \end{Bmatrix} = \begin{Bmatrix} C_T \\ -C_M \end{Bmatrix}$$
(3.39)

It is clear from Equation 3.39 that the present study models the wake curvature effect as a modification to the system gain matrix. Equation 3.39 can be simplified as

$$[M]\begin{Bmatrix} \overset{\star}{\lambda_0} \\ \lambda_{1c} \end{Bmatrix} + \begin{bmatrix} 2V_m\lambda_0 + \dfrac{15\pi X}{64(1-X^2)}V_m\lambda_{1c} \\ -\dfrac{15\pi X}{64(1-X^2)}\bar{V}\lambda_{1c} + \dfrac{1}{2(1-X^2)}\bar{V}(\lambda_{1c} - K_{Re}\kappa_c\lambda_0) \end{bmatrix} = \begin{Bmatrix} C_T \\ -C_M \end{Bmatrix}$$
(3.40)

60

Generally, the perturbations in the total mean inflow λ_0 in Equations 3.38 and 3.40 are small. Therefore the equation for the longitudinal inflow gradient appearing in Equations 3.38 and 3.40 are the same if the following expression is true

$$K_R(\bar{q} - \overset{\star}{\beta}_{1c}) = K_{Re}\kappa_c\lambda_0 \tag{3.41}$$

After substituting the definition for the longitudinal wake curvature, it can be seen that if

$$K_R = K_{Re} \tag{3.42}$$

is satisfied, then the augmented Pitt-Peters dynamic wake distortion model and the Keller's model are consistent if only rotor mean loading effect is considered.

CHAPTER IV

MAIN ROTOR/TAIL ROTOR/EMPENNAGE
INTERACTION DURING MANEUVERING FLIGHT

The higher maneuverability and agility requirements of modern helicopters often require that the rotor be closer to the body, higher rotor speed and higher disk loading, which severely increase the aerodynamic interactions among main rotor, fuselage, tail rotor and empennage. Prouty et al [63] discussed the difficulties in designing the empennage and tail rotor of the YAH-64 helicopter due to a poor understanding of the aerodynamic interaction effect among main rotor, tail rotor and empennage. There have been several research studies carried out in the literature [43, 52, 64, 65, 66, 67, 68, 69, 70, 71, 72, 73, 74, 75, 76, 77] to study the aerodynamic interaction effect among different components of helicopters. However, most flight dynamics simulation programs of rotorcraft only account for the aerodynamic interaction effect among main rotor, tail rotor and empennage during a steady axial and steady forward flight condition, i.e., the rotor wake is either vertically down or skewed. For helicopters carrying out maneuvers such as that schematically shown in Figure 1.1, where the rotor wake is not straight anymore, it is perceivable that the aerodynamic interaction phenomena among main rotor, tail rotor and empennage will be significantly different from those during steady flight, and therefore, the rotor wake distortion effect will also play a role in the interaction during maneuvering flight and need to be assessed. However, the aerodynamic interaction among main rotor, tail rotor and empennage is complicated even in steady flight condition. To properly account for the aerodynamic interaction effect among main rotor, tail rotor and empennage during maneuvering flight, a reduced order model based on a vortex tube analysis is developed in this chapter to model the aerodynamic interaction caused by rotor wake distortion effect.
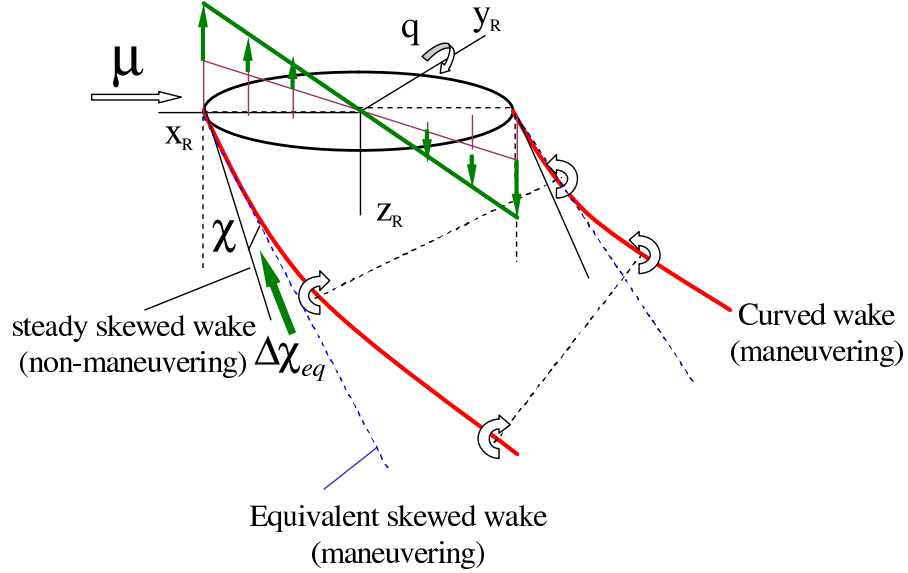
Figure 4.1: Schematic of the equivalent wake skew during helicopter maneuvering flight

4.1 Equivalent Wake Skew Due To Main Rotor Wake Curvature

When a helicopter is operating in forward flight condition, the skewed main rotor wake will sweep through the tail rotor and empennage, and induce downwash at these aerodynamic components. For a helicopter in a steady forward flight condition, the steady wake skew angle χ is the parameter used to calculate the main rotor downwash at the tail rotor and the empennage in a simulation environment. However, for a helicopter carrying out maneuvers, the curved main rotor wake will impact the main rotor downwash at these aerodynamic components. To account for the main rotor downwash at the tail rotor and empennage due to main rotor wake curvatures during maneuvering flight, an approximate method based on equivalence between wake curvature and wake skew (as developed in Appendix C) can be used, which is schematically shown in Figure 4.1. The analysis is based on the augmented Pitt-Peters dynamic inflow model (Equation 3.20). The rotor dynamic wake distortion

model (Equation 2.27) developed in Chapter II can be written as

$$
\begin{bmatrix} \tau_X & & & O \\ & \tau_S & & \\ & & \tau_R & \\ O & & & \tau_R \end{bmatrix} \begin{Bmatrix} \dot{X} \\ \dot{S} \\ \dot{\kappa}_c \\ \dot{\kappa}_s \end{Bmatrix} + \begin{Bmatrix} X \\ S \\ \kappa_c \\ \kappa_s \end{Bmatrix} = \begin{Bmatrix} X \\ S \\ \kappa_c \\ \kappa_s \end{Bmatrix}_{qs}
\tag{4.1}
$$

Also, the augmented Pitt-Peters dynamic inflow model (Equation 3.20) developed in Chapter III for helicopter maneuvering flight can be written as

$$
[M] \begin{Bmatrix} \overset{\star}{\lambda_0} \\ \lambda_{1s} \\ \lambda_{1c} \end{Bmatrix} + [V][L]^{-1} \begin{Bmatrix} \lambda_0 \\ \lambda_{1s} \\ \lambda_{1c} \end{Bmatrix} = \begin{Bmatrix} C_T \\ -C_L \\ -C_M \end{Bmatrix}
\tag{4.2}
$$

The quasi-steady induced inflow due to rotor loading can be obtained from the above equation as

$$
\begin{Bmatrix} \lambda_0 \\ \lambda_{1s} \\ \lambda_{1c} \end{Bmatrix}_{qs} = [L][V]^{-1} \begin{Bmatrix} C_T \\ -C_L \\ -C_M \end{Bmatrix}
\tag{4.3}
$$

where subscript qs means quasi-steady. Substituting expressions for the mass flow parameter matrix $[V]$ (Equation 3.18) and the augmented inflow gain matrix $[L]$ (Equation 3.21) into the above expression gives rise to the quasi-steady longitudinal inflow gradient (λ_{1c}) across the rotor disk in terms of rotor thrust coefficient as

$$
\frac{\lambda_{1c}}{\bar{V}} = \left[\frac{15\pi}{64} X + \frac{K_{Re}}{2} \kappa_c \left(1 - \frac{3}{2} X^2 \right) + \frac{5K_{Re}}{4} \kappa_s \mu X \right] C_T
\tag{4.4}
$$

where the first term inside the bracket is the same as that during a steady forward flight and the remaining terms are due to main rotor wake curvature effect during maneuvering flight. For low advance ratio μ, using the approximation of

$$
X = tan(\frac{\chi}{2}) \approx \frac{\mu}{2(\lambda_0 + V_c)}
\tag{4.5}
$$

Equation 4.4 can be rewritten as

$$
\frac{\lambda_{1c}}{\bar{V}} = \left[\frac{15\pi}{64} X + \frac{K_{Re}}{2} \kappa_c \left(1 - \frac{3}{2} X^2 \right) + \frac{5K_{Re}}{2} \kappa_s (\lambda_0 + V_c) X^2 \right] C_T
\tag{4.6}
$$

Therefore, an equivalent wake skew due to main rotor wake curvature effect during maneuvering flight can be defined as

$$\Delta X_{eq} = \frac{32 K_{Re}}{15\pi} \kappa_c \left(1 - \frac{3}{2}X^2\right) + \frac{32 K_{Re}}{3\pi} \kappa_s (\lambda_0 + V_c) X^2 \tag{4.7}$$

which can also be written approximately in terms of an equivalent wake skew angle as

$$\Delta \chi_{eq} = \frac{64 K_{Re}}{15\pi} \kappa_c \left(1 - \frac{3}{2}X^2\right) + \frac{64 K_{Re}}{3\pi} \kappa_s (\lambda_0 + V_c) X^2 \tag{4.8}$$

This equivalent wake skew can be added to the steady wake skew from momentum theory to model the main rotor downwash effect on the tail rotor and empennage during helicopter maneuvering flight.

4.2 Sidewash At Vertical Tail Due To Main Rotor Wake Curvature

As shown in Figure 4.2, when a helicopter is carrying out a roll maneuver, the curved main rotor wake will induce an additional sidewash at the aerodynamic centers of the tail rotor and vertical tail. By using a vortex tube representation as developed in Appendix C, this additional sidewash $(\Delta \nu_{y_{MR}}^{VT})$ at the aerodynamic centers of the tail rotor and vertical tail induced by the distorted main rotor wake during maneuvering flight, when expressed along the main rotor $y-$ axis, can be obtained as [78]

$$\Delta v_{y_{MR}}^{VT} = (\kappa_s \lambda_0)_{MR} \left(i_0^{MR} + i_1^{MR} X + i_2^{MR} X^2\right) \tag{4.9}$$

where superscript VT denotes that the side wash is calculated at the aerodynamic centers of vertical tail and/or tail rotor, subscript and superscript MR denotes that this effect is due to the main rotor wake curvature effect, $i_0^{MR}, i_1^{MR}, i_2^{MR}$ are the interference coefficients given in Appendix C by Equations C.16.a, C.16.b and C.16.c, which are determined by the relative geometric positions of the main rotor and the aerodynamic centers of vertical tail and tail rotor.

4.3 Up/Down Wash At Horizontal Tail Due to Tail Rotor Wake Curvature

Similarly, as shown in Figure 4.3, when a helicopter is carrying out a roll maneuver, the curved tail rotor wake will also induce an additional up/down wash at the aerodynamic center of the horizontal tail, which will affect the pitch moment and consequently the off-axis pitch rate response to a lateral cyclic control stick input. By using a vortex tube representation as developed in Appendix C, this additional up/down wash ($\Delta\nu_{y_{TR}}^{HT}$) at the aerodynamic center of the horizontal tail induced by the distorted tail rotor wake during maneuvering flight, when expressed along the tail rotor $y-$ axis, can be obtained from the vortex tube analysis as [78]

$$\Delta v_{y_{TR}}^{HT} = (\kappa_s \lambda_0)_{TR} \left(i_0^{TR} + i_1^{TR} X + i_2^{TR} X^2 \right) \tag{4.10}$$

where superscript HT denotes that the up/down is calculated at the aerodynamic center of the horizontal tail, subscript and superscript TR denotes that this effect is due to the tail rotor wake curvature effect, $i_0^{TR}, i_1^{TR}, i_2^{TR}$ are the interference coefficients given in Appendix C by Equations C.18.a, C.18.b and C.18.c, which are determined by the relative geometric positions of the tail rotor and the aerodynamic center of the horizontal tail.

4.4 Main Rotor/Tail Rotor/Empennages Interaction Effect On Response Prediction

In this section, the aerodynamic interaction effect among main rotor, tail rotor and empennage during helicopter maneuvering flight on response predictions, especially on the off-axis response prediction will be investigated. Figures 4.4 and 4.5, respectively, are the on-axis roll rate and off-axis pitch rate responses of a UH-60 Black Hawk helicopter to a lateral cyclic control stick doublet input of Figure 3.11, predicted with including the main rotor wake distortion effect, i.e., including [ΔL_1], [ΔL_2] and [ΔL_3], and the main rotor/tail rotor/empennage interaction effect developed in this chapter. A value of 1.0 for the wake curvature parameter K_{Re} is used. From Figure 4.4, which is the on-axis roll rate response to the lateral cyclic control stick doublet input of Figure 3.11, it can be seen that including
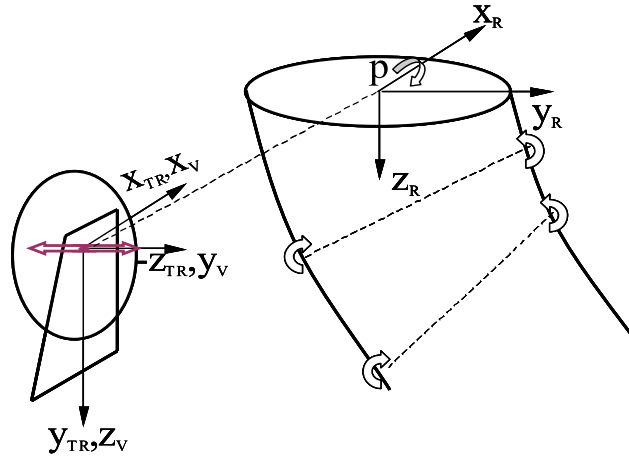
Figure 4.2: Schematic of the interaction between main rotor, tail rotor and empennage during a roll maneuver
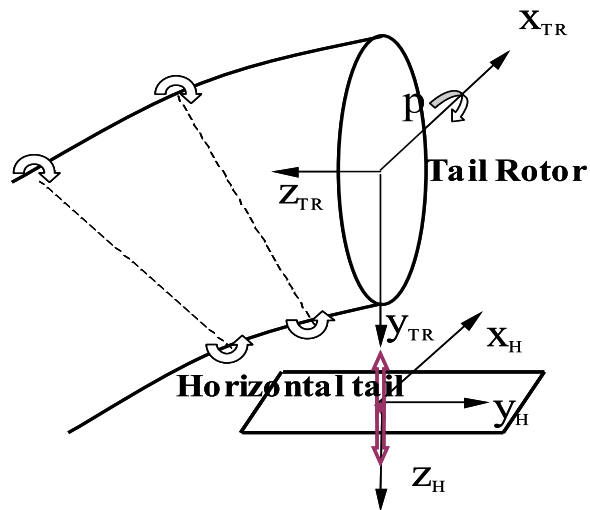
Figure 4.3: Schematic of the interaction between tail rotor and horizontal tail during a roll maneuver
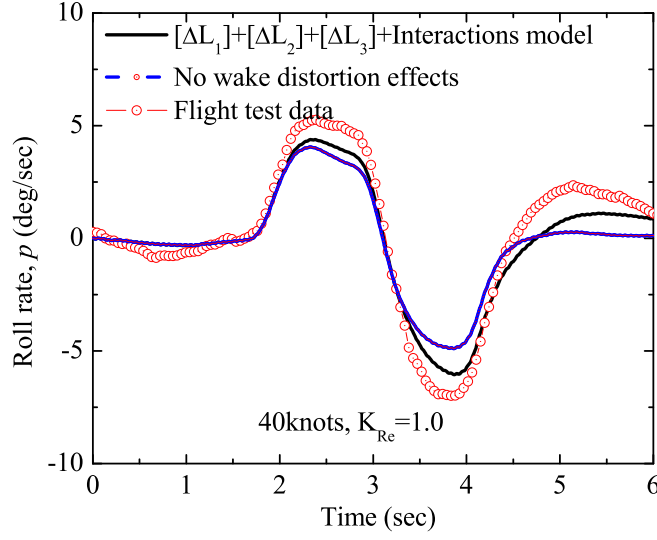
Figure 4.4: Combined effect of main rotor wake distortion and main rotor/tail rotor/empennage interaction on the on-axis roll rate response of a UH-60 Black Hawk helicopter at 40 knots flight speed to the lateral cyclic control stick doublet input of Figure 3.11

both the main rotor wake distortion effect and the main rotor/tail rotor/empennage interaction effect improves the on-axis roll rate response prediction as compared with the case without any wake distortion effect. Also, From Figure 4.5, which is the off-axis pitch rate response prediction to the same lateral cyclic control stick doublet input of Figure 3.11, it can be seen that the off-axis pitch rate response predicted with the main rotor wake distortion effect and the main rotor/tail rotor/empennage interaction effect correlates well with the corresponding flight test data when compared with the results predicted without any wake distortion effects. More importantly, it is noted that with both the main rotor wake distortion effect and the main rotor/tail rotor/empennage interaction model, the value of K_{Re} needed for good off-axis response correlation is 1.0, which is the value obtained from momentum theory.
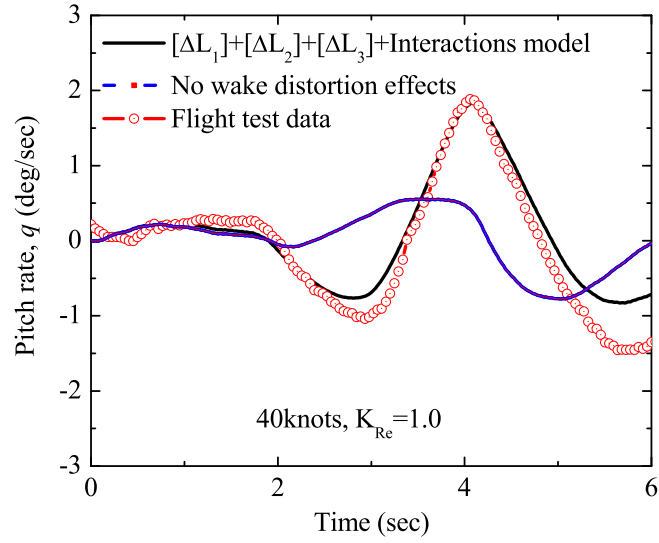
Figure 4.5: Combined effect of main rotor wake distortion and main rotor/tail rotor/empennage interaction on the off-axis pitch rate response of a UH-60 Black Hawk helicopter at 40 knots flight speed to the lateral cyclic control stick doublet input of Figure 3.11

CHAPTER V

MODEL REFINEMENT IN HOVER

The investigations [58, 79] of rotor dynamic wake distortion effect on helicopter response predictions, especially on the off-axis response predictions, and the preliminary results in Chapter III show that a value of 3.8 for the wake curvature parameter K_{Re} is needed in the model to correlate well with flight test data of a UH-60 Black Hawk helicopter in hover condition. However, the value of 3.8 is considerably higher than the value of $K_{Re} = 1.0$ obtained from momentum theory. It is felt that this discrepancy may be due to several other sources, such as the effect of airfoil unsteady aerodynamics, the fuselage blockage effect on the mean induced velocity across the main rotor disk and the gyroscopic feathering moment effect during a pitch and/or roll motion, etc. In this chapter, these effects on the off-axis response predictions during maneuvering flight are investigated.

5.1 Effect of Airfoil Unsteady Aerodynamics

For helicopters in maneuvering flight, rotor blades encounter a broad spectrum of unsteady effects such as the excursion in angle of attack resulting from blade and fuselage motions. Therefore, the effect of airfoil unsteady aerodynamics needs to be examined and its impact on the correct off-axis response prediction during helicopter maneuvering flight needs to be assessed. For rotorcraft applications, the dynamic inflow model [47] and the Peters-He finite state inflow model [48] capture the dynamic response of rotor inflow to changes in rotor disk loading. Similarly, when rotor inflow changes, the response of the rotor disk loading will also be dynamic. In most rotorcraft simulation programs using a blade-element model, the lift and drag coefficients for each blade element at each time instant are obtained through table look-up, which is a quasi-steady representation. From this point of view, airfoil unsteady aerodynamics may also be a potential factor to improve the off-axis response correlation. Since rotor inflow and rotor loading calculations are both necessary parts of the closed loop

system in helicopter flight mechanics and aeroelasticity applications, it is possible to combine the rotor dynamic wake distortion effect and the effect of airfoil unsteady aerodynamics in the off-axis response prediction. Schulein and Tischler [51] carried out some preliminary investigations on combining the effects of wake distortion and the aerodynamic phase lag model [80], which is an empirical method to account for the two dimensional compressibility effect.

In this study, the state-space representation proposed by Leishman, et al, [81, 82, 83, 84, 85] is used to account for the effect of airfoil unsteady aerodynamics. This state-space representation inherently includes the compressibility effect and accounts for the effect of airfoil unsteady aerodynamics in the form of ordinary differential equations, which is suitable for time-marching in a simulation environment. The state-space model can be written as

$$
\begin{Bmatrix} \overset{\star}{x_1} \\ x_2 \\ x_3 \\ x_4 \end{Bmatrix} = \frac{[A_{UA}]}{\Omega} \begin{Bmatrix} x_1 \\ x_2 \\ x_3 \\ x_4 \end{Bmatrix} + \frac{[B_{UA}]}{\Omega} \begin{Bmatrix} \alpha_{af} \\ q_{af} \end{Bmatrix} \tag{5.1}
$$

with the output equation for the normal force coefficient at each blade section as

$$
C_n = [C_{UA}]x^T + [D_{UA}] \begin{Bmatrix} \alpha_{af} \\ q_{af} \end{Bmatrix} \tag{5.2}
$$

where, $\overset{\star}{()}$ denotes differentiation with respect to nondimensional time, α_{af} and q_{af} are the airfoil angle of attack and angle-of-attack rate, respectively, x_i $(i = 1, 2, 3, 4)$ are the state variables, C_n is the airfoil section normal force coefficient and the matrices $[A_{UA}]$, $[B_{UA}]$, $[C_{UA}]$, $[D_{UA}]$ can be written as

$$
[A_{UA}] = \begin{bmatrix} a_{11} & & & O \\ & a_{22} & & \\ & & a_{33} & \\ O & & & a_{44} \end{bmatrix} \tag{5.3}
$$

71

$$[B_{UA}] = \begin{bmatrix} 1 & \frac{1}{2} \\ 1 & \frac{1}{2} \\ 1 & 0 \\ 0 & 1 \end{bmatrix} \tag{5.4}$$

$$[C_{UA}] = \begin{bmatrix} c_{11} & c_{22} & c_{33} & c_{44} \end{bmatrix} \tag{5.5}$$

$$[D_{UA}] = \begin{bmatrix} \dfrac{4}{M_{mach}} & \dfrac{1}{M_{mach}} \end{bmatrix} \tag{5.6}$$

where M_{mach} is the Mach number and the detailed expressions for the elements in the above matrices are given by Leishman, et al, [81, 82, 83, 84, 85] as follows

$$a_{11} = -\frac{2V_{sec}}{c}\beta_{pg}^2 b_1 \tag{5.7.a}$$

$$a_{22} = -\frac{2V_{sec}}{c}\beta_{pg}^2 b_2 \tag{5.7.b}$$

$$a_{33} = -\frac{1}{K_\alpha T_I} \tag{5.7.c}$$

$$a_{44} = -\frac{1}{K_q T_I} \tag{5.7.d}$$

$$c_{11} = \frac{2\pi}{\beta_{pg}}\left(\frac{2V_\infty}{c}\right)\beta_{pg}^2 A_1 b_1 \tag{5.7.e}$$

$$c_{12} = \frac{2\pi}{\beta_{pg}}\left(\frac{2V_\infty}{c}\right)\beta_{pg}^2 A_2 b_2 \tag{5.7.f}$$

$$c_{13} = -\frac{4}{M_{mach}}\frac{1}{K_\alpha T_I} \tag{5.7.g}$$

$$c_{14} = -\frac{4}{M_{mach}}\frac{1}{K_q T_I} \tag{5.7.h}$$

where, $A_1 = 0.3$, $A_2 = 0.7$, $b_1 = 0.14$, $b_2 = 0.53$, V_{sec} is the section resultant velocity, $\beta_{pg} = \sqrt{1 - M_{mach}^2}$ is the Prandtl-Glauert compressibility factor, T_I is the non-circulatory time constant given by

$$T_I = \frac{c}{a_{sound}} \tag{5.8}$$

where c is the airfoil chord length and a_{sound} is the sound velocity. K_α and K_q, respectively,

are given by

$$K_\alpha = \left[(1 - M_{mach}) + \pi\beta_{pg}M_{mach}^2(A_1b_1 + A_2b_2)\right]^{-1} \tag{5.9}$$

$$K_q = \left[(1 - M_{mach}) + 2\pi\beta_{pg}M_{mach}^2(A_1b_1 + A_2b_2)\right]^{-1} \tag{5.10}$$

To implement the above state-space unsteady aerodynamics model in a rotorcraft simulation environment, which uses the Pitt-Peters dynamic inflow model or the Peters-He finite state inflow model (both implicitly include the Theodorsen's function effect), the contributions to the airfoil normal force coefficient (C_n) from the circulatory lift part due to the angle of attack in the above model must be excluded to avoid duplicating the rotor wake effect [86]. This can be obtained by setting the corresponding element in the $[B_{UA}]$ matrix (Equation 5.4) in the state space model to be zero and the resulting $[B_{UA}]$ matrix can be obtained as follows

$$[B_{UA}] = \begin{bmatrix} 0 & \dfrac{1}{2} \\ 0 & \dfrac{1}{2} \\ 1 & 0 \\ 0 & 1 \end{bmatrix} \tag{5.11}$$

5.2 Fuselage Blockage Effect

For helicopters operating near hover condition, the rotor wake will be significantly influenced by the fuselage. The rotor wake/fuselage interaction problem, even in steady flight condition, is very complicated and highly nonlinear. There have been many research works [87, 88, 89, 90, 91, 92, 93, 94, 95, 96, 97, 98, 99, 100] carried out to study the rotor wake/fuselage interaction during steady flight condition in the recent past. However, the global blockage effect of fuselage on rotor inflow is to reduce the mean induced velocity across rotor disk. From Equations 2.29.c and 2.29.d, it can be seen that the quasi-steady longitudinal and lateral wake curvatures are defined in terms of the total inflow across the rotor disk, therefore, the reduced mean induced velocity across the rotor disk due to the fuselage blockage effect will impact the quasi-steady rotor wake curvatures, consequently, the vehicle's response to control stick inputs. To represent the first order effect of the fuselage blockage effect on rotor wake curvature dynamics near hover condition for helicopter

maneuvering flight simulation applications, the fuselage is treated as an equivalent flat plate panel in the present study. Similar to the modeling of partial ground effect developed by Xin [101] , the equivalent flat plate panel is treated as a pressure perturbation, Φ_F, which is presented as a source-like singularity. It is assumed that the rotor and fuselage panel pressure perturbations share a common free stream since the source-like pressure perturbation of the fuselage panel creates no energy of its own. Therefore, the total pressure perturbation in the flow field of combined rotor and fuselage, is the superposition of the contributions from the rotor and the equivalent fuselage panel, i.e.,

$$\Phi = \Phi_R + \Phi_F \tag{5.12}$$

where the rotor and fuselage panel pressure perturbations, i.e., Φ_R and Φ_F, respectively, can be expanded in terms of the normalized associated Legendre functions and trigonometric functions as

$$\Phi_R(\nu, \eta, \psi) = \frac{1}{2} \sum_{m=0}^{\infty} \sum_{n=m+1,\cdots}^{\infty} \bar{P}_n^m(\nu) \bar{Q}_n^m(i\eta) \left[\tau_n^{mc} cos(m\psi) + \tau_n^{ms} sin(m\psi) \right] \tag{5.13}$$

$$\Phi_F(\hat{\nu}, \hat{\eta}, \hat{\psi}) = \frac{1}{2} \sum_{l=0}^{\infty} \sum_{k=l,l+2,\cdots}^{\infty} \bar{P}_k^l(\hat{\nu}) \bar{Q}_k^l(i\hat{\eta}) \left[\sigma_k^{lc} cos(l\hat{\psi}) + \sigma_k^{ls} sin(l\hat{\psi}) \right] \tag{5.14}$$

where $\sigma_k^{lc}, \sigma_k^{ls}$ are the fuselage panel pressure coefficients, τ_n^{mc}, τ_n^{ms} are the rotor pressure coefficients (also called rotor forcing functions), $\bar{P}$ and $\bar{Q}$ are the normalized associated Legendre functions of the first kind and the second kind, respectively. (ν, η, ψ) and $(\hat{\nu}, \hat{\eta}, \hat{\psi})$, respectively, are the nondimensinal rotor and fuselage panel ellipsoidal coordinates.

The fuselage panel pressure coefficients can be related to the rotor pressure coefficients through applying the pressure condition at the fuselage panel, which states that the fuselage panel pressure perturbation at the fuselage must be equal to the rotor pressure perturbation at the fuselage, that is,

$$\Phi_F|_{fus} = \Phi_R|_{fus} \tag{5.15}$$

Using the orthogonality propertiess of the normalized associated Legendre functions and the trigonometric functions, the fuselage panel pressure coefficients $(\sigma_k^{lc}, \sigma_k^{ls})$ can be related

74

to the rotor pressure coefficients $(\tau_n^{mc}, \tau_n^{ms})$ in a matrix form as

$$
\left\{ \begin{array}{c} \sigma_k^{lc} \\ \sigma_k^{ls} \end{array} \right\} = [B_F] \left\{ \begin{array}{c} \tau_n^{mc} \\ \tau_n^{ms} \end{array} \right\} = \left[\begin{array}{cc} \left(B_{F,kn}^{lm}\right)^{cc} & \left(B_{F,kn}^{lm}\right)^{cs} \\ \left(B_{F,kn}^{lm}\right)^{sc} & \left(B_{F,kn}^{lm}\right)^{ss} \end{array} \right] \left\{ \begin{array}{c} \tau_n^{mc} \\ \tau_n^{ms} \end{array} \right\} \tag{5.16}
$$

where expressions for the elements of the fuselage blockage effect matrix $[B_F]$ are similar to those expressions for the partial ground effect matrix given by Xin [101], but with integration carried over the surface of the equivalent fuselage panel.

Analogous to the expansion for rotor induced velocity in the Peters-He finite state inflow model [48], the fuselage interference velocity distribution at rotor disk (w_F) can be expanded in terms of the associated Legendre functions and trigonometric functions as,

$$
w_F = \sum_{r=0}^{\infty} \sum_{j=r+1, r+3, \cdots}^{\infty} \bar{P}_j^r(\nu) \left[f_j^{rc} cos(r\psi) + f_j^{rs} sin(r\psi) \right] \tag{5.17}
$$

where f_j^{rc}, f_j^{rs} are the fuselage panel interference velocity coefficients, which can be related to the pressure coefficients of the fuselage panel $(\sigma_k^{lc}, \sigma_k^{ls})$ as

$$
\left\{ \begin{array}{c} f_j^{rc} \\ f_j^{rs} \end{array} \right\} = [A_F] \left\{ \begin{array}{c} \sigma_k^{lc} \\ \sigma_k^{ls} \end{array} \right\} = \left[\begin{array}{cc} \left(A_{F,jk}^{rl}\right)^{cc} & \left(A_{F,jk}^{rl}\right)^{cs} \\ \left(A_{F,jk}^{rl}\right)^{sc} & \left(A_{F,jk}^{rl}\right)^{ss} \end{array} \right] \left\{ \begin{array}{c} \sigma_k^{lc} \\ \sigma_k^{ls} \end{array} \right\} \tag{5.18}
$$

where the elements of the matrix $[A_F]$ are the same as those given by Xin [101] for the influence coefficient matrix of ground interference velocity due to ground pressure.

Combining Equations 5.16 and 5.18, the relationship between the fuselage interference velocity coefficients and the rotor pressure coefficients can be written as

$$
\{f\} = \frac{1}{V_m}[A_F][B_F] \left\{ \frac{\tau}{2} \right\} = \frac{1}{V_m}[F] \left\{ \frac{\tau}{2} \right\} \tag{5.19}
$$

where matrix $[F]$ represents the influence of the fuselage blockage effect on the rotor induced velocity. Therefore, the ratio (K_F) of the mean induced velocity in hover at the rotor disk plane with fuselage blockage effect to that without fuselage blockage effect can be written as

$$
K_F \approx 1 - (F_{11}^{00})^{cc} \tag{5.20}
$$

In general, the fuselage blockage effect depends on the normalized height $(\bar{h})$ of the rotor center above the fuselage panel and the normalized half-width $(\bar{b})$ of the fuselage, both of

them are normalized by the rotor radius. In this study, the parameters used for a UH-60 Black Hawk helicopter are $\bar{b} = 0.1$ and $\bar{h} = 0.2$, respectively, and the corresponding value of K_F is approximately 0.91.

Assuming that the unsteady part of the pressure perturbation due to the fuselage blockage effect is negligible, the quasi-steady wake curvatures defined in Equations 2.29.c and 2.29.d can be rewritten as

$$(\kappa_c)_{qs} = \frac{\bar{q} - \overset{\star}{\beta}_{1c}}{K_F\lambda_0 + V_c} \tag{5.21.a}$$

$$(\kappa_s)_{qs} = \frac{\bar{p} - \overset{\star}{\beta}_{1s}}{K_F\lambda_0 + V_c} \tag{5.21.b}$$

5.3 Effect of Gyroscopic Feathering Moment

For helicopters in a pitch and/or roll maneuver, there will be gyroscopic forces acting on rotor blades due to the blade rotating and pitch/roll motions. Due to the blade chordwise mass distribution, these gyroscopic forces will form a gyroscopic feathering moment. Simons, et al, [18] proposed that the rotor blade elastic feathering motion incurred due to this gyroscopic feathering moment during a pitch and/or roll motion would have some influence on the off-axis coupling prediction. Zhao, et al, [102] studies the gyroscopic feathering moment effect on the off-axis response prediction and showed that this gyroscopic feathering moment effect was very small when compared with rotor wake distortion effect.

For simplicity, It is assumed that the feathering hinge, center of mass and elastic feathering axis are coincident so that pitch-flap coupling is absent. The equation governing the elastic twisting motion due to the gyroscopic feathering moment takes the form as

$$\overset{\star\star}{\Delta\theta} + \lambda_\theta^2\Delta\theta = -2(\bar{p}sin\psi + \bar{q}cos\psi) \tag{5.22}$$

where $\Delta\theta = \Delta\theta_{1c}cos\psi + \Delta\theta_{1s}sin\psi$ is the blade elastic twist about feathering hinge due to the gyroscopic feathering moment and λ_θ is the blade nondimensional natural feathering frequency in the rotating frame, $\bar{q}$ and $\bar{p}$, respectively, are the nondimensional pitch and roll rates. The elastic twist incurred due to the gyroscopic feathering moment can be obtained

by using the harmonic balancing technique as follows

$$\Delta\theta_{1c} = -\frac{2\bar{p}}{\lambda_\theta^2 - 1} \tag{5.23}$$

$$\Delta\theta_{1s} = -\frac{2\bar{q}}{\lambda_\theta^2 - 1} \tag{5.24}$$

The perturbed equation governing the flapping dynamics in hover for an articulated rotor without flapping hinge offset and hinge spring takes the form as

$$\overset{\star\star}{\Delta\beta} + \frac{\gamma_{lock}}{8}\overset{\star}{\Delta\beta} + \Delta\beta = \frac{\gamma_{lock}}{8}[\Delta\theta_{1c}cos\psi + \Delta\theta_{1s}sin\psi]$$
$$+ \frac{\gamma_{lock}}{8}[(\bar{p} - \Delta\lambda_{1s})sin\psi + (\bar{q} - \Delta\lambda_{1c})cos\psi]$$
$$+ \frac{\gamma_{lock}}{8}[2\bar{p}cos\psi - 2\bar{q}sin\psi] \tag{5.25}$$

where γ_{lock} is the blade Lock number, $\Delta\lambda_{1c}$ and $\Delta\lambda_{1s}$, respectively, are the quasi-steady longitudinal and lateral inflow gradients across the rotor disk due to wake curvature effect and can be obtained from Equation 3.20 as

$$\Delta\lambda_{1c} = K_{Re}\bar{q} \tag{5.26}$$

$$\Delta\lambda_{1s} = K_{Re}\bar{p} \tag{5.27}$$

The steady state flapping response can be obtained from Equation 5.25 by using the harmonic balancing technique as

$$\Delta\beta_{1s} = \frac{16}{\gamma_{lock}}\bar{p} + \bar{q}\left[1 - K_{Re} - \frac{2}{\lambda_\theta^2 - 1}\right] \tag{5.28}$$

$$\Delta\beta_{1c} = \frac{16}{\gamma_{lock}}\bar{q} - \bar{p}\left[1 - K_{Re} - \frac{2}{\lambda_\theta^2 - 1}\right] \tag{5.29}$$

where the first terms in Equations 5.28 and 5.29 are the on-axis lateral flapping due to the roll rate and the on-axis longitudinal flapping due to the pitch rate, respectively. The second terms in Equations 5.28 and 5.29 are the off-axis lateral flapping due to the pitch rate and the off-axis longitudinal flapping due to the roll rate, respectively. For the off-axis response, it can be seen that

$$\frac{\Delta\beta_{1s}}{\bar{q}} = -\frac{\Delta\beta_{1c}}{\bar{p}} = 1 - K_{Re} - \frac{2}{\lambda_\theta^2 - 1} \tag{5.30}$$

where the first term in the right hand side of Equation 5.30 is due to the kinematic effect, the second term is due to rotor wake curvature effect and the third term is due to gyroscopic feathering moment effect. Therefore, it can be clearly seen that the gyroscopic feathering moment effect on the off-axis response is equivalent to rotor wake curvature effect in hover with a change in the equivalent wake curvature parameter as

$$\Delta K_{Re} = \frac{2}{\lambda_\theta^2 - 1} \tag{5.31}$$

where λ_θ is the blade nondimensional torsional natural frequency. Typical range of this parameter is from 4.0 to 5.0. Therefore, it can be seen that the equivalent wake curvature parameter ΔK_{Re} is around 2/15, which shows that the gyroscopic feathering moment effect cannot be a primary source of the off-axis response problem for typical values of blade nondimensional torsional frequency.

CHAPTER VI

SIMULATION RESULTS AND DISCUSSION

To study the influence of rotor wake distortion dynamics on helicopter response predictions, especially on the off-axis response predictions, and to validate the developed rotor dynamic wake distortion model for helicopter maneuvering flight, both the augmented Pitt-Peters dynamic inflow model (Equation 3.20) and the augmented Peters-He finite state inflow model (Equation 3.30), together with the main rotor/tail rotor/empennage interaction model, combined with the dynamic wake distortion model (Equation 2.27), are implemented in a generic helicopter flight simulation program [53]. Simulated response predictions are compared with flight test data [54] of a UH-60 Black Hawk helicopter in both hover and forward flight conditions in this chapter. The simulation results are predicted with three levels of modeling, i.e.,

Level 1: predictions without any wake distortion effect.

Level 2 (Model A): predictions using the augmented Peters-He finite state inflow model together with the interaction model and the dynamic wake distortion model developed in this study.

Level 3 (Model B): predictions using the augmented Pitt-Peters dynamic inflow model together with the interaction model and the dynamic wake distortion model.

6.1 Validation In Hover Condition

The effect of rotor wake distortion dynamics on response predictions of a UH-60 Black Hawk in hover is examined first. It is observed during simulation in hover that there are no significant differences between the results predicted using models A and B (up to fifteen states for Model A is tried). Therefore, only the results predicted with model B are shown and compared with the corresponding flight test data in hover in both the frequency domain and the time domain as follows.

6.1.1 Frequency Domain

The simulation program is run to obtain vehicle responses to frequency sweep input signals and the frequency response is extracted from the time history of responses using the CIFER (Comprehensive Identification from FrEquency Responses) program [103]. For current applications, the lower frequencies (below 10 rad/sec) are of interest since the effect of rotor wake distortion dynamics is expected to be a low frequency phenomenon.

Figures 6.1 and 6.3, respectively, show the on-axis roll rate-to-lateral cyclic stick input and the on-axis pitch rate-to-longitudinal cyclic stick input frequency response predictions of the UH-60A Black Hawk helicopter in hover condition. In the plots, the response predictions using Model B with $K_{Re} = 1.0$, which is the value obtained from momentum theory, and the model without any wake distortion effect, i.e., $K_{Re} = 0.0$, are superimposed and compared with the corresponding flight test results. From Figures 6.1 and 6.3, it can be clearly seen that rotor dynamic wake distortion has very little effect on the on-axis response prediction in hover. Figures 6.2 and 6.4, respectively, are the off-axis pitch rate-to-lateral cyclic stick input and the off-axis roll rate-to-longitudinal cyclic stick input frequency response predictions of a UH-60 Black Hawk helicopter in hover, predicted using model B with a value of 1.0 for the wake curvature parameter K_{Re}. Also, for comparison purposes, the predictions without any wake distortion effect, i.e., $K_{Re} = 0.0$, are included in these plots. Both Figures 6.2 and 6.4 clearly indicate that there is a significant phase discrepancy of approximately 180 degrees between the flight test results and the simulation results predicted without any wake distortion effect, which also indicates that there is a sign reversal between the actual flight test data and the simulation results predicted without any wake distortion effect. However, as shown in Figures 6.2 and 6.4, when the rotor dynamic wake distortion effect is included, the response predictions with a value of 1.0 for the wake curvature parameter K_{Re} correlate well with flight test results in the phase. The good correlation in phase indicates that using the rotor dynamic wake distortion model with $K_{Re} = 1.0$, the sign of the response is qualitatively captured. This finding is important because for flight simulation and control law design, an accurate representation of phase behavior in the model is important for the stability of the closed-loop system. However, it can be seen from Figures 6.2 and 6.4 that

there is still some discrepancy in the magnitude correlation between the simulation results and the corresponding flight test results.

6.1.2 Time Domain

The vehicle response to a lateral cyclic control stick doublet input with a control profile as shown in Figure 3.5 is considered first. Figures 6.5 and 6.6, respectively, show the on-axis roll rate and off-axis pitch rate response predictions using model B with a value of 1.0 for the wake curvature parameter K_{Re}, including comparisons with the corresponding flight test data. For comparison purposes, the results predicted without any wake distortion effect, i.e., $K_{Re} = 0$, are also superimposed on the plots. Again, from Figure 6.5, which is the on-axis roll rate response to the lateral cyclic control stick doublet input of Figure 3.5, it can be seen that rotor dynamic wake distortion model has very little effect on on-axis response prediction in hover, which is consistent with the frequency domain results in hover (Figures 6.1 and 6.3). From Figure 6.6, which is the off-axis pitch rate response to the lateral cyclic control stick doublet input of Figure 3.5, it can be clearly seen that the initial off-axis pitch rate response predicted without any wake distortion effect goes opposite to the actual flight test data. However, it can be seen that the rotor dynamic wake distortion model with a value of 1.0 for the wake curvature parameter K_{Re} qualitatively captures the correct off-axis response behavior as observed in the flight test data when compared with the results without any wake distortion effect. The vehicle response to a longitudinal cyclic control stick doublet input is considered next. Figures 6.7 and 6.8, respectively, are the on-axis pitch rate and off-axis roll rate response predictions of a UH-60 helicopter in hover to a longitudinal cyclic control stick doublet input of Figure 3.8, with comparisons to the corresponding flight test data. Once again, it can be seen that the off-axis roll rate response predictions as shown in Figure 6.8 are improved using the rotor dynamic wake distortion model together with a value of 1.0 for the wake curvature parameter K_{Re}, when compared with the results predicted without any wake distortion effect.
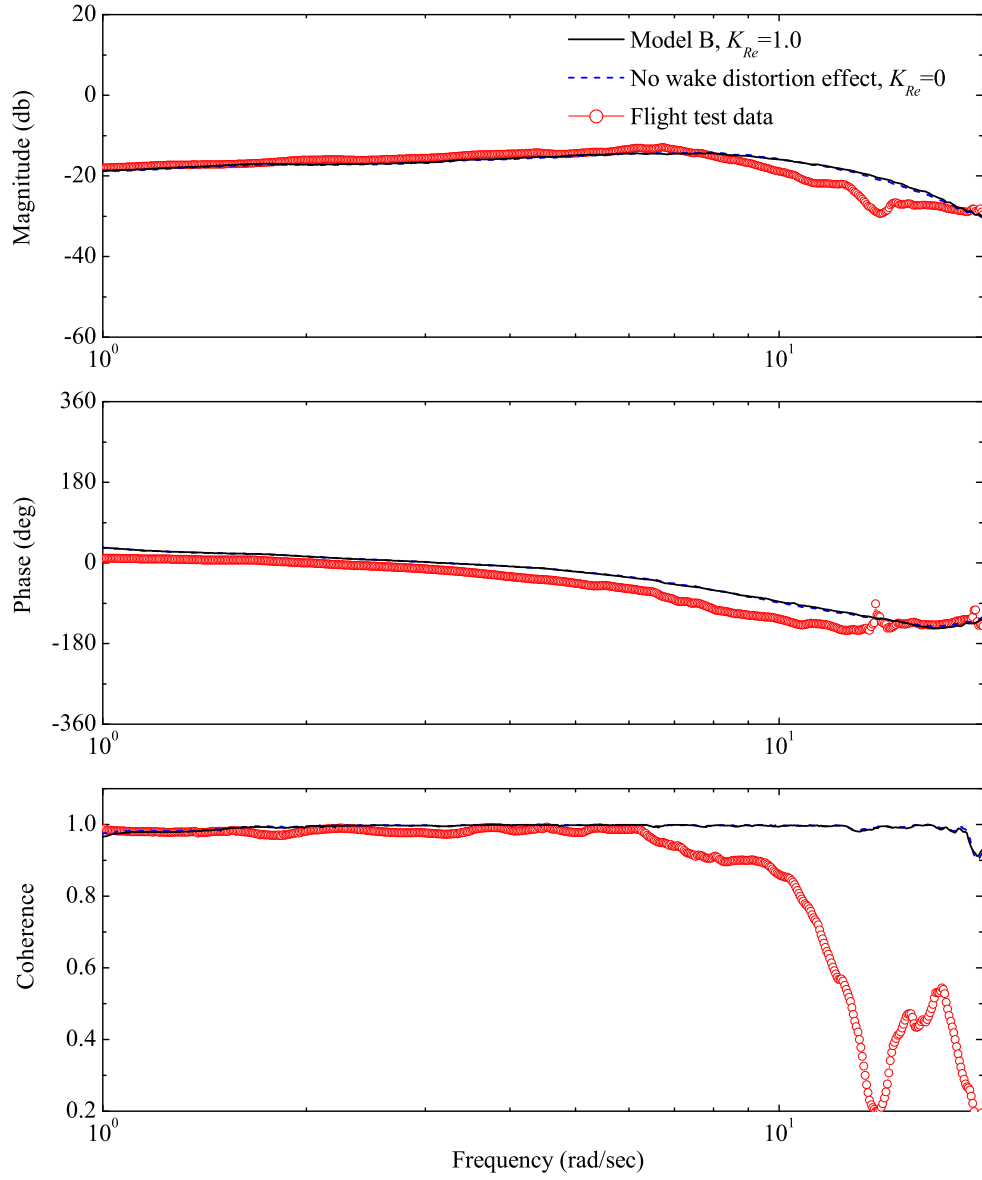
Figure 6.1: On-axis roll rate-to-lateral cyclic stick input frequency response of a UH-60 Black Hawk helicopter in hover
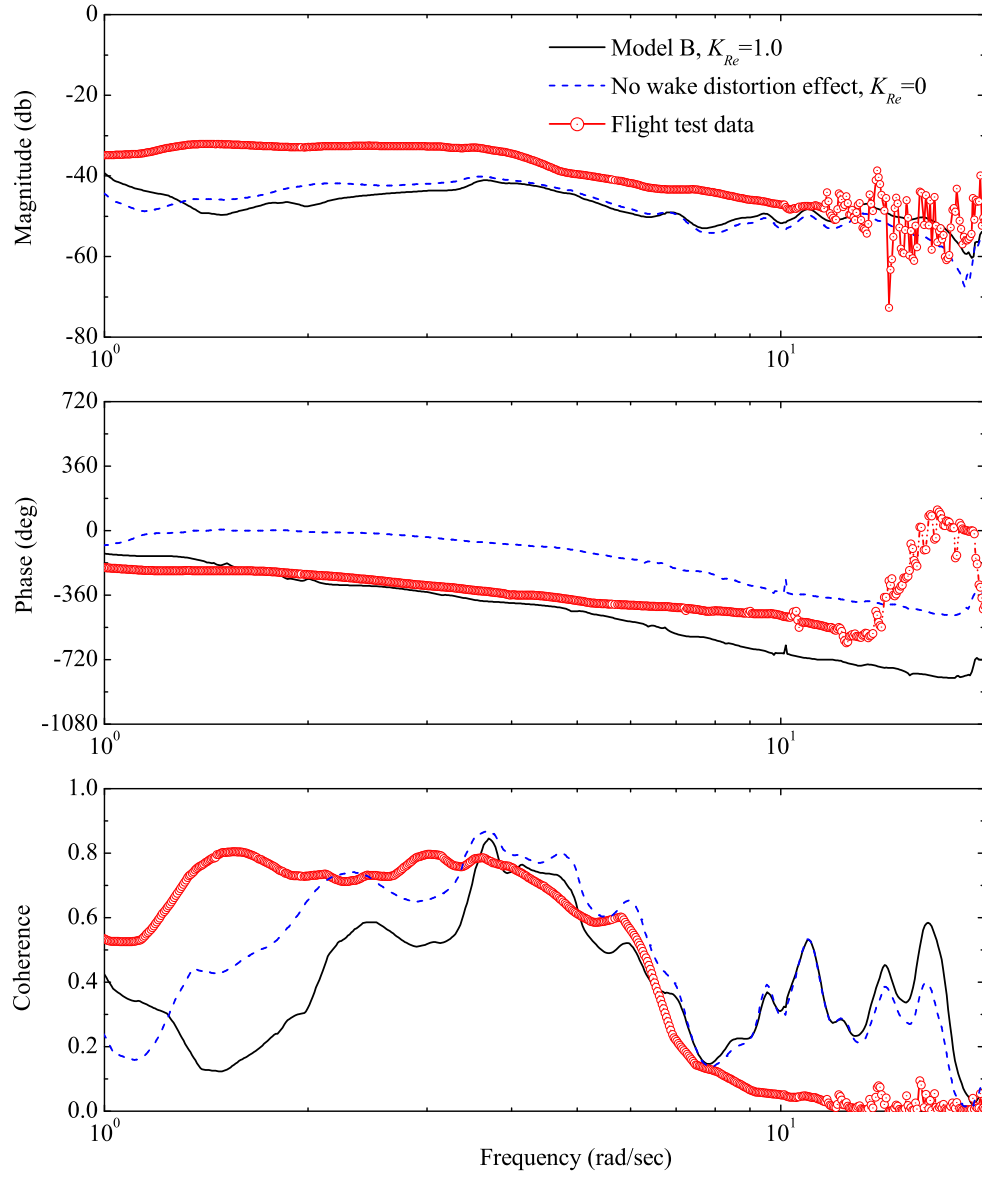
Figure 6.2: Off-axis pitch rate-to-lateral cyclic stick input frequency response of a UH-60 Black Hawk helicopter in hover
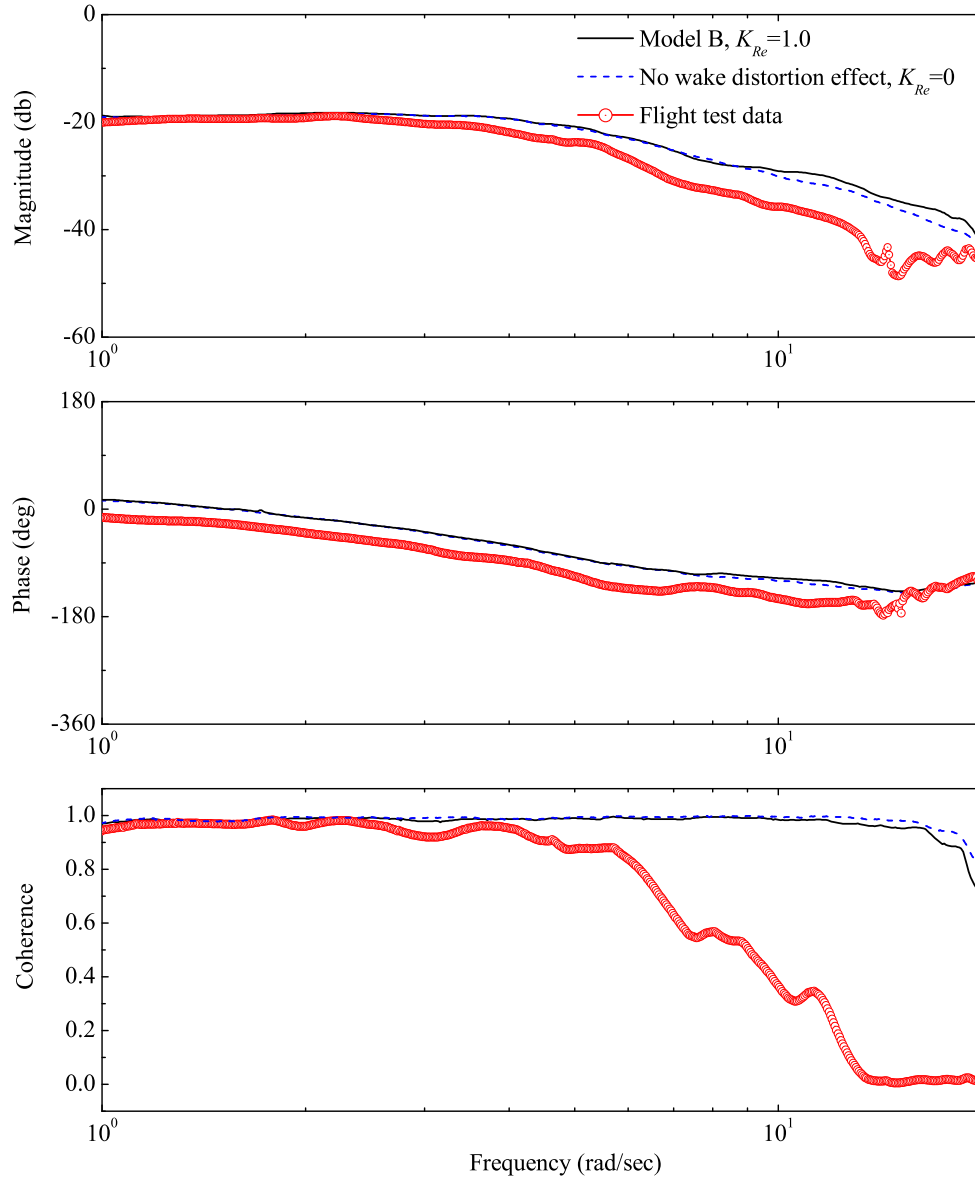
Figure 6.3: On-axis pitch rate-to-longitudinal cyclic stick input frequency response of a UH-60 Black Hawk helicopter in hover
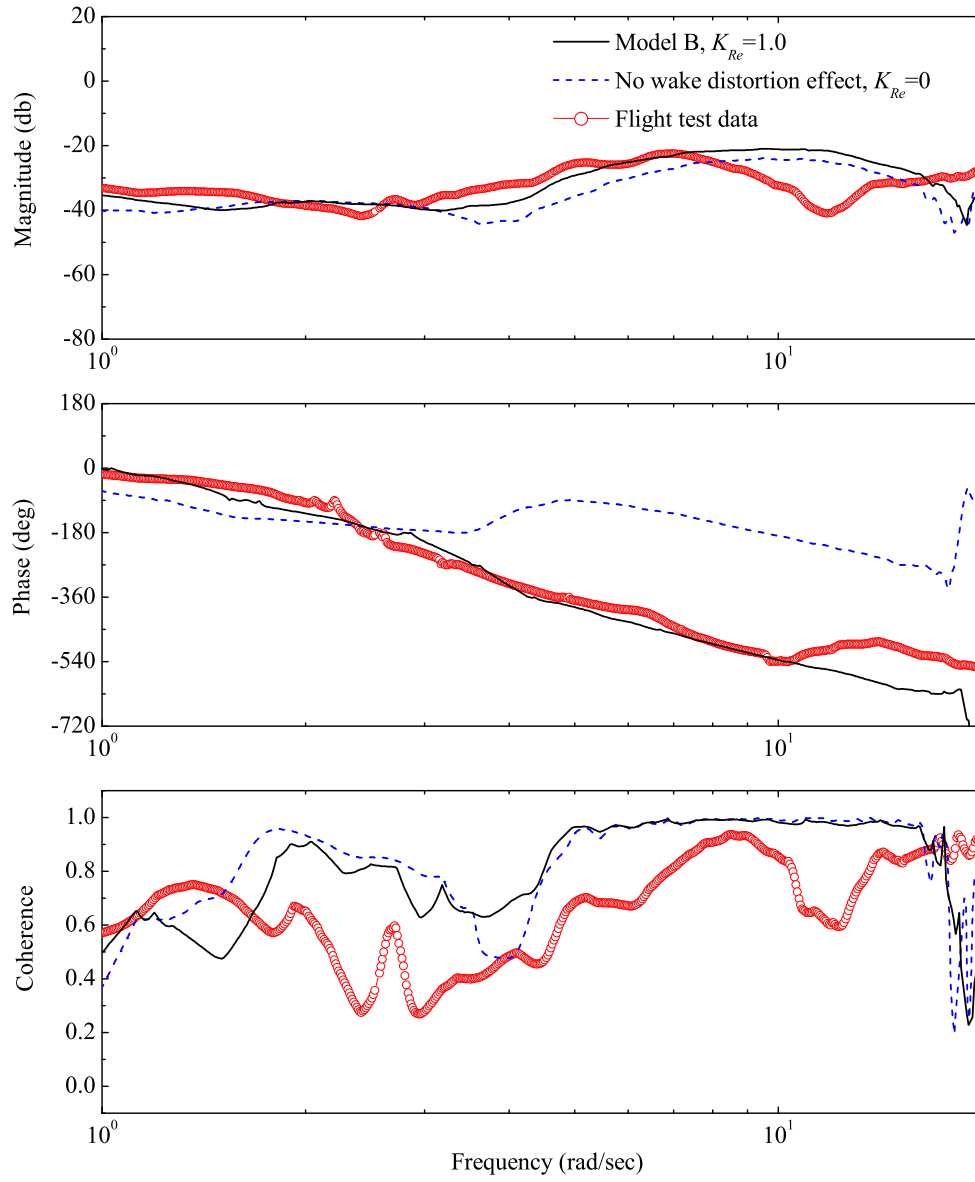
Figure 6.4: Off-axis roll rate-to-longitudinal cyclic stick input frequency response of a UH-60 Black Hawk helicopter in hover

Figure 6.5: On-axis roll rate response of a UH-60 Black Hawk helicopter in hover to the lateral cyclic control stick doublet input of Figure 3.5

Figure 6.6: Off-axis pitch rate response of a UH-60 Black Hawk helicopter in hover to the lateral cyclic control stick doublet input of Figure 3.5
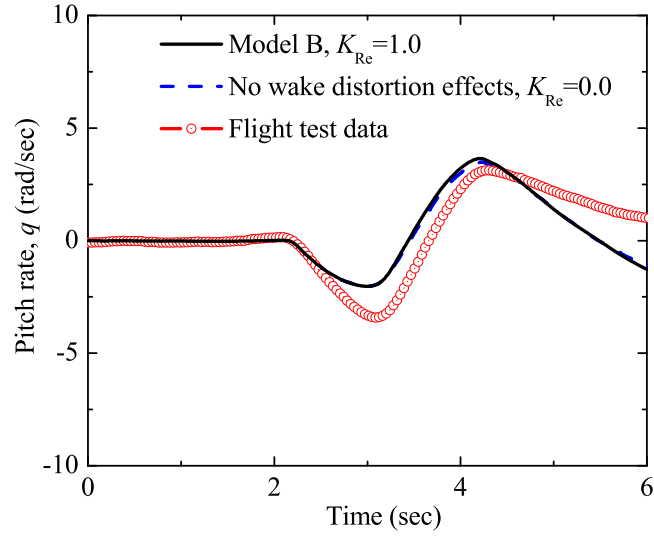
Figure 6.7: On-axis pitch rate response of a UH-60 Black Hawk helicopter in hover to the longitudinal cyclic control stick doublet input of Figure 3.8
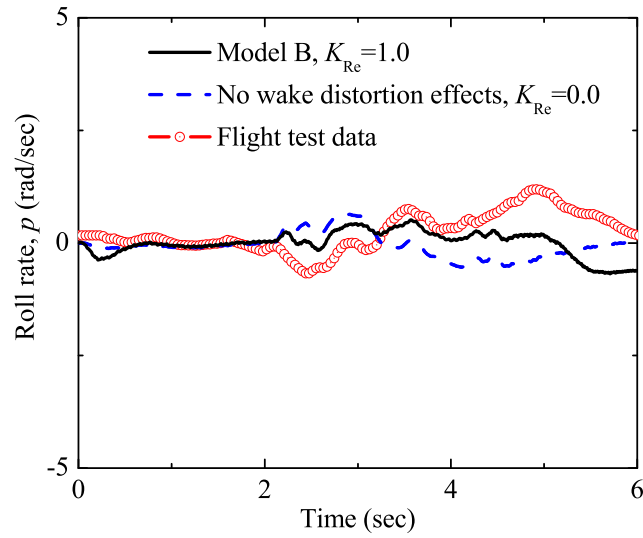
Figure 6.8: Off-axis roll rate response of a UH-60 Black Hawk helicopter in hover to the longitudinal cyclic control stick doublet input of Figure 3.8

6.1.3   Effect of Model Refinement In Hover

Comparisons of the off-axis response predictions in hover with flight test data of a UH-60 Black Hawk helicopter in both the frequency domain (Figures 6.2 and 6.4) and the time domain (Figures 6.6 and 6.8) show that the results predicted using the developed rotor dynamic wake distoriton model with a value of 1.0 for the wake curvature parameter K_{Re} qualitatively capture the correct off-axis response, although there is still some quantitative discrepancy in the magnitude correlation. Previous investigations carried out by Zhao, et al, [58, 79] and the results in Chapter III show that a value of 3.8 for the wake curvature parameter K_{Re}, which is significantly higher than the value of 1.0 obtained from momentum theory [37, 38], is needed to correlate well in magnitude with flight test data of a UH-60 Black Hawk helicopter in hover condition. It is felt that this discrepancy in magnitude could be due to several other sources, such as the difference between the predicted on-axis response and the corresponding flight test data, the effect of airfoil unsteady aerodynamics, the fuselage blockage effect on the main rotor mean induced velocity and the gyroscopic feathering moment effect, etc. Zhao, et al, [58, 79] studied the effect of specifying the on-axis roll rate response directly from the flight test data on the off-axis pitch rate response prediction of a UH-60 Black Hawk helicopter to a lateral cyclic control doublet stick input in hover. The results show that with the on-axis roll rate directly specified from the flight test data, a lower value for the wake curvature parameter is sufficient to capture the correct off-axis response. In this section, the impacts of airfoil unsteady aerodynamics, fuselage blockage effect on the mean induced velocity across the main rotor disk plane and the gyroscopic feathering moment effect on the off-axis response predictions during maneuvering in hover are investigated.

Figure 6.9 shows comparisons of the simulated off-axis pitch rate response of a UH-60 Black Hawk helicopter to a lateral cyclic control doublet stick input starting from hover as shown in Figure 3.5, predicted with different levels of modeling. Starting with the baseline model which does not include any wake distortion effect, the dynamic wake distortion effect, fuselage blockage effect, gyroscopic feathering moment effect and the effect of airfoil unsteady aerodynamics are successively included in the simulation program. It can be
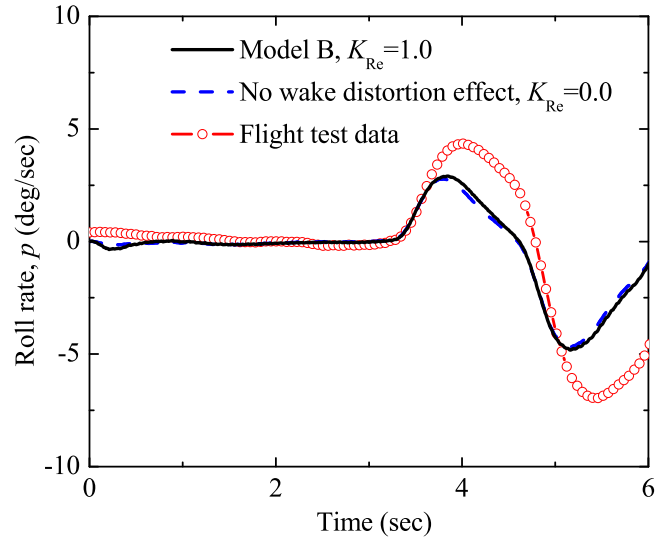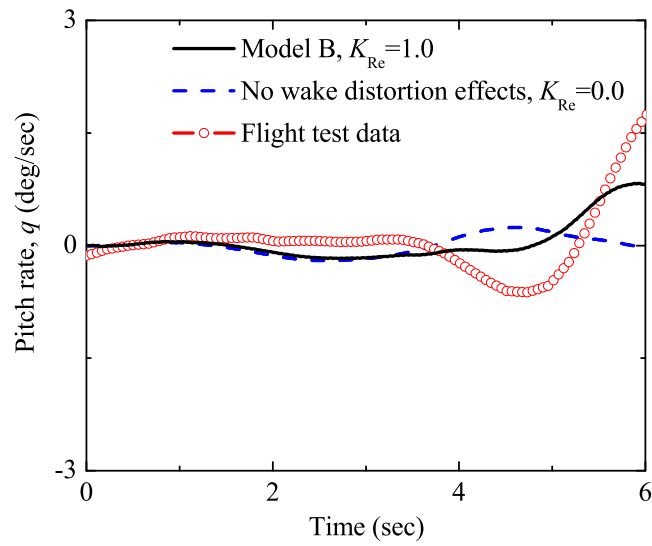
Figure 6.9: Effects of different factors on the off-axis pitch rate response of a UH-60 Black Hawk helicopter in hover to the lateral cyclic control stick doublet input of Figure 3.5

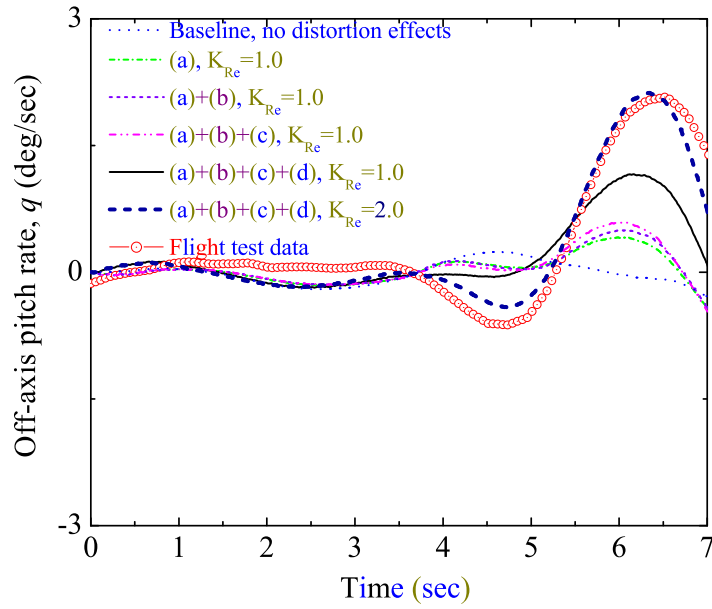clearly seen that inclusion of the dynamic wake distortion effect with $K_{Re} = 1.0$ qualitatively captures the correct reversal-in-sign phenomena when compared with the corresponding flight test data, although the magnitude is under-predicted. Inclusions of the fuselage blockage effect, gyroscopic feathering moment effect and airfoil unsteady aerodynamics effect further improve the correlation in magnitude with the flight test data. With the final combined model, which includes the dynamic wake distortion effect, fuselage blockage effect, gyroscopic feathering moment effect and the effect of airfoil unsteady aerodynamics, a value of 1.0 for the wake curvature parameter K_{Re} significantly improves the correlation of the off-axis pitch rate response with flight test data as compared with the results using only the rotor dynamic wake distortion effect with $K_{Re} = 1.0$. But there is still some discrepancy in magnitude correlation between the results predicted using the combined model with $K_{Re} = 1.0$ and the flight test data. To further investigate the effect of the wake curvature parameter K_{Re} on the off-axis pitch rate response predictions, the results predicted using the combined model with a value of 2.0 for the wake curvature parameter K_{Re} are also superimposed on Figure 6.9. It can be seen that the predictions using the combined model with $K_{Re} = 2.0$ capture the correct off-axis response behavior as observed in the flight test data. Therefore, it can be seen that the value of the wake curvature parameter needed for accurate off-axis response prediction in hover is influenced by several other sources, such as the effect of airfoil unsteady aerodynamics, the fuselage blockage effect and the gyroscopic feathering moment effect, which individually may be small.

Figure 6.10 shows the comparison of the simulated off-axis pitch rate-to-lateral cyclic stick input frequency response of the UH-60A Black Hawk helicopter in hover, predicted using the combined model with two values for the wake curvature parameter ($K_{Re} = 1.0$ and $K_{Re} = 2.0$). For comparison purposes, the predictions using only the dynamic wake distortion model with $K_{Re} = 1.0$ is also superimposed on the plots. It can be seen that the results predicted using the combined model with $K_{Re} = 2.0$ correlate well with the flight test results as compared with the results using the dynamic wake distortion model only, which is consistent with the results in the time domain shown before.

Figure 6.10: Off-axis pitch rate-to-lateral cyclic stick input frequency response of a UH-60 Black Hawk helicopter in hover, predicted with the combined model

6.2   Validation In Forward Flight

6.2.1   Frequency Domain

The vehicle response to both a lateral and a longitudinal cyclic stick input at 30 knots of flight speed is examined first. Shown in Figures 6.11 and 6.12, respectively, are the on-axis roll rate-to-lateral cyclic stick input frequency response and the off-axis pitch rate-to-lateral cyclic stick input frequency response of a UH-60 Black Hawk helicopter at 30 knots of flight speed. To separate the effect due to the aerodynamic interaction among main rotor, tail rotor and empennage, the simulation program is also run with the main rotor wake distortion effect only, i.e., without the developed main rotor/tail rotor/empennage interaction model in Chapter IV, and the predicted frequency responses are also superimposed on the plots. Similarly, Figures 6.13 and 6.14 are the vehicle on-axis pitch rate-to-longitudinal cyclic stick input frequency response and the off-axis roll rate-to-longitudinal cyclic stick input frequency response of the helicopter at 30 knots of flight speed. For comparison purposes, the simulation results without any rotor wake distortion effect, i.e., with a value of zero for the wake curvature parameter K_{Re}, are also superimposed on these plots. From Figures 6.11 and 6.13, which are the on-axis roll rate-to-lateral cyclic stick input frequency response and the on-axis pitch rate-to-longitudinal cyclic stick input frequency response, it can be seen that the three levels of modeling give basically the same on-axis frequency response predictions as compared with the corresponding flight test results. However, as can be clearly seen from Figures 6.12 and 6.14, which are the off-axis pitch rate to lateral cyclic stick input frequency response and the off-axis roll rate to longitudinal cyclic stick input frequency response, there is a phase discrepancy of approximately 180 degrees between the results predicted using model A (or model B) with a value of 1.0 for the wake curvature parameter K_{Re} and the results predicted without any wake distortion effect as compared with the corresponding flight test results. Also, as clearly shown in Figure 6.12, the phase response prediction matches the flight test data well with only including the main rotor wake distortion effect and with a value of 1.0 for the wake curvature parameter K_{Re}, although there is still some discrepancy in the magnitude correlation. Therefore, from the

Figure 6.11: On-axis roll rate-to-lateral cyclic stick input frequency response of a UH-60 Black Hawk helicopter at 30 knots of flight speed

Figure 6.12: Off-axis pitch rate-to-lateral cyclic stick input frequency response of a UH-60 Black Hawk helicopter at 30 knots of flight speed

Figure 6.13: On-axis pitch rate-to-longitudinal cyclic stick input frequency response of a UH-60 Black Hawk helicopter at 30 knots of flight speed

Figure 6.14: Off-axis roll rate-to-longitudinal cyclic stick input frequency response of a UH-60 Black Hawk helicopter at 30 knots of flight speed

results shown in Figure 6.12, it can be seen that inclusion of the main rotor wake distortion effect with $K_{Re} = 1.0$, which is the value obtained from momentum theory, captures the sign of the off-axis response when compared with the corresponding flight test results and it seems that the effect of main rotor/tail rotor/empennage interaction is mainly to improve the magnitude correlation. The good correlation in phase is of importance since for flight simulation and control law design, it is essential for the stability of the closed-loop system. More over, from the magnitude comparisons of the off-axis responses as shown in Figures 6.12 and 6.14, it is seen that both the off-axis roll rate-to-longitudinal cyclic stick input frequency response and the off-axis pitch rate-to-lateral cyclic stick input frequency response are significantly improved with the augmented Peters-He finite state inflow model, when it is combined with the main rotor/tail rotor/empennage interaction model (Model A).

Next, frequency response predictions at 50 knots of flight speed are considered. Figures 6.15 and 6.16, respectively, are the on-axis roll rate-to-lateral cyclic stick input frequency response and the off-axis pitch rate-to-lateral cyclic stick input frequency response of a UH-60 Black Hawk helicopter at 50 knots of flight speed. Figures 6.17 and 6.18, respectively, show the on-axis pitch rate-to-longitudinal cyclic stick input frequency response and the off-axis roll rate-to-longitudinal cyclic stick input frequency response of the helicopter at 50 knots of flight speed. Similar to the results for the 30 knots case, it is seen from Figures 6.16 and 6.18 that both the magnitude and phase correlations with the flight test results are significantly improved with Model A (augmented Peters-He finite state inflow model combined with the main rotor/tail rotor/empennage interaction model). Again, a value of 1.0 for the wake curvature parameter K_{Re} is used in these results.

6.2.2 Time Domain

To further validate the developed dynamic wake distortion model, the vehicle response predictions to cyclic control doublet stick inputs at forward flight are compared with the flight test data in the time domain. The first case studied is the vehicle response to a lateral/longitudinal cyclic control doublet stick input starting from 40 knots of flight speed.
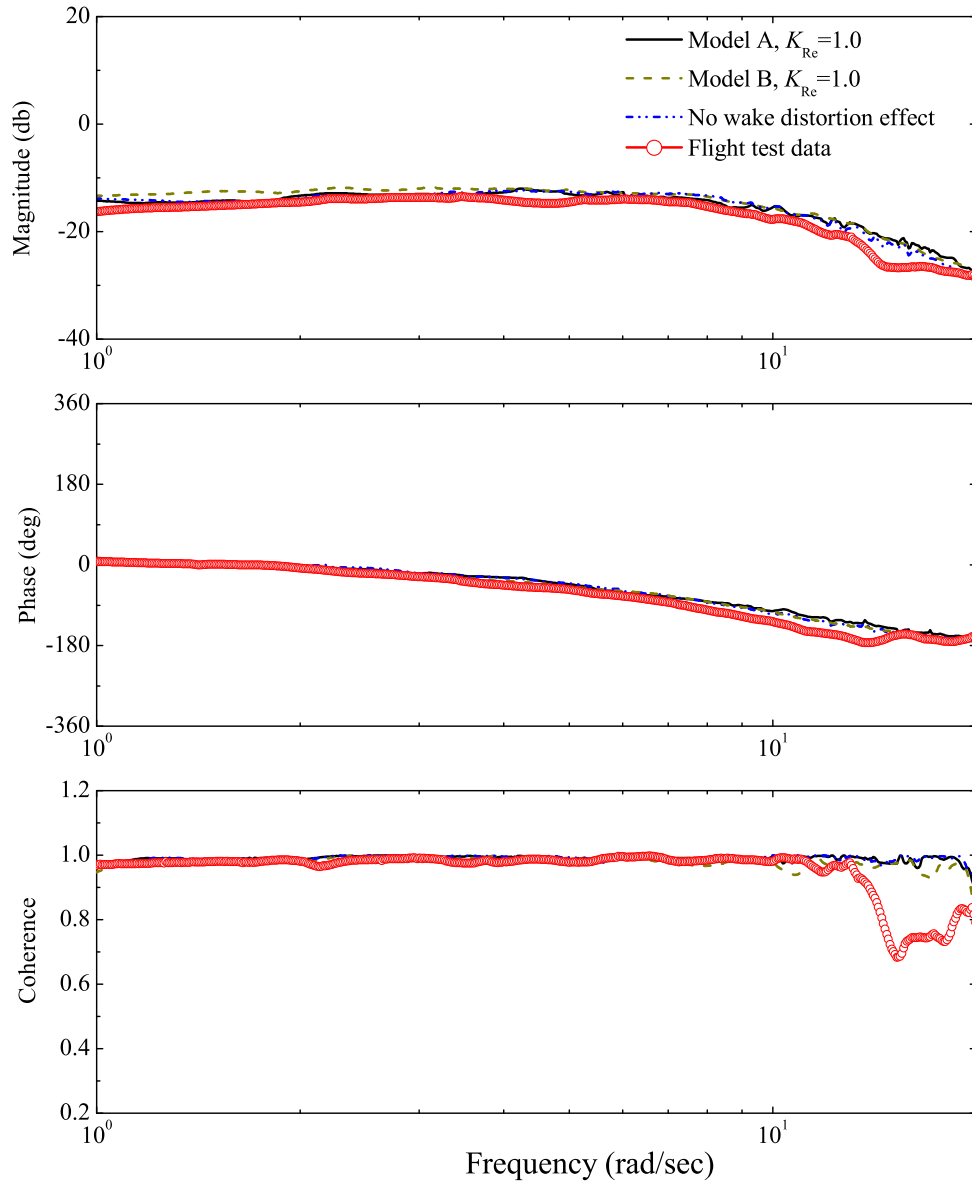
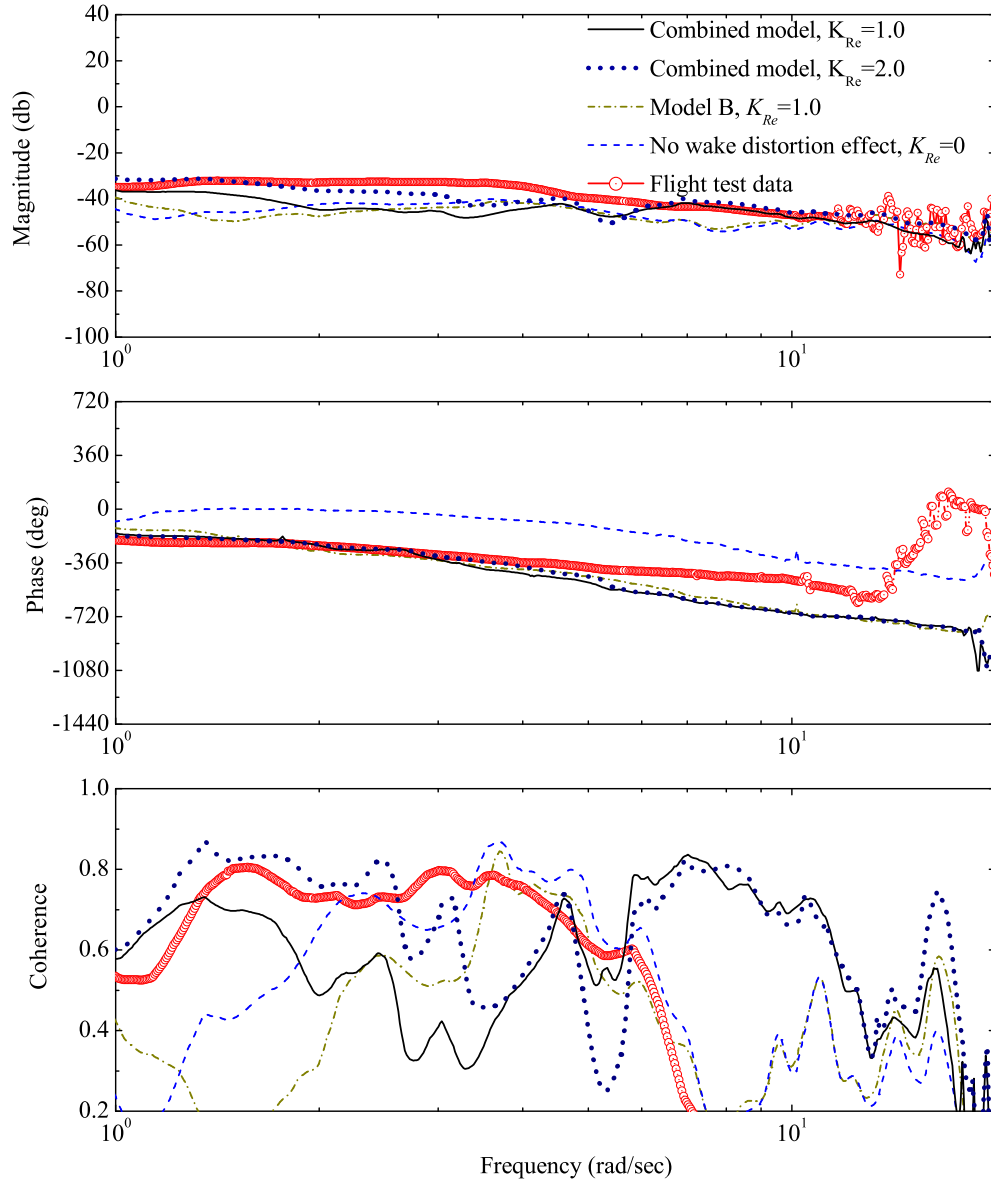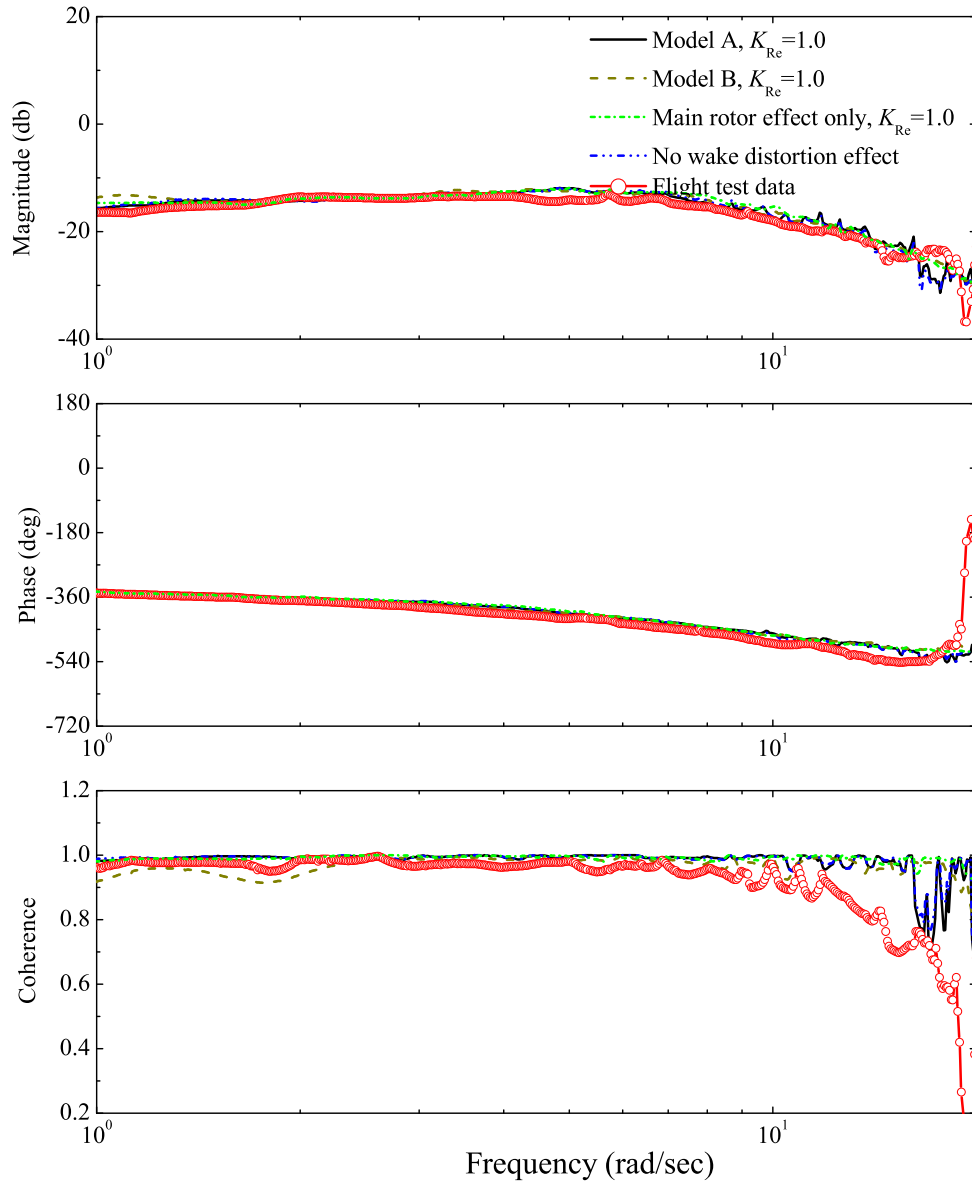**Figure 6.15:** On-axis roll rate-to-lateral cyclic stick input frequency response of a UH-60 Black Hawk helicopter at 50 knots of flight speed
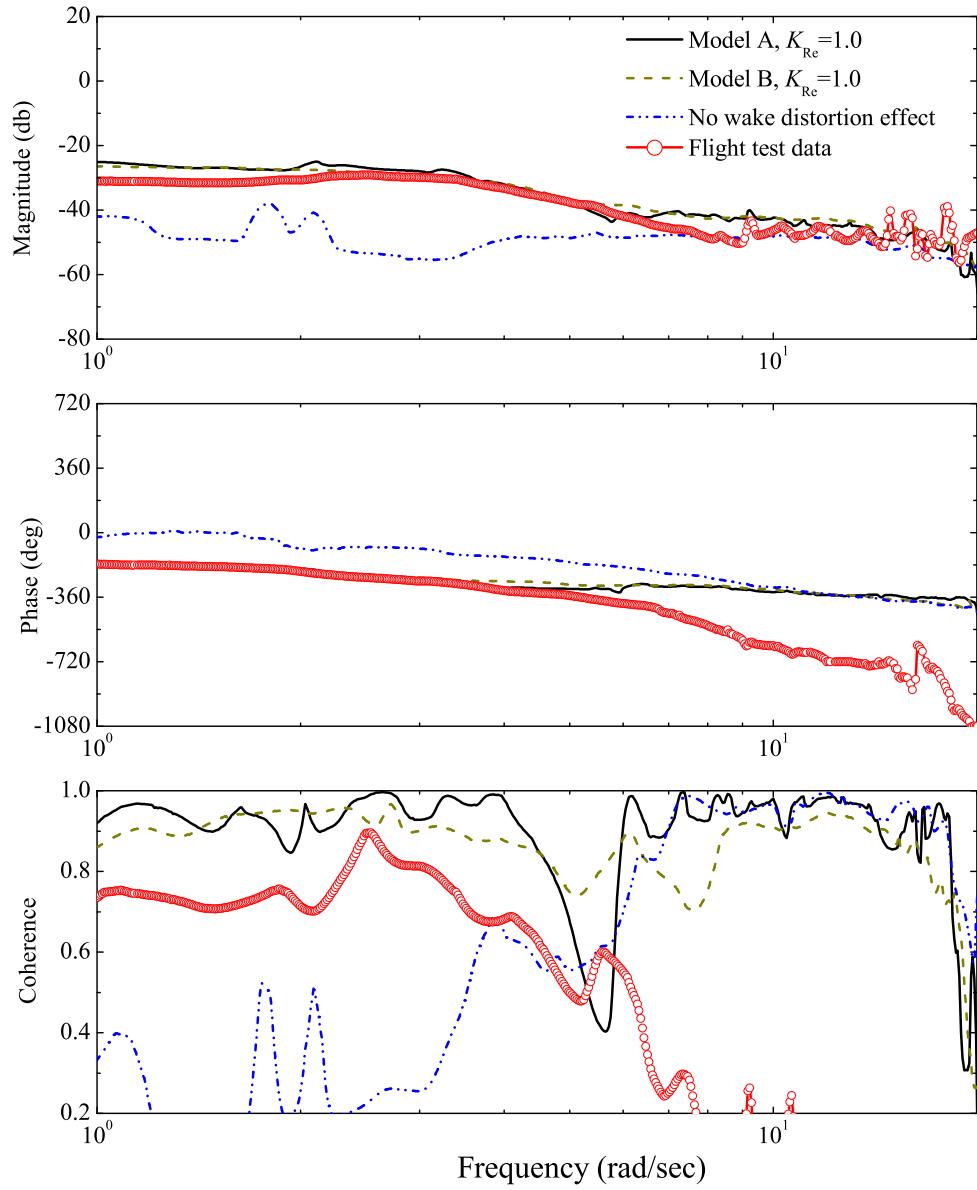
Figure 6.16: Off-axis pitch rate-to-lateral cyclic stick input frequency response of a UH-60 Black Hawk helicopter at 50 knots of flight speed
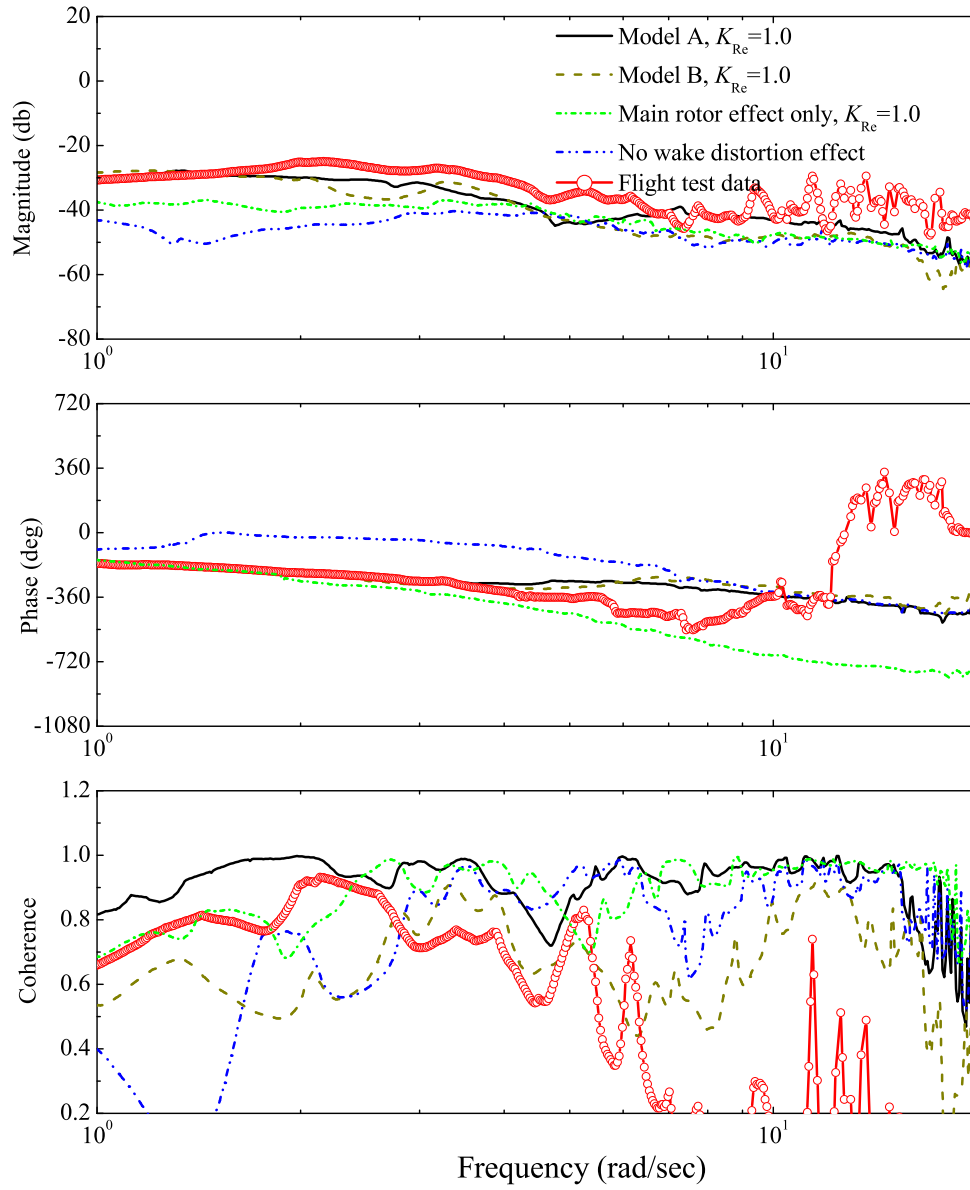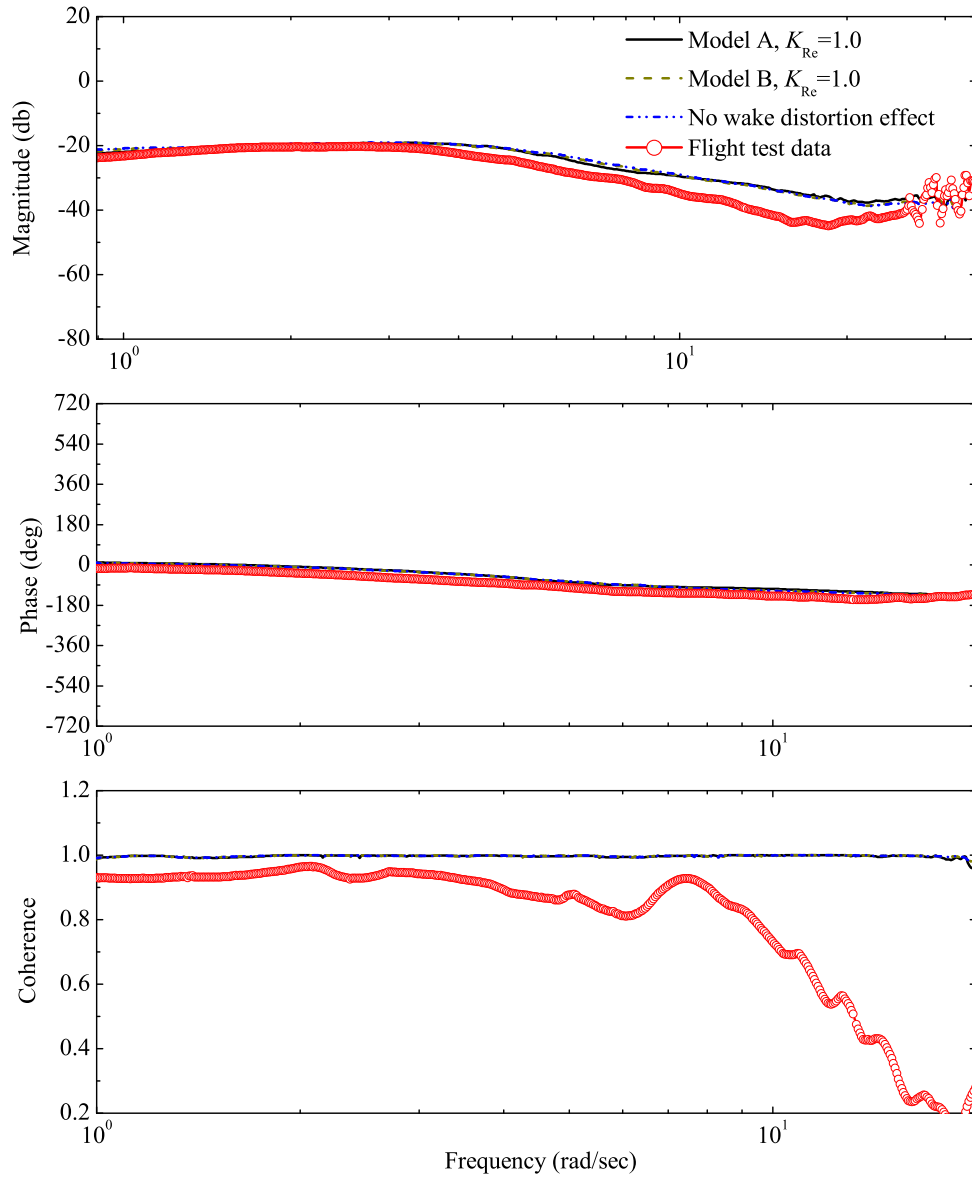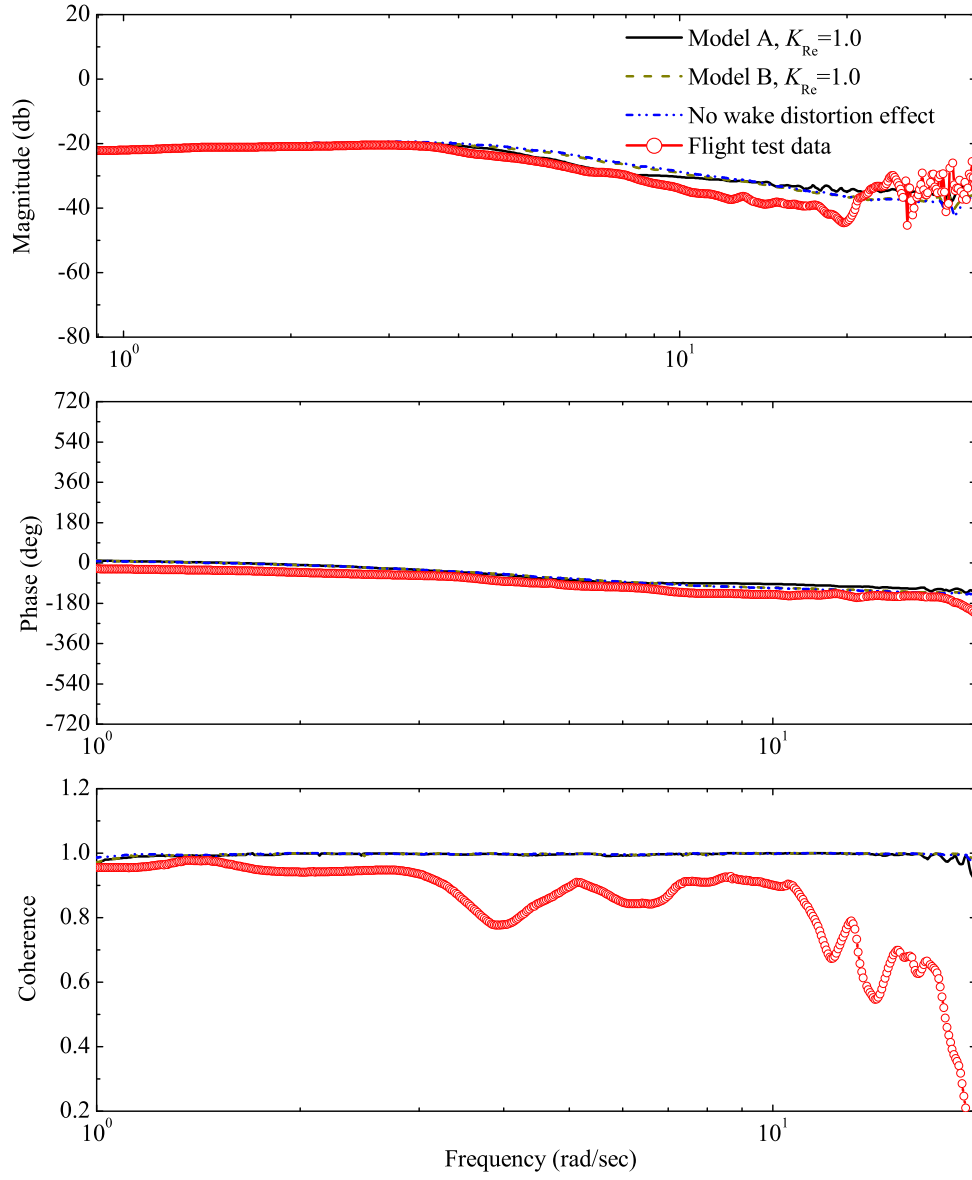
Figure 6.17: On-axis pitch rate-to-longitudinal cyclic stick input frequency response of a UH-60 Black Hawk helicopter at 50 knots of flight speed
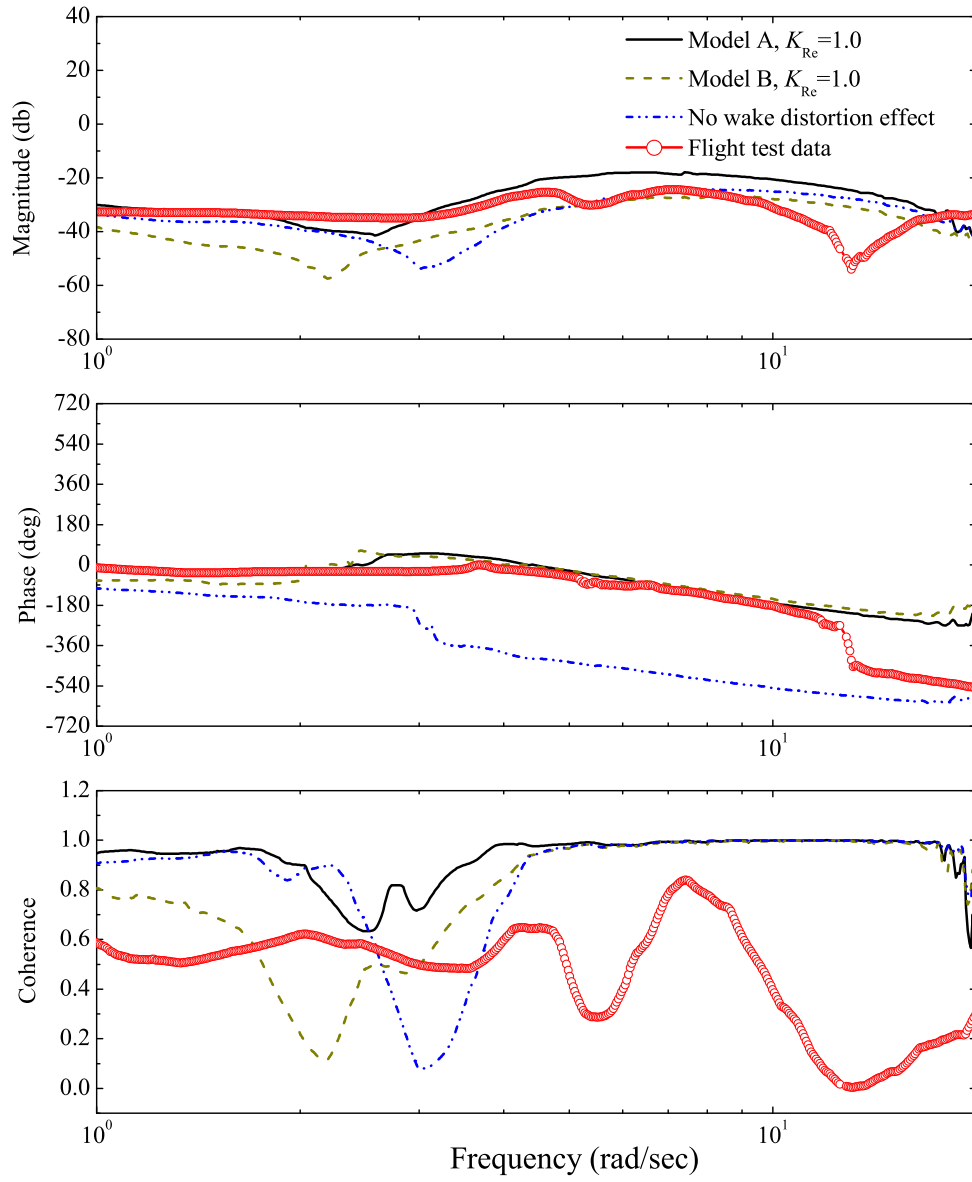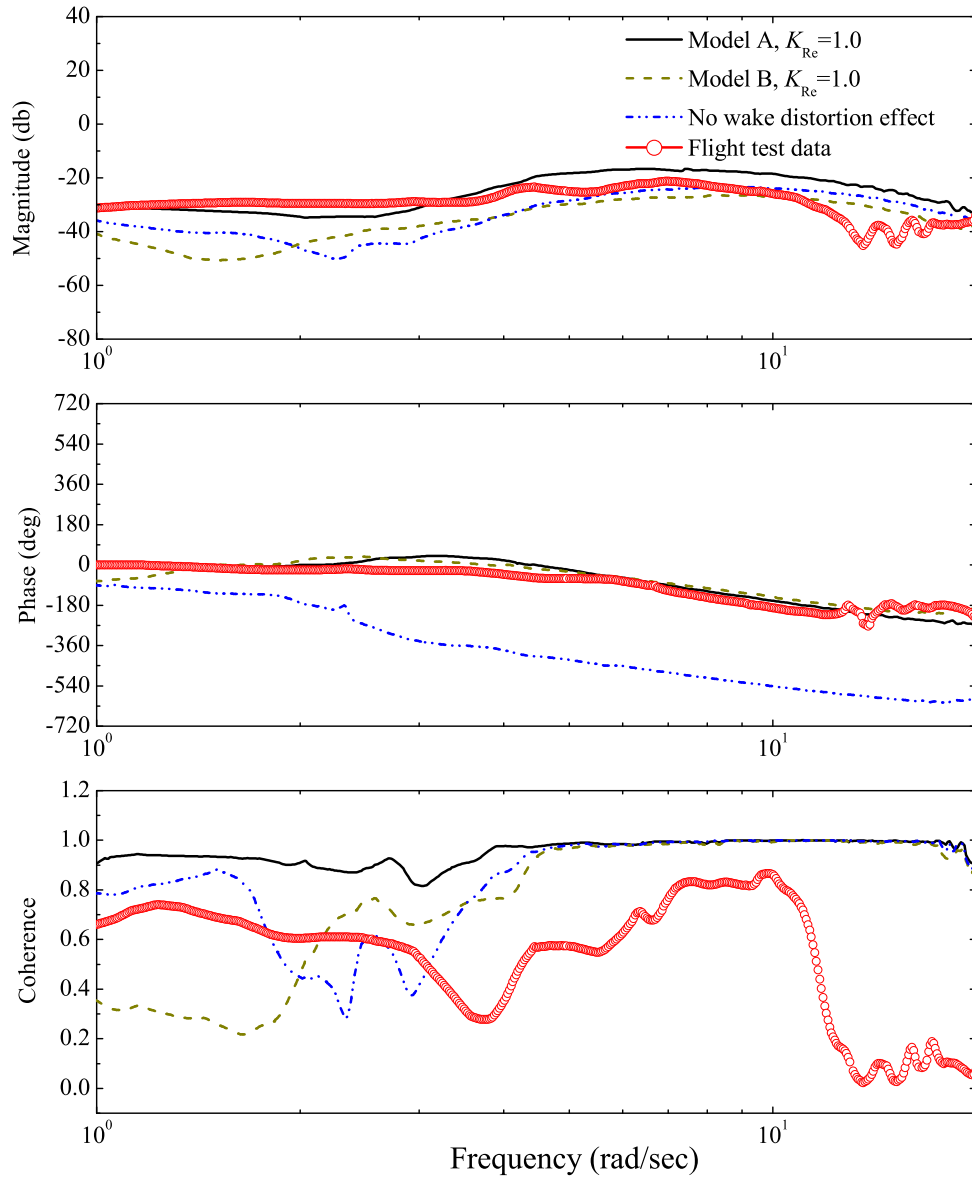
Figure 6.18: Off-axis roll rate-to-longitudinal cyclic stick input frequency response of a UH-60 Black Hawk helicopter at 50 knots of flight speed

Figures 6.19 and 6.20, respectively, show the on-axis roll rate and the off-axis pitch rate responses of the helicopter to a lateral cyclic control doublet stick input of Figure 3.11. From Figure 6.19, it can be seen that both models A and B slightly improve the on-axis roll rate response predictions as compared to the case without any wake distortion effect. As in the frequency domain analysis, to distinguish the effect of the main rotor/tail rotor/empennage interaction, the off-axis pitch rate response predicted by including only the main rotor wake distortion effect with K_{Re}=1.0 is also superimposed in Figure 6.20. From Figure 6.20, it is seen that the off-axis pitch rate response prediction without any wake distortion effect goes opposite to the flight test data. However, including the main rotor wake distortion effect with K_{Re}=1.0 captures qualitatively the correct off-axis response behavior as observed in the flight test data when compared with the results without any wake distortion effects, which is consistent with the results in the frequency domain as shown in Figure 6.12. However, the response magnitude is under predicted. Also, as shown in Figure 6.20, with a value of 1.0 for the wake curvature parameter K_{Re}, both models A and B, which include the main rotor/tail rotor/empennage interaction effect, correlate well with flight test data. From the off-axis response correlations in the time domain (Figure 6.20) and in the frequency domain (Figure 6.12), it can be clearly seen that inclusion of the main rotor wake distortion effect with a value of 1.0 for the wake curvature parameter K_{Re} captures qualitatively the correct sign of the off-axis response when compared with the corresponding flight test data and that the effect of main rotor/tail rotor/empennage interaction is mainly to improve the magnitude correlation.

Figure 6.21 shows the longitudinal cyclic control stick doublet input used in the flight test program at 40 knots of flight speed. Figures 6.22 and 6.23, respectively, are the on-axis pitch rate and off-axis roll rate responses to the longitudinal cyclic control stick doublet input of Figure 6.21. From Figure 6.23, it can be seen that the off-axis roll rate response predictions using Model A correlate well with the flight test data, which is again consistent with the frequency domain results.

Next, the vehicle response to a lateral/longitudinal cyclic control stick doublet input at 80 knots of flight speed is considered. Figures 6.25 and 6.26, respectively, show the on-axis

roll rate and off-axis pitch rate responses to a lateral cyclic control stick doublet input of Figure 6.24. From Figure 6.26, it is clear that using both models A and B with a value of 1.0 for the wake curvature parameter K_{Re}, the off-axis pitch rate response predictions are significantly improved when compared with the case without any wake distortion effects. The vehicle response to a longitudinal cyclic control stick doublet input of Figure 6.27 are shown in Figures 6.28 and 6.29. From Figure 6.29, it is seen that the off-axis roll rate response predictions are significantly improved with Model A.

From the validations in hover presented in the previous section, it can be seen that the augmented inflow models, combined with the developed dynamic wake distortion model, using a value of 1.0 for the wake curvature parameter capture the correct off-axis phase response in hover. However, the off-axis magnitude response is under predicted in hover. Also, it is shown that the correct off-axis magnitude response is dependent on several other effects, such as fuselage blockage effect, airfoil unsteady aerodynamics effect and gyroscopic feathering moment effect. With all the effects considered in this study included, it is shown that a value of 2.0 for the wake curvature parameter captures the correct off-axis response in hover. From the validations in forward flight, it is shown that both Models A and B, with a value of 1.0 for the wake curvature parameter, capture the correct off-axis response behavior. Therefore, an equivalent wake wake curvature parameter $(K_{Re})_{eq}$ can be defined as

$$(K_{Re})_{eq} = \frac{\bar{V}}{V_m} \tag{6.1}$$

where V_m and $\bar{V}$, respectively, are the mass flow parameters associated the mean and higher harmonics of inflow. From equation 6.1, it can be seen that the equivalent wake curvature parameter has a value of 2.0 in hover and gradually reduces to a value of 1.0 at forward flight. Therefore, this equivalent wake curvature parameter can be used to capture the correct off-axis response in both hover and forward flight conditions .
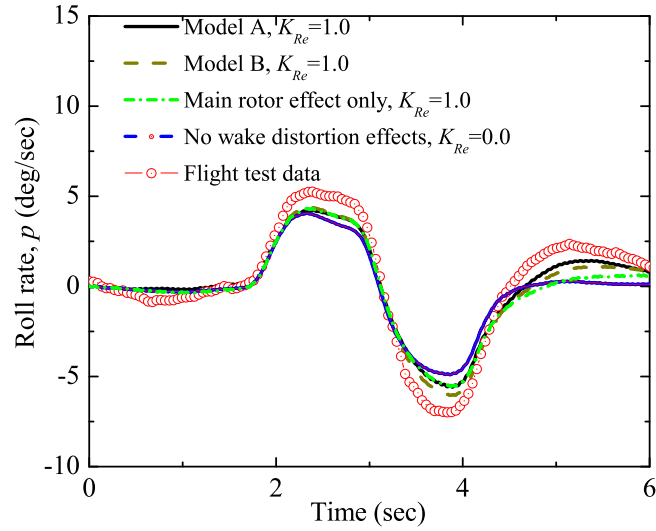
Figure 6.19: On-axis roll rate response of a UH-60 Black Hawk helicopter at 40 knots of flight speed to the lateral cyclic control stick doublet input of Figure 3.11
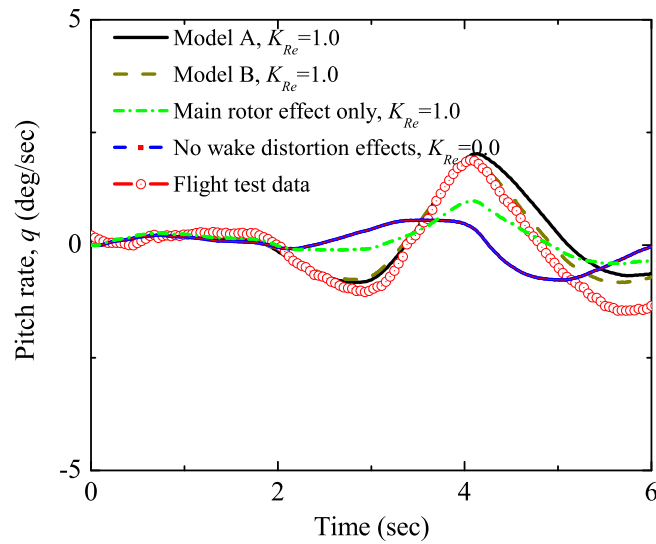
Figure 6.20: Off-axis pitch rate response of a UH-60 Black Hawk helicopter at 40knots of flight speed to the lateral cyclic control stick doublet input of Figure 3.11
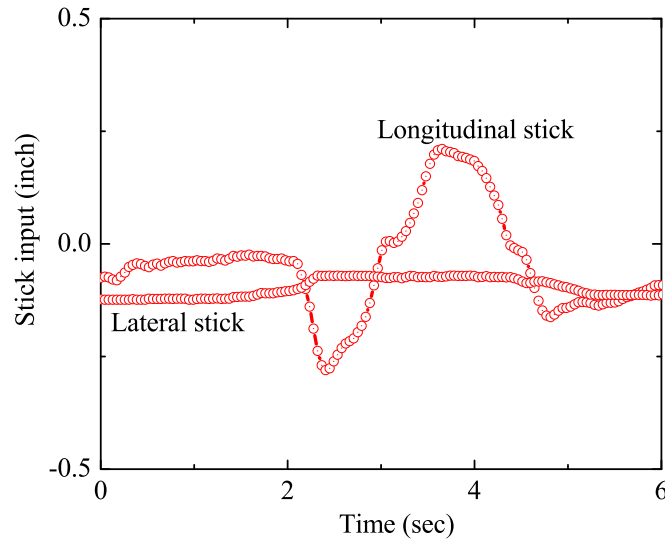
Figure 6.21: Profile of the longitudinal cyclic control stick doublet input used in the UH-60 Black Hawk helicopter flight test program at 40 knots of flight speed
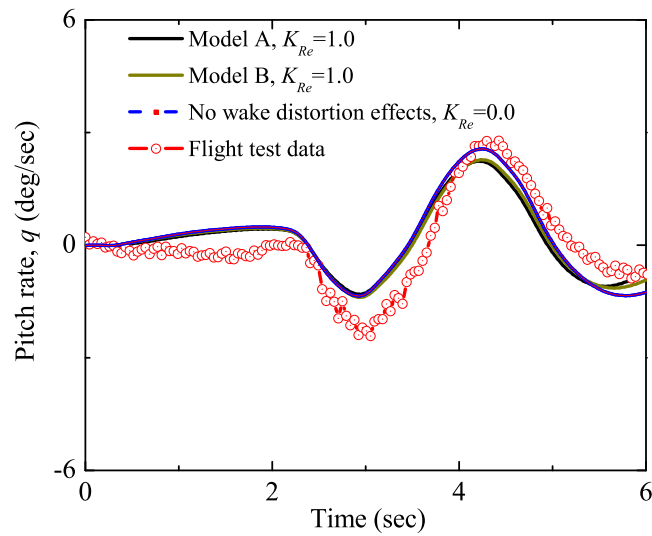
Figure 6.22: On-axis pitch rate response of a UH-60 Black Hawk helicopter at 40 knots of flight speed to the longitudinal cyclic control stick doublet input of Figure 6.21
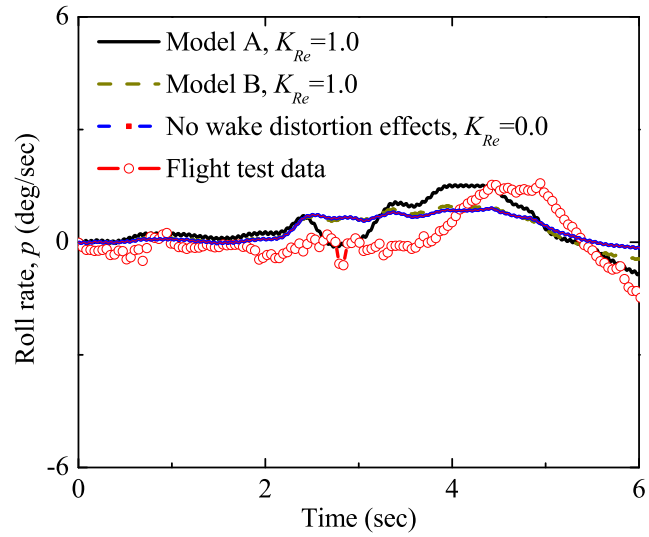
Figure 6.23: Off-axis roll rate response of a UH-60 Black Hawk helicopter at 40knots of flight speed to the longitudinal cyclic control stick doublet input of Figure 6.21
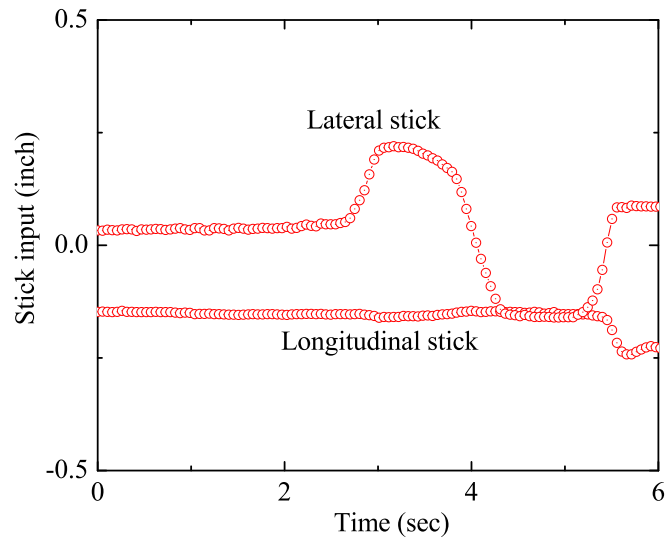
Figure 6.24: Profile of the lateral cyclic control stick doublet input used in the UH-60 Black Hawk helicopter flight test program at 80 knots of flight speed
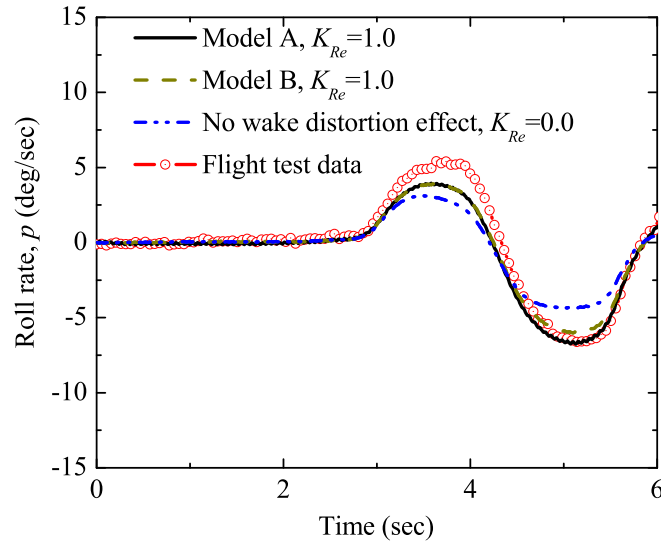
Figure 6.25: On-axis roll rate response of a UH-60 Black Hawk helicopter at 80 knots of flight speed to the lateral cyclic control stick doublet input of Figure 6.24
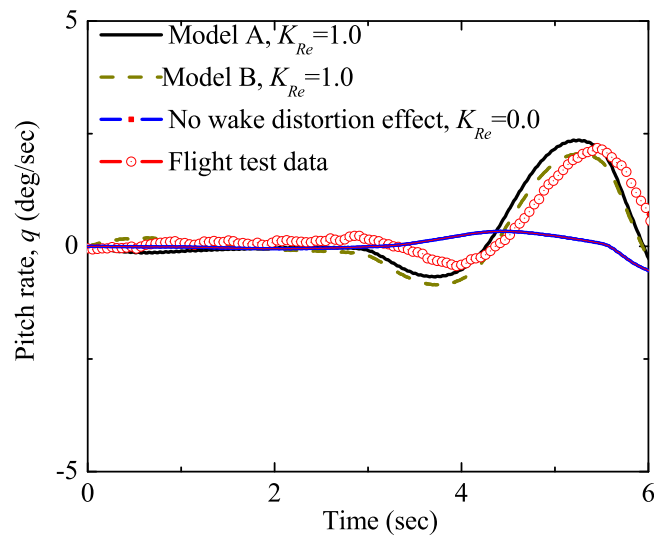
Figure 6.26: Off-axis pitch rate response of a UH-60 Black Hawk helicopter at 80knots of flight speed to the lateral cyclic control stick doublet input of Figure 6.24
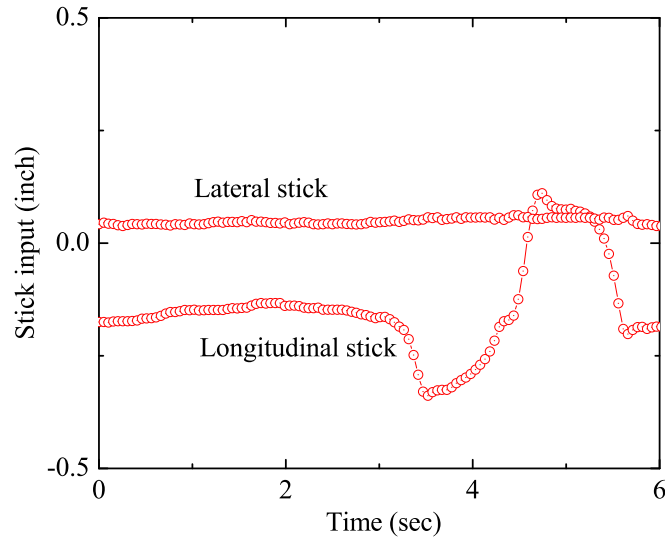
Figure 6.27: Profile of the longitudinal cyclic control stick doublet input used in the UH-60 Black Hawk helicopter flight test program at 80 knots of flight speed
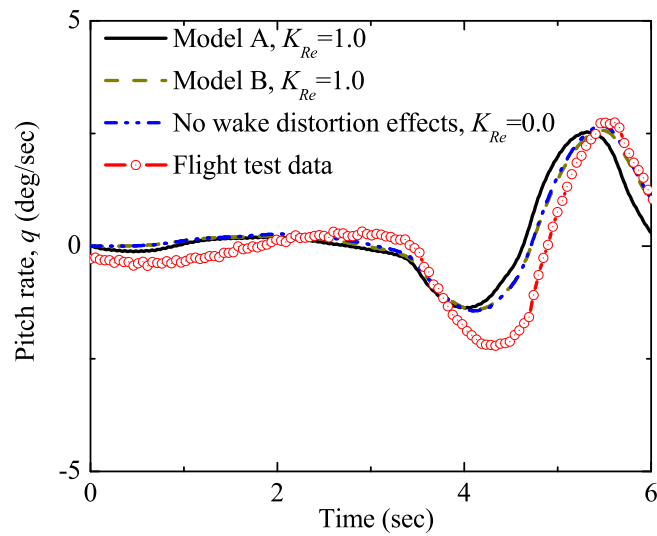
Figure 6.28: On-axis pitch rate response of a UH-60 Black Hawk helicopter at 80 knots of flight speed to the longitudinal cyclic control stick doublet input of Figure 6.27
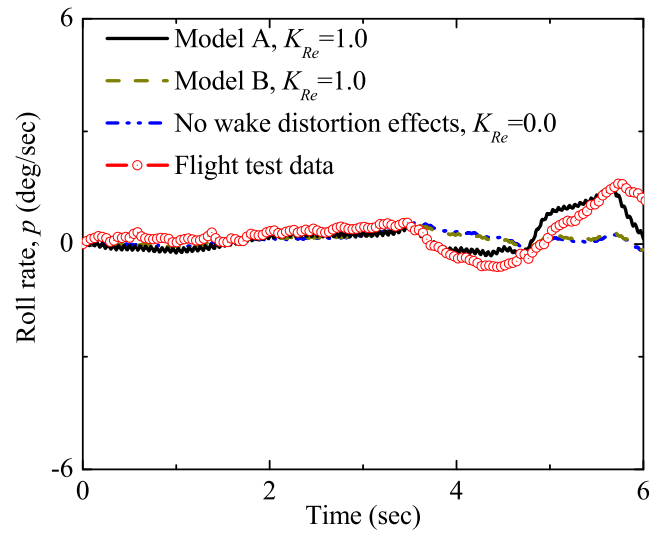
Figure 6.29: Off-axis roll rate response of a UH-60 Black Hawk helicopter at 80knots of flight speed to the longitudinal cyclic control stick doublet input of Figure 6.27

CHAPTER VII

CONCLUSIONS AND RECOMMENDATIONS

7.1 Conclusions

In this study, a rotor dynamic wake distortion model is developed and the effect of rotor dynamic wake distortion on helicopter response predictions, especially on the off-axis response predictions, during maneuvering flight is studied. In developing the rotor dynamic wake distortion model, the following conclusions have been obtained:

1. The inflow perturbations across the rotor disk during different transient maneuvers, such as a step pitch and/or roll rate, a step climb rate and a step change in advance ratio, are investigated using a dynamic vortex tube analysis and the results are compared with available results from a free wake analysis results. It is shown that the inflow perturbation during maneuvering flight exhibit a first order behavior with time.

2. A rotor dynamic wake distortion model, expressed in terms of a set of ordinary differential equations, which use the longitudinal and lateral wake curvatures, wake skew and wake spacing as four states, is developed. The time constant matrix of the rotor dynamic wake distortion model is extracted from the dynamic vortex tube analysis results.

3. Based on the vortex tube analysis results, both the Pitt-Peters dynamic inflow model and the Peters-He finite state inflow model are augmented to account for coupling effect among rotor inflow, rotor wake distortion, rotor mean and cyclic loadings during helicopter maneuvering in both hover and forward flight condition.

4. The augmented Pitt-Peters dynamic inflow model is compared with the inflow model proposed by Keller in oder to clarify any difference between the two models. It is shown that the two models are consistent with each other if only the rotor mean

loading effect is considered (Keller's model only considers the rotor mean loading effect while the augmented Pitt-Peters dynamic inflow model considers both the rotor mean/cyclic loading effect and the wake curvature/skew coupling effect).

5. A reduced order model is developed to account for the aerodynamic interaction among main rotor, tail rotor and empennage due to main rotor and tail rotor wake curvatures during helicopter maneuvering flight. An equivalent wake skew angle is used to represent the main rotor wake curvature on main rotor downwash at tail rotor and empennage. The additional side wash induced at the aerodynamic centers of the vertical tail and tail rotor due to the main rotor wake curvature effect is obtained by using a vortex tube analysis. Similarly, the additional up/down wash induced at the aerodynamic centers of the horizontal tail due to tail rotor wake curvature effect is obtained by using the vortex tube analysis.

6. A reduce order model is developed to account for the fuselage blockage effect on the main rotor mean induced inflow. A fuselage blockage effect factor, which is the ratio of the mean induced inflow with fuselage blockage effect to that without fuselage blockage effect is obtained.

7. Both the augmented Pitt-Peters dynamic inflow model and the augmented Peters-He finite state inflow model, combined with the developed rotor dynamic wake distortion model, together with the main rotor/tail rotor/empennage interaction model, are implemented in a generic helicopter simulation program of UH-60 Black Hawk helicopter to investigate the effect of rotor dynamic wake distortion on control response predictions, especially on the off-axis response predictions, during helicopter maneuvering flight. Simulated control responses in both time domain and frequency domain are compared with flight test data of a UH-60 Black Hawk helicopter in both hover and forward flight conditions.

8. Using a quasi-steady wake distortion model, the high frequency progressive flapping mode is destabilized, which causes simulation divergence problem. However, using the developed rotor dynamic wake distortion model, the high frequency progressive

flapping mode is still stable, and therefore, it alleviates the simulation divergence problem observed with a quasi-steady wake distortion model.

9. The augmented Peters-He finite state inflow model with a value of 1.0 for the wake curvature parameter K_{Re}, combined with the dynamic wake distortion model and the main rotor/tail rotor/empennage interaction model, captures the correct off-axis response behavior at forward flight conditions.

10. The primary effect of the aerodynamic interaction among main rotor, tail rotor and empennage during maneuvering flight is on the off-axis response magnitude correlation in forward flight.

11. With a value of 1.0 for the wake curvature parameter K_{Re}, the dynamic wake distortion model captures qualitatively the correct off-axis response behavior in hover, although there is still some quantitative discrepancy in the magnitude correlation.

12. The value of K_{Re} needed to accurately predict the off-axis magnitude response in hover is influenced by several sources, such as the fuselage blockage effect on rotor mean induced inflow, the airfoil unsteady aerodynamics effect, the gyroscopic feathering moment effect and the correct on-axis response prediction, which individually may be small.

13. With the combined model in this study, which includes rotor dynamic wake distortion effect, airfoil unsteady aerodynamics effect, fuselage blockage effect and gyroscopic feathering moment effect, a value of 2.0 for the wake curvature parameter captures the correct off-axis response behavior of the UH-60 Black Hawk helicopter in hover.

14. An equivalent wake curvature parameter, which is the ratio of the mass flow parameter associated with higher harmonics of inflow to that associated with the mean inflow, is shown to capture the correct off-axis response in both hover and forward flight.

7.2   Recommendations For Future Work

1. In this study, assuming that all vortex tubes bend with the same curvature, a series of concentric vortex tubes are used to represent the helicopter rotor wake for a general load distribution. The wake curvature is defined in terms of tip-path-plane pitch and roll rates and the mean inflow across the rotor disk. Since the real rotor inflow varies around the radial direction, future work is recommended to carry out the investigation where each vortex tube follows its own local wake curvature, which is defined in terms of the tip-path-plane pitch and roll rates and the local inflow at which the vortex tube convects. In this manner, it is possible to get a larger value for the equivalent wake curvature parameter ($K_{Re} > 1.0$), which is needed to improve the off-axis magnitude response correlation in hover condition. The main reason is that by using a local wake curvature for each tube, an inner tube will have a larger wake curvature due to the reduced inflow there than an outer tube. In forward flight, the free stream velocity will wash this effect out and therefore it should have small effect at forward flight.

2. In the present study, the time constant matrix associated with rotor wake dynamic distortion effect is assumed to take a diagonal form, i.e., neglecting couplings between the wake curvature, wake skew and wake spacing states. It is recommended that further CFD analyses be performed on maneuvering rotors so as to identify the off-diagonal elements in the time constant matrix and to fully understand and assess the coupling effect between wake curvature state, wake skew state and wake spacing state on response predictions.

3. The effect of rotor disk loading on inflow perturbations across the rotor disk due to wake distortion effect is addressed. Only the effect of rotor mean loading and first harmonic cyclic loading terms are considered. But real rotors are with finite number of blades, and therefore, higher harmonics of rotor loading on inflow across the rotor disk during maneuvering flight should be studied and their effects on helicopter response predictions need to be assessed.

4. In the present study, only the coupling between rotor wake distortion effect and the

blade rigid flapping motion is considered. Although the blade elastic motion alone on the correct off-axis response prediction is studied in the literature, the coupling effect between rotor dynamic wake distortion and blade elastic motion need to be studied and their effect on helicopter response predictions need to be assessed.

5. It is recommended to study the effect of rotor dynamic wake distortion on the rotor inplane inflow perturbations and investigate their effect on helicopter response predictions during maneuvering near hover.

6. Further work needs to be carried out to fully understand the contributing factors to the wake curvature parameter K_{Re} in hover condition.

7. In this study, a limited set of correlations with flight test data of a UH-60 Black Hawk helicopter is considered. It is recommended to carry out additional correlations with available flight test data of different helicopters.

8. The motivation for this study is to develop a rotor inflow model that would be suitable for real-time simulation and control law development. Therefor, the next logical step would be to implement the current inflow model in a full helicopter simulation model to carry out pilot-in-the-loop simulation. Also, it is recommended to use the current wake distortion model in control law development.

APPENDIX A

DYNAMIC VORTEX TUBE MODEL

A.1 Dynamic Vortex Tube For a Pitching Rotor

Figure A.1 schematically shows the dynamic vortex tube definition for a helicopter rotor undergoing a step pitch rate q. The dynamic vortex tube is composed of two parts, one curved part (part I) and the other uncurved part (Part II). A typical point (P_0) on the curved wake tube (Part I) can be written as

$$x_0^I = \frac{\lambda}{\bar{q}}(1 - cos\alpha) + \frac{\mu}{\bar{q}}sin\alpha + \bar{r}_0 cos\psi_0 cos\alpha \tag{A.1.a}$$

$$y_0^I = \bar{r}_0 sin\psi_0 \tag{A.1.b}$$

$$z_0^I = \bar{r}_0 cos\psi_0 sin\alpha - \frac{\lambda}{\bar{q}}sin\alpha + \frac{\mu}{\bar{q}}(1 - cos\alpha) \tag{A.1.c}$$

and a typical point (P_0) on the uncurved wake tube (Part II) can be formulated as

$$
\begin{aligned}
x_0^{II} &= \frac{\lambda}{\bar{q}}(1 - cos\alpha_0) + \frac{\mu}{\bar{q}}sin\alpha_0 + \bar{r}_0 cos\psi_0 cos\alpha_0 \\
&\quad + \frac{\mu}{\bar{q}}tan(\alpha - \alpha_0) + \frac{\lambda}{\bar{q}}tan(\alpha - \alpha_0)sin\alpha_0
\end{aligned} \tag{A.2.a}
$$

$$y_0^{II} = \bar{r}_0 sin\psi_0 \tag{A.2.b}$$

$$z_0^{II} = \bar{r}_0 cos\psi_0 sin\alpha_0 - \frac{\lambda}{\bar{q}}sin\alpha_0 + \frac{\mu}{\bar{q}}(1 - cos\alpha_0) - \frac{\lambda}{\bar{q}}tan(\alpha - \alpha_0) \tag{A.2.c}$$

where μ is advance ratio, λ is the total mean inflow across the rotor disk, $\bar{r}_0$ is the vortex tube radius, ψ_0 is the azimuth angle on a cross section of vortex tube and α is the angle of a typical circular cross section of the vortex tube subtends to the rotor disk plane (as shown in Figure A.1), superscripts I and II denote contributions from the curved wake tube part and uncurved wake tube part, respectively.

Assuming a constant vorticity strength $\bar{\gamma}$ around the vortex tube, the vorticity distribution around the vortex tube can be written as

$$\vec{\gamma}_I = \vec{i}(\bar{\gamma}sin\psi_0 cos\alpha) - \vec{j}(\bar{\gamma}cos\psi_0) + \vec{k}(\bar{\gamma}sin\psi_0 sin\alpha) \tag{A.3}$$
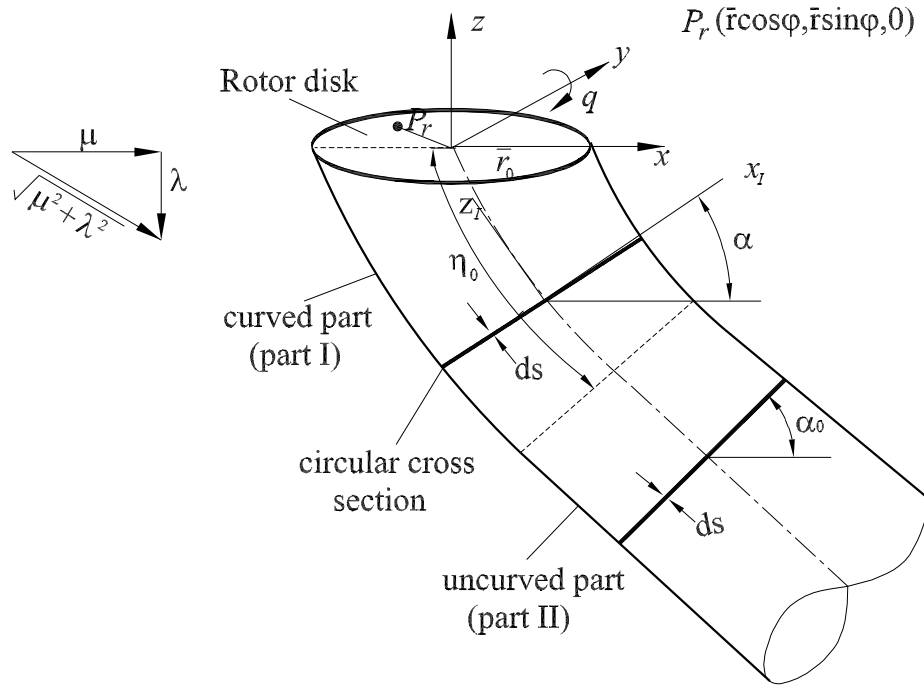
(a) Dynamic vortex tube for a pitching rotor
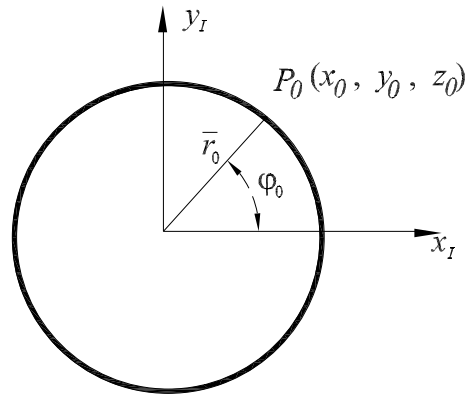
(b) A typical cross section of the vortex tube

Figure A.1: Dynamic vortex tube definition for a pitching rotor

for the curveud wake tube (Part I) and

$$\vec{\gamma}_{II} = \vec{i}(\bar{\gamma}sin\psi_0 cos\alpha_0) - \vec{j}(\bar{\gamma}cos\psi_0) + \vec{k}(\bar{\gamma}sin\psi_0 sin\alpha_0) \tag{A.4}$$

for the uncurved wake tube (Part II). where $(\vec{i}, \vec{j}, \vec{k})$ are unit vectors along the rotor disk coordinate system as shown in Figure A.1.

A typical point (P_r) on the rotor disk plane can be written as

$$x = \bar{r}cos\psi \tag{A.5.a}$$

$$y = \bar{r}sin\psi \tag{A.5.b}$$

$$z = 0 \tag{A.5.c}$$

where $\bar{r}$ is the radial position on the rotor disk and ψ is the azimuth angle on the rotor disk.

The induced velocity on point P_r by the whole dynamic vortex tube can be obtained using the Biot-Savart law as follows

$$\vec{\nu} = \frac{1}{4\pi} \int_0^{2\pi} \int_0^{\infty} \frac{\vec{\gamma} \times (\vec{P}_r - \vec{P}_0)}{|\vec{P}_r - \vec{P}_0|^3} dS = \vec{\nu}_I + \vec{\nu}_{II} \tag{A.6}$$

where $\vec{\nu}_I$ and $\vec{\nu}_{II}$ denote contributions from the curved wake tube part (part I) and the uncurved wake tube part (part II), respectively, and can be written as

$$\vec{\nu}_I = \frac{1}{4\pi} \int_0^{2\pi} \int_0^{\eta_0} \frac{\vec{\gamma}_I \times (\vec{P}_r - \vec{P}_0^I)}{|\vec{P} - \vec{P}_0^I|^3} dS \tag{A.7}$$

$$\vec{\nu}_{II} = \frac{1}{4\pi} \int_0^{2\pi} \int_{\eta_0}^{\infty} \frac{\vec{\gamma}_{II} \times (\vec{P}_r - \vec{P}_0^{II})}{|\vec{P} - \vec{P}_0^{II}|^3} dS \tag{A.8}$$

where

$$\vec{P}_r = \vec{i}x + \vec{j}y + \vec{k}z \tag{A.9.a}$$

$$\vec{P}_0^I = \vec{i}x_0^I + \vec{j}y_0^I + \vec{k}z_0^I \tag{A.9.b}$$

$$\vec{P}_0^{II} = \vec{i}x_0^{II} + \vec{j}y_0^{II} + \vec{k}z_0^{II} \tag{A.9.c}$$

After defining $\bar{r} = \hat{r}\bar{r}_0, \eta = \dfrac{\alpha\sqrt{\mu^2 + \lambda^2}}{\bar{q}} = \bar{\eta}\bar{r}_0, \bar{b} = \sqrt{1 + \hat{r}^2 - 2\hat{r}cos(\psi_0 - \psi)}$, for small $\bar{q}$ and μ, $\vec{\nu}_I$ and $\vec{\nu}_{II}$ can be obtained as

$$\vec{\nu}_I = \nu_{x_I}\vec{i} + \nu_{y_I}\vec{j} - \nu_{z_I}\vec{k} \tag{A.10}$$

$$\vec{\nu}_{II} = \nu_{x_{II}}\vec{i} + \nu_{y_{II}}\vec{j} - \nu_{z_{II}}\vec{k} \tag{A.11}$$

117

where

$$\nu_{x_I} = \frac{\bar{\gamma}}{4\pi} \int_0^{2\pi} \int_0^{\bar{\eta}_0} \frac{\left[\frac{\bar{\eta}\bar{q}\bar{r}_0}{\lambda}(1+\hat{r}sin\psi \sin\psi_0) - \bar{\eta}cos\psi_0 + \frac{\bar{\eta}^2\mu\bar{q}\bar{r}_0}{2\lambda^2}cos\psi_0\right] d\bar{\eta}\, d\psi_0}{\left[\bar{b}^2 + \bar{\eta}^2 - 2\frac{\mu\bar{\eta}}{\lambda}(\hat{r}cos\psi - cos\psi_0) - \frac{\bar{\eta}^2\bar{q}\bar{r}_0}{\lambda}(\hat{r}cos\psi + cos\psi_0)\right]^{3/2}} \quad (A.12.a)$$

$$\nu_{x_{II}} = \frac{\bar{\gamma}}{4\pi} \int_0^{2\pi} \int_{\bar{\eta}_0}^{\infty} \frac{\left[\frac{\bar{\eta}_0\bar{q}\bar{r}_0}{\lambda}(1+\hat{r}sin\psi \sin\psi_0) - \bar{\eta}cos\psi_0 + \frac{\bar{\eta}_0^2\mu\bar{q}\bar{r}_0}{2\lambda^2}cos\psi_0\right] d\bar{\eta}\, d\psi_0}{\left[\bar{b}^2 + \bar{\eta}^2 - 2\frac{\mu\bar{\eta}}{\lambda}(\hat{r}cos\psi - cos\psi_0) - \frac{\bar{\eta}_0^2\bar{q}\bar{r}_0}{\lambda}(\hat{r}cos\psi + cos\psi_0)\right]^{3/2}} \quad (A.12.b)$$

$$\nu_{y_I} = \frac{\bar{\gamma}}{4\pi} \int_0^{2\pi} \int_0^{\bar{\eta}_0} \frac{\left[\frac{\bar{\eta}\bar{q}\hat{r}\bar{r}_0}{\lambda}cos\psi \sin\psi_0 - \bar{\eta}sin\psi_0 - \frac{\bar{\eta}^2\mu\bar{q}\bar{r}_0}{2\lambda^2}sin\psi_0\right] d\bar{\eta}\, d\psi_0}{\left[\bar{b}^2 + \bar{\eta}^2 - 2\frac{\mu\bar{\eta}}{\lambda}(\hat{r}cos\psi - cos\psi_0) - \frac{\bar{\eta}^2\bar{q}\bar{r}_0}{\lambda}(\hat{r}cos\psi + cos\psi_0)\right]^{3/2}} \quad (A.12.c)$$

$$\nu_{y_{II}} = \frac{\bar{\gamma}}{4\pi} \int_0^{2\pi} \int_{\bar{\eta}_0}^{\infty} \frac{\left[\frac{\bar{\eta}_0\bar{q}\hat{r}\bar{r}_0}{\lambda}cos\psi \sin\psi_0 - \bar{\eta}sin\psi_0 - \frac{\bar{\eta}_0^2\mu\bar{q}\bar{r}_0}{2\lambda^2}sin\psi_0\right] d\bar{\eta}\, d\psi_0}{\left[\bar{b}^2 + \bar{\eta}^2 - 2\frac{\mu\bar{\eta}}{\lambda}(\hat{r}cos\psi - cos\psi_0) - \frac{\bar{\eta}_0^2\bar{q}\bar{r}_0}{\lambda}(\hat{r}cos\psi + cos\psi_0)\right]^{3/2}} \quad (A.12.d)$$

$$\nu_{z_I} = \frac{\bar{\gamma}}{4\pi} \int_0^{2\pi} \int_0^{\bar{\eta}_0} \frac{\left[1 - \hat{r}cos(\psi_0 - \psi) + \frac{\mu\bar{\eta}}{\lambda}cos\psi_0 + \frac{\bar{\eta}^2\bar{q}\bar{r}_0}{2\lambda}cos\psi_0\right] d\bar{\eta}\, d\psi_0}{\left[\bar{b}^2 + \bar{\eta}^2 - 2\frac{\mu\bar{\eta}}{\lambda}(\hat{r}cos\psi - cos\psi_0) - \frac{\bar{\eta}^2\bar{q}\bar{r}_0}{\lambda}(\hat{r}cos\psi + cos\psi_0)\right]^{3/2}} \quad (A.12.e)$$

$$\nu_{z_{II}} = \frac{\bar{\gamma}}{4\pi} \int_0^{2\pi} \int_{\bar{\eta}_0}^{\infty} \frac{\left[1 - \hat{r}cos(\psi_0 - \psi) + \frac{\mu\bar{\eta}}{\lambda}cos\psi_0 + \frac{\bar{\eta}_0^2\bar{q}\bar{r}_0}{2\lambda}cos\psi_0\right]}{\left[\bar{b}^2 + \bar{\eta}^2 - 2\frac{\mu\bar{\eta}}{\lambda}(\hat{r}cos\psi - cos\psi_0) - \frac{\bar{\eta}_0^2\bar{q}\bar{r}_0}{\lambda}(\hat{r}cos\psi + cos\psi_0)\right]^{3/2}} \quad (A.12.f)$$

where $\bar{\eta}_0$ is the length of the curved tube part (part I) along the tube axis.

A.2 Dynamic Vortex Tube For A Rolling Rotor

Figure A.2 schematically shows the dynamic vortex tube definition for a helicopter rotor undergoing a step roll rate p. The dynamic vortex tube is composed of two parts, one curved part (part I) and the other uncurved part (part II). A typical point (P_0) on the curved wake tube(Part I) can be written as

$$x_0^I = \bar{r}_0 cos\psi_0 + \frac{\mu}{\lambda}\alpha \tag{A.13.a}$$

$$y_0^I = \bar{r}_0 sin\psi_0 cos\alpha + \frac{\lambda}{\bar{p}}(1 - cos\alpha) \tag{A.13.b}$$

$$z_0^I = \bar{r}_0 sin\psi_0 sin\alpha - \frac{\lambda}{\bar{p}}sin\alpha \tag{A.13.c}$$

118

(a) Dynamic vortex tube for a rolling rotor
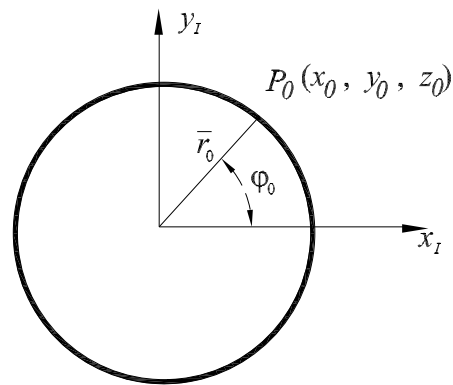
(b) A typical cross section of the vortex tube

Figure A.2: Dynamic vortex tube definition for a rolling rotor

and a typical point (P_0) on the uncurved wake tube (Part II) can be formulated as

$$x_0^{II} = \bar{r}_0 cos\psi_0 + \frac{\mu}{\lambda}\alpha \tag{A.14.a}$$

$$y_0^{II} = \bar{r}_0 sin\psi_0 cos\alpha_0 + \frac{\lambda}{\bar{p}}(1 - cos\alpha_0) + \frac{\lambda}{\bar{p}}tan(\alpha - \alpha_0)sin\alpha_0 \tag{A.14.b}$$

$$z_0^{II} = \bar{r}_0 sin\psi_0 sin\alpha_0 - \frac{\lambda}{\bar{p}}sin\alpha_0 - \frac{\lambda}{\bar{p}}tan(\alpha - \alpha_0)cos\alpha_0 \tag{A.14.c}$$

where superscripts I and II denote contributions from the curved wake tube part and uncurved wake tube part, respectively.

Assuming a constant vorticity strength $\bar{\gamma}$ around the vortex tube, the vorticity distribution around the tube can be written as

$$\vec{\gamma}_I = \vec{i}(\bar{\gamma}sin\psi_0) - \vec{j}(\bar{\gamma}cos\psi_0 cos\alpha) - \vec{k}(\bar{\gamma}cos\psi_0 sin\alpha) \tag{A.15}$$

for the curved tube part (part I) and

$$\vec{\gamma}_{II} = \vec{i}(\bar{\gamma}sin\psi_0) - \vec{j}(\bar{\gamma}cos\psi_0 cos\alpha_0) - \vec{k}(\bar{\gamma}cos\psi_0 sin\alpha_0) \tag{A.16}$$

for the uncurved wake tube part (part II). where $(\vec{i}, \vec{j}, \vec{k})$ are unit vectors along the rotor disk coordinate system as shown in Figure A.2.

A typical point on the rotor disk plane (P_r) is

$$x = \bar{r}cos\psi \tag{A.17.a}$$

$$y = \bar{r}sin\psi \tag{A.17.b}$$

$$z = 0 \tag{A.17.c}$$

where $\bar{r}$ is the radial position on the rotor disk and ψ is the azimuth angle on the rotor disk.

The induced velocity on point P_r by the whole dynamic vortex tube can be obtained using the Biot-Savart law as follows

$$\vec{\nu} = \frac{1}{4\pi} \int_0^{2\pi} \int_0^{\infty} \frac{\vec{\gamma} \times (\vec{P}_r - \vec{P}_0)}{|\vec{r} - \vec{r}_0|^3} dS = \vec{\nu}_I + \vec{\nu}_{II} \tag{A.18}$$

where $\vec{\nu}_I$ and $\vec{\nu}_{II}$ denote contributions from the curved wake tube part (part I) and the uncurved wake tube part (part II), respectively, and can be written as

$$\vec{\nu}_I = \frac{1}{4\pi} \int_0^{2\pi} \int_0^{\eta_0} \frac{\vec{\gamma}_I \times (\vec{P}_r - \vec{P}_0^I)}{|\vec{P} - \vec{P}_0^I|^3} dS \tag{A.19}$$

$$\vec{\nu}_{II} = \frac{1}{4\pi} \int_0^{2\pi} \int_{\eta_0}^{\infty} \frac{\vec{\gamma}_{II} \times (\vec{P}_r - \vec{P}_0^{II})}{|\vec{P} - \vec{P}_0^{II}|^3} \, dS \tag{A.20}$$

where

$$\vec{P}_r = \vec{i}x + \vec{j}y + \vec{k}z \tag{A.21.a}$$

$$\vec{P}_0^I = \vec{i}x_0^I + \vec{j}y_0^I + \vec{k}z_0^I \tag{A.21.b}$$

$$\vec{P}_0^{II} = \vec{i}x_0^{II} + \vec{j}y_0^{II} + \vec{k}z_0^{II} \tag{A.21.c}$$

After defining $\bar{r} = \hat{r}\bar{r}_0, \eta = \dfrac{\alpha\sqrt{\mu^2 + \lambda^2}}{\bar{p}} = \bar{\eta}\bar{r}_0, \bar{b} = \sqrt{1 + \hat{r}^2 - 2\hat{r}cos(\psi_0 - \psi)}$, for small $\bar{p}$ and μ, $\vec{\nu}_I$ and $\vec{\nu}_{II}$ can be obtained as

$$\vec{\nu}_I = \nu_{x_I}\bar{i} + \nu_{y_I}\bar{j} - \nu_{z_I}\bar{k} \tag{A.22}$$

$$\vec{\nu}_{II} = \nu_{x_{II}}\bar{i} + \nu_{y_{II}}\bar{j} - \nu_{z_{II}}\bar{k} \tag{A.23}$$

where

$$\nu_{x_I} = \frac{\bar{\gamma}}{4\pi} \int_0^{2\pi} \int_0^{\bar{\eta}_0} \frac{\left[\dfrac{\bar{\eta}\bar{p}\hat{r}\bar{r}_0}{\lambda}sin\psi cos\psi_0 - \eta cos\psi_0\right] d\bar{\eta}\,d\psi_0}{\left[\bar{b}^2 + \bar{\eta}^2 - 2\dfrac{\mu\bar{\eta}}{\lambda}(\hat{r}cos\psi - cos\psi_0) - \dfrac{\bar{\eta}^2\bar{p}\bar{r}_0}{\lambda}(\hat{r}sin\psi + sin\psi_0)\right]^{3/2}} \tag{A.24.a}$$

$$\nu_{x_{II}} = \frac{\bar{\gamma}}{4\pi} \int_0^{2\pi} \int_{\bar{\eta}_0}^{\infty} \frac{\left[\dfrac{\bar{\eta}_0\bar{p}\hat{r}\bar{r}_0}{\lambda}sin\psi cos\psi_0 - \eta cos\psi_0\right] d\bar{\eta}\,d\psi_0}{\left[\bar{b}^2 + \bar{\eta}^2 - 2\dfrac{\mu\bar{\eta}}{\lambda}(\hat{r}cos\psi - cos\psi_0) - \dfrac{\bar{\eta}^2\bar{p}\bar{r}_0}{\lambda}(\hat{r}sin\psi + sin\psi_0)\right]^{3/2}} \tag{A.24.b}$$

$$\nu_{y_I} = \frac{\bar{\gamma}}{4\pi} \int_0^{2\pi} \int_0^{\bar{\eta}_0} \frac{\left[\dfrac{\bar{\eta}\bar{p}\bar{r}_0}{\lambda_0} - \dfrac{\bar{\eta}\bar{p}\bar{r}_0}{\lambda}\hat{r}cos\psi cos\psi_0 - \bar{\eta}sin\psi_0 + \dfrac{\mu\bar{\eta}^2\bar{p}\bar{r}_0}{\lambda^2}cos\psi_0\right] d\bar{\eta}\,d\psi_0}{\left[\bar{b}^2 + \bar{\eta}^2 - 2\dfrac{\mu\bar{\eta}}{\lambda}(\hat{r}cos\psi - cos\psi_0) - \dfrac{\bar{\eta}^2\bar{p}\bar{r}_0}{\lambda}(\hat{r}sin\psi + sin\psi_0)\right]^{3/2}} \tag{A.24.c}$$

$$\nu_{y_{II}} = \frac{\bar{\gamma}}{4\pi} \int_0^{2\pi} \int_{\bar{\eta}_0}^{\infty} \frac{\left[\dfrac{\bar{\eta}_0\bar{p}\bar{r}_0}{\lambda} - \dfrac{\bar{\eta}_0\bar{p}\bar{r}_0}{\lambda}\hat{r}cos\psi cos\psi_0 - \bar{\eta}sin\psi_0 + \dfrac{\mu\bar{\eta}_0^2\bar{p}\bar{r}_0}{\lambda^2}cos\psi_0\right] d\bar{\eta}\,d\psi_0}{\left[\bar{b}^2 + \bar{\eta}^2 - 2\dfrac{\mu\bar{\eta}}{\lambda}(\hat{r}cos\psi - cos\psi_0) - \dfrac{\bar{\eta}^2\bar{p}\bar{r}_0}{\lambda}(\hat{r}sin\psi + sin\psi_0)\right]^{3/2}} \tag{A.24.d}$$

$$\nu_{z_I} = \frac{\bar{\gamma}}{4\pi} \int_0^{2\pi} \int_0^{\bar{\eta}_0} \frac{\left[1 - \hat{r}cos(\psi_0 - \psi) + \dfrac{\mu\bar{\eta}}{\lambda_0}cos\psi_0 + \dfrac{\bar{\eta}^2\bar{p}\bar{r}_0}{2\lambda}sin\psi_0\right] d\bar{\eta}\,d\psi_0}{\left[\bar{b}^2 + \bar{\eta}^2 - 2\dfrac{\mu\bar{\eta}}{\lambda}(\hat{r}cos\psi - cos\psi_0) - \dfrac{\bar{\eta}^2\bar{p}\bar{r}_0}{\lambda}(\hat{r}sin\psi + sin\psi_0)\right]^{3/2}} \tag{A.24.e}$$

$$\nu_{z_{II}} = \frac{\bar{\gamma}}{4\pi} \int_0^{2\pi} \int_{\bar{\eta}_0}^{\infty} \frac{\left[1 - \hat{r}cos(\psi_0 - \psi) + \dfrac{\mu\bar{\eta}}{\lambda}cos\psi_0 + \dfrac{\bar{\eta}_0^2\bar{p}\bar{r}_0}{2\lambda}sin\psi_0\right]}{\left[\bar{b}^2 + \bar{\eta}^2 - 2\dfrac{\mu\bar{\eta}}{\lambda}(\hat{r}cos\psi - cos\psi_0) - \dfrac{\bar{\eta}^2\bar{p}\bar{r}_0}{\lambda}(\hat{r}sin\psi + sin\psi_0)\right]^{3/2}} \tag{A.24.f}$$

A.3 Dynamic Vortex Tube For A Rotor Undergoing A Step Change In Advance Ratio
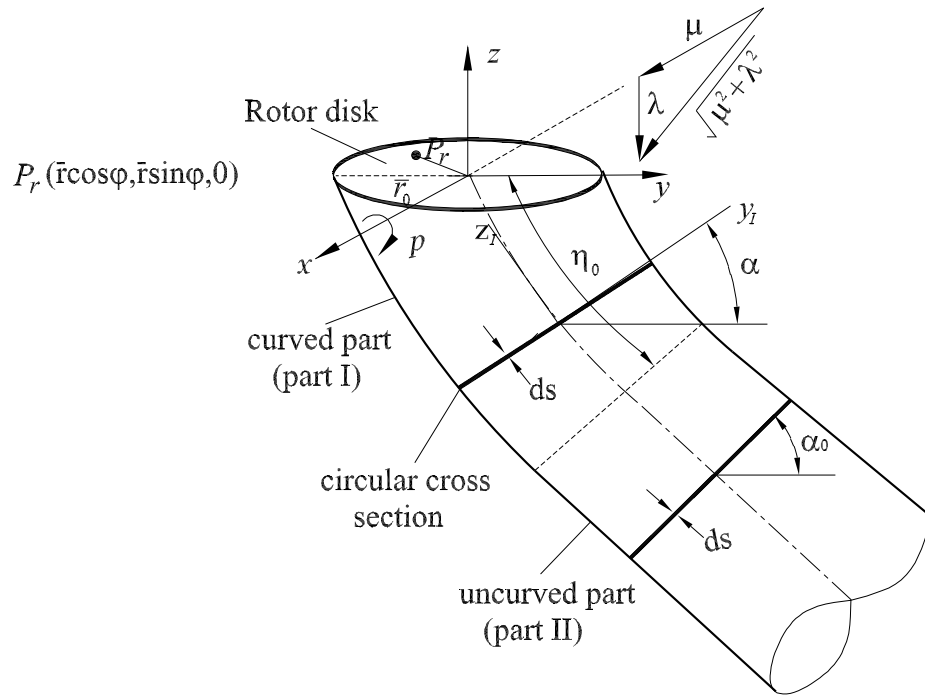
Figure A.3 schematically shows the dynamic vortex tube definition for a helicopter rotor undergoing a step change in advance ratio ($\Delta\mu$). The dynamic vortex tube is composed of two parts, i.e., part I and part II as shown in Figure A.3. Part I has a skew angle of $\chi + \Delta\chi$ corresponding to an advance ratio of $\mu + \Delta\mu$ and part II has a skew angle of χ corresponding to an advance ratio of μ. A typical point (P_0) on part I of the vortex tube can be written as

$$x_0^I = \bar{r}_0 cos\psi_0 + \eta sin(\chi + \Delta\chi) \tag{A.25.a}$$

$$y_0^I = \bar{r}_0 sin\psi_0 \tag{A.25.b}$$

$$z_0^I = -\eta cos(\chi + \Delta\chi) \tag{A.25.c}$$

and a typical point (P_0) on part II of the vortex tube can be written as

$$x_0^{II} = \bar{r}_0 cos\psi_0 + \eta_0 sin(\chi + \Delta\chi) + (\eta - \eta_0)sin\chi \tag{A.26.a}$$

$$y_0^{II} = \bar{r}_0 sin\psi_0 \tag{A.26.b}$$

$$z_0^{II} = -\eta_0 cos(\chi + \Delta\chi) - (\eta - \eta_0)cos\chi \tag{A.26.c}$$

where η is distance along the vortex tube axis and η_0 is the length of part I along the vortex tube axis.

Assuming a constant vorticity strength $\bar{\gamma}$ around the vortex tube, the vorticity distribution around the vortex tube can be written as

$$\vec{\gamma} = \vec{\gamma}_I = \vec{\gamma}_{II} = \vec{i}(\bar{\gamma}sin\psi_0) - \vec{j}(\bar{\gamma}cos\psi_0) \tag{A.27}$$

A typical point (P_r) on the rotor disk plane can be written as

$$x = \bar{r}cos\psi \tag{A.28.a}$$

$$y = \bar{r}sin\psi \tag{A.28.b}$$

$$z = 0 \tag{A.28.c}$$

(a) Dynamic vortex tube for a rotor
undergoing a step advance ratio

(b) A typical cross section of the vortex tube

Figure A.3: Dynamic vortex tube definition for a rotor undergoing a step change of advance ratio

The induced velocity on point P_r by the whole dynamic vortex tube can be obtained using the Biot-Savart law as follows

$$\vec{\nu} = \frac{1}{4\pi} \int_0^{2\pi} \int_0^{\infty} \frac{\vec{\gamma} \times (\vec{P}_r - \vec{P}_0)}{|\vec{r} - \vec{r}_0|^3} dS = \vec{\nu}_I + \vec{\nu}_{II} \tag{A.29}$$

where $\vec{\nu}_I$ and $\vec{\nu}_{II}$ denote contributions from the tube part I and tube part II, respectively, and can be written as

$$\vec{\nu}_I = \frac{1}{4\pi} \int_0^{2\pi} \int_0^{\eta_0} \frac{\vec{\gamma}_I \times (\vec{P}_r - \vec{P}_0^I)}{|\vec{P} - \vec{P}_0^I|^3} dS \tag{A.30}$$

$$\vec{\nu}_{II} = \frac{1}{4\pi} \int_0^{2\pi} \int_{\eta_0}^{\infty} \frac{\vec{\gamma}_{II} \times (\vec{P}_r - \vec{P}_0^{II})}{|\vec{P} - \vec{P}_0^{II}|^3} dS \tag{A.31}$$

where

$$\vec{P}_r = \vec{i}x + \vec{j}y + \vec{k}z \tag{A.32.a}$$

$$\vec{P}_0^I = \vec{i}x_0^I + \vec{j}y_0^I + \vec{k}z_0^I \tag{A.32.b}$$

$$\vec{P}_0^{II} = \vec{i}x_0^{II} + \vec{j}y_0^{II} + \vec{k}z_0^{II} \tag{A.32.c}$$

The induced velocity (positive along negative z axis) can be obtained as

$$\nu_z = -\vec{\nu} \cdot \vec{k} = \nu_{z_I} + \nu_{z_{II}} \tag{A.33}$$

where

$$\nu_{z_I} = \frac{\bar{\gamma}}{4\pi} \int_0^{2\pi} \int_0^{\bar{\eta}_0} \frac{[1 - \hat{r}cos\psi_0 + \bar{\eta}sin(\chi + \Delta\chi)cos\psi_0] \, d\bar{\eta} \, d\psi_0}{[\bar{b}^2 + \bar{\eta}^2 - 2\bar{\eta}sin(\chi + \Delta\chi)(\hat{r} - cos\psi_0)]^{3/2}} \tag{A.34.a}$$

$$\nu_{z_{II}} = \frac{\bar{\gamma}}{4\pi} \int_0^{2\pi} \int_{\bar{\eta}_0}^{\infty} \frac{[1 - \hat{r}cos\psi_0 + \bar{\eta}_0 sin(\chi + \Delta\chi) + (\bar{\eta} - \bar{\eta}_0)sin\chi cos\psi_0] \, d\bar{\eta} \, d\psi_0}{[\bar{b}^2 + \bar{\eta}^2 - 2\bar{\eta}_0 sin(\chi + \Delta\chi)(\hat{r} - cos\psi_0) - 2(\bar{\eta} - \bar{\eta}_0)sin\chi(\hat{r} - cos\psi_0)]^{3/2}} \tag{A.34.b}$$

where $\bar{b} = \sqrt{1 + \hat{r}^2 - 2\hat{r}cos\psi_0}$, $\hat{r} = \bar{r}/\bar{r}_0$, $\bar{\eta} = \eta/\bar{r}_0$.

A.4 Dynamic Vortex Tube For A Rotor Undergoing A Step Change in Climb Rate

Figure A.4 schematically shows the dynamic vortex tube definition for a helicopter rotor undergoing a step climb rate (V_c). The dynamic vortex tube is composed of two parts, i.e., part I and part II as shown in Figure A.4. Part I has a higher wake spacing and part II has

(a) Dynamic vortex tube for a rotor
undergoing a step climb rate

(b) A typical cross section of the vortex tube
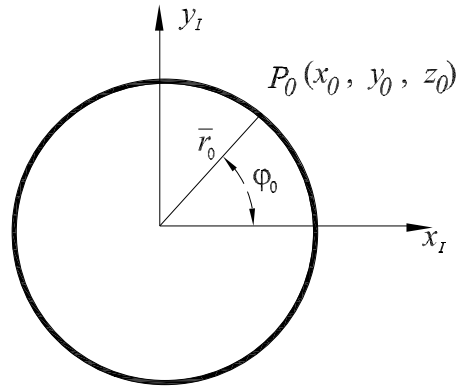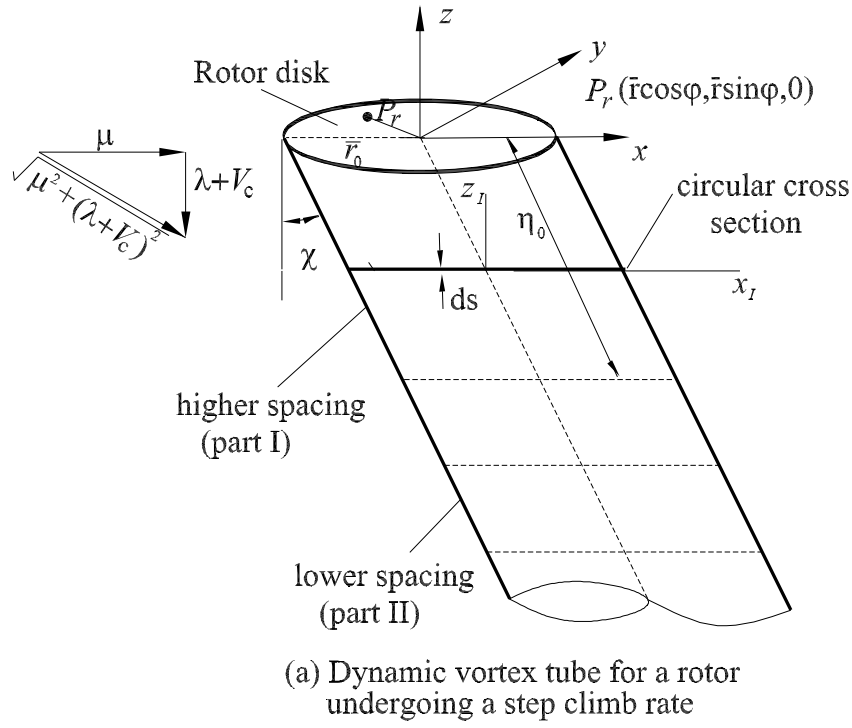
Figure A.4: Dynamic vortex tube definition for a rotor undergoing a step change of advance ratio

a lower wake spacing. A typical point (P_0) on the vortex tube (for both part I and part II) can be written as

$$x_0 = \bar{r}_0 cos\psi_0 + \eta sin\chi \qquad \text{(A.35.a)}$$

$$y_0 = \bar{r}_0 sin\psi_0 \qquad \text{(A.35.b)}$$

$$z_0 = -\eta cos\chi \qquad \text{(A.35.c)}$$

The vorticity on the vortex tube can be written as

$$\vec{\gamma}_I = \vec{i}(\bar{\gamma}_I sin\psi_0) - \vec{j}(\bar{\gamma}_I cos\psi_0) \qquad \text{(A.36)}$$

for tube part I and

$$\vec{\gamma}_{II} = \vec{i}(\bar{\gamma}_{II} sin\psi_0) - \vec{j}(\bar{\gamma}_{II} cos\psi_0) \qquad \text{(A.37)}$$

for tube part II. Where $\bar{\gamma}_I$ and $\bar{\gamma}_{II}$, respectively, denote vorticity strengths along tube part I (with higher wake spacing) and tube part II (with lower wake spacing), respectively.

A typical point (P_r) on the rotor disk plane can be written as

$$x = \bar{r}cos\psi \qquad \text{(A.38.a)}$$

$$y = \bar{r}sin\psi \qquad \text{(A.38.b)}$$

$$z = 0 \qquad \text{(A.38.c)}$$

The induced velocity on point P_r by the whole dynamic vortex tube can be obtained using the Biot-Savart law as follows

$$\vec{v} = \frac{1}{4\pi} \int_0^{2\pi} \int_0^\infty \frac{\vec{\gamma} \times (\vec{P}_r - \vec{P}_0)}{|\vec{r} - \vec{r}_0|^3} dS = \vec{v}_I + \vec{v}_{II} \qquad \text{(A.39)}$$

where $\vec{v}_I$ and $\vec{v}_{II}$ denote contributions from the tube part I and tube part II, respectively, and can be written as

$$\vec{v}_I = \frac{1}{4\pi} \int_0^{2\pi} \int_0^{\eta_0} \frac{\vec{\gamma}_I \times (\vec{P}_r - \vec{P}_0)}{|\vec{P} - \vec{P}_0^I|^3} dS \qquad \text{(A.40)}$$

$$\vec{v}_{II} = \frac{1}{4\pi} \int_0^{2\pi} \int_{\eta_0}^\infty \frac{\vec{\gamma}_{II} \times (\vec{P}_r - \vec{P}_0)}{|\vec{P} - \vec{P}_0^{II}|^3} dS \qquad \text{(A.41)}$$

where

$$\vec{P}_r = \vec{i}x + \vec{j}y + \vec{k}z \qquad \text{(A.42.a)}$$

$$\vec{P}_0 = \vec{i}x_0 + \vec{j}y_0 + \vec{k}z_0 \qquad \text{(A.42.b)}$$

The induced velocity (positive along negative z axis) can be obtained as

$$\nu_z = -\vec{\nu} \cdot \vec{k} = \nu_{z_I} + \nu_{z_{II}} \tag{A.43}$$

where

$$\nu_{z_I} = \frac{\bar{\gamma}_I}{4\pi} \int_0^{2\pi} \int_0^{\bar{\eta}_0} \frac{[1 - \hat{r}cos\psi_0 + \bar{\eta}sin\chi cos\psi_0] \, d\bar{\eta} \, d\psi_0}{[1 + \hat{r}^2 - 2\hat{r}cos\psi_0 + \bar{\eta}^2 - 2\bar{\eta}sin\chi(\hat{r} - cos\psi_0)]^{3/2}} \tag{A.44.a}$$

$$\nu_{z_I} = \frac{\bar{\gamma}_{II}}{4\pi} \int_0^{2\pi} \int_{\bar{\eta}_0}^{\infty} \frac{[1 - \hat{r}cos\psi_0 + \bar{\eta}sin\chi cos\psi_0] \, d\bar{\eta} \, d\psi_0}{[1 + \hat{r}^2 - 2\hat{r}cos\psi_0 + \bar{\eta}^2 - 2\bar{\eta}sin\chi(\hat{r} - cos\psi_0)]^{3/2}} \tag{A.44.b}$$

where $\bar{b} = \sqrt{1 + \hat{r}^2 - 2\hat{r}cos\psi_0}$, $\hat{r} = \bar{r}/\bar{r}_0$, $\bar{\eta} = \eta/\bar{r}_0$.

APPENDIX B

ROTOR INFLOW PERTURBATIONS DURING MANEUVERING FLIGHT

B.1 Inflow Perturbations Due To Mean Loading Effect

B.1.1 Rotor In Pitching Motion

The normal inflow distribution across the rotor disk of a pitching rotor induced by a single dynamic vortex tube with tube radius $\bar{r}_0$ and mean loading $\bar{\gamma}_0$ is developed in Appendix A (Equations A.12.e and A.12.f). When the wake shape is fully developed, i.e., $\bar{\eta}_0 = \infty$ in Equations A.12.e and A.12.f, the normal inflow distribution across the rotor disk can be written as

$$v_z(\bar{r}, \psi) = \frac{\bar{\gamma}_0}{4\pi} \int_0^{2\pi} \int_0^\infty K\left(\frac{\mu}{\lambda}, \frac{\bar{q}}{\lambda}\right) d\bar{\eta} \, d\psi_0 \tag{B.1}$$

where function $K(\cdot, \cdot)$ is given by,

$$K\left(\frac{\mu}{\lambda}, \frac{\bar{q}}{\lambda}\right) = \frac{\left(1 - \hat{r}\cos(\psi_0 - \psi) + \frac{\bar{q}\bar{r}_0}{2\lambda}\bar{\eta}^2\cos\psi_0 + \frac{\mu}{\lambda}\bar{\eta}\cos\psi_0\right)}{\Delta^{3/2}} \tag{B.2}$$

$$\hat{r} = \bar{r}/\bar{r}_0 \tag{B.3}$$

with,

$$\Delta = 1 + \hat{r}^2 - 2\hat{r}\cos(\psi_0 - \psi) + \bar{\eta}^2 - 2\frac{\mu}{\lambda}\bar{\eta}(\hat{r}\cos\psi - \cos\psi_0) - \frac{\bar{q}\bar{r}_0}{\lambda}\bar{\eta}^2(\cos\psi_0 + \hat{r}\cos\psi) \tag{B.4}$$

Expanding function $K(\cdot, \cdot)$ (Equation B.2) into Taylor series about $\frac{\mu}{\lambda}$ and $\frac{\bar{q}}{\lambda}$ and neglecting high order terms gives rise to

$$K\left(\frac{\mu}{\lambda}, \frac{\bar{q}}{\lambda}\right) = K(0,0) + K_1(0,0)\frac{\mu}{\lambda} + K_2(0,0)\frac{\bar{q}}{\lambda} + K_{12}(0,0)\frac{\mu\bar{q}}{\lambda^2} + K_{112}(0,0)\frac{\mu^2\bar{q}}{2\lambda^3} \tag{B.5}$$

where subscripts 1 and 2 denote differentiation with respect to the first and the second variables in function $K(\cdot,\cdot)$, respectively. These derivatives can be formulated as

$$K(0,0) = \frac{(1-\hat{r}cos(\psi_0-\psi))}{[1+\hat{r}^2-2\hat{r}cos(\psi_0-\psi)+\bar{\eta}^2]^{3/2}} \tag{B.6.a}$$

$$K_1(0,0) = \frac{\bar{\eta}cos\psi_0}{[1+\hat{r}^2-2\hat{r}cos(\psi_0-\psi)+\bar{\eta}^2]^{3/2}}$$
$$+\frac{3\bar{\eta}[1-\hat{r}cos(\psi_0-\psi)](\hat{r}cos\psi-cos\psi_0)}{[1+\hat{r}^2-2\hat{r}cos(\psi_0-\psi)+\bar{\eta}^2]^{5/2}} \tag{B.6.b}$$

$$K_2(0,0) = \frac{\bar{r}_0\bar{\eta}^2cos\psi_0}{2[1+\hat{r}^2-2\hat{r}cos(\psi_0-\psi)+\bar{\eta}^2]^{3/2}}$$
$$+\frac{3\bar{r}_0\bar{\eta}^2[1-\hat{r}cos(\psi_0-\psi)](\hat{r}cos\psi+cos\psi_0)}{2[1+\hat{r}^2-2\hat{r}cos(\psi_0-\psi)+\bar{\eta}^2]^{5/2}} \tag{B.6.c}$$

$$K_{12}(0,0) = \frac{3\bar{r}_0\hat{r}\bar{\eta}^3cos\psi cos\psi_0}{[1+\hat{r}^2-2\hat{r}cos(\psi_0-\psi)+\bar{\eta}^2]^{5/2}}$$
$$+\frac{15\bar{r}_0\bar{\eta}^3[1-\bar{r}cos(\psi_0-\psi)](\hat{r}cos\psi-cos\psi_0)(\hat{r}cos\psi+cos\psi_0)}{2[1+\hat{r}^2-2\hat{r}cos(\psi_0-\psi)+\bar{\eta}^2]^{7/2}} \tag{B.6.d}$$

$$K_{112}(0,0) = \frac{15\bar{r}_0\bar{\eta}^4cos\psi_0(\hat{r}cos\psi-cos\psi_0)(\hat{r}cos\psi+cos\psi_0)}{[1+\hat{r}^2-2\hat{r}cos(\psi_0-\psi)+\bar{\eta}^2]^{7/2}}$$
$$+\frac{15\bar{r}_0\bar{\eta}^4cos\psi_0(\hat{r}cos\psi-cos\psi_0)^2}{2[1+\hat{r}^2-2\hat{r}cos(\psi_0-\psi)+\bar{\eta}^2]^{7/2}}$$
$$+\frac{105\bar{r}_0\bar{\eta}^4(1-\hat{r}cos(\psi_0-\psi))(\hat{r}cos\psi-cos\psi_0)^2(\hat{r}cos\psi+cos\psi_0)}{2[1+\hat{r}^2-2\hat{r}cos(\psi_0-\psi)+\bar{\eta}^2]^{9/2}} \tag{B.6.e}$$

Therefore, the inflow perturbation across the rotor disk induced by a single vortex tube during a pitch motion of the rotor can be obtained as

$$\Delta v_z(\bar{r},\psi) = \frac{\bar{\gamma}_0}{4\pi}\int_0^{2\pi}\int_0^\infty \left[K_2(0,0)\frac{\bar{q}}{\lambda} + K_{12}(0,0)\frac{\mu\bar{q}}{\lambda^2} + K_{112}(0,0)\frac{\mu^2\bar{q}}{2\lambda^3}\right]d\bar{\eta}\,d\psi_0 \tag{B.7}$$

Defining the longitudinal wake curvature for a pitching rotor as

$$\kappa_c = \frac{\bar{q}}{\lambda} \tag{B.8}$$

For small advance ratio μ, The following approximations can be made

$$\frac{\mu}{\lambda_0} = 2X \tag{B.9}$$

Substituting expressions for the partial derivatives given by Equations B.6.c, B.6.d and B.6.e

into Equation B.7 and carrying out integrations gives rise to

$$\Delta v_z(\bar{r}, \psi) =$$

$$\begin{cases} \dfrac{\bar{\gamma}_0}{2}\kappa_c X\bar{r}_0 e_1(\hat{r}) + \dfrac{\bar{\gamma}_0}{2}\kappa_c \bar{r}\left(1 - \dfrac{3}{2}X^2\right)cos\psi + \dfrac{\bar{\gamma}_0}{2}\kappa_c X\bar{r}_0 e_2(\hat{r})cos2\psi & \hat{r} < 1 \\[4mm] \dfrac{\bar{\gamma}_0}{2}\kappa_c X\bar{r}_0 e_3(\hat{r}) + \dfrac{3\bar{\gamma}_0}{4}\kappa_c X^2\bar{r}_0 e_5(\hat{r})cos\psi + \dfrac{\bar{\gamma}_0}{2}\kappa_c X\bar{r}_0 e_4(\hat{r})cos2\psi \\[4mm] + \dfrac{3\bar{\gamma}_0}{4}\kappa_c X^2\bar{r}_0 e_6(\hat{r})cos3\psi & \hat{r} > 1 \end{cases}$$

$$(B.10)$$

where,

$$e_1(\hat{r}) = \frac{3(\hat{r}-1)^2 E(k) - (3\hat{r}^2+1)F(k)}{\hat{r}-1} \tag{B.11.a}$$

$$e_2(\hat{r}) = \frac{(\hat{r}-1)^2(2+5\hat{r}^2)E(k) - (2+5\hat{r}^2+5\hat{r}^4)F(k)}{3\hat{r}^2(\hat{r}-1)} \tag{B.11.b}$$

$$e_3(\hat{r}) = \frac{-3(\hat{r}-1)^2 E(k) + (3\hat{r}^2+1)F(k)}{\hat{r}-1} \tag{B.11.c}$$

$$e_4(\hat{r}) = \frac{(-\hat{r}-1)^2(2+5\hat{r}^2)E(k) + (2+5\hat{r}^2+5\hat{r}^4)F(k)}{3\hat{r}^2(\hat{r}-1)} \tag{B.11.d}$$

$$e_5(\hat{r}) = \frac{1}{\hat{r}} \tag{B.11.e}$$

$$e_6(\hat{r}) = \frac{\hat{r}^2+1}{\hat{r}^3} \tag{B.11.f}$$

$$E(k) = \int_0^{\frac{\pi}{2}} \sqrt{1 - ksin^2\theta}\, d\theta \tag{B.11.g}$$

$$F(k) = \int_0^{\frac{\pi}{2}} \frac{1}{\sqrt{1 - ksin^2\theta}}\, d\theta \tag{B.11.h}$$

$$k(\hat{r}) = \frac{-4\hat{r}}{(\hat{r}-1)^2} \tag{B.11.i}$$

B.1.2 Rotor In Rolling Motion

The normal inflow distribution across the rotor disk of a rolling rotor induced by a single dynamic vortex tube with tube radius $\bar{r}_0$ and mean loading $\bar{\gamma}_0$ is developed in Appendix A (Equations A.24.e and A.24.f). When the wake shape is fully developed, i.e., $\bar{\eta}_0 = \infty$ in Equations A.24.e and A.24.f, the normal inflow distribution across the rotor disk can be written as

$$v_z(\bar{r}, \psi) = \frac{\bar{\gamma}_0}{4\pi} \int_0^{2\pi} \int_0^\infty K\left(\frac{\mu}{\lambda}, \frac{\bar{p}}{\lambda}\right) d\bar{\eta}\, d\psi_0 \tag{B.12}$$

where funciton $K(\cdot, \cdot)$ is given by,

$$K\left(\frac{\mu}{\lambda}, \frac{\bar{p}}{\lambda}\right) = \frac{\left(1 - \hat{r}cos(\psi_0 - \psi) + \dfrac{\bar{p}\bar{r}_0}{2\lambda}\bar{\eta}^2 sin\psi_0 + \dfrac{\mu}{\lambda}\bar{\eta}cos\psi_0\right)}{\Delta^{3/2}} \tag{B.13}$$

130

with,

$$\Delta = 1 + \hat{r}^2 - 2\hat{r}cos(\psi_0 - \psi) + \bar{\eta}^2 - 2\frac{\mu}{\lambda}\bar{\eta}(\hat{r}cos\psi - cos\psi_0) - \frac{\bar{p}\bar{r}_0}{\lambda}\bar{\eta}^2(sin\psi_0 + \hat{r}sin\psi) \quad \text{(B.14)}$$

Expanding function $K(\cdot, \cdot)$ (Equation B.13) into Taylor series about $\frac{\mu}{\lambda}$ and $\frac{\bar{p}}{\lambda}$ and neglecting high order terms gives rise to

$$K\left(\frac{\mu}{\lambda}, \frac{\bar{p}}{\lambda}\right) = K(0,0) + K_1(0,0)\frac{\mu}{\lambda} + K_2(0,0)\frac{\bar{p}}{\lambda} + K_{12}(0,0)\frac{\mu\bar{p}}{\lambda^2} + K_{112}(0,0)\frac{\mu^2\bar{p}}{2\lambda^3} \quad \text{(B.15)}$$

where subscripts 1 and 2 denote differentiation with respect to the first and second variables in function $K(\cdot, \cdot)$, respectively. These derivatives can be formulated as,

$$K(0,0) = \frac{(1 - \hat{r}cos(\psi_0 - \psi))}{[1 + \hat{r}^2 - 2\hat{r}cos(\psi_0 - \psi) + \bar{\eta}^2]^{3/2}} \quad \text{(B.16.a)}$$

$$K_1(0,0) = \frac{\bar{\eta}cos\psi_0}{[1 + \hat{r}^2 - 2\hat{r}cos(\psi_0 - \psi) + \bar{\eta}^2]^{3/2}}$$
$$+ \frac{3\bar{\eta}[1 - \hat{r}cos(\psi_0 - \psi)](\hat{r}cos\psi - cos\psi_0)}{[1 + \hat{r}^2 - 2\hat{r}cos(\psi_0 - \psi) + \bar{\eta}^2]^{5/2}} \quad \text{(B.16.b)}$$

$$K_2(0,0) = \frac{\bar{r}_0\bar{\eta}^2 sin\psi_0}{2[1 + \hat{r}^2 - 2\hat{r}cos(\psi_0 - \psi) + \bar{\eta}^2]^{3/2}}$$
$$+ \frac{3\bar{r}_0\bar{\eta}^2[1 - \hat{r}cos(\psi_0 - \psi)](\hat{r}sin\psi + sin\psi_0)}{2[1 + \hat{r}^2 - 2\hat{r}cos(\psi_0 - \psi) + \bar{\eta}^2]^{5/2}} \quad \text{(B.16.c)}$$

$$K_{12}(0,0) = \frac{3\bar{r}_0\hat{r}\bar{\eta}^3 sin(\psi_0 + \psi)}{2[1 + \hat{r}^2 - 2\hat{r}cos(\psi_0 - \psi) + \bar{\eta}^2]^{5/2}}$$
$$+ \frac{15\bar{r}_0\bar{\eta}^3[1 - \bar{r}cos(\psi_0 - \psi)](\hat{r}cos\psi - cos\psi_0)(\hat{r}sin\psi + sin\psi_0)}{2[1 + \hat{r}^2 - 2\hat{r}cos(\psi_0 - \psi) + \bar{\eta}^2]^{7/2}} \quad \text{(B.16.d)}$$

$$K_{112}(0,0) = \frac{15\bar{r}_0\bar{\eta}^4 cos(\psi_0)(\hat{r}cos\psi - cos\psi_0)(\hat{r}sin\psi + sin\psi_0)}{[1 + \hat{r}^2 - 2\hat{r}cos(\psi_0 - \psi) + \bar{\eta}^2]^{7/2}}$$
$$+ \frac{15\bar{r}_0\bar{\eta}^4 sin\psi_0(\hat{r}cos\psi - cos\psi_0)^2}{2[1 + \hat{r}^2 - 2\hat{r}cos(\psi_0 - \psi) + \bar{\eta}^2]^{7/2}}$$
$$+ \frac{105\bar{r}_0\eta^4(1 - \hat{r}cos(\psi_0 - \psi))(\hat{r}cos\psi - cos\psi_0)^2(\hat{r}sin\psi + sin\psi_0)}{2[1 + \hat{r}^2 - 2\hat{r}cos(\psi_0 - \psi) + \bar{\eta}^2]^{9/2}} \quad \text{(B.16.e)}$$

Therefore, the inflow perturbation across the rotor disk induced by a single vortex tube during a roll motion of the rotor can be obtained as

$$\Delta v_z(\bar{r}, \psi) = \frac{\bar{\gamma}_0}{4\pi} \int_0^{2\pi} \int_0^\infty \left[K_2(0,0)\frac{\bar{p}}{\lambda} + K_{12}(0,0)\frac{\mu\bar{p}}{\lambda^2} + K_{112}(0,0)\frac{\mu^2\bar{p}}{2\lambda^3}\right] d\bar{\eta}\, d\psi_0 \quad \text{(B.17)}$$

Defining the lateral wake curvature for a rolling rotor as

$$\kappa_s = \frac{\bar{p}}{\lambda} \quad \text{(B.18)}$$

131

Substituting expressions for the partial derivatives given by Equations B.16.c, B.16.d and B.16.e into Equation B.17 and carrying out integrations gives rise to

$$
\Delta v_z(\bar{r}, \psi) =
\begin{cases}
\dfrac{\bar{\gamma}_0}{2}\kappa_s\bar{r}\left(1 + \dfrac{3}{2}X^2\right)sin\psi + \dfrac{\bar{\gamma}_0}{2}\kappa_s X\bar{r}_0 e_2(\hat{r})sin2\psi & \hat{r} < 1 \\
\\
-\dfrac{3\bar{\gamma}_0}{4}\kappa_s X^2\bar{r}_0 e_5(\hat{r})sin\psi + \dfrac{\bar{\gamma}_0}{2}\kappa_s X\bar{r}_0 e_4(\hat{r})sin2\psi & \\
+\dfrac{3\bar{\gamma}_0}{4}\kappa_s X^2\bar{r}_0 e_6(\hat{r})sin3\psi & \hat{r} > 1
\end{cases}
\tag{B.19}
$$

Combining Equations B.10 and B.19 gives rise to the inflow perturbations across the rotor disk induced by a single distorted vortex tube due to rotor mean loading effect during a steady pitch and/or roll motion as follows

$$
\Delta v_z(\bar{r}, \psi) =
\begin{cases}
\dfrac{\bar{\gamma}_0}{2}\kappa_c X\bar{r}_0 e_1(\hat{r}) + \dfrac{\bar{\gamma}_0}{2}\kappa_c\bar{r}\left(1 - \dfrac{3}{2}X^2\right)cos\psi + \dfrac{\bar{\gamma}_0}{2}\kappa_s\bar{r}\left(1 + \dfrac{3}{2}X^2\right)sin\psi & \\
+\dfrac{\bar{\gamma}_0}{2}\kappa_c X\bar{r}_0 e_2(\hat{r})cos2\psi + \dfrac{\bar{\gamma}_0}{2}\kappa_s X\bar{r}_0 e_2(\hat{r})sin2\psi & \hat{r} < 1 \\
\\
\dfrac{\bar{\gamma}_0}{2}\kappa_c X\bar{r}_0 e_3(\hat{r}) + \dfrac{3\bar{\gamma}_0}{4}\kappa_c X^2\bar{r}_0 e_5(\hat{r})cos\psi - \dfrac{3\bar{\gamma}_0}{4}\kappa_s X^2\bar{r}_0 e_5(\hat{r})sin\psi & \\
+\dfrac{\bar{\gamma}_0}{2}\kappa_c X\bar{r}_0 e_4(\hat{r})cos2\psi + \dfrac{\bar{\gamma}_0}{2}\kappa_s X\bar{r}_0 e_4(\hat{r})sin2\psi & \hat{r} > 1 \\
+\dfrac{3\bar{\gamma}_0}{4}\kappa_c X^2\bar{r}_0 e_6(\hat{r})cos3\psi + \dfrac{3\bar{\gamma}_0}{4}\kappa_s X^2\bar{r}_0 e_6(\hat{r})sin3\psi &
\end{cases}
\tag{B.20}
$$

B.2 Inflow Perturbations Due to Cyclic Loading Effect

When rotor bound circulation changes around the azimuth by a $d\bar{\Gamma}$, there is released at the same time a free radial vortex of strength $-d\bar{\Gamma}$ and the free tip vortex strength is increased by a $d\bar{\Gamma}$. The calculation of the induced inflow perturbations due to the cyclic loading distribution around the rotor disk is very complicated. A reduced order model to account for the effect of rotor cyclic loading effect during maneuvering flight is developed in this section. As illustrated in Figures B.1 and B.2, the radial and tip vortex due to rotor cyclic circulation variation will be taken together and it is assumed that they form two cylinders with a circular cross-section. Therefore, two hypothetical rotors will be formed on both sides of the x-axis and y-axis, respectively, to account for the effects of longitudinal circulation variation $\bar{\Gamma}_{1c}$ and lateral circulation variation $\bar{\Gamma}_{1s}$, respectively. Since vortex
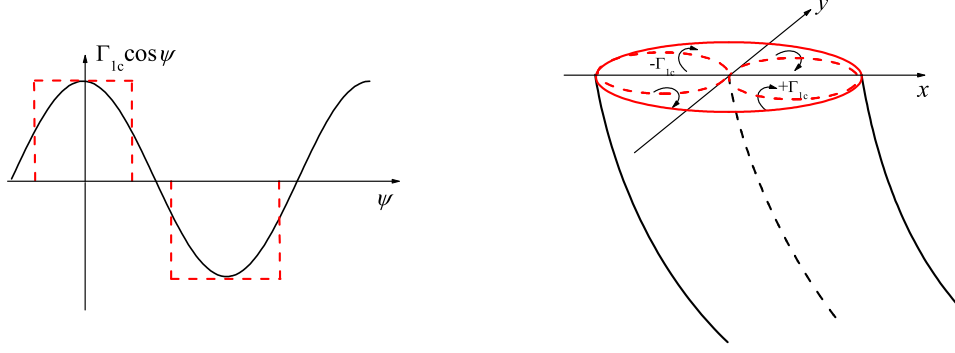
Figure B.1: Simplified approximate method to calculate the inflow perturbation across rotor disk due to the cosine part of cyclic loading during maneuvering flight
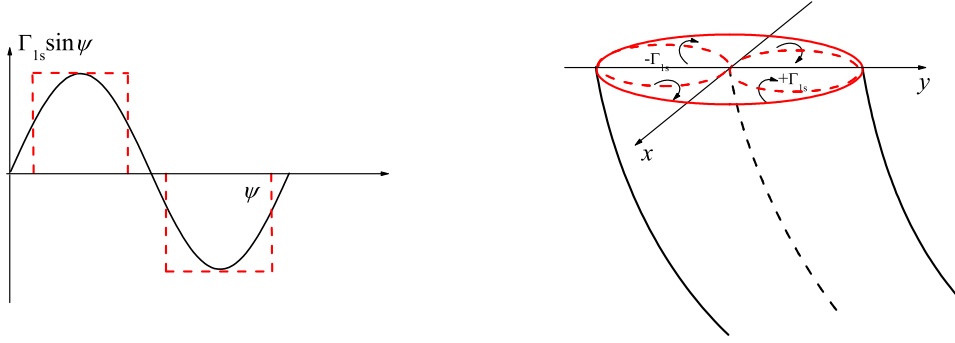
Figure B.2: Simplified approximate method to calculate the inflow perturbations across rotor disk due to the sine part of cyclic loading during maneuvering flight

tubes of the two hypothetical rotors have uniform vorticity density, Equation B.20 can be used to calculate the inflow perturbations due to the cyclic loading effect when the rotor is undergoing a pitch and/or roll motion.

B.2.1 $\bar{\Gamma}_{1c}$ Effect

As shown in Figure B.1, the vortices due to rotor lateral cyclic loading effect are approximated by two hypothetical vortex tubes placed along the x-axis, each of them with a radius of $\bar{r}_0/2$, one tube has a vorticity strength of $\bar{\gamma}_{1c}$ and the other one has a vorticity strength of $-\bar{\gamma}_{1c}$. The inflow perturbations at points A,B,C and D as shown in Figure B.3 can be obtained by using Equation B.20. Only contributions to the mean and first harmonic variations of inflow will be considered and contributions to all the other higher harmonic terms
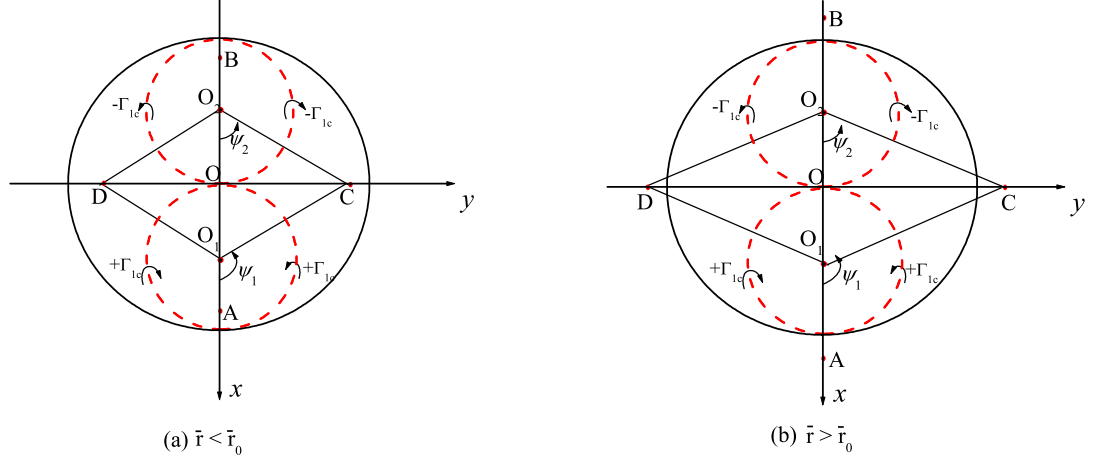
(a) $\bar{r} < \bar{r}_0$

(b) $\bar{r} > \bar{r}_0$

Figure B.3: Illustration of calculation points for the inflow perturbation induced by the cosine part of the cyclic loading during maneuvering flight

will be dropped off. Denoting

$$\bar{r} = |OA| = |OB| = |OC| = |OD| \tag{B.21.a}$$

$$\bar{r}_1 = |O_1A| = |O_2B| = \bar{r} - \frac{\bar{r}_0}{2} \tag{B.21.b}$$

$$\bar{r}_2 = |O_1B| = |O_2A| = \bar{r} + \frac{\bar{r}_0}{2} \tag{B.21.c}$$

$$\bar{r}_3 = |O_1C| = |O_1D| = |O_2C| = |O_2D| = \frac{\sqrt{4\bar{r}^2 + \bar{r}_0}}{2} \tag{B.21.d}$$

and normalizing $\bar{r}$ by $\bar{r}_0$ and $\bar{r}_1, \bar{r}_2, \bar{r}_3$ by $\bar{r}_0/2$ gives rise to

$$\hat{r} = \bar{r}/\bar{r}_0 \quad \hat{r}_1 = 2\hat{r} - 1 \quad \hat{r}_2 = 2\hat{r} + 1 \quad \hat{r}_3 = \sqrt{4\hat{r}^2 + 1} \tag{B.21.e}$$

B.2.1.1 Case I: Calculation Points Inside of Vortex Tube ($\bar{r} < \bar{r}_0$)

The calculation points A, B, C and D are shown in Figure B.3(a). The inflow perturbations at points A, B, C and D can be obtained as

Inflow Perturbation at Point A:

$$\begin{aligned}
(\Delta v_z)_A = \quad & \frac{\bar{\gamma}_{1c}}{2} \left\{ \frac{1}{2}\kappa_c X \bar{r}_0 [e_1(\hat{r}_1) + e_2(\hat{r}_1)] + \kappa_c \bar{r}_1 \left(1 - \frac{3}{2}X^2\right) \right\} \\
& - \frac{\bar{\gamma}_{1c}}{2} \left\{ \frac{1}{2}\kappa_c X \bar{r}_0 [e_3(\hat{r}_2) + e_4(\hat{r}_2)] + \frac{3}{4}\kappa_c X^2 [e_5(\hat{r}_2) + e_6(\hat{r}_2)] \right\}
\end{aligned} \tag{B.22}$$

134

Inflow Perturbation at Point B:

$$(\Delta v_z)_B = \quad \frac{\bar{\gamma}_{1c}}{2} \left\{ \frac{1}{2} \kappa_c X \bar{r}_0 [e_3(\hat{r}_2) + e_4(\hat{r}_2)] - \frac{3}{4} \kappa_c X^2 [e_5(\hat{r}_2) + e_6(\hat{r}_2)] \right\}$$
$$- \frac{\bar{\gamma}_{1c}}{2} \left\{ \frac{1}{2} \kappa_c X \bar{r}_0 [e_1(\hat{r}_1) + e_2(\hat{r}_1)] - \kappa_c \bar{r}_1 \left(1 - \frac{3}{2} X^2 \right) \right\} \qquad \text{(B.23)}$$

Inflow Perturbation at Point C:

$$(\Delta v_z)_C = \quad \frac{\bar{\gamma}_{1c}}{2} \left\{ \kappa_s X \bar{r}_0 e_4(\hat{r}_3) sin2\psi_1 + \frac{3}{2} X^2 \bar{r}_0 \kappa_c [e_5(\hat{r}_3) cos\psi_1 + e_6(\hat{r}_3) cos3\psi_1] \right\}$$
$$\text{(B.24)}$$

Inflow Perturbation at Point D:

$$(\Delta v_z)_D = \quad \frac{\bar{\gamma}_{1c}}{2} \left\{ -\kappa_s X \bar{r}_0 e_4(\hat{r}_3) sin2\psi_1 + \frac{3}{2} X^2 \bar{r}_0 \kappa_c [e_5(\hat{r}_3) cos\psi_1 + e_6(\hat{r}_3) cos3\psi_1] \right\}$$
$$\text{(B.25)}$$

By comparing the inflow perturbations at points A, B, C and D in Equations B.22 through B.25, it can be seen that the contributions to the mean and first harmonic inflow perturbations can be written as

$$\Delta v_z = \quad \frac{\bar{\gamma}_{1c}}{2} \left\{ \kappa_c X \bar{r}_0 d_1(\hat{r}) cos\psi + \kappa_s X \bar{r}_0 d_2(\hat{r}) sin\psi \right\} \qquad \text{(B.26)}$$

where,

$$d_1(\hat{r}) = \quad \frac{1}{2} [e_1(\hat{r}_1) + e_2(\hat{r}_1) - e_3(\hat{r}_2) - e_4(\hat{r}_2)] \qquad \text{(B.27)}$$

$$d_2(\hat{r}) = \quad e_4(\hat{r}_3) sin2\psi_1 = -\frac{4e_4(\hat{r}_3)}{4\hat{r}^2 + 1} \qquad \text{(B.28)}$$

B.2.1.2 Case II: Calculation Points Outside of Vortex Tube ($\bar{r} > \bar{r}_0$)

The calculation points A, B, C and D are shown in Figure B.3(b). The inflow perturbations at points A, B, C and D can be obtained as

Inflow Perturbation at Point A:

$$(\Delta v_z)_A = \quad \frac{\bar{\gamma}_{1c}}{2} \left\{ \frac{1}{2} \kappa_c X \bar{r}_0 [e_3(\hat{r}_1) + e_4(\hat{r}_1)] + \frac{3}{4} \kappa_c X^2 \bar{r}_0 [e_5(\hat{r}_1) + e_6(\hat{r}_1)] \right\}$$
$$- \frac{\bar{\gamma}_{1c}}{2} \left\{ \frac{1}{2} \kappa_c X \bar{r}_0 [e_3(\hat{r}_2) + e_4(\hat{r}_2)] + \frac{3}{4} \kappa_c X^2 \bar{r}_0 [e_5(\hat{r}_2) + e_6(\hat{r}_6)] \right\}$$
$$\text{(B.29)}$$

135

Inflow Perturbation at Point B:

$$(\Delta v_z)_B = \quad \frac{\bar{\gamma}_{1c}}{2}\left\{\frac{1}{2}\kappa_c X\bar{r}_0[e_3(\hat{r}_2) + e_4(\hat{r}_2)] - \frac{3}{4}\kappa_c X^2\bar{r}_0[e_5(\hat{r}_2) + e_6(\hat{r}_2)]\right\}$$
$$-\frac{\bar{\gamma}_{1c}}{2}\left\{\frac{1}{2}\kappa_c X\bar{r}_0[e_3(\hat{r}_1) + e_4(\hat{r}_1)] - \frac{3}{4}\kappa_c X^2\bar{r}_0[e_5(\hat{r}_1) + e_6(\hat{r}_1)]\right\}$$

$$(B.30)$$

Inflow Perturbation at Point C:

$$(\Delta v_z)_C = \quad \frac{\bar{\gamma}_{1c}}{2}\left\{\kappa_s X\bar{r}_0 e_4(\hat{r}_3)sin2\psi_1 + \frac{3}{2}X^2\bar{r}_0\kappa_c[e_5(\hat{r}_3)cos\psi_1 + e_6(\hat{r}_3)cos3\psi_1]\right\}$$

$$(B.31)$$

Inflow Perturbation at Point D:

$$(\Delta v_z)_D = \quad \frac{\bar{\gamma}_{1c}}{2}\left\{-\kappa_s X\bar{r}_0 e_4(\hat{r}_3)sin2\psi_1 + \frac{3}{2}X^2\bar{r}_0\kappa_c[e_5(\hat{r}_3)cos\psi_1 + e_6(\hat{r}_3)cos3\psi_1]\right\}$$

$$(B.32)$$

By comparing the inflow perturbations at points A, B, C and D in Equations B.29 through B.32, it can be seen that the contributions to the mean and first harmonic inflow perturbations can be written as

$$\Delta v_z = \quad \frac{\bar{\gamma}_{1c}}{2}\left\{\kappa_c X\bar{r}_0 d_3(\hat{r})cos\psi + \kappa_s X\bar{r}_0 d_2(\hat{r})sin\psi\right\}$$

$$(B.33)$$

where,

$$d_3(\hat{r}) = \quad \frac{1}{2}\left[e_3(\hat{r}_1) + e_4(\hat{r}_1) - e_3(\hat{r}_2) - e_4(\hat{r}_2)\right]$$

$$(B.34)$$

B.2.2 $\bar{\Gamma}_{1s}$ Effect

As shown in Figure B.1, the vortices due to rotor lateral cyclic loading effect are approximated by two hypothetical vortex tubes placed along the y-axis, each of them with a radius of $\bar{r}_0/2$, one tube has a vorticity strength of $\bar{\gamma}_{1s}$ and the other one has a vorticity strength of $-\bar{\gamma}_{1s}$. The inflow perturbations at points A,B,C and D as shown in Figure B.4 can be obtained by using Equation B.20. Only contributions to the mean and first harmonic variations of inflow will be considered and contributions to all the other higher harmonic terms

(a) $\bar{r} < \bar{r}_0$ (b) $\bar{r} > \bar{r}_0$
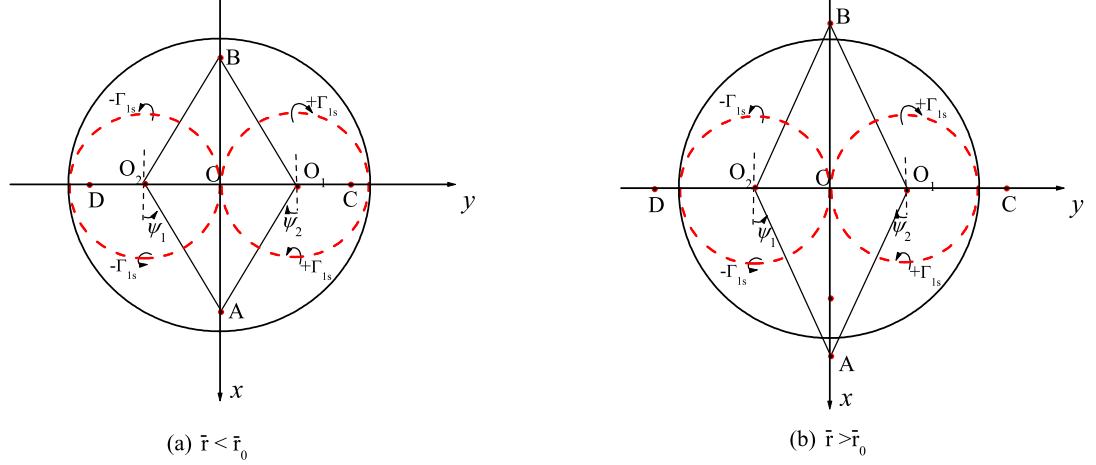
Figure B.4: Illustration of calculation points for the inflow perturbation induced by the sine part of the cyclic loading during maneuvering flight

will be dropped off. Denoting

$$\bar{r} = \quad |OA| = |OB| = |OC| = |OD| \tag{B.35.a}$$

$$\bar{r}_1 = \quad |O_1C| = |O_2D| = \bar{r} - \frac{\bar{r}_0}{2} \tag{B.35.b}$$

$$\bar{r}_2 = \quad |O_1D| = |O_2C| = \bar{r} + \frac{\bar{r}_0}{2} \tag{B.35.c}$$

$$\bar{r}_3 = \quad |O_1A| = |O_1B| = |O_2A| = |O_2B| = \frac{\sqrt{4\bar{r}^2 + \bar{r}_0}}{2} \tag{B.35.d}$$

and ormalizing $\bar{r}$ by $\bar{r}_0$ and $\bar{r}_1, \bar{r}_2, \bar{r}_3$ by $\bar{r}_0/2$ gives rise to

$$\hat{r} = \bar{r}/\bar{r}_0 \quad \hat{r}_1 = 2\hat{r} - 1 \quad \hat{r}_2 = 2\hat{r} + 1 \quad \hat{r}_3 = \sqrt{4\hat{r}^2 + 1} \tag{B.35.e}$$

B.2.2.1   Case I: Calculation Points Inside Vortex Tube ($\bar{r} < \bar{r}_0$)

The calculation points A, B, C and D are shown in Figure B.4(a). The inflow perturbations at points A, B, C and D can be obtained as

Inflow Perturbation at Point A:

$$(\Delta v_z)_A = \quad \frac{\bar{\gamma}_{1s}}{2} \left\{ -\kappa_s X \bar{r}_0 e_4(\hat{r}_3) sin2\psi_1 + \frac{3}{2} X^2 \bar{r}_0 \kappa_s [e_5(\hat{r}_3) sin\psi_1 - e_6(\hat{r}_3) sin3\psi_1] \right\}$$

$$\tag{B.36}$$

137

Inflow Perturbation at Point B:

$$(\Delta v_z)_B = \frac{\bar{\gamma}_{1s}}{2}\left\{\kappa_s X\bar{r}_0 e_4(\hat{r}_3)sin2\psi_1 + \frac{3}{2}X^2\bar{r}_0\kappa_s[e_5(\hat{r}_3)sin\psi_1 - e_6(\hat{r}_3)sin3\psi_1]\right\}$$

(B.37)

Inflow Perturbation at Point C:

$$(\Delta v_z)_C = \frac{\bar{\gamma}_{1s}}{2}\left\{\frac{1}{2}\kappa_c X\bar{r}_0[e_1(\hat{r}_1) - e_2(\hat{r}_1)] + \kappa_s\bar{r}_1\left(1 + \frac{3}{2}X^2\right)\right\}$$
$$- \frac{\bar{\gamma}_{1s}}{2}\left\{\frac{1}{2}\kappa_c X\bar{r}_0[e_3(\hat{r}_2) - e_4(\hat{r}_2)] - \frac{3}{4}\kappa_c X^2[e_5(\hat{r}_2) + e_6(\hat{r}_2)]\right\}$$

(B.38)

Inflow Perturbation at Point D:

$$(\Delta v_z)_D = \frac{\bar{\gamma}_{1s}}{2}\left\{\frac{1}{2}\kappa_c X\bar{r}_0[e_3(\hat{r}_2) - e_4(\hat{r}_2)] + \frac{3}{4}\kappa_s X^2[e_5(\hat{r}_2) + e_6(\hat{r}_2)]\right\}$$
$$- \frac{\bar{\gamma}_{1s}}{2}\left\{\frac{1}{2}\kappa_c X\bar{r}_0[e_1(\hat{r}_1) - e_2(\hat{r}_1)] - \kappa_s\bar{r}_1\left(1 - \frac{3}{2}X^2\right)\right\}$$

(B.39)

By comparing the inflow perturbations at points A, B, C and D in Equations B.36 through B.39, it can be seen that the contributions to the mean and first harmonic inflow perturbations can be written as

$$\Delta v_z = \frac{\bar{\gamma}_{1s}}{2}\left\{\kappa_s X\bar{r}_0 d_2(\hat{r})cos\psi + \kappa_c X\bar{r}_0 d_4(\hat{r})sin\psi\right\}$$

(B.40)

where,

$$d_4(\hat{r}) = \frac{1}{2}\left[e_1(\hat{r}_1) - e_2(\hat{r}_1) - e_3(\hat{r}_2) + e_4(\hat{r}_2)\right]$$

(B.41)

B.2.2.2 Case II: Calculation Points Outside of Vortex Tube $(\bar{r} > \bar{r}_0)$

The calculation points A, B, C and D are shown in Figure B.4(b). The inflow perturbations at points A, B, C and D can be obtained as

Inflow Perturbation at Point A:

$$(\Delta v_z)_A = \frac{\bar{\gamma}_{1s}}{2}\left\{-\kappa_s X\bar{r}_0 e_4(\hat{r}_3)sin2\psi_1 + \frac{3}{2}X^2\bar{r}_0\kappa_s[e_5(\hat{r}_3)sin\psi_1 - e_6(\hat{r}_3)sin3\psi_1]\right\}$$

(B.42)

Inflow Perturbation at Point B:

$$(\Delta v_z)_B = \frac{\bar{\gamma}_{1s}}{2}\left\{\kappa_s X\bar{r}_0 e_4(\hat{r}_3)sin2\psi_1 + \frac{3}{2}X^2\bar{r}_0\kappa_s[e_5(\hat{r}_3)sin\psi_1 - e_6(\hat{r}_3)sin3\psi_1]\right\}$$

(B.43)

Inflow Perturbation at Point C:

$$(\Delta v_z)_C = \quad \frac{\bar{\gamma}_{1s}}{2}\left\{\frac{1}{2}\kappa_c X\bar{r}_0[e_3(\hat{r}_1) - e_4(\hat{r}_1)] - \frac{3}{4}\kappa_s X^2[e_5(\hat{r}_1) + e_6(\hat{r}_1)]\right\}$$

$$-\frac{\bar{\gamma}_{1s}}{2}\left\{\frac{1}{2}\kappa_c X\bar{r}_0[e_3(\hat{r}_2) - e_4(\hat{r}_2)] - \frac{3}{4}\kappa_s X^2[e_5(\hat{r}_2) + e_6(\hat{r}_2)]\right\}$$

$$(B.44)$$

Inflow Perturbation at Point D:

$$(\Delta v_z)_D = \quad \frac{\bar{\gamma}_{1s}}{2}\left\{\frac{1}{2}\kappa_c X\bar{r}_0[e_3(\hat{r}_2) - e_4(\hat{r}_2)] + \frac{3}{4}\kappa_s X^2[e_5(\hat{r}_2) + e_6(\hat{r}_2)]\right\}$$

$$-\frac{\bar{\gamma}_{1s}}{2}\left\{\frac{1}{2}\kappa_c X\bar{r}_0[e_3(\hat{r}_1) - e_4(\hat{r}_1)] + \frac{3}{4}\kappa_s X^2[e_5(\hat{r}_1) + e_6(\hat{r}_1)]\right\}$$

$$(B.45)$$

By comparing the inflow perturbations at points A, B, C and D in Equations B.36 through B.39, it can be seen that the contributions to the mean and first harmonic inflow perturbations can be written as

$$\Delta v_z = \quad \frac{\bar{\gamma}_{1s}}{2}\left\{\kappa_s X\bar{r}_0 d_2(\hat{r})cos\psi + \kappa_c X\bar{r}_0 d_5(\hat{r})sin\psi\right\} \quad (B.46)$$

where,

$$d_5(\hat{r}) = \quad \frac{1}{2}\left[e_3(\hat{r}_1) - e_4(\hat{r}_1) - e_3(\hat{r}_2) + e_4(\hat{r}_2)\right] \quad (B.47)$$

Combining Equations B.26, B.33, B.40 and B.46 gives rise to the inflow perturbations induced by the distorted rotor wake due to rotor cyclic loading effect during a steady pitch and/or roll motion as follows

$$\Delta v_z = \begin{cases} \dfrac{\bar{\gamma}_{1c}}{2}\left\{\kappa_c X\bar{r}_0 d_1(\hat{r})cos\psi + \kappa_s X\bar{r}_0 d_2(\hat{r})sin\psi\right\} \\[2mm] +\dfrac{\bar{\gamma}_{1s}}{2}\left\{\kappa_c X\bar{r}_0 d_4(\hat{r})sin\psi + \kappa_s X\bar{r}_0 d_2(\hat{r})cos\psi\right\} \quad\quad (\hat{r} < 1) \\[4mm] \dfrac{\bar{\gamma}_{1c}}{2}\left\{\kappa_c X\bar{r}_0 d_3(\hat{r})cos\psi + \kappa_s X\bar{r}_0 d_2(\hat{r})sin\psi\right\} \\[2mm] +\dfrac{\bar{\gamma}_{1s}}{2}\left\{\kappa_c X\bar{r}_0 d_5(\hat{r})sin\psi + \kappa_s X\bar{r}_0 d_2(\hat{r})cos\psi\right\} \quad\quad (\hat{r} < 1) \end{cases} \quad (B.48)$$

where $d_i(\hat{r}), i = 1, 2, \ldots, 5$ are defined in Equations B.27, B.28, B.34, B.41 and B.47.

APPENDIX C

MAIN ROTOR/TAIL ROTOR/EMPENNAGE

INTERACTION DURING MANEUVERING FLIGHT

C.1 Equivalent Wake Skew Due To Main Rotor Wake Curvatures

The dynamic wake distortion model developed in Chapter II (Equation 2.27) can be written as

$$
[\tau_D]
\begin{Bmatrix}
X \\
S \\
\kappa_c \\
\kappa_s
\end{Bmatrix}^{\star}
+
\begin{Bmatrix}
X \\
S \\
\kappa_c \\
\kappa_s
\end{Bmatrix}
=
\begin{Bmatrix}
X \\
S \\
\kappa_c \\
\kappa_s
\end{Bmatrix}_{qs}
\tag{C.1}
$$

The augmented Pitt-Peters dynamic inflow model developed in Chapter III (Equation 3.20) during maneuvering flight can be written as

$$
[M]
\begin{Bmatrix}
\lambda_0 \\
\lambda_{1s} \\
\lambda_{1c}
\end{Bmatrix}^{\star}
+
[V][L]^{-1}
\begin{Bmatrix}
\lambda_0 \\
\lambda_{1s} \\
\lambda_{1c}
\end{Bmatrix}
=
\begin{Bmatrix}
C_T \\
-C_L \\
-C_M
\end{Bmatrix}
\tag{C.2}
$$

where the augmented inflow gain matrix $[L]$ can be written as

$$
[L] = [\tilde{L} + \Delta L_1 + \Delta L_2 + \Delta L_3]
\tag{C.3}
$$

where

$$
[\Delta L_1] = K_{Re}
\begin{bmatrix}
0 & 0 & 0 \\
\dfrac{\kappa_s}{2} & 0 & 0 \\
\dfrac{\kappa_c}{2} & 0 & 0
\end{bmatrix}
\tag{C.4.a}
$$

$$
[\Delta L_2] = K_{Re}
\begin{bmatrix}
0 & 0 & 0 \\
\dfrac{3}{4}\kappa_s X^2 & 0 & 0 \\
-\dfrac{3}{4}\kappa_c X^2 & 0 & 0
\end{bmatrix}
\tag{C.4.b}
$$

140

$$[\Delta L_3] = K_{Re} \begin{bmatrix} 0 & 0 & 0 \\ \dfrac{5}{4}\mu\kappa_c X & a_{22} & -\dfrac{5}{2}\kappa_s X \\ \dfrac{5}{4}\mu\kappa_s X & a_{32} & -\dfrac{3}{10}\kappa_c X \end{bmatrix} \qquad (C.4.c)$$

From Equations C.1 and C.2, it can be seen that the wake skew and wake curvatures can be treated as equivalent to each other. From Equations C.4.a, C.4.b, C.4.c, it can be seen that the coupling between the longitudinal inflow gradient and rotor thrust coefficient can be written as

$$\frac{\lambda_{1c}}{\bar{V}} = \left[\frac{15\pi}{64}X + \frac{K_{Re}}{2}\kappa_c\left(1 - \frac{3}{2}X^2\right) + \frac{5K_{Re}}{4}\kappa_s\mu X \right] C_T \qquad (C.5)$$

For low advance ratio μ, using the approximation of

$$X = tan(\frac{\chi}{2}) \approx \frac{\mu}{2(\lambda_0 + V_c)} \qquad (C.6)$$

Equation C.5 can be rewritten as

$$\frac{\lambda_{1c}}{\bar{V}} = \left[\frac{15\pi}{64}X + \frac{K_{Re}}{2}\kappa_c\left(1 - \frac{3}{2}X^2\right) + \frac{5K_{Re}}{2}\kappa_s(\lambda_0 + V_c)X^2 \right] C_T \qquad (C.7)$$

Therefore, an equivalent wake skew due to main rotor wake curvature effect during maneuvering flight can be defined as

$$\Delta X_{eq} = \frac{32K_{Re}}{15\pi}\kappa_c\left(1 - \frac{3}{2}X^2\right) + \frac{32K_{Re}}{3\pi}\kappa_s(\lambda_0 + V_c)X^2 \qquad (C.8)$$

which can also be written approximately in terms of an equivalent wake skew angle as

$$\Delta\chi_{eq} = \frac{64K_{Re}}{15\pi}\kappa_c\left(1 - \frac{3}{2}X^2\right) + \frac{64K_{Re}}{3\pi}\kappa_s(\lambda_0 + V_c)X^2 \qquad (C.9)$$

This equivalent wake skew can be added to the steady wake skew (non-maneuvering) from momentum theory to model the main rotor downwash effect on the tail rotor and empennage during helicopter maneuvering flight.

C.2 Side Wash At Vertical Tail Due to Main Rotor Wake Curvature

When a helicopter is in a roll maneuver, the curved main rotor wake will induce an additional sidewash at the aerodynamic centers of the vertical tail and tail rotor. It is assumed that the the aerodynamic centers of the vertical tail and tail rotor are in the main rotor disk plane

in the following derivations. Also, only the vortex tube with constant vorticity strength $\bar{\gamma}_0$ and tube radius $\bar{r}_0 = 1$, corresponding to the main rotor tip vortex, is considered.

For a helicopter in a roll maneuver, the induced velocity along the y axis of the main rotor disk coordinate can be obtained from the dynamic vortex tube analysis in Appendix A (Equations A.24.c and A.24.d). When the curved wake shape is fully developed, i.e., $\bar{\eta}_0 = \infty$, Equations A.24.c and A.24.d can be written as

$$\nu_y = \frac{\bar{\gamma}_0}{4\pi} \int_0^{2\pi} \int_0^\infty \frac{\left[\bar{\eta}\kappa_s(1 - \hat{r}cos\psi cos\psi_0) - \bar{\eta}sin\psi_0 + 2\bar{\eta}^2\kappa_s X\bar{r}_0 cos\psi_0\right] d\bar{\eta}\, d\psi_0}{\bar{b}^2 + \bar{\eta}^2 - 4\bar{\eta}X(\hat{r}cos\psi - cos\psi_0) - \bar{\eta}^2\kappa_s(\hat{r}sin\psi + sin\psi_0)} \quad \text{(C.10)}$$

Therefore, the induced velocity perturbation at the aerodynamic centers of the vertical tail and tail rotor, $\Delta\nu_y$, due to the roll maneuver can be written as

$$\Delta\nu_y = \frac{\bar{\gamma}_0\kappa_s}{4\pi} \left[A_p + A_{pX}X + A_{pX^2}X^2\right] \quad \text{(C.11)}$$

where,

$$A_p = \int_0^{2\pi} \int_0^\infty \left[\frac{\bar{\eta}(1 - \hat{r}cos\psi cos\psi_0)}{(\bar{b}^2 + \bar{\eta}^2)^{3/2}} - \frac{3\bar{\eta}^3 sin\psi_0(sin\psi_0 + \bar{r}sin\psi)}{2(\bar{b}^2 + \bar{\eta}^2)^{5/2}}\right] d\bar{\eta}\, d\psi_0 \quad \text{(C.12.a)}$$

$$\begin{aligned}A_{pX} &= \int_0^{2\pi} \int_0^\infty \left[\frac{2\bar{\eta}^2 cos\psi_0}{(\bar{b}^2 + \bar{\eta}^2)^{3/2}} + \frac{6\bar{\eta}^2(1 - \hat{r}cos\psi cos\psi_0)(\hat{r}cos\psi - cos\psi_0)}{(\bar{b}^2 + \bar{\eta}^2)^{5/2}}\right] d\bar{\eta}\, d\psi_0 \\ &\quad - \int_0^{2\pi} \int_0^\infty \frac{15\bar{\eta}^4 sin\psi_0(\hat{r}sin\psi + sin\psi_0)(\hat{r}cos\psi - cos\psi_0)}{(\bar{b}^2 + \bar{\eta}^2)^{7/2}} d\bar{\eta}\, d\psi_0\end{aligned} \quad \text{(C.12.b)}$$

$$\begin{aligned}A_{pX^2} &= \int_0^{2\pi} \int_0^\infty \frac{12\bar{\eta}^3 cos\psi_0(\hat{r}cos\psi - cos\psi_0)}{(\bar{b}^2 + \bar{\eta}^2)^{5/2}} d\bar{\eta}\, d\psi_0 \\ &\quad + \int_0^{2\pi} \int_0^\infty \frac{30\bar{\eta}^3(1 - \hat{r}cos\psi cos\psi_0)(\hat{r}cos\psi - cos\psi_0)^2}{(\bar{b}^2 + \bar{\eta}^2)^{7/2}} d\bar{\eta}\, d\psi_0 \\ &\quad - \int_0^{2\pi} \int_0^\infty \frac{105\bar{\eta}^5 sin\psi_0(sin\psi_0 + \hat{r}sin\psi)(\hat{r}cos\psi - cos\psi_0)^2}{(\bar{b}^2 + \bar{\eta}^2)^{9/2}} d\bar{\eta}\, d\psi_0\end{aligned} \quad \text{(C.12.c)}$$

where $\bar{b} = \sqrt{1 + \hat{r}^2 - 2\hat{r}cos(\psi - \psi_0)}$. After making the following substitutions

$$\bar{\eta} = \bar{b}tan\theta \quad d\bar{\eta} = \bar{b}sec^2\theta \quad \text{(C.13)}$$

these integrals can be carried out to be

$$
A_p = \frac{2[(\hat{r}-1)^2 E(k) - \hat{r}^2 F(k)]}{|\hat{r}-1|}
$$
$$
- \frac{2[(\hat{r}^2+1)(\hat{r}-1)^2 E(k) - (\hat{r}^4+\hat{r}^2+1)F(k)]}{3\hat{r}^2|\hat{r}-1|}cos2\psi \tag{C.14.a}
$$

$$
A_{pX} = \frac{\pi\left[(8\hat{r}^2-5\hat{r})cos\psi - 3\hat{r}^2 cos3\psi\right]}{2(\hat{r}-1)} \qquad (\hat{r}<1) \tag{C.14.b}
$$

$$
A_{pX} = \frac{\pi\left[(4\hat{r}^3-7\hat{r}^2)cos\psi - (2\hat{r}^3-5\hat{r}^2-3\hat{r}+3)cos3\psi\right]}{2\hat{r}^3(\hat{r}-1)} \quad (\hat{r}>1) \tag{C.14.c}
$$

$$
A_{pX^2} = \frac{3\left[(\hat{r}^2-1)E(k) - (\hat{r}^2+5)F(k)\right]}{|\hat{r}-1|}
$$
$$
- \frac{4[(7\hat{r}^2+4)(\hat{r}-1)^2 E(k) - (7\hat{r}^4+7\hat{r}^2+4)F(k)]}{3\hat{r}^2|\hat{r}-1|}cos2\psi
$$
$$
- \frac{\left[(3\hat{r}^4-8\hat{r}^2-32)(\hat{r}-1)^2 E(k) - (3\hat{r}^6+7\hat{r}^4-8\hat{r}^2-32)F(k)\right]}{5\hat{r}^4|\hat{r}-1|}cos4\psi
$$
$$
\tag{C.14.d}
$$

Using the fact that $\bar{\gamma}_0 = 2\lambda_0$ (Equation 2.3) and assuming that the aerodynamic centers of the vertical tail and tail rotor lie on the main rotor y axis, the sidewash at the aerodynamic center of horizontal tail due to main rotor wake curvature effect can be written as (expressed along the main rotor $y-$ axis)

$$
\Delta\nu_{y_{MR}}^{VT} = (\kappa_s\lambda_0)_{MR}\left(i_0^{MR} + i_1^{MR}X + i_2^{MR}X^2\right) \tag{C.15}
$$

where subscript VT means that the sidewash are calcualted at the aerodynamic center of the vertical tail and tail rotor, subscript and superscript MR denotes that this effect is due to the main rotor wake curvature. $i_0^{MR}, i_1^{MR}, i_2^{MR}$ are the interference coefficients, which are determined by the relative geometric positions of the main rotor and vertical tail/tail rotor, which are given by

$$
i_0^{MR} = \frac{A_p(\psi^{VT/MR}, \bar{l}^{VT/MR})}{2\pi} \tag{C.16.a}
$$

$$
i_1^{MR} = \frac{A_{pX}(\psi^{VT/MR}, \bar{l}^{VT/MR})}{2\pi} \tag{C.16.b}
$$

$$
i_2^{MR} = \frac{A_{pX^2}(\psi^{VT/MR}, \bar{l}^{VT/MR})}{2\pi} \tag{C.16.c}
$$

where $\psi^{VT/MR}$ is the azimuth angle of the vertical tail/tail rotor in the main rotor disk plane, $\bar{l}^{VT/MR}$ is the distance between main rotor center and the aerodynamic center of vertical tail/tail rotor.

143

C.3 Up/Down Wash At Horizontal Tail Due to Tail Rotor Wake Curvature

When a helicopter is in a roll maneuver, the curved tail rotor wake will also induce an additional up/down wash at the aerodynamic center of the horizontal tail. It is assumed that the the aerodynamic center of the horizontal tail is in the tail rotor disk plane and only a vortex tube with constant vorticity strength $\bar{\gamma}_0$ and tube radius $\bar{r}_0 = 1$, corresponding to the tail rotor tip vortex, is considered.

The up/down wash velocity on the horizontal tail induced by the distorted tail rotor wake can be obtained similarly to the side wash velocity on the vertical tail/tail rotor induced by the distorted main rotor wake and can be formulated as (expressed along the tail rotor y axis)

$$\Delta \nu_y^{HT} = (\kappa_s \lambda_0)_{TR} \left(i_0^{TR} + i_1^{TR} X + i_2^{TR} X^2 \right) \tag{C.17}$$

where subscript HT means that the up/down wash is calculated at the aerodynamic center of the horizontal tail, subscript and superscript TR denotes that this effect is due to the tail rotor wake curvature effect. $i_0^{TR}, i_1^{TR}, i_2^{TR}$ are the interference coefficients, which are determined by the relative geometric positions of the tail rotor and horizontal, which are given by

$$i_0^{TR} = \frac{A_p(\psi^{HT/TR}, \bar{l}^{HT/TR})}{2\pi} \tag{C.18.a}$$

$$i_1^{TR} = \frac{A_{pX}(\psi^{HT/TR}, \bar{l}^{HT/TR})}{2\pi} \tag{C.18.b}$$

$$i_2^{TR} = \frac{A_{pX^2}(\psi^{HT/TR}, \bar{l}^{HT/TR})}{2\pi} \tag{C.18.c}$$

where $\psi^{HT/TR}$ is the azimuth angle of the aerodynamic center of horizontal tail in the tail rotor disk plane, $\bar{l}^{HT/TR}$ is the distance between tail rotor center and the aerodynamic center of horizontal tail.

APPENDIX D

SUMMARY OF ROTOR DYNAMIC WAKE DISTORTION MODEL AND AUGMENTED INFLOW MODELS

For reference, the developed rotor dynamic wake distortion model, the augmented Pitt-Peters dynamic inflow model and the augmented Peters-He finite state inflow model are summarized as follows.

D.1 Rotor Dynamic Wake Distortion Model

The developed rotor dynamic wake distortion model can be written as

$$[\tau_D] \left\{ \begin{array}{c} \overset{\star}{X} \\ S \\ \kappa_c \\ \kappa_s \end{array} \right\} + \left\{ \begin{array}{c} X \\ S \\ \kappa_c \\ \kappa_s \end{array} \right\} = \left\{ \begin{array}{c} X \\ S \\ \kappa_c \\ \kappa_s \end{array} \right\}_{qs} \tag{D.1}$$

where X, S, κ_c, κ_s, are wake skew, wake spacing, longitudinal and lateral wake curvatures, respectively, $\overset{\star}{()}$ denotes differentiation with respect to nondimensional time, subscript qs denotes quasi-steady values. Matrix $[\tau_D]$ contains the nondimensional time constants associated with dynamic wake distortion effects and is assumed to take a diagonal form as

$$[\tau_D] = \begin{bmatrix} \tau_X & & & O \\ & \tau_S & & \\ & & \tau_R & \\ O & & & \tau_R \end{bmatrix} \tag{D.2}$$

Where τ_X, τ_S, τ_R are given by

$$\tau_X = \frac{32}{15\pi\bar{V}} \tag{D.3.a}$$

$$\tau_S = \frac{32}{15\pi V_m} \tag{D.3.b}$$

$$\tau_R = \frac{32}{15\pi\bar{V}} \tag{D.3.c}$$

145

where V_m and $\bar{V}$, respectively, are the mass flow parameters associated with mean and higher harmonics of inflow and are given by

$$V_m = \sqrt{\mu^2 + (\lambda_0 + V_c)^2} \tag{D.4.a}$$

$$\bar{V} = \frac{\mu^2 + (\lambda_0 + V_c)(2\lambda_0 + V_c)}{V_m} \tag{D.4.b}$$

where λ_0 is the mean induced inflow across rotor disk, μ is advance ratio and V_c is climb rate.

The right hand side of Equation D.1 corresponds to the quasi-steady wake skew, wake spacing, longitudinal and lateral wake curvatures, which are given by

$$(X)_{qs} = tan\left(\frac{\chi}{2}\right) \tag{D.5.a}$$

$$(S)_{qs} = 2\pi V_m \tag{D.5.b}$$

$$(\kappa_c)_{qs} = \frac{\bar{q} - \overset{\star}{\beta}_{1c}}{\lambda_0 + V_c} \tag{D.5.c}$$

$$(\kappa_s)_{qs} = \frac{\bar{p} - \overset{\star}{\beta}_{1s}}{\lambda_0 + V_c} \tag{D.5.d}$$

In the above equations, $\bar{q}$ and $\bar{p}$, respectively, denote the nondimensional pitch and roll rates. $\overset{*}{\beta}_{1c}, \overset{*}{\beta}_{1s}$ are the rotor disk longitudinal and lateral flapping rates. χ is the steady wake skew angle given by

$$\chi = tan^{-1}\left(\frac{\mu}{\lambda_0 + V_c}\right) \tag{D.6}$$

D.2   Augmented Pitt-Peters Dynamic Inflow Model

The augmented Pitt-Peters dynamic inflow model for helicopter maneuvering flight can be written as

$$[M]\left\{\begin{array}{c} \overset{\star}{\lambda}_0 \\ \lambda_{1s} \\ \lambda_{1c} \end{array}\right\} + [V][L]^{-1}\left\{\begin{array}{c} \lambda_0 \\ \lambda_{1s} \\ \lambda_{1c} \end{array}\right\} = \left\{\begin{array}{c} C_T \\ -C_L \\ -C_M \end{array}\right\} \tag{D.7}$$

where the apparent mass matrix $[M]$ and mass flow parameter matrix $[V]$, respectively, can be written as

$$[M] = \begin{bmatrix} \dfrac{128}{75\pi} & & O \\ & \dfrac{16}{45\pi} & \\ O & & \dfrac{16}{45\pi} \end{bmatrix} \tag{D.8}$$

$$[V] = \begin{bmatrix} V_m & & O \\ & \bar{V} & \\ O & & \bar{V} \end{bmatrix} \tag{D.9}$$

where V_m and $\bar{V}$ are given by Equations D.4.a and D.4.b. The augmented inflow gain matrix $[L]$ in Equation D.7 can be written as

$$[L] == [\tilde{L} + \Delta L] = [\tilde{L} + \Delta L_1 + \Delta L_2 + \Delta L_3] \tag{D.10}$$

where $[\tilde{L}]$ is the original inflow gain matrix, $[\Delta L_1]$ denotes coupling between wake curvature and rotor mean loading. $[\Delta L_2]$ accounts for the coupling effect between wake curvature/wake skew and rotor mean loading, and matrix $[\Delta L_3]$ represents the coupling effect between wake curvature/wake skew and rotor cyclic loading. They can expressed as

$$[\tilde{L}] = \begin{bmatrix} \dfrac{1}{2} & 0 & -\dfrac{15\pi}{64}X \\ 0 & 2(1+X^2) & 0 \\ \dfrac{15\pi}{64}X & 0 & 2(1-X^2) \end{bmatrix} \tag{D.11}$$

$$[\Delta L_1] = K_{Re} \begin{bmatrix} 0 & 0 & 0 \\ \dfrac{\kappa_s}{2} & 0 & 0 \\ \dfrac{\kappa_c}{2} & 0 & 0 \end{bmatrix} \tag{D.12}$$

$$[\Delta L_2] = K_{Re} \begin{bmatrix} 0 & 0 & 0 \\ \dfrac{3}{4}\kappa_s X^2 & 0 & 0 \\ -\dfrac{3}{4}\kappa_c X^2 & 0 & 0 \end{bmatrix} \tag{D.13}$$

$$[\Delta L_3] = K_{Re} \begin{bmatrix} 0 & 0 & 0 \\ \dfrac{5}{4}\mu\kappa_c X & l_{22} & -\dfrac{5}{2}\kappa_s X \\ \dfrac{5}{4}\mu\kappa_s X & l_{32} & -\dfrac{3}{10}\kappa_c X \end{bmatrix} \tag{D.14}$$

with

$$l_{22} = -\frac{5}{2}\kappa_c X - \frac{3\mu}{2}\kappa_s\left(1+\frac{3}{2}X^2\right)$$

$$l_{32} = -\frac{5}{2}\kappa_s X - \frac{3\mu}{2}\kappa_c\left(1-\frac{3}{2}X^2\right)$$

where K_{Re} is the wake curvature parameter.

D.3   Augmented Peters-He Finite State Inflow Model

The augmented Peters-He finite state inflow model for helicopter maneuvering flight can be written as

$$[K] \left\{ \begin{array}{c} \overset{\star}{\alpha^r_j} \\ \beta^r_j \end{array} \right\} + [V][L]^{-1} \left\{ \begin{array}{c} \alpha^r_j \\ \beta^r_j \end{array} \right\} = \frac{1}{2} \left\{ \begin{array}{c} \tau^{mc}_n \\ \tau^{ms}_n \end{array} \right\} \tag{D.15}$$

where $[K]$ and $[V]$, respectively, are the apparent mass matrix and the mass flow parameter matrix given by He [48]. The augmented inflow gain matrix $[L]$ can be written as

$$[L] = \left[[\tilde{L}] + [\Delta L] \right] \tag{D.16}$$

In Equation D.16, $[\tilde{L}]$ retains its original form from the Peters-He finite state inflow model, $[\Delta L]$ accounts for the inflow perturbations induced by the distorted wake tube during maneuvering flight, which can be written as

$$[\Delta L] = K_{Re} \left([D]_0 + [D]_1 X + [D]_2 X^2 \right) \tag{D.17}$$

where

$$[D]_0 = \kappa_c [C]_{c1} + \kappa_s [C]_{s1} \tag{D.18.a}$$

$$[D]_1 = \kappa_c [C]_{cX} + \kappa_s [C]_{sX} \tag{D.18.b}$$

$$[D]_2 = \kappa_c [C]_{cX^2} + \kappa_s [C]_{sX^2} \tag{D.18.c}$$

where K_{Re} is the wake curvature parameter, the $[C]$'s matrices denote coupling effects among rotor inflow, wake curvatures and wake skew. For example, $[C]_{c1}$ and $[C]_{s1}$ denote coupling effect between rotor inflow, longitudinal and lateral wake curvatures, respectively. $[C]_{cX}$ and $[C]_{sX}$, respectively, denote the inflow-wake curvatures-linear wake skew coupling effect. Similarly, $[C]_{cX^2}$ and $[C]_{sX^2}$, respectively, represent the inflow-wake curvatures-quadratic wake skew coupling effect.

REFERENCES

[1] Padfield, G. D., *Helicopter Flight Dynamics: The Theory and Application of Flying Qualities and Simulation Modeling*, AIAA Education Series, 1995.

[2] Crawford, C. C., "Rotorcraft Analytical Improvement Needed to Reduce Development Risk-The 1989 Alexander A. Nikolsky Lecture," *Journal of the American Helicopter Society*, Vol. 35, No. 1, 1990.

[3] Anon., *Helicopter Simulator Qualification*, Advisory Circular, FAA AC No. 120-64, October 1994.

[4] Takahashi, M. D., *A Flight Dynamic Helicopter Mathematical Model with a Single Flap-Lag-Torsion Main Rotor*, NASA TM 102267, USAAVSCOM TM 90A004, Feburary 1990.

[5] Chaimovitch, M., Rosen, A., Mansur, M. H., and Tischler, M. B., "Investigation of the Flight Mechanics Simulation of a Hovering Helicopter," *the 48th Annual Forum of the American Helicopter Society*, Washington, D.C., June 1999, pp. 1237–1256.

[6] He, C. J. and Lewis, W. D., "A Parametric Study of Real-Time Mathematical Modeling Incorporating Dynamic Wake and Elastic Blades," *the 48th Annual Forum of the American Helicopter Society*, Washington, D.C., June 1999, pp. 1181–1196.

[7] Tischler, M. B., Driscoll, J. T., Cauffman, M. G., and Freedman, C. J., "Study of Bearingless Main Rotor Dynamics from Frequency Response Wind Tunnel Test Data," *American Helicopter Society Aeromechanics Specialists Conference*, San Francisco, CA, Jan 19-21 1994.

[8] Harding, J. W. and Bass, S. M., "Validation of a Flight Simulatio Model of the AH-64 Apache Attack Helicopter Against Flight Test Data," *the American Helicopter Society 46th Annual Forum*, Washington D.C., May 1990.

[9] Eshow, M. M., Orlandi, I. D., and Bonaita, D. G., "Results of an A109 Simulation Validation and Handling Qualities Study," *14th European Rotorcraft Forum*, Milano, Italy, September 1998.

[10] Prouty, R. W., "The Case of the Cross-Coupling Mystery," *Rotor and Wing*, Vol. 28, No. 6, 1994, pp. 48–49.

[11] Von Grünhagen, W., "Dynamic Inflow Modeling for Helicopter Rotors and Its Influence on the Prediction of Cross-Couplings," *Proceedings of the AHS Aeromechanics Specialists Conference*, Bridgeport,CT, October 1995.

[12] Ballin, M. G. and Dalang-Secretan, M. A., "Validation of the Dynamic Response of a Blade-Element UH-60 Simulation Model in Hovering Flight," *proceedings of the American Helicopter Society 46th Annual Forum*, Washington D.C., May 1990.

[13] Mansur, H. M. and Tischler, M. B., "An Empirical Correction Method for Improving Off-Axis Response Prediction in Component Type Flight Mechanics Helicopter Model," *AGARD Flight Vehichle Integration Panel on Advances in Rotorcraft Technology*, Ottawa, Canada, May 1996.

[14] Mansur, M. H. and Tischler, M. B., "An Empirical Correction for Improving Off-Axes Responses in Flight Mechanics Helicopter Models," *Journal of the American Helicopter Society*, Vol. 43, No. 2, April 1998, pp. 94–102.

[15] Takahashi, M. D., Fletcher, J. W., and Tischler, M. B., "Development of a Model Following Control Law for Inflight Simulation Using Analytical and Identifed Models," *Proceedings of the 51st Annual Forum of the American Helicopter Society*, Ft. Worth, Texas, May 1995.

[16] Tischler, M. B., "Identification of Bearingless Main Rotor Dynamic Characteristics from Frequency-Response Wind-Tunnel Test Data," *Journal of the American Helicopter Society*, January 1999, pp. 63–76.

[17] Fletcher, J. M. and Tischler, M. B., "Improving Helicopter Flight Mechanics Models with Laser Measurements of Flapping," *American Helicopter Society 53th Annual Forum Proceedings*, Virginia Beach, VA, April 29-May 1 1997.

[18] Simons, I. A. and Modha, A. N., "Gyroscopic Feathering Moments and the "Bell Stabilizer Bar" on Helicopter Rotors," *the 2002 European Rotorcraft Forum*, Bristol, England, September 17-20 2002, pp. 90.1–90.8.

[19] Rosen, A. and Isser, A., "A New Model of Rotor Dynamics During Pitch and Roll of a Hovering Helicopter," *Journal of the American Helicopter Society*, Vol. 40, No. 3, July 1995, pp. 17–28.

[20] Rosen, A. and Isser, A., "A Model of the Unsteady Aerodynamics of a Hovering Helicopter Rotor That Includes Variations of the Wake Geometry," *Journal of the American Helicopter Society*, , No. 3, July 1995, pp. 6–16.

[21] Bagai, A., Leishman, J. G., and Park, J. S., "Aerodynamic Analysis of a Helicopter in Steady Maneuvering Flight Using a Free-Vortex Rotor Wake Model," *Journal of the American Helicopter Society*, April 1999, pp. 109–120.

[22] Park, J. S. and Leishman, J. G., "Investigation of Unsteady Aerodynamics on Rotor Wake Effects in Maneuvering Flight," *the 55th Annual Forum of the American Helicopter Society*, Montreal, Cananda, May 25-27 1999.

[23] Bhagwat, M. J. and Leishman, J. G., "Rotor Aerodynamics During Maneuvering Flight Using Time-Accurate Free-Vortex Wake," *the 57th Annual Forum of the American Helicopter Society*, Washington, DC, May 9-11 2001.

[24] Bhagwat, M. J., *Mathematical Modeling of the Transient Dynamics of Rotor Wakes Using A Time-Accurate Free Vortex Method*, Ph.D. thesis, Department of Aerospace Engineering, University of Maryland at College Park, College Park, MD, 2001.

[25] Theodore, C. and Celi, R., "Prediction of the Off-Axis Response to Cyclic Pitch Using a Maneuvering Free Wake Model," *Twenty Fifth European Rotorcraft Forum*, Rome, Italy, September 14-16 1999.

[26] Basset, P.-M., "Modeling of the Dynamic Inflow on the Main Rotor and the Tail Components in Helicopter Flight Mechanics," *Proceedings of the 22nd European Rotorcraft Forum*, Brighton,UK, September 1996.

[27] Basset, P.-M., "Study of the Rotor Wake Distortion Effects on the Helicopter Pitch-Roll Cross-Couplings," *Proceedings of the 24th European Rotorcraft Forum*, Marseilles,France, September 1998.

[28] Basset, P. M. and Elomari, A., "A Rotor Vortex Wake Model For Helicopter Flight Mechanics and Its Applications to the Prediction of The Pitch-Up Phenomena," *25th European Rotorcraft Forum*, Rome, Italy, September 14-16 1999.

[29] Keller, J. D., "An Investigation of Helicopter Dynamic Coupling Using an Analytical Model," *Journal of the American Helicopter Society*, October 1996, pp. 322–330.

[30] Keller, J. D. and Curtiss, H. C., "Modeling the Induced Velocity of a Maneuvering Helicopter," *the Amernican Helicopter Society 52th Annual Forum*, Washington D.C, June 4-6 1996.

[31] Keller, J. D. and Curtiss, H. C., "A Critical Examination of the Methods to Improve the Off-Axis Response Prediction of Helicopters," *the American Helicopter 54th Annual Forum*, Washington D.C., May 1998, pp. 1134–1147.

[32] Arnold, U. T. P., Keller, J. D., Curtiss, H. C., and Rechert, G., "The Effect of Inflow Models on the Predicted Response of Helicopters," *Journal of the American Helicopter Society*, January 1998, pp. 25–36.

[33] Arnold, U. T. P., Keller, J. D., and Curtiss, H. C., "The Effect of Inflow Models on the Dynamic Response of Helicopters," *21th European Rotorcraft Forum*, Saint-Petersburg, Russia, August 30-September 1 1995.

[34] Schulein, G., *Improvements to a High Fidelity Helicopter Math Model*, Master's thesis, California Polytechnic State University, San Luis Obispo, 1999.

[35] Rosen, A., "Approximate Actuator Disk Model of a Rotor in Hover or Axial Flow Based on Vortex Modeling," *Journal of American Helicopter Society*, Vol. 49, No. 1, 2004, pp. 66–79.

[36] Rosen, A., "Approximate Actuator Disk Model of a Rotor in Hover or Axial Flow Based on Potential Flow Equations," *Journal of the American Helicopter Society*, Vol. 49, No. 1, 2004, pp. 80–92.

[37] Barocela, E. B., Peters, D. A., Krothapalli, K. R., and Prasad, J. V. R., "The Effect of Wake Distortion on Rotor Inflow Gradients and Off-Axis Coupling," *Proceedings of the Atmospheric Flight Mechanics Conference of the American Institute of Aeronautics and Astronautics*, New Orleans, Louisiana, August 1997.

[38] Barocela, E. B., *The Effect of Wake Distortion on Dynamic Inflow for Lifting Rotors*, Master's thesis, School of Mechanical Engineering, Washington University, St. Louis, Missouri, 1997.

[39] Krothapalli, K. R., Prasad, J. V. R., and Peters, D. A., "Improved Wake Geometry Model for a Maneuvering Rotor," *Proceedings of the American Helicopter Society Technical Specialists' Meeting for Rotorcraft Acoustics and Aerodyamics*, Williamsburg, Virginia, October 1997.

[40] Krothapalli, K. R., Prasad, J. V. R., and Peters, D. A., "Development of a Comprehensive Wake Theory for Lifting Rotors," *Proceedings of the Atmospheric Flight Mechanics Conference of the American Institute of Aeronautics and Astronautics*, San Diego, California, July 1996.

[41] Krothapalli, K. R., *Helicpoter Rotor Dynamic Inflow Modeling For Maneuvering FLight*, Ph.D. thesis, School of Aerospace Engineering, Georgia Institute of Technology, Atlanta, Georgia, 1998.

[42] Krothapalli, K. R., Prasad, J. V. R., and Peters, D. A., "Helicpoter Rotor Dynamic Inflow Modeling For Maneuvering FLight," *Journal of the American Helicopter Society*, Vol. 46, No. 2, 2001.

[43] He, C., Lee, C. S., and Chen, W., "Rotorcraft Simulation Model Enhancement to Support Design, Testing and Operational Analysis," *the Amernican Helicopter Society 55th Annual Forum*, Montreal, Canada, May 25-27 1999.

[44] Bagai, A. and Leishman, J. G., "Rotor Free-Wake Modeling Using a Pseudo-Implicit Algorithm," *Journal of Aircraft*, Vol. 32, No. 6, 1996.

[45] Bagai, A. and Leishman, J. G., "Adaptive Grid Sequencing and Interpolation Schemes for Helicotper Rotor Wake Analysis," *AIAA Journal*, Vol. 36, No. 9, 1998.

[46] Leishman, J. G., *Principles of Helicopter Aerodynamics*, Cambridge University Press, 2000.

[47] Pitt, D. M. and Peters, D. A., "Theoretical Prediction of Dynamic Inflow Derivatives," *Vertica*, Vol. 5, No. 1, 1981.

[48] He, C., *Development and Application of a Generalized Dynamic Wake Theory for Lifting Rotors*, Ph.D. thesis, School of Aerospace Engineering, Georgia Institute of Technology, Atlanta, Georgia, 1989.

[49] Lewis, W. D., *An Aeroelastic Model Structure Identification for a Manned Real-Time Rotorcraft Simulation*, Ph.D. thesis, School of Aerospace Engineering, Georgia Institute of Technology, Atlanta, Georgia, 1992.

[50] Sturisky, S., *A Linear System Identification and Validation of an AH-64 Apache Aeroelastic Simulation Model*, Ph.D. thesis, School of Aerospace Engineering, Georgia Institute of Technology, Atlanta, Georgia, 1983.

[51] Schulein, G. J., Tischler, M. B., Mansur, M. H., and Rosen, A., "Validation of Cross-Coupling Modeling Improvements for UH-60 Flight Mechanics Simulations," *Journal of the American Helicopter Society*, Vol. 47, No. 3, July 2002, pp. 209–213.

[52] He, C.-J., "Finite State Dynamic Wake Interference Modeling for Rotorcraft Simulation," *the American Helicopter 53th Annual Forum*, Virginia Beach, Virginia, April 29-May 1 1997.

152

[53] Howlett, J. J., "UH-60 Black Hawk Engineering Simulation Program, Volume I-Mathematical Model," Tech. rep., NASA CR 166309, December 1981.

[54] Abott, W. Y., Benson, J. O., Oliver, R. G., and Williams, R. A., "Validation Flight Test of UH-60A for Rotorcraft Systems Integration Simulator," Tech. rep., Final Report USAAEFA Project, No. 79-24, September 1982.

[55] Prasad, J. V. R., Zhao, J., and Peters, D. A., "Modeling of Rotor Dynamic Wake Distortion During Helicopter Maneuvering Flight," *the 2001 AIAA Atmosphere Flight Mechanics Conference*, Montreal, Canada, August 6-9 2001.

[56] Prasad, J. V. R., Franciullo, T., Zhao, J., and Peters, D. A., "Toward a High Fidelity Inflow Model for Maneuvering and In-Ground Effect Flight Simulation," *the Amernican Helicopter Society 57th Annual Forum*, Washington D.C., May 9-11 2001.

[57] Johnson, W., *Helicopter Theory*, Dover Publications, Inc., 1990.

[58] Zhao, J., Prasad, J. V. R., and Peters, D. A., "Rotor Dynamic Wake Distortion Model for Helicopter Maneuvering Flight," *the 58th Annual Forum of the American Helicopter Society*, Montreal, Canada, 2002.

[59] Zhao, J., Prasad, J. V. R., and Peters, D. A., "Simplified Dynamic Wake Distortion Model for Helicopter Transitional Flight," *the 2002 AIAA Atmospheric Flight Mechanics Conference*, Monterey, California, Augest 5-8 2002.

[60] Prasad, J. V. R., Zhao, J., and Peters, D. A., "Helicopter Rotor Dynamic Wake Distortion Models for Maneuvering Flight," *the 28th European Rotorcraft Forum*, Bristol, UK, September 17-20 2002.

[61] Dress, J. M., "A Theory of Airflow Through Rotors and Its Applications to Some Helicopter Problem," *Journal of the helicopter association of great britain*, Vol. 3, No. 2, 1949.

[62] Kell, J. D., *The Effect of Rotor Motion on the Induced Velocity In Predicting the Response of Rotorcraft*, Ph.D. thesis, Department of Mechanical and Aerospace Engineering, Princeton University, Princeton, NJ, 1998.

[63] Prouty, R. W. and Amer, K. B., "The YAH-64 Empennage and Tail Rotor-A Technical History," *American Helicopter Society 38th Annual Forum Proceedings*, May 4-7.

[64] Peters, D. A. and Cao, W., "Off-Rotor Induced Flow by a Finite State Wake Model," *37th AIAA SDM Conference*, Salt Lake City, Utah, April 15-17 1996.

[65] Heyson, H. and Katzoff, S., "Induced Velocities Near A Lifting Rotor With Nonuniform Disk Loading," Tech. rep., NACA Report 1319, 1956.

[66] Yin, J. and Ahmed, S. R., "Helicopter Main Rotor-Tail Rotor Interaction," *Journal of the American Helicopter Society*, Vol. 45, No. 4, 2000, pp. 293–302.

[67] Sheridan, P. F. and Smith, R. F., "Interactional Aerodynamics-A New Challenge to Helicopter Technology," *Journal of the American Helicopter Society*, Vol. 25, No. 1, 1980, pp. 3–22.

[68] McCrosky, W. J., "Vortex Wakes of Rotorcraft," *AIAA paper 95-0530*, 1995.

[69] Leishman, J. G. and Bi, N., "Experimental Investigation of Rotor/Lifting Surface Interactions," *Journal of Aircraft*, Vol. 31, No. 4, July-August 1994.

[70] Torok, M. S. and Ream, D. T., "Investigation of Empennage Airloads Induced by a Helicopter Main Rotor Wake," *American Helicopter Society 49th Annual Forum Proceedings*, St. Louis, MO, May 1993.

[71] Frederickson, K. C. and Lamb, J. R., "Experimental Investigation of Main Rotor Wake Induced Vibratory Empennage Airloads for the RAH-66 Comanche Helicopter," *American Helicopter Society 49th Annual Forum Proceedings*, St. Louis, MO, May 1993.

[72] Funk, R. B. and Komerath, N. M., "Rotor Wake Interaction with a Lifting Surface," *American Helicopter Society 51th Annual Forum Proceedings*, Ft. Worth, TX, May 1995.

[73] Foley, S. M., Funk, R. B., and Komerath, N. M., "Rotor-Wake-Induced Flow Separation on a Lifting Surface," *Journal of the American Helicopter Society*, Vol. 40, No. 2, April 1995.

[74] Gangwani, S. T., "Calculation of Rotor Wake Induced Empennage Airloads," *Journal of the American Helicopter Society*, Vol. 29, No. 2, April 1983.

[75] Mello, O. and Rand, O., "Unsteady Frequency Domain Analysis of Helicopter Non-Rotating Lifting Surfaces," *Journal of the American Helicopter Society*, Vol. 36, No. 2, April 1991.

[76] Weinstock, S., "Formulation of a Simplified Model of Rotor-Horizontal Stabilizer Interactions and Comparison with Experimental Measurements," *17th European Rotorcraft Forum*, Berlin, Germany, September 1991.

[77] Howe, M. S., "On Unsteady Surface Forces, and Sound Produced by the Normal Chopping of a Rectilinear Vortex," *Journal of Fluid Mechanics*, Vol. 206, September 1989.

[78] Zhao, J., Prasad, J. V. R., and Peters, D. A., "Study of Rotor Wake Curvature Dynamics For Helicopter Maneuvering Flight," *the 2003 AIAA Atmospheric Flight Mechanics Conference*, Austin, TX, 2003.

[79] Zhao, J., Prasad, J. V. R., and Peters, D. A., "Rotor Dynamic Wake Distortion Model for Helicopter Maneuvering Flight," *Journal of the American Helicopter Society*, Vol. 49, No. 4, October 2004, pp. 414–424.

[80] Mansur, M. H. and Tischler, M. B., "An Empirical Correction Method for Improving Off-Axis Response in Flight Mechanics Helicopter Models," *Journal of the American Helicopter Society*, Vol. 43, No. 2, 1998, pp. 94 102.

[81] Leishman, J. G. and Nguyen, K. Q., "State-Space Representation of Unsteady Airfoil Behavior," *AIAA journal*, Vol. 28, No. 5, May 1990, pp. 836–844.

[82] Leishman, J. G., "Modeling of Subsonic Unsteady Aerodynamics for Rotary Wing Applications," *Journal of the American Helicopter Society*, January 1990, pp. 29–38.

[83] Leishman, J. G., "Practical Modeling of Unsteady Airfoil Behavior in Nominally Attached Two-Dimensional Compressible Flow," April 1987.

[84] Leishman, J. G., "Validation of Approximate Indicial Aerodynamic Functions for Two-Dimensional Subsonic Flow," *Journal of Aircraft*, Vol. 25, No. 10, October 1988, pp. 914–922.

[85] Beddoes, T. S., "Practical Computation of Unsteady Lift," *Vertica*, Vol. 8, No. 1, 1984, pp. 55–71.

[86] Johnson, W., "Rotorcraft Aerodynamics Models for a Comprehensive Analysis," *the 54th Annual Forum of the American Helicopter Society*, Washington, DC, 1998.

[87] Liou, S. G., Komerath, N. M., and McMahon, H. M., "Measurement of the Interaction Between a Rotor Tip Vortex and a Cylinder," *AIAA Journal*, Vol. 28, No. 6, June 1990.

[88] Liou, S. G., Komerath, N. M., and McMahon, H. M., "An Unsteady Helicopter Rotor-Fuselage Aerodynamic Interaction Analysis," *Journal of the American Helicopter Society*, Vol. 35, No. 3, July 1990.

[89] Freeman, C. E., "Development and Validation of a Combined Rotor-Fuselage Induced Flow-Field Computational Method," Tech. rep., NASA TP-1656, June 1980.

[90] Leishman, J. G. and Bi, N. P., "Measurement of a Rotor Flowfield and the Effects on a Fuselage in Forward Flight," *Vertica*, Vol. 14, No. 3, 1990, pp. 401–415.

[91] Leishman, J. G. and Bi, N. P., "Investigation of Rotor Tip Vortex Interactions with a Body," *Journal of Aircrat*, Vol. 30, No. 6, 1993, pp. 879–888.

[92] Mavris, D. N., Komerath, N. M., and McMahon, H. M., "Prediction of Aerodynamic Rotor-Airframe Interactions in Forward Flight," *Journal of the American Helicopter Society*, Vol. 34, No. 4, October 1989.

[93] Crouse, G. L., Leishman, J. G., and Bi, N. P., "Theoretical and Experimental Study of Unsteady Rotor/Body Aerodynamic Interactions," *Journal of the American Helicopter Society*, Vol. 37, No. 4, January 1992.

[94] Quackenbush, T. R., "Vortex Method for the Computational Analysis of Rotor/Body Interaction," *American Helicopter Society 48th Annual Forum Proceedings*, May 1992.

[95] Radcliff, T. D. and Burggraf, O. R., "Modeling of the Collision of a Rotor-Tip Vortex with an Airframe," *35th AIAA Aerospace Science Meeting, AIAA-97-0658*, Reno, Nv, January 1997.

[96] Chaffin, M. S. and Berry, J. D., "Helicopter Fuselage Aerodynamics Undera Rotor by Navier-Stokes Simulation," *Journal of the American Helicopter Society*, Vol. 42, No. 3, July 1997.

[97] Berry, J. D., Letnikov, V., Bavykina, I., and Chaffin, M. S., "A Comparison of Interactional Aerodynamics Methods for a Helicopter in Low Speed Flight," Tech. rep., NASA TM-1998-208420, June 1998.

[98] Zhao, J., Xu, G. H., and Gao, Z., "Investigation of Unsteady Aerodynamic Interference Between Rotor/Bodies by Free Wake Method and Comparison with Experimental Results," *Journal of Nanjing University of Aeronautics and Astronautics*, 2000.

[99] Boyd, D. and Barnwell, R., "A Computational Model for Rotor-Fuselage Interactional Aerodynamics," *38th AIAA Aerospace Science Meeting and Exhibit, AIAA-2000-0256*, Reno, Nv, January 10-13 2000.

[100] Renaud, T., Brien, D., and Smith, M., "Evaluation of Isolated Fuselage and Rotor-Fuselage Interaction Using CFD," *American Helicopter Society 60th Annual Forum Proceedings*, Baltimore, MD, June 7-10 2004.

[101] Xin, H., *Development and Validation of a Generalized Ground Effect Model for Lifting Rotors*, Ph.D. thesis, School of Aerospace Engineering, Georgia Institute of Technology, Atlanta, Georgia, 1999.

[102] Zhao, J., Prasad, J. V. R., and Peters, D. A., "Investigation of Wake Curvature Dynamics for Helicopter Maneuvering Flight Simulation," *American Helicopter Society 59th Annual Forum Proceedings*, Phoenix, Arizona, May 6-8 2003.

[103] Tischler, M. B. and Cauffman, M. G., "Frequency Response Method for Rotorcraft System Identification: Flight Applications to BO-105 Rotor/Fuselage Identification," *journal of the American Helicopter Society*, Vol. 37, No. 3, July 1992, pp. 3–17.

VITA

Jinggen Zhao was born on August 14, 1975 in Jing'An county, JiangXi Province, People's Republic of China. He joined Nanjing University of Aeronautics & Astronautics (NUAA) for his undergraduate study in Aerospace Engineering with a specialization in Helicopter Design Technology, where he received his Bachelor of Science degree in July, 1997. He continued to engage in his graduate study in Aerospace Engineering at NUAA with a specialization in Helicopter Aerodynamics and Flight Mechanics, and received his Master of Science degree in March 2000, with research performed under the supervision of Professor Z. Gao and Prefosser G.H. Xu, titled "Study On Helicopter Rotor/Body Aerodynamic Interaction". In August of 2000 he joined the School of Aerospace Engineering at the Georgia Institute of Technology to pursue his Ph.D degree. His thesis work was performed under the supervision of Professor J.V.R. Prasad, titled "Dynamic Wake Distortion Model For Helicopter Maneuvering Flight". He was awarded the Vertical Fight Foundation Scholarship in 2002. He is a student member of the American Institute of Aeronautics and Astronautics and a student member of the American Helicopter Society.